

Abstract

SAYED, ISLAM ESMAT MOHAMED MOHAMED HASHEM SAYED. Quantum Wells to Improve the Performance of III/V Multi-junction Solar Cells. (Under the direction of Dr. Salah M. Bedair.)

The current state of the art solar cells based on four-junction III/V materials have realized efficiencies of ~46% under high solar concentration. Multiple studies have reported that improving the efficiency of solar cells to higher than 50% will reduce the cost of solar (\$/watt) and might open new opportunities in the solar photovoltaic concentrator market. In this dissertation, we aim to develop a new approach to enhance the efficiency and reduce the cost of solar (\$/watt) through providing new materials and device architectures that can be part of next-generation photovoltaic devices with target efficiencies higher than 50%.

This dissertation demonstrates two novel quantum well structures that can be part of next-generation five (or more) junction devices with a prospective efficiency higher than 50% under high solar concentration. The first quantum well structure is strain-balanced InGaAsP/InGaP quantum wells, where the InGaAsP quantum well is grown under compressive stress and the InGaP barrier is grown under tensile stress. The second quantum well structure is lattice-matched InGaAsP/InGaP, where InGaAsP and InGaP layers have lattice constants similar to the underlying substrate. In both structures, the quantum wells are included in the unintentionally doped region of $\text{In}_{0.49}\text{Ga}_{0.51}\text{P}$ p-i-n on GaAs substrates. The two quantum well structures are characterized and analyzed by optical microscopy, X-ray diffraction, photoluminescence, current-voltage characteristics, and external quantum efficiency.

We demonstrate that the two quantum well solar cells can extend the absorption threshold of InGaP-based cells from 1.85 eV to the 1.5-1.8 eV range. In the strain-balanced InGaAsP/InGaP quantum well structure, external quantum efficiency and light current-voltage measurements indicate that minority carriers generated in the depletion and quantum well regions are transported by drift through thermionic emission. In the lattice-matched InGaAsP/InGaP quantum well structure, the carriers are transported across the barriers by tunneling through an electric field. The sub-bandgap external quantum efficiency of lattice-matched InGaAsP/InGaP QW solar cell is higher than 75% at 700 nm. The bandgap-voltage offset of these quantum well devices indicates excellent voltages while maintaining efficient carrier

transport for both electrons and holes. The short circuit current density of the lattice-matched InGaAsP/InGaP quantum well solar cell is 26% higher than that of a standard InGaP cell that does not include quantum wells.

To incorporate these quantum well structures in next-generation multi-junction solar cells, more optimization of quantum well absorption is essential. This can be realized through reducing background doping to enhance the carrier transport and reducing the stress across the quantum well region.

© Copyright 2018 by Islam Esmat Mohamed Mohamed Hashem Sayed
All Rights Reserved

Quantum Wells to Improve the Performance of III/V Multi-junction Solar Cells

by
Islam Esmat Mohamed Mohamed Hashem Sayed

A dissertation submitted to the Graduate Faculty of
North Carolina State University
in partial fulfillment of the
requirements for the degree of
Doctor of Philosophy

Electrical Engineering

Raleigh, North Carolina

2018

APPROVED BY:

Salah M. Bedair
Chair of Advisory Committee

Robert Kolbas

Mehmet Ozturk

Nadia El-Masry

Dedication

To my parents: Samia Azzazi and Esmat Hashem,

To my brother, Amr,

To my sister, Marwa

Biography

I was born in Cairo, Egypt on October 4th, 1988. My father, Esmat, is a mechanical engineer and former Colonel in the Egyptian Army, and my mother, Samia, is an accountant manager. My love for mathematics and physics has driven me to join the faculty of engineering at Cairo University. In 2010, I received the B.Sc. (Hons.) in Electronics and Electrical Communications Engineering. In the same year, I joined the staff at the Department of Engineering Physics, Cairo University, as a teaching and research assistant. From 2011 to 2013, I was research assistant at The Youssef Jameel Center for Science and Technology, The American University in Cairo. My masters research project was about developing nano-rectennas for infrared energy harvesting.

Under the direction of Prof. S. M. Bedair, I started my Ph.D. journey at North Carolina State University in 2013. During my Ph.D., I interned with the III/V group at the National Renewable Energy Laboratory. My Ph.D. research investigated new materials and device architectures for next-generation photovoltaic devices. During my MSc and Ph.D. graduate career, I have authored or co-authored more than 15 publications in the field of renewable energies. I received first place award at the 2016 NCSU ECE GSA research symposium, first place award at the 2017 State Energy Conference of North Carolina, overall grand prize award at the 5th annual North Carolina MRS Triangle Student Research Competition, third place award at the 2017 NCSU ECE GSA research symposium, and second place-best oral presenter award at the Carolina Science Symposium. I was a finalist at the 2017 Three Minute Thesis Competition organized by NCSU Graduate School and a finalist in best student paper award competition at the 44th IEEE Photovoltaic Specialist Conference (PVSC). In 2017, I was named Preparing the Professoriate Fellow by NCSU Graduate School.

I plan to work as a postdoctoral researcher at the University of California, Santa Barbara, after my Ph.D. graduation.

Acknowledgments

I am indebted to my Ph.D. advisor, Dr. S. M. Bedair, for giving me an invaluable opportunity to work under his supervision at NCSU. I value all what Dr. Bedair has taught me through our discussions about my research and life as a scientist. Thank you for helping me grow into the researcher that I am today. There is no doubt that Dr. Bedair's exceptional love for science has a great impact on my graduate career and that my life would be very different today if I did not work under his supervision.

I would like to thank my advisory committee, Dr. Mehmet Öztürk, Dr. Robert Kolbas, and Dr. Nadia El-Masry. I have a great respect for their research, and I am thankful that they agreed to serve on my committee.

I would like to thank the current and former members of the Bedair group who helped me immensely to progress with my research. I would like to thank Zachary Carlin for mentoring me at the beginning of my research career at NCSU. I thank Zach for many useful discussions that enriched our research and for being my friend. I would like to thank Peter Colter for all the “sciency” conversations that I will certainly miss. Peter is one of the most knowledgeable people that I have worked with and he helped me considerably as I progressed with my research. Thanks to Brandon Hagar for his valuable input on my project. Thanks to Brent Allen for helping me progress faster in the MOCVD lab during my first few weeks. I would like to thank current and former members of the LED group, Dennis Van Den Broeck, Deon Bharrat, William Campbell, and Judi Reynolds, for many useful discussions. I would like also to thank Mostafa Abdelhamid whose exceptional personality made my life inside and outside the lab more fun.

During my Ph.D., I had an invaluable opportunity to conduct research at the National Renewable Energy Laboratory (NREL). I would like to thank my scientific mentors John Geisz and Myles Steiner for mentoring me, for their great flexibility, and for always being open for discussions. I would like to thank Nikhil Jain, Daniel Friedman, Kevin Schulte, W. E. McMahon, John Simon, Emmett Perl, Katie Sautter and Adele Tamboli for very useful

discussions. I would like to thank Waldo Olavarria for the MOVPE growth of my QW samples and Michelle Young for processing my devices. I would like to thank Nasser Karam for facilitating this opportunity for me.

This research was supported by the National Science Foundation: GoalI 1102060 and 1407772. The research conducted at NREL was supported by the U.S. Department of Energy under contract no. DE-AC36-08GO28308.

I would like to thank my friends in Raleigh who were my family while I am thousand miles away from Egypt.

A few weeks before the completion of this research, a great and very humble person has left our world with a pleasant smile on his face, my uncle Abdelaziz. I love you and will always miss you.

Finally, I would like to thank my parents, Samia Azzazi and Esmat Hashem, for their unconditional love, daily encouragement, and for having my education as a top priority in their life. I would like to thank my sister Marwa and my brother Amr for their love and support.

This dissertation would not have been possible without everyone I acknowledged here!

Table of Contents

List of Tables	ix
List of Figures.....	x
Chapter 1: Introduction	1
1.1. P-N Junction.....	2
1.2. P-N Junction under Illumination	7
1.3. Losses in Single-junction Solar Cells	11
1.4. Multi-junction Solar Cells.....	14
1.5. Research Objectives	17
1.6. Synopsis of Dissertation.....	19
Chapter 2: Principles of Quantum Well Solar Cells.....	21
2.1. Motivation	21
2.2. Quantum Well Solar Cells (Review).....	22
2.2.1. Quantum Well Material Systems.....	24
2.2.2. Advantages of Quantum Well Solar Cells.....	25
2.3. Bandgap Tunability	27
2.4. Critical Layer Thickness Constraints	29
2.5. Strain Balance Design and Criteria	31
2.6. Carrier Transport	33
Chapter 3: Review of Recent Progress in Quantum Well Solar Cells	37
3.1. Strain-balanced InGaAs/GaAsP Quantum Wells (1.1-1.3 eV Subcell).....	37
3.2. Strained InGaN/GaN Quantum Wells (> 2.1 eV subcell).....	42
Chapter 4: Growth and Characterization of Strain-Balanced InGaP-based Quantum Wells.....	48
4.1. Motivation	48
4.2. Potential Solar Cells with Bandgaps in the 1.6-1.8 eV range	49
4.3. Experimental Approaches	52
4.3.1. Growth details.....	53
4.3.2. Fabrication Details.....	55
4.3.3. Characterization Details	56

4.4. Results and Discussion.....	56
4.4.1. Well and Barrier Calibrations	56
4.4.2. Critical Layer Thickness Constraints.....	58
4.4.3. Zero-stress Balance Model and X-ray Diffraction.....	59
4.4.4. Optical Microscopy.....	61
4.4.5. Photoluminescence Results of InGaAsP/InGaP and InGaP/InGaP SBMQWs (emission and modeling).....	61
4.4.6. Quantum Efficiency and Light Current-voltage Characteristics	64
Chapter 5: Strain-balanced InGaAsP/ InGaP Quantum Well Solar Cells	67
5.1. Introduction	67
5.2. Experimental Details	68
5.3. Results and Discussion.....	69
5.3.1. Photoluminescence and Electroluminescence of SBMQWs: red-shift	70
5.3.2. X-ray Diffraction	72
5.3.3. Carrier Transport and Well Thickness Effect.....	73
5.3.4. Quantum Efficiency and Current Voltage Characteristics (well thickness effects)	74
5.3.5. Quantum Efficiency: Measurements and Modeling	79
5.3.6. Effect of Number of Period on InGaAsP/InGaP SBMQWs	80
5.4. Advantages and Limitations of Strain-balanced InGaAsP/InGaP Quantum Well Solar Cells	85
Chapter 6: Growth and Characterization of Lattice-matched InGaAsP/InGaP Quantum Wells.....	87
6.1. Introduction	87
6.2. Experimental Details	89
6.3. Results and Discussion.....	91
6.3.1. Effect of Arsenic to Phosphorus Ratio in InGaAsP on Stress and XRD Peaks Sharpness	91
6.3.2. Effect of Substrate Miscut	95
6.3.3. Effect of Growth Interruptions	98
6.3.4. Growth of 100-period QW with minimal stress relaxation	100

Chapter 7: Lattice-matched InGaAsP/ InGaP Quantum Well Solar Cells.....	102
7.1. Introduction	102
7.2. Experimental Details	104
7.3. Results and Discussion.....	104
Chapter 8: Photon recycling in multi-junction solar cells using the Inter-Metallic Bonding Approach: Concept	114
8.1. Motivation	114
8.2. Current status of photon recycling and light trapping in “single-junction” cells.....	116
8.3. Current status and approaches of photon recycling in “MJ solar cells” and limitations (Review).....	118
8.3.1. Use of Distributed Bragg Reflectors (DBRs)	118
8.3.2. Use of buried Al ₂ O ₃ through lateral oxidation of AlAs [172].....	118
8.3.3. Use of n = 1.5 epoxy as a reflector and ZnS as an antireflection coating [173].	119
8.3.4. Use of photoresist to print one cell on another	120
8.4. Photon recycling in 2J tandem cells by an Intermetallic Bonding (IMB) approach..	120
8.5. Analysis of photon recycling in dual-junction solar cell structures: Open circuit voltage and external Luminescence efficiency	122
8.6. Analysis of photon recycling in dual-junction solar cell structures: Air gap effects .	125
8.6.1. Modeling the front and back reflectance across multiple layers	125
8.6.2. Front and back reflectance results	127
Chapter 9: Summary and Future Outlook.....	130
9.1. Summary of Research	130
9.2. Challenges and Future Outlook.....	132
9.2.1 Stress management issue	134
9.2.2 Carrier transport issue.....	134
9.2.3 Electric field and background doping issue.....	134
Bibliography	139

List of Tables

Table 3.1: Tunneling (P_{tun}) and thermionic-emission (P_{therm}) escape probabilities for electrons and heavy hole states for different InGaAs/GaAsP QW designs	39
Table 5.1: Thickness of well and barrier, peak PL emission, short circuit current density, open circuit voltage, bandgap-voltage offset (W_{oc}), FF and efficiency (η) for standard cell and SBMQW cells. The devices did not contain antireflection coatings or a window.	74
Table 5.2: Number of periods, grown MQW layer thickness, short circuit current density, open circuit voltage, and fill factor for series of InGaAsP/InGaP SBMQW cells. The devices did not contain antireflection coatings or windows.	81
Table 7.1: One-sun AM1.5 short circuit current contribution of the QWs (ΔJ_{sc}), effective junction bandgap (E_g), open circuit voltage (V_{oc}), and bandgap-voltage offset (W_{oc}) for the studied samples.....	106
Table 7.2: Tunneling escape and thermionic emission escape probabilities for electrons and heavy hole states.....	112
Table 8.1: Comparison between the ideal V_{oc} of the tandem cell connected using the three approaches of Figure 8.7, as calculated by Eqn. (8.1). The expressions for the η_{ext} in the figures are from ref. [167]	124

List of Figures

Figure 1.1: (a) schematic of p-n junction, (b) doping concentration profile of InGaP p-n junction.....	2
Figure 1.2: Schematics of $\text{In}_{0.49}\text{Ga}_{0.51}\text{P}$ p-n junction at thermal equilibrium (zero-bias/without illumination): (a) Energy band diagram, showing the drift and diffusion carriers' components. The horizontal black dotted line is the Fermi level, (b) charge density within space charge region, (c) electric field distribution, and (d) electrostatic potential. Simulations were performed using PC1D.....	3
Figure 1.3: (a) Band profiles and (b) carrier densities for an $\text{In}_{0.49}\text{Ga}_{0.51}\text{P}$ p-n junction at zero bias (blue) and forward bias (red). (c) Band profiles and (d) carrier densities for an $\text{In}_{0.49}\text{Ga}_{0.51}\text{P}$ p-n junction at zero bias (blue)and reverse bias (red). The arrows in Figures (a) and (c) show the direction of the electron and hole transport following forward and reverse bias.....	5
Figure 1.4: Measured dark current-voltage characteristics of InGaP p/n junction, grown and processed at NCSU.....	6
Figure 1.5: The solar spectrum irradiance, AM0, AM1.5G, and AM1.5D	7
Figure 1.6: (a) Illuminated P-N junction, (b) energy band diagram and (c) carrier densities for illuminated InGaP p-n junction. The arrows in Figure (b) show the direction of the electron and hole transport following photo-generation.....	8
Figure 1.7: Measured dark and illuminated current-voltage characteristics of $\text{In}_{0.49}\text{Ga}_{0.51}\text{P}$ p-n junction. The figure also shows the metrics that are used to assess the solar cell performance, V_{oc} , J_{sc} , and maximum power point.	10
Figure 1.8: Energy band diagram of a PN junction with incident photons of energies higher than, equal to, or less than the bandgap, showing both the thermalization and sub-bandgap losses that exist in single-junction solar cells... ...	12
Figure 1.9: Schematics of AM1.5 spectrum showing the thermalization and sub-bandgap losses for single junction solar cells: (a) silicon, with an E_g of 1.1 eV, (b) subcell, with an E_g of 1.70 eV.	13
Figure 1.10: Thermalization loss, sub-bandgap loss, and total loss in ideal single-junction solar cells, versus the bandgap. The ultimate efficiency values are calculated assuming only the thermalization and sub-bandgap losses are	

included. The efficiency will be more reduced if radiative-recombination and SRH recombination losses are included. These calculations were performed on the AM1.5G spectrum.....	14
Figure 1.11: Multi-junction solar cell concept.....	15
Figure 1.12: Schematics of AM1.5 spectrum showing the thermalization and sub-bandgap losses for multi-junction solar cell devices: (a) dual-junction structure (1.7eV/1.1 eV), (b) six-junction structure (2.1 eV/1.7 eV/1.4 eV/1.1 eV/0.91 eV/0.7 eV).	15
Figure 1.13: Cumulative loss from carrier thermalization to the band edges of single-junction 1.1 eV, three-junction (1.87/1.4/0.7 eV), and six-junction (2.1 eV/1.7 eV/1.4 eV/1.1 eV/0.91 eV/0.7 eV) devices. The integrated power density of AM1.5G is 1000 watt/m ²	16
Figure 1.14: Quantum well solar cells	17
Figure 1.15: Schematic of photon dynamic in multi-junction cells with an ideal reflector placed at the back of the top cell. Antireflection coatings (ARCs) are not shown for simplicity. This will be experimentally realized using the using the Inter-Metallic Bonding (IMB) Approach [28]	19
Figure 2.1: Schematics of: (a) GaAs p-i-n solar cell that includes strain-balanced InGaAs/GaAsP quantum wells, grown on GaAs substrate, and (b) GaN p-i-n solar cell that includes strained InGaN/GaN quantum wells, grown on GaN templates on sapphire substrate.....	23
Figure 2.2: Bandgap versus lattice constants showing the well and barrier compositions for the three QW structures in Figure 1: (a) strain-balanced InGaAs/GaAsP QWs, and (b) strained InGaN/GaN QWs. The vertical dotted line in each figure represents the lattice-matched condition to GaAs/GaN. The horizontal dotted lines represent the region of interest in each QW structure.	24
Figure 2.3: Effective bandgap versus well thickness (t_w) for various indium compositions in wells for the following structures: (a) strain-balanced InGaAs/GaAs _{0.35} P _{0.65} , and (b) strained InGaN/GaN. The barrier thickness (t_b) of GaAs _{0.35} P _{0.65} was adjusted to achieve the strain-balance condition. The GaN barrier thickness was fixed at 80 Å.....	29
Figure 2.4: Critical layer thickness versus the indium content for: (a) In _x Ga _{1-x} As well, and (b) In _x Ga _{1-x} N well.....	30

Figure 2.5: Thickness of wells and barriers as estimated by zero-stress balance model to strain-balance the following two structures to GaAs substrates: InGaAs/GaAs _{0.35} P _{0.65} with various indium% in InGaAs well. The CLT of each well composition is added to the figure.	32
Figure 2.6: Band diagram of quantum well solar cells with two different designs: (a) structure with thin wells and low effective barrier height to promote thermionic emission, and (b) structure with thin barriers to allow carrier tunneling. In both scenarios, the carriers are swept across the depletion region by an electric field.	34
Figure 3.1: External quantum efficiency of multiple InGaAs/GaAsP quantum well solar cells designs: (a) structure with thin wells and low effective barrier height to promote thermionic emission, by Adams et al. [69], (b) structure with thin barriers to allow carrier tunneling, by Bradshaw et al.[41, 70], and (c) high-performance structure with peak excitonic values exceeding 70%, by Fuji et al. [40]. More details about these structures such as the presence of window, back surface field or antireflection coatings are discussed in the references.....	38
Figure 3.2: AM1.5 current-voltage characteristics of InGaAs/GaAsP QW and GaAs standard solar cells, with the inset showing a schematic of the two structures, by Fuji et al. [40].	41
Figure 3.3: The effect of the number of QWs in the intrinsic region on one-sun AM0 current-voltage characteristics: (a) J_{sc} (mA/cm ²) and V_{oc} (Volts) and (b) FF and η ; study by Bushnell et al. [78].....	42
Figure 3.4: External quantum efficiency of InGaN/GaN QW solar cells with high indium percentage ($x > 0.2$): (a) eight periods of In _{0.30} Ga _{0.70} N ($t_w = 30 \text{ \AA}$)/GaN ($t_b = 80\text{\AA}$) that has a cut-off wavelength at ~450 nm, by Dahal et al. [43] and (b) 30-period In _{0.28} Ga _{0.72} N ($t_w = 22 \text{ \AA}$)/GaN ($t_b = 80\text{\AA}$) that has a cut-off wavelength at ~500 nm by Farrell et al. [46], that includes heavily doped GaN layers to help in screening the polarization-induced in the QW region and rough GaN window to reduce front reflection	43
Figure 3.5: 1.2 suns AM1.5 current-voltage characteristics of 30-period In _{0.28} Ga _{0.72} N ($t_w = 22 \text{ \AA}$)/GaN ($t_b = 80\text{\AA}$) by Farrell et al. [46], with the inset showing a schematic of this structure.....	44
Figure 3.6: The effect of the number of QWs in the intrinsic region on 1.2-suns AM1.5G current-voltage characteristics: (a) J_{sc} (mA/cm ²) and V_{oc} (Volts) and (c) FF and η ; study by Farrell et al. [46].....	45

Figure 4.1: Potential solar cells for the 1.6-1.8 eV bandgap range: (a) AlGaAs solar cell lattice matched to GaAs substrate, (b) Bulk InGaAsP solar cell lattice matched to GaAs substrate, and (c) proposed InGaAsP/InGaP quantum wells, strain-balanced or lattice-matched, to GaAs substrates.....	50
Figure 4.2: Contours for miscibility gap of InGaAsP at different growth temperatures from ref. [105]. The hashed red dotted lines represent the miscibility gap region for the InGaAsP. The orange dotted line represents the compositions of InGaAsP that are lattice-matched to GaAs substrates. InGaAsP with composition that lead to a 1.7 eV is immiscible.	51
Figure 4.3: Schematics of (a) InGaP <i>p-i-n</i> solar cell structure, (b) $In_xGa_{1-x}As_{1-z}P_z$ / $In_yGa_{1-y}P$ ($x > y$) SBMQWs, and (c) $In_xGa_{1-x}P$ / $In_yGa_{1-y}P$ ($x > y$) SBMQWs.	54
Figure 4.4: (a) Indium compositions of InGaP with [TMIn]/[TMGa]. (b) Arsenic compositions of GaAsP with [TBP]/[TBAs]. The substrate temperature is 585 °C for the two presented SBMQWs.....	57
Figure 4.5: Calculated critical layer thickness using Matthews and Blakeslee model of: (a) $In_xGa_{1-x}As_{1-z}P_z$ and $In_xGa_{1-x}P$ wells used in strain-balanced $In_xGa_{1-x}As_{1-z}P_z$ / $In_yGa_{1-y}P$ and $In_xGa_{1-x}P$ / $In_yGa_{1-y}P$ quantum wells, respectively, (b) $In_yGa_{1-y}P$ barrier used in the two strain-balanced QW structures.....	58
Figure 4.6: Thickness of wells and barriers as estimated by zero-stress balance model to strain-balance both the $In_{0.70}Ga_{0.30}As_{0.05}P_{0.95}$ / $In_{0.40}Ga_{0.60}P$ and $In_{0.75}Ga_{0.25}P$ / $In_{0.40}Ga_{0.60}P$ structures to the GaAs substrates.....	59
Figure 4.7: Single crystal XRD of (a) $In_{0.70}Ga_{0.30}As_{0.05}P_{0.95}$ / $In_{0.40}Ga_{0.60}P$ and (b) $In_{0.75}Ga_{0.25}P$ / $In_{0.40}Ga_{0.60}P$ SBMQWs, of 30 periods.....	60
Figure 4.8: Nomarski interference contrast micrographs of the 30 periods InGaAsP/InGaP MQWs. (a) A mirrorlike surface indicates that the MQWs is closely lattice matched to the GaAs substrate. (b) Crosshatching feature indicates misfit dislocations in the MQW structure.....	61
Figure 4.9: Experimental and modeling results of the emission wavelength (energy) versus well thickness for both $In_{0.70}Ga_{0.30}As_{0.05}P_{0.95}$ / $In_{0.40}Ga_{0.60}P$ and $In_{0.75}Ga_{0.25}P$ / $In_{0.40}Ga_{0.60}P$ SBMQWs.....	62
Figure 4.10: External quantum efficiency (EQE) for (a) $In_{0.70}Ga_{0.30}As_{0.05}P_{0.95}$ / $In_{0.40}Ga_{0.60}P$ SBMQWs and InGaP standard <i>p-i-n</i> device, and (b) $In_{0.75}Ga_{0.25}P$ /	

In _{0.40} Ga _{0.60} P SBMQWs and InGaP standard p-i-n device. No window or antireflection coatings are used.....	64
Figure 4.11: Illuminated current voltage characteristics for In _{0.70} Ga _{0.30} As _{0.05} P _{0.95} / In _{0.40} Ga _{0.60} P SBMQWs and InGaP standard p-i-n device. No window or antireflection coatings are used.....	66
Figure 5.1: Schematics of (a) the InGaAsP/GaInP SBMQW structure grown on a GaAs substrate and (b) the energy band diagram of SBMQW, illustrating thermionic emission dominating the current transport in this structure. The compressive stress in InGaAsP wells is balanced by the tensile stress in GaInP barriers. The MQWs are grown unintentionally doped. The doping level used here for the emitter and base 1 x 10 ¹⁷ and 1 x 10 ¹⁸ cm ⁻³ , respectively. The thickness of the well is altered in this study to tune the emission of the wells and understand the carrier transport. The well and barrier thicknesses are adjusted for each structure to achieve the strain-balanced condition.....	68
Figure 5.2: The (a)photoluminescence spectra and (b) photoluminescence spectra, for a series of In _{0.70} Ga _{0.30} As _{0.05} P _{0.95} / In _{0.40} Ga _{0.60} P, 30-period MQW with varying well thickness. The MQWs tune the bandgap of GaInP to lower energy values. The emission energy decreases with the increase of the well thickness. Thicker wells exhibit wider full width half maximum and lower intensity.....	71
Figure 5.3: The peak PL emission of In _{0.70} Ga _{0.30} As _{0.05} P _{0.95} /Ga _{0.60} In _{0.40} P SBMQWs versus 1/t _w ² . EGInGaAsP, relaxed = 1.54 eV, ΔEGStrain = 56 meV. ΔEGQCSE and ΔEGQSE varies with the well thickness. The measured values for the thick wells do not follow the trend as the thin ones due to relaxation taking place for layers approaching the critical layer thickness.	72
Figure 5.4: Single XRD Diffraction of In _{0.70} Ga _{0.30} As _{0.05} P _{0.95} / Ga _{0.60} In _{0.40} P SBMQWs of thin-well (t_w = 45 Å) device and thick-well device (t_w = 75 Å).	73
Figure 5.5: External quantum efficiency (EQE) versus wavelength (energy) for series of SBMQWs with different well thickness and GaInP standard device measured at room temperature. SBMQWs exhibit absorption beyond the band-edge of GaInP due to the inclusion of the quantum wells in the intrinsic region of the p-i-n structure. MQW with thick wells exhibits poor quantum efficiency.	75
Figure 5.6: External quantum efficiency (EQE) versus wavelength (energy) for SBMQW3 measured at room temperature and 100 °C in addition to the standard device. The well thickness of the SBMQW device is 75Å. The EQE degrades at high temperature for thick-well devices.....	76

Figure 5.7: External quantum efficiency (EQE) versus wavelength (energy) for SBMQW2 measured at different temperatures in addition to the standard device. The well thickness of the SBMQW device is 55Å.....	77
Figure 5.8: 1 sun current density vs voltage curves for the standard GaInP cell and SBMQW devices. Thin-well SBMQWs have higher J _{sc} in comparison to the standard device. Thick-well SBMQW device has degraded current.....	78
Figure 5.9: Modeling of external quantum efficiency of strain-balanced InGaAsP/InGaP quantum well solar cells showing the contributions of the emitter, base, and quantum wells into the total response.....	79
Figure 5.10: XRD scans for samples SBMQW10, SMQW20, SBMQW30 and SBMQW45.....	82
Figure 5.11: External quantum efficiency for $\text{In}_{0.70}\text{Ga}_{0.30}\text{As}_{0.05}\text{P}_{0.95}/\text{In}_{0.40}\text{Ga}_{0.60}\text{P}$ with varying number of periods.....	83
Figure 5.12: Effect of number of quantum wells on J _{sc}	83
Figure 5.13: Simulation of the maximum depletion width as a function of p-type background doping at zero bias. The intrinsic carrier concentration (n _i) used was 100 cm ⁻³	84
Figure 5.14: Simulation of the impact of the number of quantum wells on the electric field across the MQW region at zero bias for a constant background p-type background doping equals to $4 \times 10^{15} \text{ cm}^{-3}$	84
Figure 5.15: External quantum efficiency of strain-balanced InGaAsP/InGaP showing two challenges that are hindering further development: (a) critical layer thickness limitation, (b) background doping constraints and its impact on the depletion region width.....	86
Figure 6.1: Illustration of the working principle of MOSS. A courtesy of Dieter Stender and Aline Fluri.	90
Figure 6.2: <i>in-situ</i> curvature monitoring of a series of $\text{In}_{0.32}\text{Ga}_{0.68}\text{AsP}/\text{In}_{0.49}\text{Ga}_{0.51}\text{P}$ quantum wells with fixed group III flows and various arsenic to phosphorus ratio, $x = [\text{AsH}_3]/([\text{AsH}_3] + [\text{PH}_3])$. The data of each sample is shifted by 0.5 m ⁻¹ along the vertical axis for visual clarity. The vertical dotted lines indicate the start and the end of QWs growth. The QWs in this study were grown on 6°A substrates.....	92

Figure 6.3: Stress-times-thickness of a series of $\text{In}_{0.32}\text{Ga}_{0.68}\text{As}_y\text{P}_{1-y}/\text{In}_{0.49}\text{Ga}_{0.51}\text{P}$ quantum wells as a function of thickness. The vertical dotted lines indicate the start and the end of QWs growth and the data of each sample is shifted by 1000 GPa*A along the vertical axis for visual clarity. The QWs in this study were grown on 6°A substrates	93
Figure 6.4: (004) XRD scans of a series of $\text{In}_{0.32}\text{Ga}_{0.68}\text{As}_y\text{P}_{1-y}/\text{In}_{0.49}\text{Ga}_{0.51}\text{P}$ quantum wells with fixed group III flows and various arsenic to phosphorus ratio. The QWs in this study were grown on 6°A substrates.....	95
Figure 6.5: Photoluminescence spectra of a series of $\text{In}_{0.32}\text{Ga}_{0.68}\text{As}_y\text{P}_{1-y}/\text{In}_{0.49}\text{Ga}_{0.51}\text{P}$ quantum wells with fixed group III flows and various arsenic to phosphorus ratio. The QWs in this study were grown on 6°A substrates	96
Figure 6.6: Effects of quantum wells growth on 6°A and 2°B substrates: (a) (004) XRD scans, (b) PL emission, and (c) 2PE- TRPL decays.....	97
Figure 6.7: Effect of growth interruptions on quantum wells.....	99
Figure 6.8: Stress-thickness versus thickness as a function of thickness, of a series of InGaAsP/InGaP QWs with 20 periods (MP159), 40 periods (MP161 and MP189), and 100 periods (MP197). The stress is calculated using Eqn. (6.2) for each structure from the fit slope. The curvature of each sample is shifted along the vertical axis for visual clarity and the vertical dotted lines indicate the start and the end of the growth of these QWs. The QWs in this study were grown on 2°B substrates	101
Figure 7.1: (left) Schematic of lattice matched InGaAsP/InGaP superlattice structure, grown in the unintentionally doped <i>i</i> layer in $\text{In}_{0.49}\text{Ga}_{0.51}\text{P}$ n-i-p solar cell structure. Samples were grown with an optional 1.2 μm GaAs filter, and two samples of each device structure were processed separately, with and without etching the GaAs filter. (right) schematic of the energy band diagram, illustrating tunneling and thermionic-emission carrier transports in this structure.....	103
Figure 7.2: External quantum efficiency (EQE) beyond the band-edge of $\text{In}_{0.49}\text{Ga}_{0.51}\text{P}$ (680 nm) versus wavelength, of InGaAsP/InGaP superlattice solar cell with different number of period. All samples are coated with ZnS/MgF ₂ . EQE showing improvements over strain balanced InGaAsP/InGaP QW approach....	105

Figure 7.3: External quantum efficiency (EQE) and photoluminescence (PL) spectra of (a) 20-period device (MP159) and (b) 100-period device (MP197), with and without ARC, processed with a gold BSR and with back-filter.	108
Figure 7.4: Light IV characteristics of 100-period device (MP197), with and without ARC, with a gold BSR and with back-filter.	110
Figure 7.5: Dark current voltage characteristics of 20-period QW device (MP159) and 100-period QW device (MP197), with a BSR and with a back-filter. The dotted lines represent diodes with ideality factors n = 1, n=1.5, and n=2.....	111
Figure 8.1: Photon dynamic of solar cells at open circuit voltages: (a) cell grown on substrate, (b) cell grown with epitaxial lift-off approach where photon recycling is taking place.....	115
Figure 8.2: Schematic of photon dynamic in multi-junction cells with an ideal reflector placed at the back of top cell. Antireflection coatings (ARCs) are not shown for simplicity.....	116
Figure 8.3: (a) solar cell with no surface texturing or back reflector, (b) solar cells with rear surface texturing.....	118
Figure 8.4: Previous activities for applying photon recycling in MJ solar cells. (a) DBRs used in the connection between upper and lower tandem [172], (b) oxidized AlAs layer [173], (c) low index epoxy with ARC on either side of the epoxy [174], and (d) top cell printed on a bottom cell using a photoresist [175].....	119
Figure 8.5: Schematic of the proposed IMB approach between two dissimilar cells in a two-terminal structure for enhancing photon recycling in MJ solar cells [28] ...	121
Figure 8.6: Photon dynamic of solar cells at open circuit voltages. (a) cell is grown on the substrate, (b) cell grown with epitaxial lift-off approach.....	122
Figure 8.7: Comparison between tandem cells grown using three different approaches: (a) lattice matched to the index-matched substrate, (b) on a perfect metal reflector, (c) the proposed IMB approach. The expressions for the η_{ext} in the figures are from ref. [167].....	124
Figure 8.8: Schematic representation of a multilayer with forward and backward-propagating electric field components shown.....	126

Figure 8.9: Two cells bonded together using the proposed IMB approach with air gap provided between them: (a) no front or rear ARCs on the two cells, (b) only front ARC on top of upper cell, and (c) front ARC on top of two cells and back ARC on back of top cell	128
Figure 8.10: Front reflectance at air/front of top cell interface for the structures showed in Figure 8.9, for the InGaP/Air/GaAs case.....	129
Figure 8.11: Back reflectance at top subcell/air interface. The inset shows where the back reflectance was calculated.....	129
Figure 9.1: External quantum efficiency versus wavelength, showing the potential strategies for enhancing the sub-bandgap quantum efficiency of QW solar cell devices. The vertical dotted line is the band-edge of emitter/base. The region beyond the band-edge is where the QWs are absorbing.....	133
Figure 9.2: Ideal bandgap energy for each junction in a multi-junction solar cell as the number of junctions is increased from one to eight. InGaAs/GaAsP, InGaAsP/InGaP, and InGaN/GaN quantum well solar cell structures can be used to realize the bandgap range identified by the horizontal dotted lines. The data for ideal bandgaps are plotted from ref. [97].....	138

Chapter 1: Introduction

It has become clear that non-renewable energy resources are not reliable sources for energy generation. Unfortunately, more than 80% of the current world's energy production is produced from fossil fuels (coal, gas, and oil) [1]. Recent studies have shown that oil, gas, and coal will significantly be diminished in the next fifty years[2]. In addition to being non-renewable, fossil fuels release carbon dioxide during the burning process which increases the global warming and adds to the climate change [3]. Moreover, the burning of coal and gas produces toxic sulfur dioxide gas as a reaction byproduct, which negatively affects our respiratory health, echo-systems and wildlife [4]. It is thus mandatory for research and development to provide more clean, renewable, and reliable sources of energy.

Solar photovoltaics is a clean and abundant source of renewable energy, but unfortunately, due to the high cost of solar cells fabrication, it currently contributes ~0.7% of the total energy generation in the United States [1]. There are two approaches to increase the potential for using solar energy in the market. The first approach is to increase the efficiency of solar cells' fabrication without increasing the cost. The second approach is to reduce the cost of solar cells without sacrificing the efficiency. The current state of the art solar cells based on the III/V semiconductor materials have realized efficiencies of ~46% under high solar concentration [5]. It has been reported that improving the efficiency of solar cells to higher than 50% will reduce the cost of solar (\$/watt) and might open new opportunities in the solar photovoltaic concentrator market [6]. In this dissertation, we aim to develop a new approach to enhance the efficiency and reduce the cost of solar (\$/watt) through providing new materials and device architectures that can be part of next-generation photovoltaic devices with target efficiencies higher than 50%.

Solar photovoltaic devices convert light energy into electrical energy through a process called the "Photovoltaic effect," which consists of two stages [7]. The first stage of the photovoltaic effect is to create minority carrier population through "absorbing" the incident flux of photons that are incident on the photovoltaic device material. The second stage relies on "extracting" the minority carriers generated during the first stage, by the electric field across the photovoltaic device. The two photovoltaic effect stages, the light absorption and the carrier collection, can both be realized using P-N junction based on semiconductor materials.

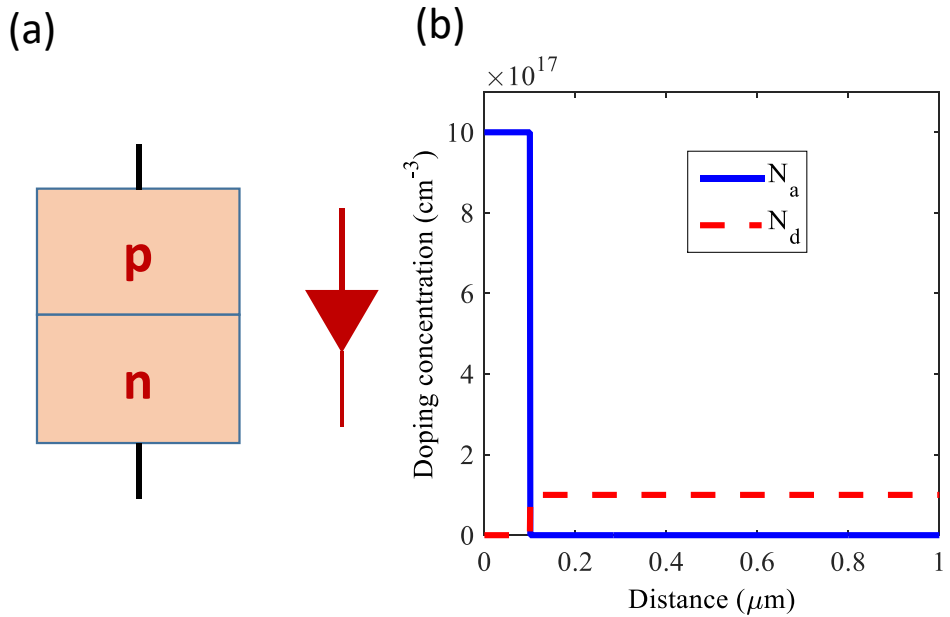


Figure 1.1: (a) schematic of p-n junction, (b) doping concentration profile of InGaP p-n junction.

This chapter will provide a brief overview of the physics behind the operation of P-N junction solar cells. Section 1.1 describes the behavior of a P-N junction in the dark. Then the physics of P-N junction solar cells is discussed in Section 1.2. The fundamental losses in single-junction solar cells are described in Section 1.3. The advantages of using multi-junction solar cell devices are presented in Section 1.4 through comparing their losses and efficiencies with single-junction devices. Then the research objectives of this dissertation are presented in Section 1.5. Finally, a preview of the dissertation is presented in Section 1.6.

1.1. P-N Junction

In this section, the electrical characteristics of a P-N junction in the “dark” are illustrated. A P-N junction diode is formed when a p-type semiconductor with acceptor concentration (N_a), is put in contact with an N-type semiconductor, of donor concentration (N_d), as shown in Figure 1.1(a). To illustrate the behavior of P-N junction in the dark and illustrate its electrical characteristics, simulations were performed using a Physics-Based Software PC1D, which solves the Poisson’s and drift-diffusion equations [8]. The P-N junction is assumed here as $\text{In}_{0.49}\text{Ga}_{0.51}\text{P}$, which is a standard material used in the fabrication of high-efficiency solar cells [9-11], and several solar cell structures/designs in this dissertation are based on this material. The thickness of p-

$\text{In}_{0.49}\text{Ga}_{0.51}\text{P}$ emitter, x_p , is $0.1 \mu\text{m}$. The thickness of n- $\text{In}_{0.49}\text{Ga}_{0.51}\text{P}$ base, x_n , is $1 \mu\text{m}$. The p- $\text{In}_{0.49}\text{Ga}_{0.51}\text{P}$ is doped with an N_d of 10^{18} cm^{-3} and the n- $\text{In}_{0.49}\text{Ga}_{0.51}\text{P}$ is doped with a N_a of 10^{17} cm^{-3} , as shown in Figure 1.1(b).

When the P-type semiconductor is put in contact with the N-type semiconductor, holes will diffuse from the P-type to N-type, as shown in Figure 1.2(a). The diffusion of holes from P-side to N-side

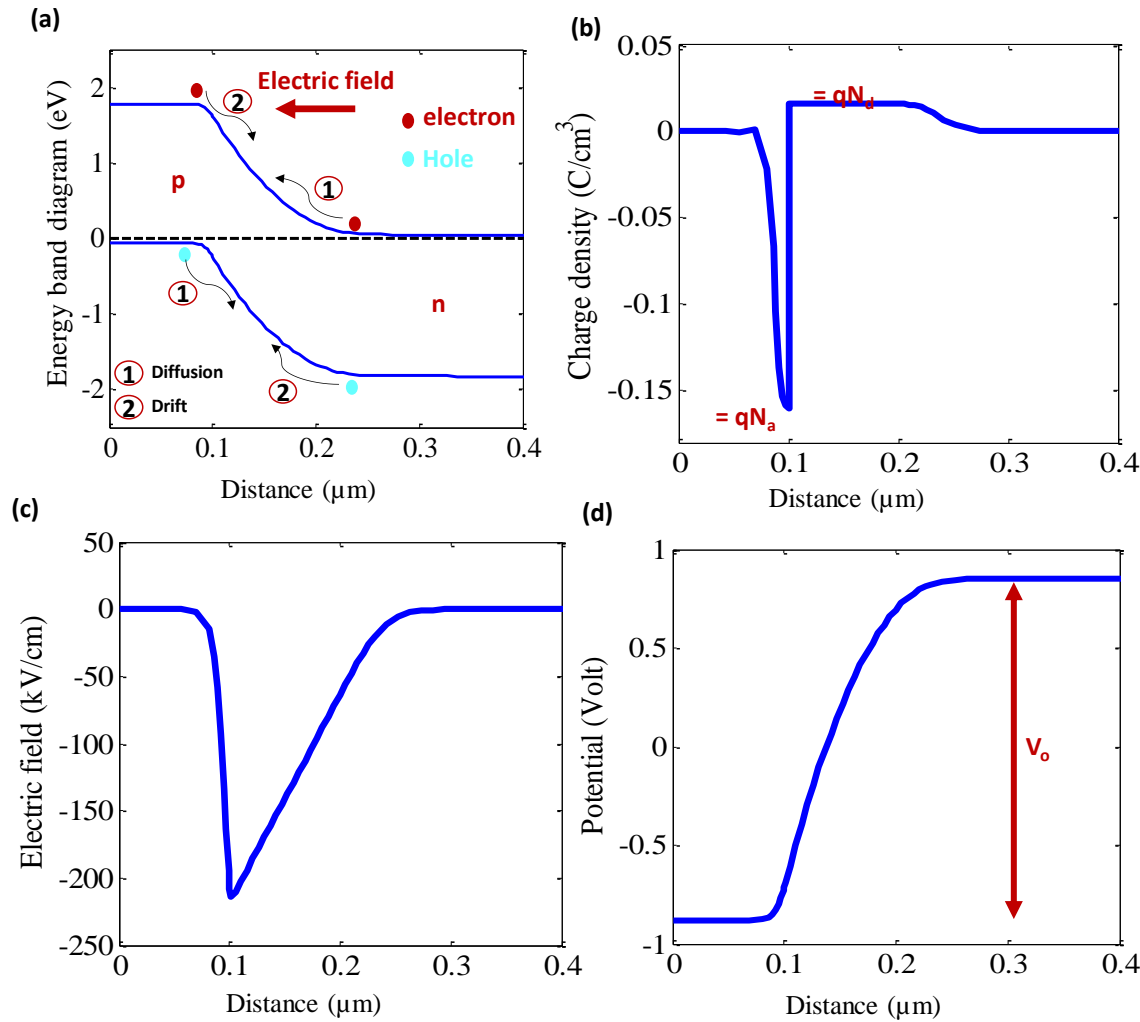


Figure 1.2: Schematics of $\text{In}_{0.49}\text{Ga}_{0.51}\text{P}$ p-n junction at thermal equilibrium (zero-bias/without illumination): (a) Energy band diagram, showing the drift and diffusion carriers' components. The horizontal black dotted line is the Fermi level, (b) charge density within space charge region, (c) electric field distribution, and (d) electrostatic potential. Simulations were performed using PC1D.

results in two effects. First, *depletion* of the P-side of free carriers up to a distance, W_p ; where W_p is the depletion region or space charge region on P-side [12]. Second, the formation of an uncompensated negative acceptors' charge on the P-side, equal to qN_a , as shown in Figure 1.2(b), where q is the elementary charge [12]. Similarly, electrons diffuse from the N-type to P-type leaving behind uncompensated positive donors' charge (qN_d) across a space charge region (W_n), as shown in Figure 1.2(b). As a result, an electric field is formed with a direction from N-side to P-side as shown in Figure 1.2(a) and Figure 1.2(c). This electric field prevents further diffusion of majority carriers and results in a drift of *minority* carriers across the junction; i.e., holes, drift from N-side to P-side and electrons, drift from P-side to N-side. The thermal equilibrium state, shown in Figure 1.2(a), is reached when the diffusion of the majority carriers is balanced by the drift of the minority carriers. As a result, the Fermi energy level is flat across the P-type and N-type as shown in Figure 1.2(a). It is worth pointing out that the source of the minority carriers in the equilibrium state is the thermal generation/excitations of electron-hole pairs. The bending of the energy band diagram of Figure 1.2(a), corresponds to the difference between the Fermi level on the N-side and P-side before contact. The potential difference between N-side and P-side, shown in Figure 1.2(d), is called built-in potential or contact potential, V_o . The total depletion region width, W , on the P- and N-sides is directly proportional square root of V_o , i.e., W .

Consider a P-N junction in the forward bias mode. This can be achieved by connecting the P-side and N-side to a positive and negative terminal of the battery (V_b), respectively [12]. The potential barrier across the junction decreases from V_o to $V_o - V_b$, as shown in Figure 1.3(a). The positive forward bias will also result in an electric field of opposite direction to the built-in electrostatic field, and thus result in a reduction of both the total electric field and depletion region across the P-N junction [12]. Schematics of energy band diagram and carrier concentration profiles of InGaP p-n junction at zero and positive bias of 1.2 V, are shown in Figure 1.3(a) and Figure 1.3(b), respectively. The arrows in Figure 1.3(a) show the direction of the electron and hole transport following forward bias. As shown in Figure 1.3(a), the reduction of the potential barrier to $V_o - V_b$, will result in holes diffusing from P-side to N-side to become a minority. Similarly, electrons will diffuse from the N-side and become a minority in the P-side. As a result, the minority carrier concentration on both the P and N sides will be significantly increased, as shown in Figure 1.3(b). Hence, the net current will be mainly due to diffusion and the drift current is the same as the zero-bias case. It should be mentioned that the increase of the forward bias should correspond to more

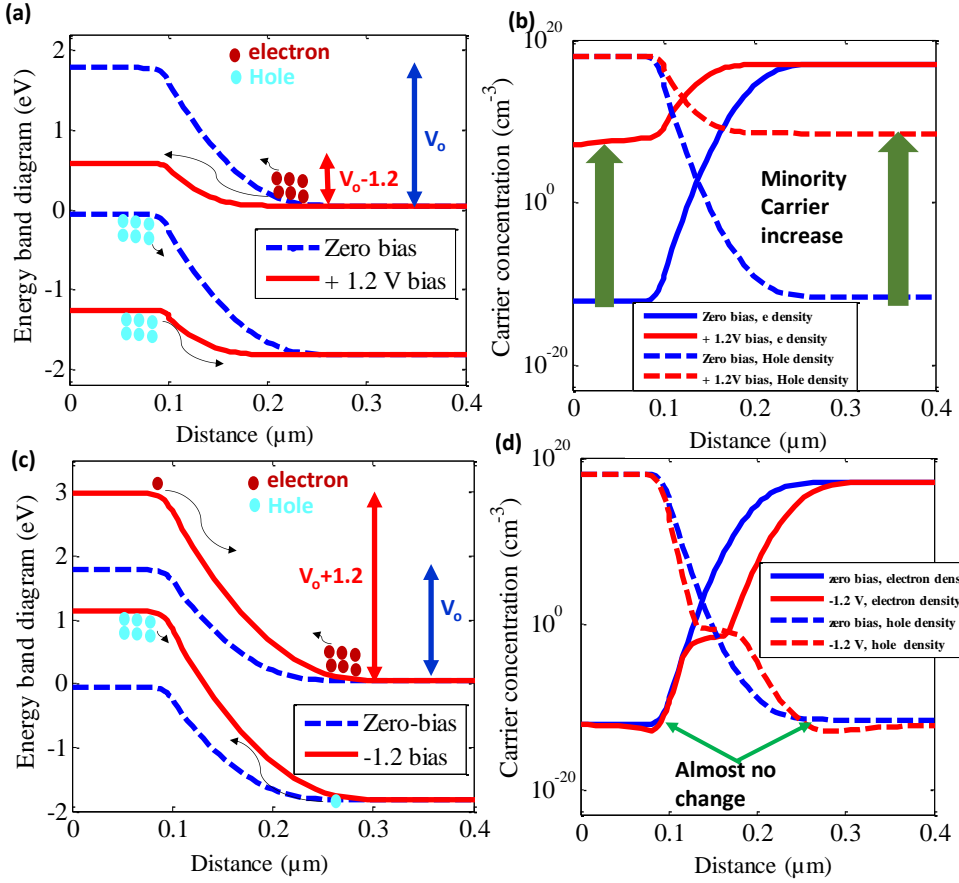


Figure 1.3: (a) Band profiles and (b) carrier densities for an In_{0.49}Ga_{0.51}P p-n junction at zero bias (blue) and forward bias (red). (c) Band profiles and (d) carrier densities for an In_{0.49}Ga_{0.51}P p-n junction at zero bias (blue) and reverse bias (red). The arrows in Figures (a) and (c) show the direction of the electron and hole transport following forward and reverse bias.

reduction in the potential barrier, and thus further enhancement in minority carrier concentration. If the negative terminal of the battery is connected to P-type, the P-N junction is considered in a reverse bias mode [12]. Schematics of band profiles and carrier densities for an In_{0.49}Ga_{0.51}P p-n junction at zero bias and reverse bias are shown in Figure 1.3 (c)-(d). The potential barrier across the P-N junction increases to $V_o + V_b$, thus reducing the probability of electron diffusion from N-Side to P-side, as shown in Figure 1.3(c). Similarly, the hole diffusion from N-side to P-side is significantly reduced. Thus, the minority carrier concentration at reverse bias is about the same as the zero-bias case, as shown in Figure 1.3(d). Therefore, the dominant current component in the reverse bias mode is the drift current. Electrons will drift from P-side to N-side to become a majority, as shown in Figure 1.3(c). Similarly, holes can drift from N-side to P-side, as shown in

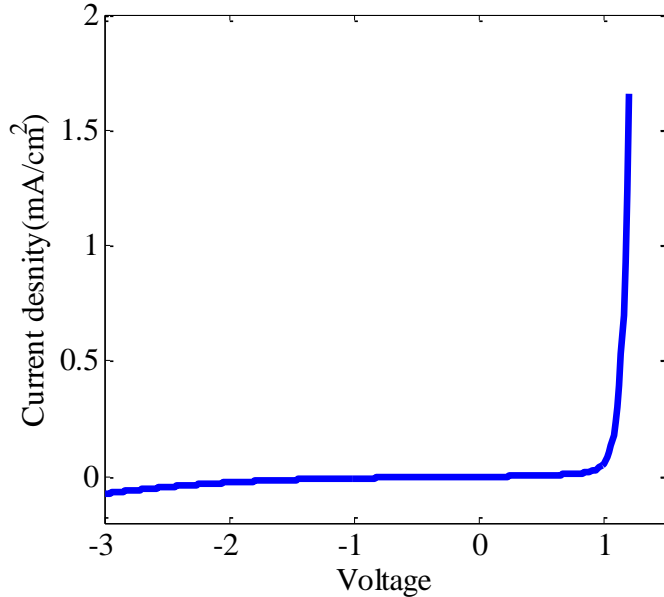


Figure 1.4: Measured dark current-voltage characteristics of InGaP p/n junction, grown and processed at NCSU.

Figure 1.3(c). However, since the electrons on the P-side and holes on the N-side are minority carriers arising from the thermal excitations, the drift current is very low if compared with the current in the forward-bias mode[12]. The reverse bias will also increase the electric field across the P-N junction and widens the depletion region, W [12].

The measured dark current-voltage (I-V) characteristics of an InGaP P-N junction that will be discussed further later in this dissertation, is shown in Figure 1.4. At forward voltages higher than \sim two-thirds of V_o , the boost in the minority carrier concentration, shown in Figure 1.3(b), results in a large increase in the current. At reverse bias, the current, mainly due to the drift of thermally excited minority carriers, is very low. The current-voltage characteristics can be described using a two-diode model as follows [7],

$$I = I_{o1} \left(e^{\frac{qV_b}{n_1 kT}} - 1 \right) + I_{o2} \left(e^{\frac{qV_b}{n_2 kT}} - 1 \right), \quad (1.1)$$

where the first term represents recombination in the neutral region ($n_1 = 1$) and the second term represents recombination in the depletion region ($n_2 = 2$), I_o is the reverse saturation current due to n_1 and n_2 , k is Boltzmann constant. When recombination occurs in neutral region dominates, the first term of Eqn. (1.1) dominates. Similarly, the second term dominates when

recombination in depletion region dominates. The latter is the so-called Shockley Read Hall recombination which is dominant in the solar cells presented in this dissertation. The two-diode model is used later in this dissertation to understand the type of recombination mechanism occurring in the solar cell.

1.2. P-N Junction under Illumination

In this section, the behavior of the P-N junction under solar illumination is discussed. The Sun is a broadband emitter that acts as a near blackbody with a temperature of $\sim 6000\text{K}$. The emission of the Sun is maximum in the visible spectrum range, 300-750 nm. The solar irradiance spectrums, AM1.50 and AM1.5, are shown in Figure 1.5 [13]. AM0 corresponds to the solar spectrum in space and has an integrated power density of $\sim 1360 \text{ watt/m}^2$. AM1.5 and AM1.5D correspond to the solar spectrum at a latitude of 48.2. AM1.5G includes both direct and diffuse sunlight, and it has an integrated power density of 1000 watt/m². AM1.5D corresponds to the direct solar spectrum, and it has an integrated power density of 900 watt/m². The AM0 is a standard measurement for space applications, while AM1.5G and AM1.5D spectrums are more commonly used for terrestrial applications. The AM1.5G spectrum is used for the rest of the analysis performed in this Chapter.

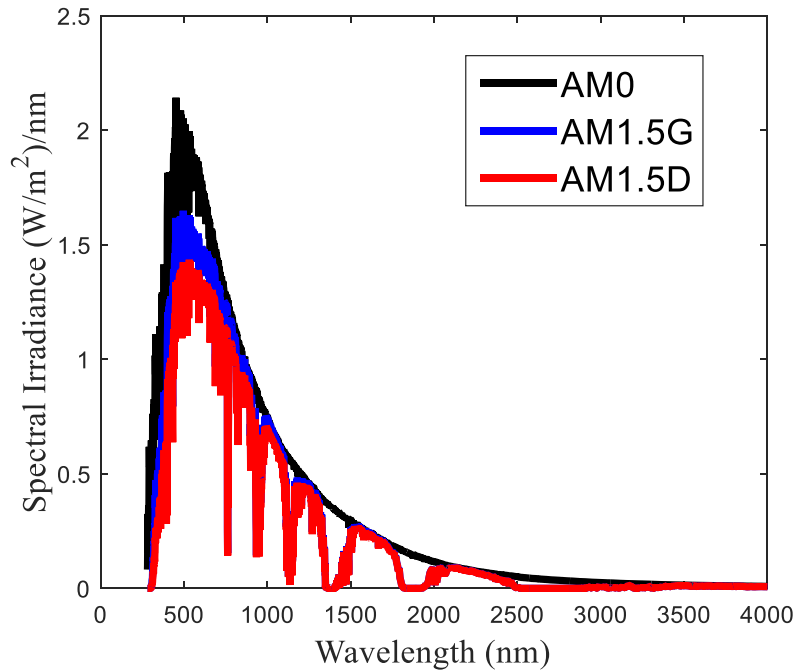


Figure 1.5: The solar spectrum irradiance, AM0, AM1.5G, and AM1.5D

When the P-N junction is illuminated with photons of energies higher than or equal to the bandgap, E_g , electron-hole pairs are generated in the neutral and space charge regions of the P-side and N-Side, as shown in Figure 1.6. Upon illumination, the P-N junction is not considered at equilibrium and the Fermi level is not flat as previously shown in Figure 1.2(a). Instead, the electron and hole Fermi levels split in the p-type and n-type into quasi-levels [7] as shown in Figure 1.6(b). If the P-semiconductor absorbs the incident photon, a minority electron and a majority hole will be created

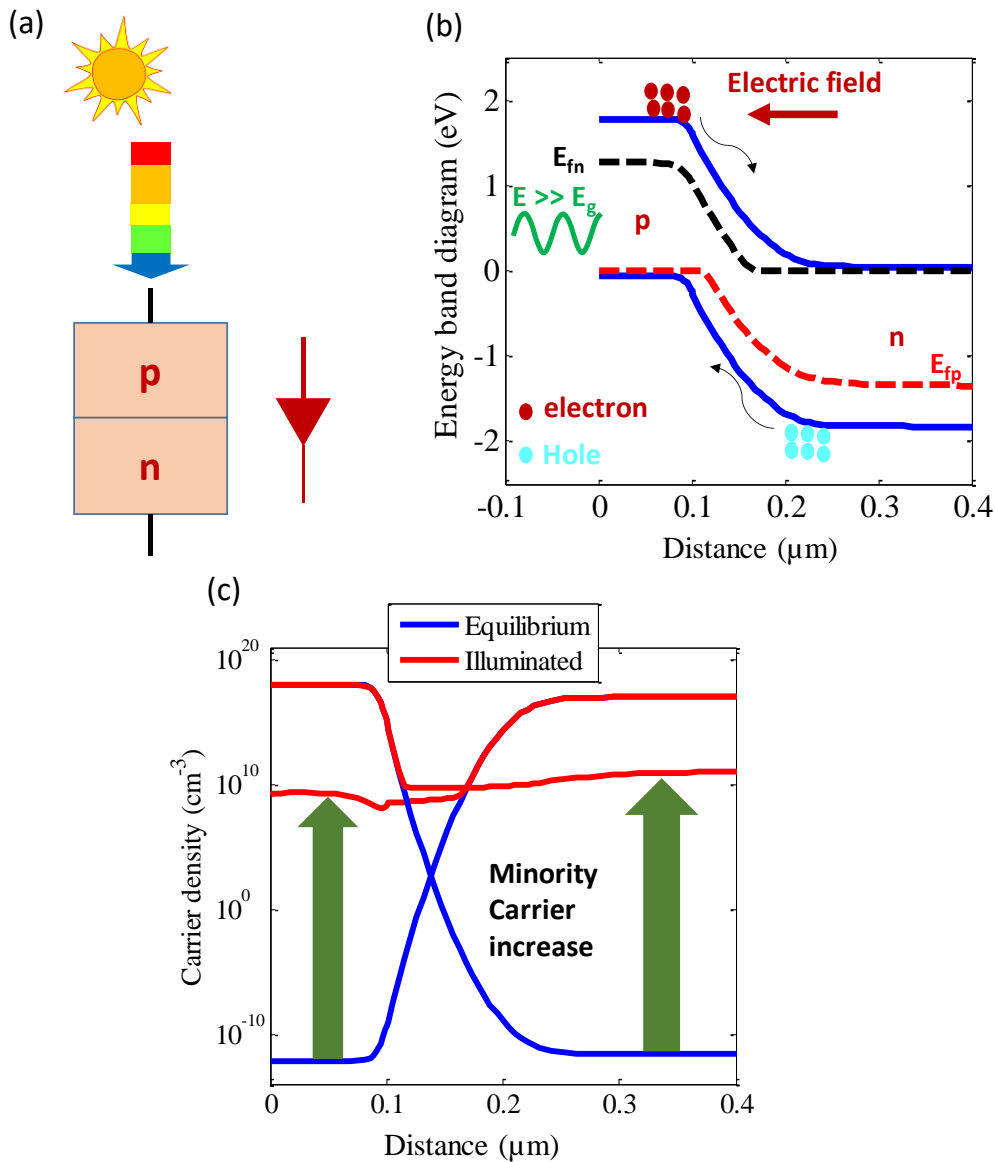


Figure 1.6: (a) Illuminated P-N junction, (b) energy band diagram and (c) carrier densities for illuminated InGaP p-n junction. The arrows in Figure (b) show the direction of the electron and hole transport following photo-generation.

in conduction and valence bands, respectively. Similarly, if the photon was absorbed by the N-semiconductor, a minority hole and a majority electron will be created in the valence and conduction bands, respectively. This results in a major increase in the minority carrier concentration at the P-side and N-side as shown in Figure 1.6(c) [7]. The built-in electric field, in the P-N junction, is directed from N-side to P-side, as shown in Figure 1.6(b). Hence, this field will prevent the majority carriers from diffusing across the junction. On the other hand, this field will sweep the minority electrons from P-side to N-side and the minority holes from N-side to P-side. The arrows in Figure 1.6(b) show the direction of the electron and hole transport following photo-generation. In order for this to occur, the minority carriers should diffuse to the junction; and this will depend on the diffusion length, $L = \sqrt{D\tau}$; where D is the diffusion coefficient and τ is the minority carrier lifetime. Hence, this does impose restrictions on the material quality. This means that, for example, if a minority electron in the P-side has a long diffusion length, it will reach the junction before recombining and be swept by the electric field and contribute to the photo-current.

The measured current-voltage (I-V) characteristics, under AM1.5 illumination, of an $\text{In}_{0.49}\text{Ga}_{0.51}\text{P}$ P-N junction that will be discussed further later in this dissertation, is shown in Figure 1.7. The current-voltage characteristics can be thus being updated as follows [7],

$$I = I_{o1}(e^{\frac{qV_b}{n_1kT}} - 1) + I_{o2}(e^{\frac{qV_b}{n_2kT}} - 1) - I_{op}, \quad (1.2)$$

where I_{op} is the optically generated current, which causes the current-voltage diagram to be shifted downwards by I_{op} at all biases.

There are a few figures of merit for characterizing any photovoltaic devices. These metrics can be used to compare different solar cell structures/designs.

- Short circuit current (J_{sc}), which is the current generated in the P-N junction upon illumination at zero bias, due to the optical generation of carriers, as shown in Figure 1.7.
- Open circuit voltage (V_{oc}), which is the extracted voltage from the solar cell when there is no current flowing in the circuit, as shown in Figure 1.7. V_{oc} can be extracted from Eqn. (1.2) by setting the current equals to zero. If the recombination in the solar cell is dominant

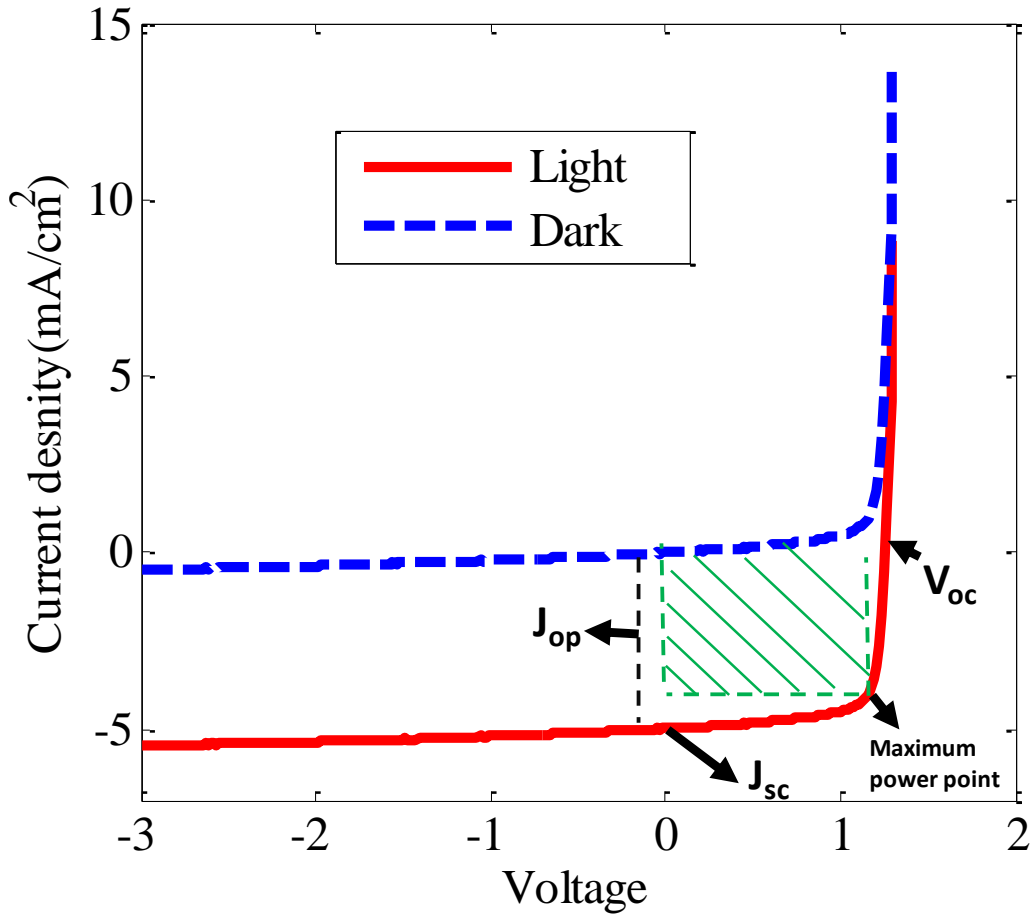


Figure 1.7: Measured dark and illuminated current-voltage characteristics of $\text{In}_{0.49}\text{Ga}_{0.51}\text{P}$ p-n junction. The figure also shows the metrics that are used to assess the solar cell performance, V_{oc} , J_{sc} , and maximum power point.

in the neutral region, i.e. $n = 1$, V_{oc} can be expressed as follows [7],

$$V_{oc} = \frac{kT}{q} \ln \left(\frac{I_{sc}}{I_{o1}} + 1 \right) \quad (1.3)$$

If the recombination is more effective in the depletion region, i.e. $n = 2$, V_{oc} can be expressed as follows,

$$V_{oc} = \frac{2kT}{q} \ln \left(\frac{I_{sc}}{I_{o2}} + 1 \right) \quad (1.4)$$

- Maximum power point is the operating point of the cell that can maximize the electrical power, Figure 1.7. The output power is zero at the open-circuit and short-circuits conditions.

- Fill factor (FF), is a parameter which determines the maximum output power from the cell. Graphically, FF is the area of the maximum rectangle that fits in the current-voltage curve of the solar cell, as shown in the shaded green area in Figure 1.7. The FF can be expressed as follows [7],

$$FF = \frac{V_{mp} I_{mp}}{V_{oc} I_{sc}} \quad (1.5)$$

A high series resistance and/or low shunt resistance will degrade the FF .

- Cell efficiency (η), is the fraction of the output electrical power generated by the solar cell and the incident power on the cell, P_{inc} . η can be expressed as follows [7],

$$\eta = \frac{FFV_{oc}J_{sc}}{P_{inc.}} \quad (1.6)$$

1.3. Losses in Single-junction Solar Cells

There are two fundamental losses in solar cells: sub-bandgap losses and thermalization losses. If a photon of energy equals to bandgap (E_g), shown in Figure 1.8, is incident on the P-N junction, it will be absorbed by the P-type semiconductor and will generate a minority electron in the conduction band and will be swept by the electric field. If the incident photon's energy is less than the bandgap, shown in Figure 1.8, both the P-type and N-type will not absorb it, and this is considered as “sub-bandgap losses”. Photons of energies much higher than the bandgap will generate electron-hole pair with energy separation equal to the energy of the incident photons. The minority carriers will relax and lose their energies to the lattice in the form of heat, then will be swept across the junction by the electric field, as shown in Figure 1.8. The difference between the photon's energy and the bandgap is considered as “thermalization losses”. Schematics that compare the thermalization and sub-bandgap losses of single junction 1.1 eV and 1.7 eV solar cells are shown in Figure 1.9. The analysis was performed on a material with an E_g of 1.1 eV because Silicon, which is the most commercial solar cell today has a bandgap of 1.11 eV. Also, 1.7 eV is an optimum bandgap for subcells in several multi-junction solar cell designs as will be discussed later in Chapter 4 of this dissertation. In this analysis, two assumptions were performed. First, each photon of energy higher than the bandgap E_g is assumed to generate an electron-hole pair. Second, other losses such as the radiative-recombination losses and non-radiative Shockley Read

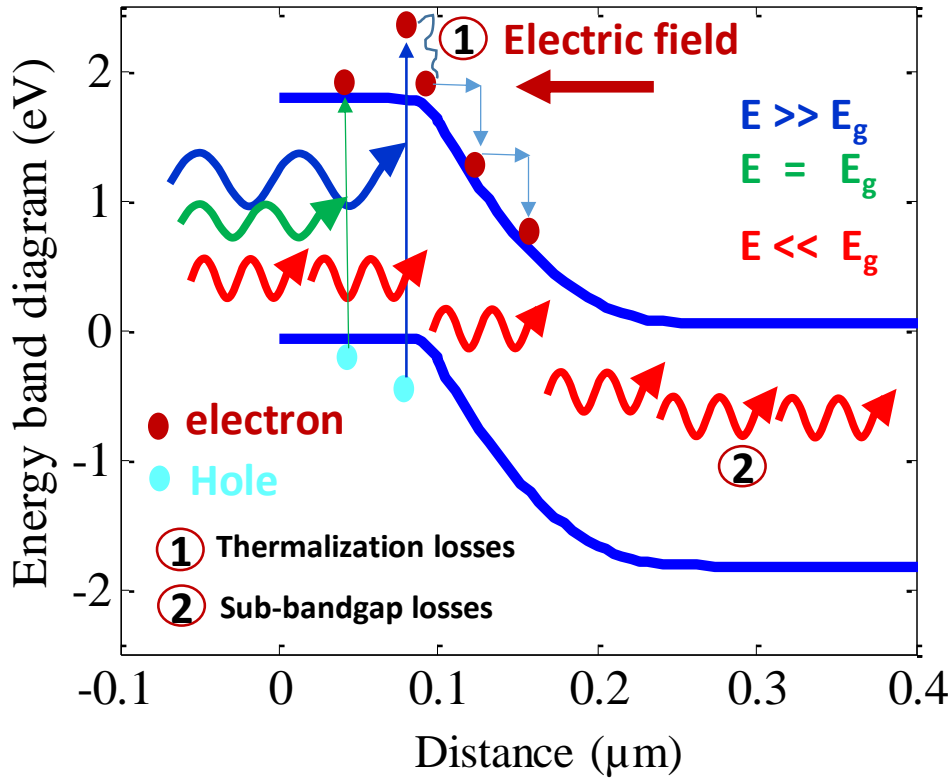


Figure 1.8: Energy band diagram of a PN junction with incident photons of energies higher than, equal to, or less than the bandgap, showing both the thermalization and sub-bandgap losses that exist in single-junction solar cells.

Hall recombination losses are neglected. The thermalization and sub-bandgap losses of the 1.1 eV silicon cell are 34.8% and 14.72%, respectively, which result in total losses of 49.52%, as shown in Figure 1.9(a). This will correspond to an ultimate efficiency of 50.48% which considers only the thermalization and sub-bandgap losses. If other losses such as the radiative-recombination and Shockley Read Hall recombination, this efficiency value will be more reduced. The 1.7 eV P-N junction has less thermalization loss (15.1%) and higher sub-bandgap loss (45.6%) due to its higher bandgap as shown in Figure 1.9(b), thus resulting in a combined total loss of 60.46%.

The analysis discussed in Figure 1.9 was further extended to calculate the thermalization and sub-bandgap losses for single p-n junctions with various bandgaps, Figure 1.10. The thermalization and sub-bandgap losses decrease and increase, respectively, with the increase of the bandgap as shown in Figure 1.10. The thermalization losses decrease with the bandgap increase because the energy generated from absorbed photons reduce with the increase of E_g . The sub-bandgap losses increase with the bandgap increase as shown in Figure 1.10 because a wider region of the solar

spectrum is not fully utilized. If both the thermalization and sub-bandgap losses are both combined using this analysis, an optimum point of minimal total losses would exist which will correspond to an ideal ultimate efficiency of 50.5% at a bandgap of \sim 1.1 eV, as shown Figure 1.10. If the analysis is extended to include the radiative recombination in the solar cell material, the maximum efficiency will be 30% at a bandgap of 1.1. eV [14]. The latter is the so-called the Shockley-Queisser efficiency, which represents the maximum theoretical efficiency of a single P-N junction[14].

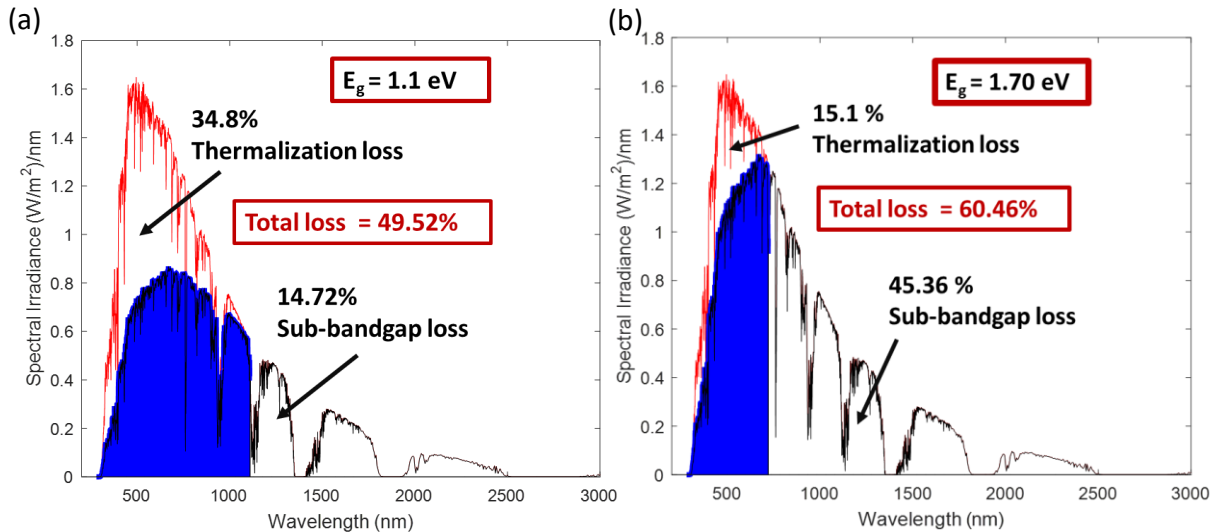


Figure 1.9: Schematics of AM1.5 spectrum showing the thermalization and sub-bandgap losses for single junction solar cells: (a) silicon, with an E_g of 1.1 eV, (b) subcell, with an E_g of 1.70 eV.

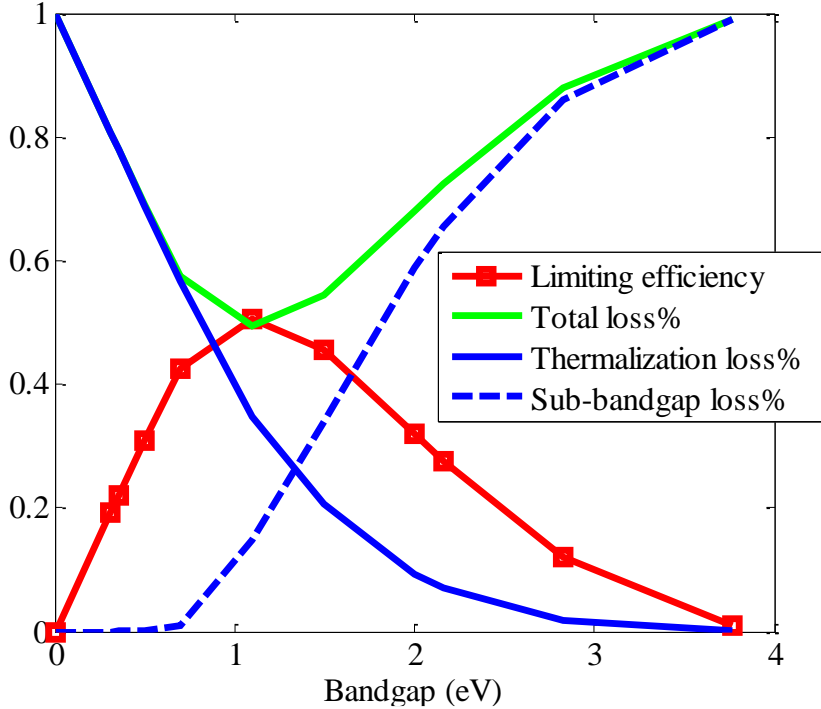


Figure 1.10: Thermalization loss, sub-bandgap loss, and total loss in ideal single-junction solar cells, versus the bandgap. The ultimate efficiency values are calculated assuming only the thermalization and sub-bandgap losses are included. The efficiency will be more reduced if radiative-recombination and SRH recombination losses are included. These calculations were performed on the AM1.5G spectrum

1.4. Multi-junction Solar Cells

In order to reduce the sub-bandgap and thermalization losses that exist in single-junction devices discussed in Section 1.3, the multi-junction solar cell concept, was demonstrated by NCSU in 1979 [15]. In a multi-junction device, multiple P-N junctions of different bandgaps are stacked on top of each other, as shown in Figure 1.11, to divide the absorption of the solar spectrum more efficiently among them. As shown in Figure 1.11, the subcell with the highest energy (E_{g1}) absorbs photons with energies higher than E_{g1} . The second highest energy subcell (E_{g2}) absorb photons with energies higher than E_{g2} and lower than E_{g1} . Similarly, the bottom cell in Figure 1.11 absorb photons in the $E_{g3}-E_{g2}$ bandgap range. If the 1.1 eV and the 1.7 eV cell shown in Figure 1.9 are combined in a multijunction device, this will lead to a more efficient utilization of the solar spectrum as shown in Figure 1.12. Using 1.1 eV and 1.7 eV as the bottom and top cell forms the optimum bandgap combination in dual-junction with a prospective AM1.5G one-sun efficiency of 35% [16]. The thermalization loss of the 1.1eV cell in the dual-junction structure is 6.11% as

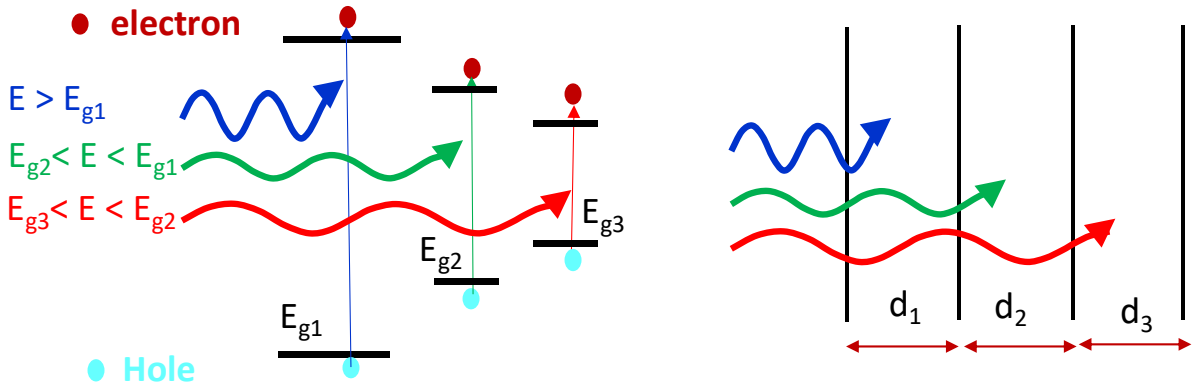


Figure 1.11: Multi-junction solar cell concept

shown in Figure 1.12(a), which is much less than its corresponding value (34.8%) in a single-junction structure shown in Figure 1.9(a). The thermalization loss of the 1.7 eV is the same in both the single-junction and dual-junction configurations because it is absorbing the same solar spectrum window. The 1.7/1.1 dual-junction device has total losses of ~36% which are much less than the losses in the single-junction 1.1 eV (49.52%) and 1.7 eV (60.46%) solar cells. This indicates that the ideal ultimate efficiency of the dual junction 1.7/1.1 eV cell is ~64% which is much higher than any single-junction shown in Figure 1.10. As mentioned earlier, these efficiency

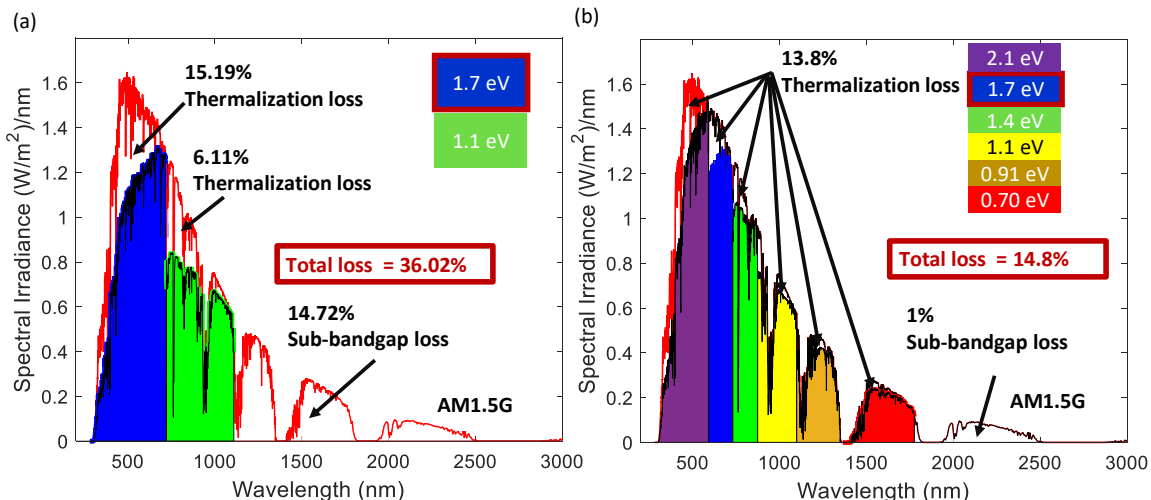


Figure 1.12: Schematics of AM1.5 spectrum showing the thermalization and sub-bandgap losses for multi-junction solar cell devices: (a) dual-junction structure (1.7 eV/1.1 eV), (b) six-junction structure (2.1 eV/1.7 eV/1.4 eV/1.1 eV/0.91 eV/0.7 eV).

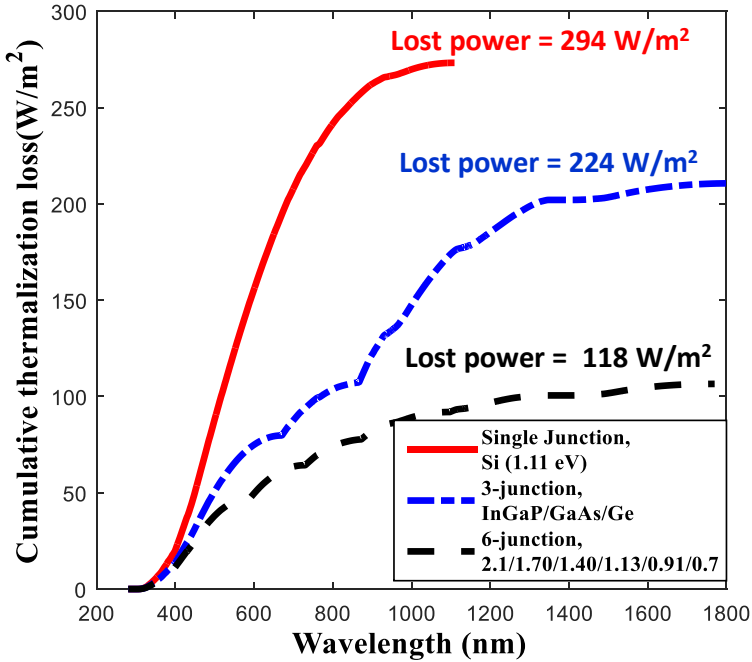


Figure 1.13: Cumulative loss from carrier thermalization to the band edges of single-junction 1.1 eV, three-junction (1.87/1.4/0.7 eV), and six-junction (2.1 eV/1.7 eV/1.4 eV/1.1 eV/0.91 eV/0.7 eV) devices. The integrated power density of AM1.5G is 1000 watt/m²

values do not include the losses due to radiative-recombination and Shockley Read Hall recombination losses.

As the number of junctions in the multi-junction stack is further increased, both the thermalization and sub-bandgap losses can be reduced. A schematic of AM1.5 spectrum showing the thermalization and sub-bandgap losses for the six-junction device (2.1 eV/1.7 eV/1.4 eV/1.1 eV/0.91 eV/0.7 eV) is shown in Figure 1.12 (b). The optimum bandgap values used in the analysis of the six-junction device is designed by Geisz et al. [17]. The thermalization and sub-bandgap losses are ~14% and 1%, thus resulting in a combined loss of ~15%. The ultimate efficiency of the six-junction device is ~21 percent point higher its corresponding value in the dual junction 1.7/1.1 eV solar cell. This confirms that the inclusion of more subcells with bandgaps scanning the entire solar spectrum results in a total thermalization loss from all subcells that is much less than each in a single-junction configuration.

Figure 1.13 shows the cumulative loss in Watt/m² as a function of wavelength from carrier thermalization to the band-edges for single-junction 1.1 eV cell, three-junction (1.87/1.4/0.7 eV),

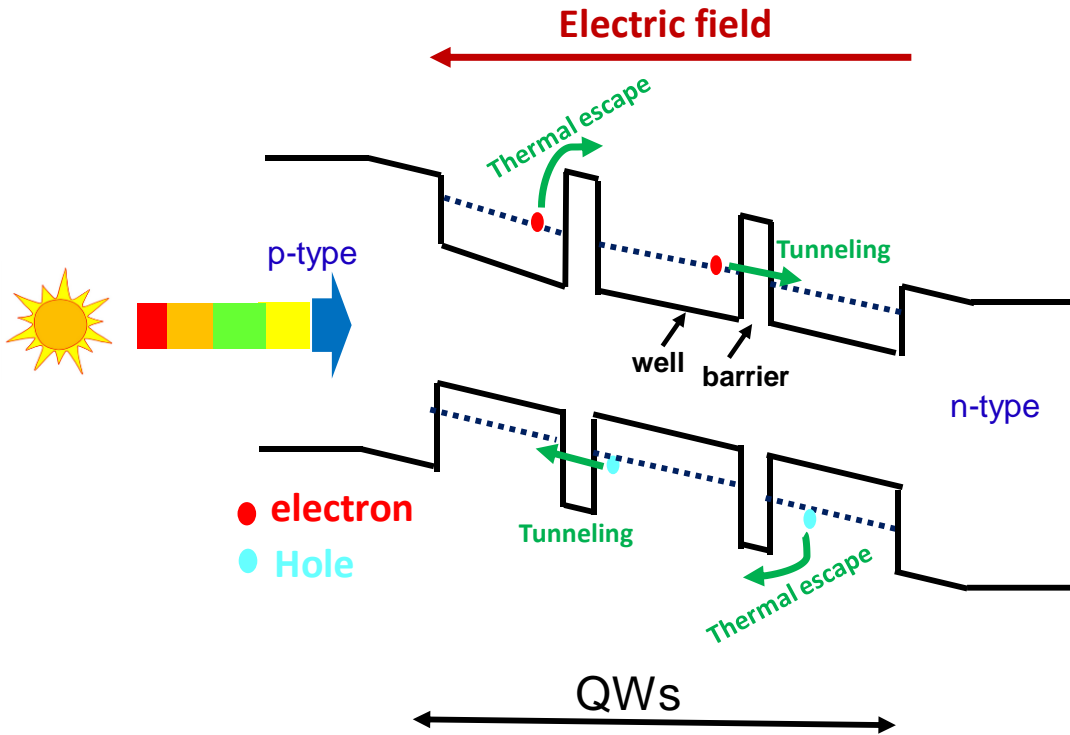


Figure 1.14: Quantum well solar cells

and six-junction (2.1 eV/1.7 eV/1.4 eV/1.1 eV/0.91 eV/0.7 eV) devices. The incident power density of AM1.5G is 1000 watt/m². The cumulative power lost due to thermalization in the six-junction device is ~ 118 watt/m², which is much less than the that of the three-junction (224 watt/m²) and single junction devices (294 watt/m²). Also, covering a wider region of the solar spectrum leads to reducing the lost energy in the sub-bandgap region.

Nowadays, multi-junction solar cells based on four-junction III-V materials are the most efficiency photovoltaics technology with efficiency of 46% under high solar concentration [9, 11, 18]. Five (or more) junctions are the next-generation devices with a prospective efficiency higher than 50% under high solar concentration [17]. In this dissertation, a novel subcell with a bandgap of 1.7 eV is developed for potential use next-generation five (or more) six junction devices as will be discussed later in the next few chapters.

1.5. Research Objectives

In multi-junction solar cells, subcells with optimal bandgaps, as indicated by modeling [19-23], typically do not attain the same lattice constants. Direct growth of materials with different lattice constants result in detrimental dislocations which lead to an increased dark current and

reduced V_{oc} , FF and η [24]. In addition, multi-junction solar cells seek to have an excellent current match between subcells or add more subcells to divide the solar spectrum evenly [25, 26]. Hence, an ideal multi-junction solar cell will have minimal defects with the identical current generated from each subcell. There are three main approaches to overcome the material quality and lattice-matching limitations: wafer bonding/ mechanical stacking, metamorphic growth, and the inclusion of quantum wells (QWs). Details about each approach will be highlighted later in Chapter 2. This dissertation focus on the use of quantum wells, as an alternative promising approach to realize multi-junction solar cell structures with optimal bandgaps without violating the lattice-matching condition [27]. Quantum wells are periodic nanostructures that consist of a low bandgap material, well, sandwiched between two higher bandgaps, barriers. Schematics of a generic quantum well structure is shown in Figure 1.14. Carriers generated in the quantum well region and neutral regions are transported by the electric field by thermal escape or by carrier tunneling as shown in Figure 1.14.

This dissertation proposes a novel QW structure based on InGaAsP/InGaP material system to realize a subcell in the 1.6-1.8 eV bandgap range. This QW solar cell can be part of next-generation five (or more) junction devices that will have a prospective efficiency of higher than 50% under solar concentration. Two quantum well designs are proposed in this dissertation. In the first design, the carriers are transported thermally by an electric field, while carriers tunnel across the barriers by the electric field in the second design as shown in Figure 1.14.

Chapter 8 of this dissertation focuses on a new concept for enabling photon recycling in multi-junction solar cells, in a two-terminal device configuration. This approach is based on recent research efforts in Bedair's lab that focus on developing two-terminal tandem solar cells of two dissimilar material systems using the Inter-Metallic Bonding (IMB) Approach [28]. The IMB approach allows combining two cells that differ in their crystalline, electrical, thermal and optical characteristics, in two-terminal device configurations, as shown in Figure 1.15 [28]. Photon recycling for the bottom cell will be provided using a back reflector. Photon recycling for the top cell will be realized using air-gap or epoxy as intermediate between top and middle cells using the inter-metallic bonding approach.

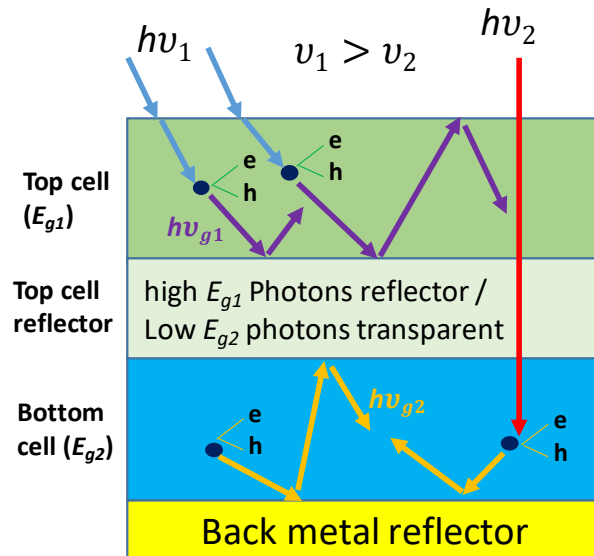


Figure 1.15: Schematic of photon dynamic in multi-junction cells with an ideal reflector placed at the back of the top cell. Antireflection coatings (ARCs) are not shown for simplicity. This will be experimentally realized using the Inter-Metallic Bonding (IMB) Approach [28]

1.6. Synopsis of Dissertation

This dissertation explores the development of novel quantum well material systems and designs to advance the performance of III/V multijunction solar cells. Two quantum well structures and designs are developed.

Chapter 2 discusses the principles of quantum well solar cells, including our modeling of the band-gap tunability, critical layer constraints, strain-balance design, and carrier transport.

Chapter 3 presents a brief literature review of recent progress in the development 1.1-1.3 eV InGaAs/GaAsP and > 2.2 eV InGaN/GaN quantum well solar cells. The motivation of the development each of these QW solar cell structures will be presented.

Chapter 4 focuses on details about the growth of strain-balanced InGaAsP/InGaP quantum well structure. The growth conditions to strain-balance this QW structure are presented in this Chapter.

Chapter 5 discusses the solar cell results of strain-balanced InGaAsP/InGaP quantum. The effects of well thickness, well number, and barrier heights on the performance of this QW structure are presented in Chapter. The carrier transport of this QW structure is discussed.

Chapter 6 focuses on the growth of lattice-matched InGaAsP/InGaP quantum well structure. Details about the in-situ curvature monitoring and X-ray diffraction results are presented in this chapter as well.

Chapter 7 discusses the solar cell results of lattice-matched InGaAsP/InGaP quantum well. The carrier transport in this QW structure is also discussed.

Chapter 8 presents the concept for the development of photon-recycling in multi-junction solar cells using the inter-metallic bonding approach.

Summary of research and future outlook of this dissertation research work is presented in Chapter 9.

Chapter 2: Principles of Quantum Well Solar Cells

This chapter provides an overview of the physics of quantum well solar cells. The advantages of using quantum well structures in multi-junction solar cells are first discussed. Research needs that open up avenues for developing the next-generation quantum wells are presented in Section 2.1. Quantum well solar cells have a wide tunable bandgap, thus making them potential candidates for subcells in next-generation multi-junction solar cell devices. This bandgap tunability advantage is discussed in Section 2.2 by modeling the quantum size and strain effects in quantum well structures. The challenges related to materials growth such as critical layer thickness (CLT) and strain-balance constraints are discussed in Section 2.3 and Section 2.4, respectively. The physics of carrier transport in quantum well solar cells is presented in Section 2.6. The discussions in this Chapter is focused on reviewing the strain-balanced InGaAs/GaAsP and strained InGaN/GaN quantum well structures which are two widely researched in the last few years. In Chapters 4, 5, 6, 7: novel strain-balanced and lattice-matched InGaAsP/InGaP quantum well solar cells are presented.

2.1. Motivation

There has been an intensive search for high-efficiency photovoltaics since the invention of first p-n silicon solar cells in the 1950s [29]. Among all alternative photovoltaic technologies, the III/V multi-junction solar cells are the most efficient photovoltaic technology nowadays [5, 30]. Inverted metamorphic (IMM) InGaAsP/InGaAs and lattice-matched InGaP/GaAs dual-junction have realized one-sun efficiencies (η) of 32.6% and 31.6%, respectively [5, 31]. Lattice-matched InGaP/Ga(In)As/Ge and IMM InGaP/GaAs/InGaAs triple-junction solar cells have realized η of 44.0% and 44.4%, respectively, under high solar concentration [32, 33]. Quadruple-junction wafer-bonded [6, 11] and IMM [18] structures have demonstrated η of ~46%, under high solar concentration. Next generation multi-junction devices will have five (or more) junctions with prospective η exceeding 50% under high solar concentration [34][17].

The realization of the ideal subcells with optimal bandgaps (E_g) in current and next-generation III-V solar cells is challenged by the relation between the bandgap and lattice constant of materials. Subcells with optimal bandgaps, as indicated by modeling [19-23], typically do not attain the same lattice constants. Direct growth of materials with different lattice constants result in detrimental

dislocations which lead to an increased dark current, and reduced open circuit voltage (V_{oc}), fill factor (FF) and η [24]. In addition, multi-junction solar cells seek to have an excellent current match between subcells or add more subcells to divide the solar spectrum evenly [25, 26]. Hence, an ideal multi-junction solar cell will have minimal defects with the identical current generated from each subcell. There are three main approaches to overcome the material quality and lattice-matching limitations: wafer bonding/ mechanical stacking, metamorphic growth, and the inclusion of quantum wells (QWs). The first approach to overcome the material quality and the lattice matching issue is the wafer bonding or mechanical stacking, which employs combining structures of different lattice constants grown on different substrates. One example of wafer bonding is InGaP (1.88 eV)/GaAs (1.42 eV)//InGaAsP (1.12 eV)/InGaAs (0.74 eV) four-junction (4J) solar cell [11], where lattice-matched InGaP/GaAs and InGaAsP/InGaAs structures were grown separately on GaAs and InP substrates, respectively. Then the two junctions are bonded to each other during processing and the GaAs substrate is lifted-off. The second approach to overcome the material quality and the lattice matching issue is the metamorphic growth, which uses a compositionally graded buffer to relieve the build-up of stress during monolithic growth in order to access subcells with optimal bandgaps that cannot be epitaxially grown without defects [9, 35]. One example of a metamorphic structure is 4J InGaP (1.8 eV)/GaAs (1.40 eV)/InGaAs (1.0 eV)/InGaAs (0.7 eV), where a compositionally graded transparent buffer of InGaP was grown to reduce the introduction of dislocations between InGaAs and GaAs subcells [9].

2.2. Quantum Well Solar Cells (Review)

The use of quantum wells is an alternative promising approach to realize multi-junction solar cell structures with optimal bandgaps without violating the lattice-matching condition [27]. Quantum wells are periodic nanostructures that consist of a low bandgap material, well, sandwiched between two higher bandgaps, barriers. Schematics of the two quantum well structures, studied in this chapter, are shown in Figure 2.1. The InGaAs/GaAsP and InGaN/GaN quantum wells are grown in the intrinsic region of p-i-n (or n-i-p) solar cell structures, as shown in the schematics of Figure 2.1. The emitter/base of InGaAs/GaAsP and InGaN/GaN quantum well

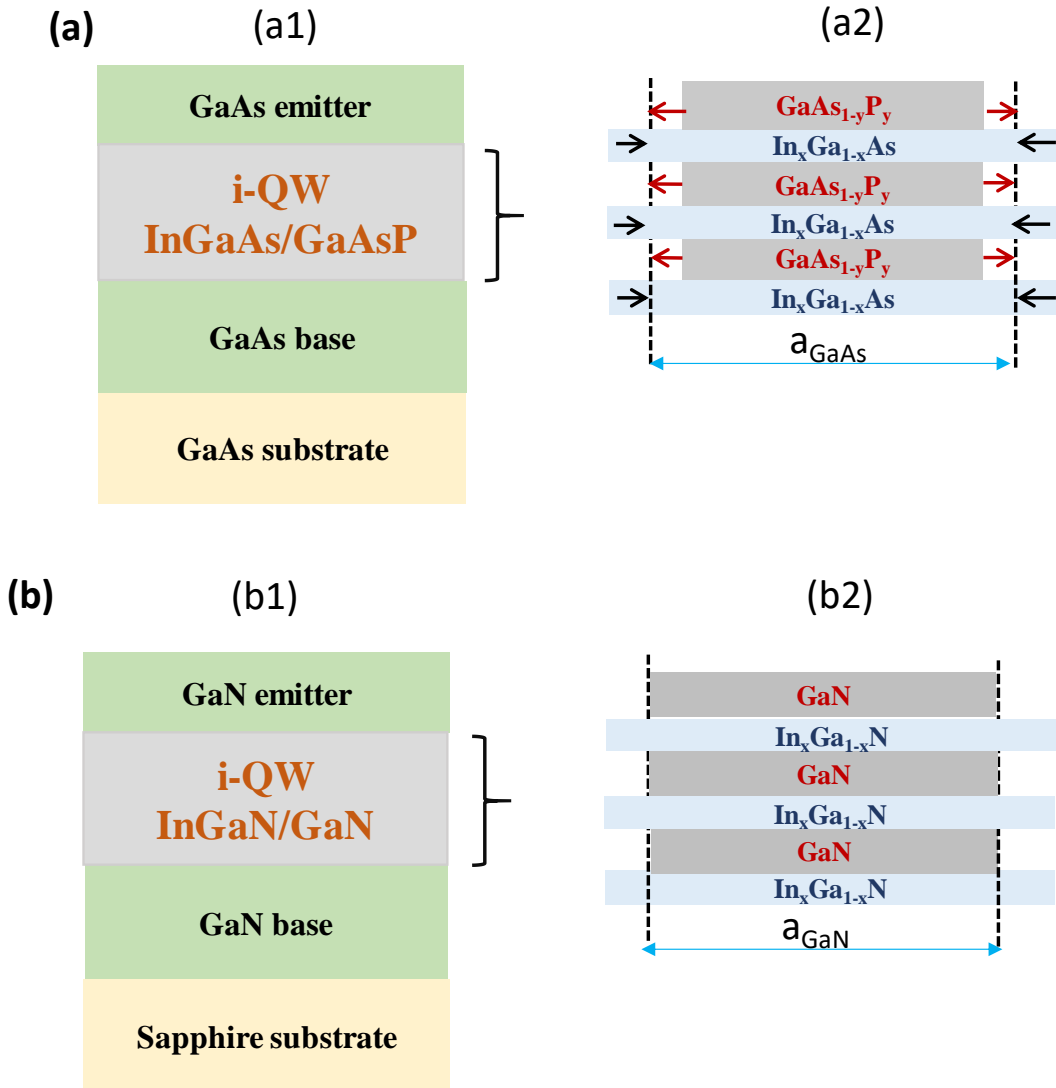


Figure 2.1: Schematics of: (a) GaAs p-i-n solar cell that includes strain-balanced InGaAs/GaAsP quantum wells, grown on GaAs substrate, and (b) GaN p-i-n solar cell that includes strained InGaN/GaN quantum wells, grown on GaN templates on sapphire substrate.

solar cells are GaAs and GaN, respectively, Figure 2.1. The lattice constant-bandgap diagram of each quantum well structure, showing the well/barrier lattice constants and bandgap range for each material system is shown in Figure 2.2. In Chapters 4-7, novel strain-balanced and lattice-matched InGaAsP/InGaP quantum well solar cells are presented.

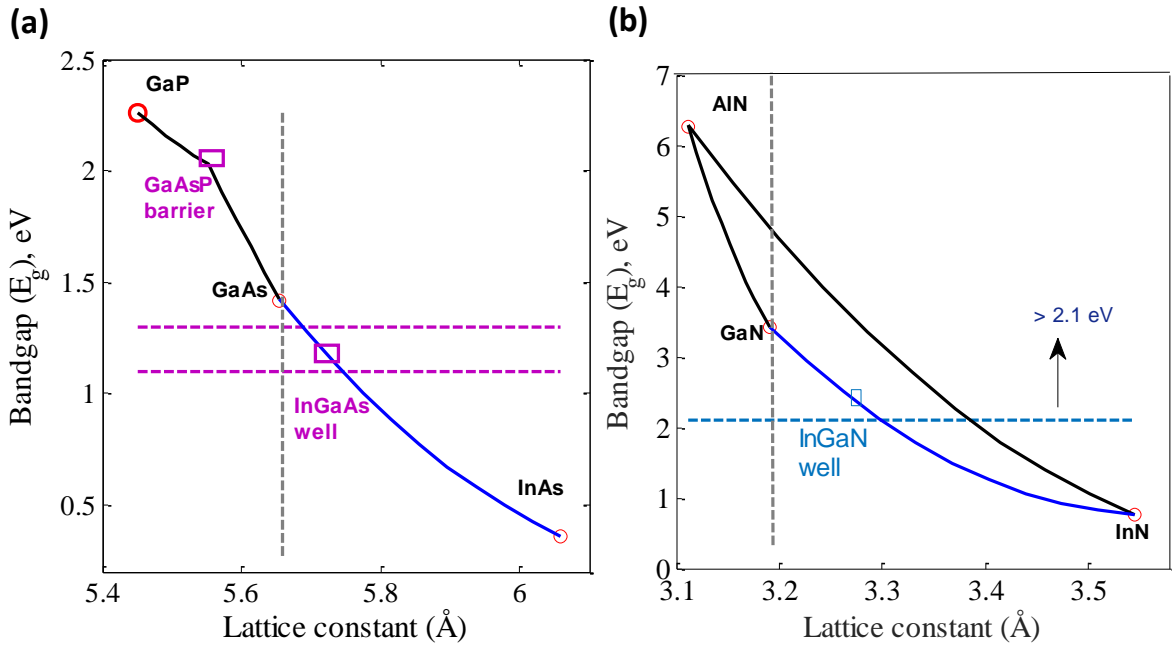


Figure 2.2: Bandgap versus lattice constants showing the well and barrier compositions for the three QW structures in Figure 1: (a) strain-balanced InGaAs/GaAsP QWs, and (b) strained InGaN/GaN QWs. The vertical dotted line in each figure represents the lattice-matched condition to GaAs/GaN. The horizontal dotted lines represent the region of interest in each QW structure.

2.2.1. Quantum Well Material Systems

The quantum wells can be either lattice-matched, strain-balanced, or strained. The first QW approach is the lattice-matched material systems, where the well and barrier have a lattice constant similar to the underlying substrate. Chapters 6 and 7 of this dissertation presents a novel lattice-matched $\text{In}_x\text{Ga}_{1-x}\text{As}_{1-z}\text{P}_z / \text{In}_{0.49}\text{Ga}_{0.51}\text{P}$ quantum well structure, where the $\text{In}_x\text{Ga}_{1-x}\text{As}_{1-z}\text{P}_z$ well and $\text{In}_{0.49}\text{Ga}_{0.51}\text{P}$ barrier are grown lattice-matched to GaAs substrate, in the intrinsic region (i) of $\text{In}_{0.49}\text{Ga}_{0.51}\text{P}$ p-i-n solar cells. The second QW approach is the strain-balanced material systems, where pseudomorphically-layered are epitaxially grown through balancing the compressive stress formed by the well with the tensile stress on the barrier, as shown in Figure 2.1(a2) and Figure 2.1(b3). An example of strain-balanced material system is InGaAs/GaAsP, grown in the intrinsic region of GaAs p-i-n structure as shown in Figure 2.1(a2). The InGaAs quantum well was grown under compressive stress, with lattice constant higher than that of GaAs, to tune the bandgap to less than 1.4 eV, as shown in Figure 2.1(a). Chapters 4 and 5 of this dissertation presents a novel strain-balanced $\text{In}_x\text{Ga}_{1-x}\text{As}_{1-z}\text{P}_z / \text{In}_y\text{Ga}_{1-y}\text{P}$ QW structure, where $\text{In}_x\text{Ga}_{1-x}\text{As}_{1-z}\text{P}_z$ is grown with

indium composition of higher than 49%, to tune the bandgap of $\text{In}_{0.49}\text{Ga}_{0.51}\text{P}$ -based cells (1.85 eV) to the 1.6-1.8 eV range as shown in Figure 2.2(b). The $\text{In}_y\text{Ga}_{1-y}\text{P}$ barrier was grown with under tensile stress with indium compositions less than 49% to strain-balance the QW structure as will be discussed later in detail in Chapters 4 and 5. The well/barrier thicknesses are adjusted to strain-balance the structure as will be discussed in detail in Section 2.5 of this Chapter. Using the strain-balance concept, the build-up of strain energy during growth can be controlled, to allow the growth of a high number of periodic quantum wells with minimal stress relaxation. This concept was developed, by Bedair, in the eighties in light emitting diodes (LEDs) to tune the bandgap of GaAs to lower energy values [36]. Then the same concept was applied to solar cells [37] to provide more design flexibility in tuning subcells in multi-junction devices. The third QW approach is the strained material system, where the lattice constants of the well and barrier are not similar as shown in Figure 2.1(c2) and Figure 2.2(b) for the InGaN/GaN material system. This results in a strained structure and the net stress in the whole structure will be compressive, which will limit the number of quantum wells that can be included in any GaN n-i-p structure. The strained InGaN/GaN QW tune the bandgap to energy values less than 3.4 eV as shown in Figure 2.2(c). Another example of strained QW structure is InGaAs/GaAs grown in the i layer of GaAs p-i-n structure to tune the bandgap of GaAs-based cells to energy values less than 1.4 eV [38], where the InGaAs quantum well was grown under compressive stress. Using the QW approach, strain-balanced InGaAs/GaAsP on GaAs substrates [37, 39-42] and strained InGaN/GaN on GaN templates on sapphire substrates [43-47] have been proposed as alternatives to realize 1.1-1.3 eV and >2.1 eV solar cells, respectively, as shown in Figure 2.2. In Chapters 4-7, novel strain-balanced and lattice-matched InGaAsP/InGaP quantum well structures are presented to tune the bandgap of InGaP-based cells to 1.6-1.8 eV.

2.2.2. Advantages of Quantum Well Solar Cells

The advantages of quantum well solar cells can be summarized as follows:

- 1- Quantum wells can be grown lattice-matched or strain-balanced to GaAs substrates thus accessing wide bandgaps that are not accessible by bulk absorbers grown lattice-matched to GaAs substrates. For example, the absorption threshold of InGaAs/GaAsP solar cell can be extended to 900-1127 nm, which is a wide range not available from any material lattice-

matched to GaAs substrates. The bandgap tunability of quantum wells will be discussed in detail in Section 2.3.

- 2- The tandem solar cell that incorporates quantum well structure in any of its subcells is grown under upright conditions without any extra fabrication steps. In the inverted metamorphic approach discussed in Section 2.1, the GaAs substrate needs to be etched during processing.
- 3- High performance quantum well solar cells can be grown at low growth temperatures (~500-600 C) which are much less than the temperatures to grow high-quality solar cells that are based on bulk absorbers. The low temperature results in less thermal degradation effects on the tunnel junctions that are grown underneath the subcell in the multi-junction device [48-50].
- 4- Quantum well maintains open-circuit voltage close to the fundamental limit set by Shockley-Quassier. By increasing the number of junctions in the multi-junction stack, there will be less current generated from each subcell. Comparing multi-junction solar cell devices based on four junctions and seven junctions, the seven-junction device will exhibit a lower-current and a higher voltage than the four-junction device. Thus, it is important to guarantee that each subcell in next-generation five (or more) junction devices, generates voltage close to the fundamental limit. To assess how close the solar cells to the fundamental limit set by Shockley-Quassier, the bandgap-voltage offset, $W_{oc} = E_g - V_{oc}$, is typically used as a figure of merit [51]. A W_{oc} close to 0.4 V indicates high internal radiative efficiency. Quantum well solar cells, typically attain W_{oc} values close to 0.4 V and thus offers this advantage and can potentially be incorporated in multi-junction solar cells to enhance the cell efficiency.

Despite these potentials, there are several challenges for the realization of high-performance QWSCs are mainly: materials growth with high-quality and realizing efficient light absorption and carrier collection. These challenges will be discussed in the next few sections by modeling the bandgap tunability, CLT and strain-balance constraints of InGaAs/GaAsP, InGaAsP/InGaP, and InGaN/GaN. The effects of layers thicknesses and compositions on carrier collection (by drift) are also discussed.

2.3. Bandgap Tunability

As shown in the lattice-constant versus bandgap diagrams of Figure 2.2(a), the strain-balance approach allows one to optimally select the bandgap of each junction to maximize the efficiency of multi-junction solar cells. For example, the use of strain-balanced InGaAs/GaAsP quantum wells allows one to access absorbing layers in the 1.1-1.3 eV range which are not available from a bulk material lattice matched to GaAs, as shown in Figure 2.2(a). This can be achieved while maintaining the lattice-matching condition to GaAs substrates. The effective bandgap ($E_{G,Eff}$), or equivalently the optical absorption threshold, of a QW structure is a function of quantum size effects (QSE), quantum confined stark effects (QCSE), and stress effects. Thus, the $E_{G,Eff}$ of these QW structures should be adjusted to account for current-matching condition in the multi-junction solar cell structure.

The $E_{G,Eff}$ of the quantum well can be estimated as follows,

$$E_{G,Eff} = E_G^{well,relaxed} + \Delta E_G^{Strain} + \Delta E_G^{QSE} + \Delta E_G^{QCSE} \quad (2.1)$$

where $E_G^{well,relaxed}$ represents the relaxed well bandgap, ΔE_G^{Strain} represents the shift in the QWs absorption due to compressive or tensile strain in the multiple-quantum well layers, ΔE_G^{QSE} represents the bandgap shift due to the QSE, and ΔE_G^{QCSE} represents the well thickness dependent shift in the effective band gap due to QCSE. The bandgaps used in the model for InGaAs, GaAsP, InGaAsP, InGaP, and InGaN are linearly interpolated between the binary compounds [52]. The conduction band and valence band offsets are estimated based on Anderson's rule. Kronig-Penney model is used to calculate the quantum states [53]. The strain has two effects on the band gap. The first effect is a change in the relative energy of the conduction and valence band energy. The magnitude of this energy difference, ΔE_1 , depends upon the strain, ε , the elastic stiffness coefficients, C_{11} and C_{12} , and the hydrostatic deformation potential, "a". These parameters depend upon the composition of the strained layer and ΔE is given as follows [54],

$$\Delta E_1 = -2a \left(\frac{C_{11} - C_{12}}{C_{11}} \right) \varepsilon \quad (2.2)$$

The second effect due to strain is the splitting of the heavy hole (hh) and light hole (lh) degeneracy. For a compressive material, the heavy hole will move to a higher energy while for a tensile material

the light hole will be at a higher energy. The magnitudes of energy splitting for heavy holes (ΔE_{hh}) and light holes (ΔE_{lh}) depend upon the shear deformation potential, “ b ” [54],

$$\begin{aligned}\Delta E_{hh} &= b \left(\frac{C_{11} + 2C_{12}}{C_{11}} \right) \varepsilon \\ \Delta E_{lh} &= -b \left(\frac{C_{11} + 2C_{12}}{C_{11}} \right) \varepsilon\end{aligned}\quad (2.3)$$

The elastic stiffness’s, hydrostatic-pressure and shear deformation potential values used in the strain effects calculations are obtained from Adachi [52]. ΔE_G^{QSE} is calculated through using the Kronig-Penney model to find the $n = 1$ quantum state for electrons and holes. The last term in Eqn. (2.1), ΔE_G^{QCSE} represents the well thickness dependent shift in the effective band gap due to the quantum-confined stark effect (QCSE) [55, 56],

$$\Delta E_{G,QCSE} = \left(\frac{15 - \pi^2}{24\pi^2} \right) \left(\frac{m_e^* L_{eff,CB}^4 + m_h^* L_{eff,VB}^4}{\hbar^2} \right) qF^2, \quad (2.4)$$

where m^* is the effective mass, q is the elemental charge, \hbar is the reduced Planck constant, $L_{eff,CB}$ and $L_{eff,VB}$ are the effective quantum well width in the conduction and valence band [57], and F is the induced electric field due to spontaneous and piezoelectric polarization.

The $E_{G,eff}$ of strain-balanced InGaAs/GaAsP was calculated using Eqn. (2.1). The $E_{G,eff}$ of strained InGaN/GaN was calculated using a physics-based software to solve Schrodinger-Poisson for the QW bound state energy. The effective bandgap of strain-balanced InGaAs/GaAs_{0.35}P_{0.65} and strained InGaN/GaN versus well thickness (t_w) for various indium compositions are shown in Figure 2.3. The barrier thickness (t_b) of GaAs_{0.35}P_{0.65} was adjusted to achieve the strain-balance condition. The GaN barrier thickness was fixed at 80 Å. The horizontal dotted lines in each sub-figure represent the region of bandgaps for each QW structure that is of interest for various multi-junction solar cell designs. As the well thickness increases, quantum size effects are being reduced thus the $n = 1$ quantum state moves downwards resulting in a red-shift in the effective bandgap. The effective bandgap reduces monotonically by increasing the indium composition. The field, F , is in the MV/cm range for the InGaN/GaN structure and is in kV/cm range in the GaAs-based and InGaP-based structures. Thus, QCSE plays a dominant role in controlling the emission and

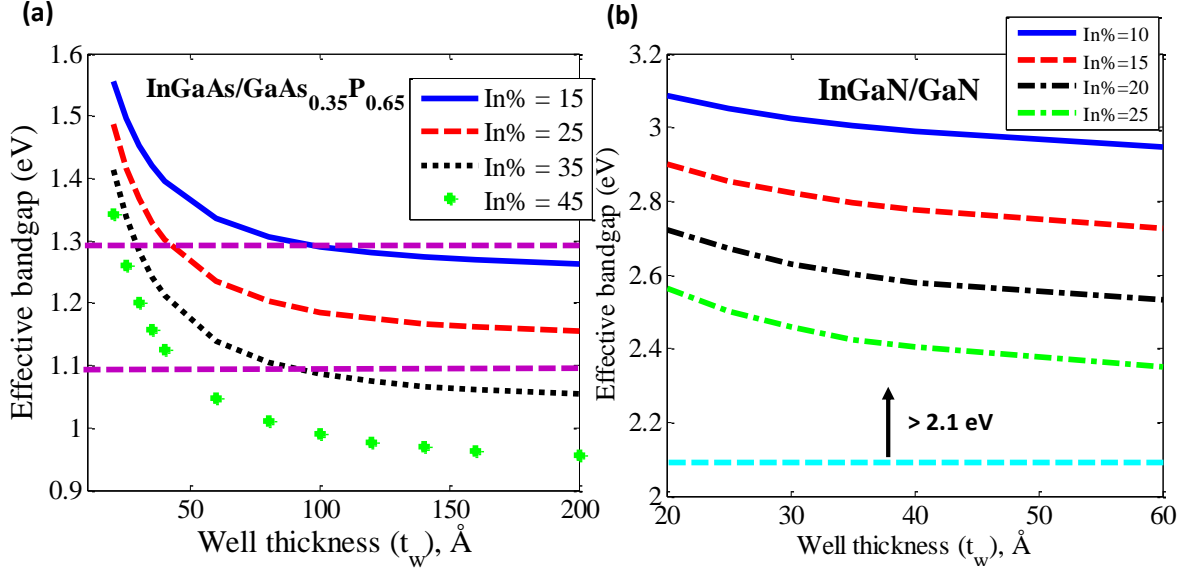


Figure 2.3: Effective bandgap versus well thickness (t_w) for various indium compositions in wells for the following structures: (a) strain-balanced InGaAs/GaAs_{0.35}P_{0.65}, and (b) strained InGaN/GaN. The barrier thickness (t_b) of GaAs_{0.35}P_{0.65} was adjusted to achieve the strain-balance condition. The GaN barrier thickness was fixed at 80 Å.

absorption processes in the GaN-based QW structures. The increase of the indium percentage in InGaN increases F and QCSE and results in a red-shift in the bandgap. It is noted that there is more than one design in each of these structures that can theoretically realize the target bandgap in each of these structures. For example, a 1.2 eV InGaAs/GaAsP QW solar cell can be achieved using an In_{0.25}Ga_{0.75}As QW of thickness 80 Å or an In_{0.45}Ga_{0.55}As QW of thickness 30 Å. The choice of the well/barrier thicknesses and compositions is a design factor that is challenged by other factors such as CLT, strain balance, material quality and carrier transport constraints as will be discussed in the next few subsections.

2.4. Critical Layer Thickness Constraints

InGaAs and InGaN quantum wells can be grown compressively strained to GaAs and GaN templates on sapphire substrates, respectively, provided that the film thickness remains less than the CLT. The CLT is a thickness below which a material can be grown fully strained without the formation of misfit dislocations [24, 58, 59]. The CLT is a function of strain, ε , caused by lattice mismatch between the film and substrate, where $\varepsilon = \frac{a_{film} - a_{sub.}}{a_{sub.}}$; a_{film} and $a_{sub.}$ are the lattice constants

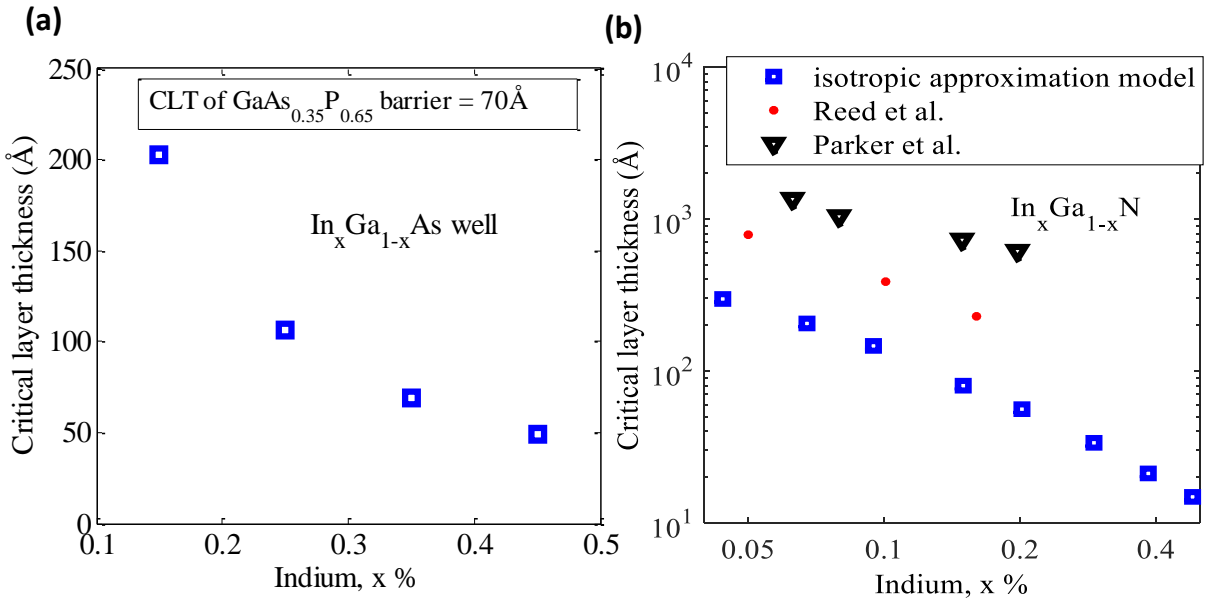


Figure 2.4: Critical layer thickness versus the indium content for: (a) $\text{In}_x\text{Ga}_{1-x}\text{As}$ well, and (b) $\text{In}_x\text{Ga}_{1-x}\text{N}$ well.

of film and substrate, respectively. A larger lattice mismatch yields a larger strain build up and results in a lower CLT. The CLT of InGaAs quantum wells are calculated using Matthews and Blakeslee [58] which has a good agreement with experimental results for III-V semiconductors, Figure 2.4(a)-(b). The CLT of InGaN was modeled using the isotropic approximation core energy method [60] and experimental values by Parker et al. and Reed et al. are also used [61, 62], Figure 2.4(b). As shown in Figure 2.4, the CLT depends critically on the value of indium for the three QW structures. For example, the CLT of $\text{In}_x\text{Ga}_{1-x}\text{As}$ films with $x = 15\%$, 25% , and 35% are 202 \AA , 106 \AA , and 70 \AA , respectively as shown in Figure 2.4 (a). Similarly, the CLT of InGaN reduces significantly by increasing the indium percentage, Figure 2.4(b). The spread in the data for the CLT of InGaN is due to whether it is estimated for a bulk InGaN layer or for InGaN as part of an InGaN/GaN QW structure.

Unfortunately, the amount of indium needed to achieve the optimum bandgap for the InGaAs(P) and InGaN would create a mismatch that limits CLT to a few hundred Angstroms or less. This thickness will not provide enough optical absorption to create an effective QW subcell in multi-junction solar cells. If the QWs were grown thicker, the material would form dislocations/defects, and the dark current from non-radiative recombination will significantly increase. Hence, researchers have focused on growing a high number of period QW devices with individual layers

thicknesses less than the CLT in order to increase the total thickness of absorbing wells without sacrificing the CLT limitations.

2.5. Strain Balance Design and Criteria

Even if the individual layers in the periodic quantum well structure are grown less than the CLT, the whole structure may relax if the strain-balance condition was not fully realized. If the strain-balance condition was not met, there will be a net accumulation of compressive or tensile stress in whole multiple QW structure that can lead to lattice-mismatch with the substrate. The excess of compressive or tensile stress will result in the relaxation of strained layers and will form dislocation defects. This is particularly observable during the growth of a high number of periods (for instance, higher than 50) which is required to enhance light absorption in the QW structures. For instance, strained InGaAs/GaAs QW solar cell has a limited external quantum efficiency of less than 20% beyond the band-edge of GaAs due to a limited number of QWs that can be included [38]. Increasing the number of strained quantum wells can increase the dark current, and degrades FF and η . This is also a challenge hindering the development of high-performance InGaN/GaN, if not grown strain-balanced because the net strain, mainly in the InGaN layers, will always be compressive and limited number of periods can be grown [43, 46, 47].

There are four parameters that can be controlled during the QW growth to strain-balance the structure: (i) t_w , (ii) t_b , (iii) lattice constant of well (a_w), and (iv) lattice constant of barrier (a_b). There are several models to strain-balance these QW structures. One simple model is the average-lattice method which arises from the thickness average of compressive and tensile parameters [63],

$$(a_w - a_{temp.})t_w = (a_b - a_{temp.})t_b \quad (2.5)$$

where $a_{temp.}$ is the lattice constant of the underlying template (GaAs or GaN). Eqn. (2.5) assumes identical elastic properties for the well and barrier which can be inaccurate. A zero-stress balance model, by Ekins-Daukes et al., takes into account the differences in elastic properties of the wells and barriers [63]. The model relies on minimizing average in-plane stress due to biaxial strain in the quantum wells/barriers, and thus give better estimates for thicknesses that realize the strain-balance condition more than the average-lattice method [63]. The condition to achieve a stress-balance the QWs is as follows [63],

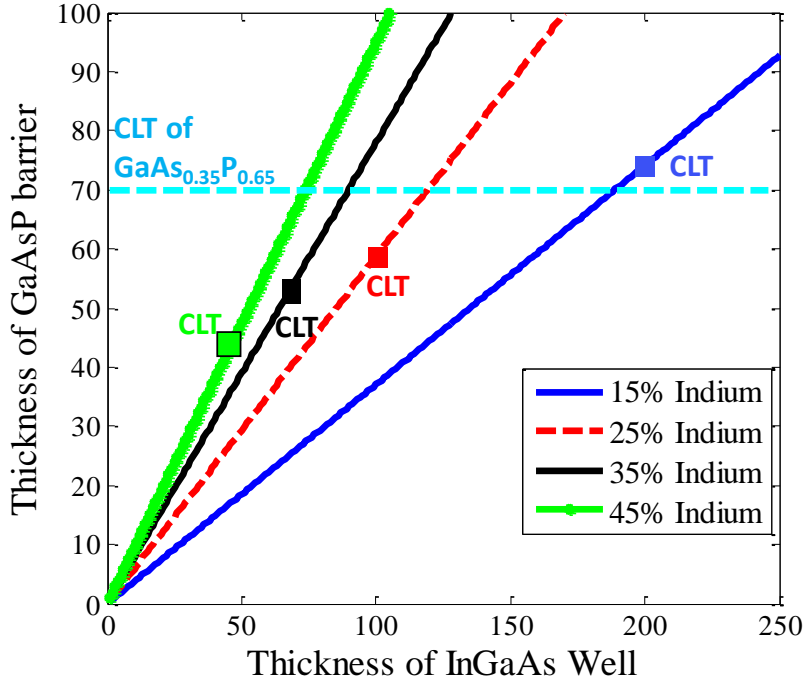


Figure 2.5: Thickness of wells and barriers as estimated by zero-stress balance model to strain-balance the following two structures to GaAs substrates:
InGaAs/GaAs_{0.35}P_{0.65} with various indium% in InGaAs well. The CLT of each well composition is added to the figure.

$$A_w t_w \epsilon_w a_b + A_b t_b \epsilon_b a_w = 0 \quad (2.6)$$

$$a_{temp.} = \frac{A_w t_w a_w a_b^2 + A_b t_b a_b a_w^2}{A_w t_w a_b^2 + A_b t_b a_w^2} \quad (2.7)$$

where ϵ_w and ϵ_b are the strain in wells and barriers, respectively. A_w and A_b are the stiffness parameters for wells and barriers, respectively, which are calculated as follows:

$$A = C_{11} + C_{12} - \frac{2C_{12}^2}{C_{11}} \quad (2.8)$$

The thicknesses of wells and barriers obtained from the zero-stress model to strain-balance In_xGa_{1-x}As/GaAs_{1-y}P_y is shown in Figure 2.5. There can be no similar graph for the strained InGaN/GaN because the net strain in whole structure will be always compressive. The effects of indium composition in InGaAs well is studied in Figure 2.5, and the composition of GaAsP is fixed. The CLT of each well composition is also added to the figure. We first notice that as the well thickness

increases, the compressive stress increases and the required barrier thickness to strain-balance the structure will also increase. For instance, In_{0.15}Ga_{0.85}As with well thickness of 25 Å and 100 Å can be strain-balanced by a GaAs_{0.35}P_{0.65} barrier with t_b of 10 Å and 40 Å, respectively. It is also noted that for a fixed barrier thickness and composition, InGaAs with wells having higher indium percentage will be thinner than those with lower indium% as shown in Figure 2.5. These curves can be used as a design guideline to estimate the thicknesses needed to achieve nearly strain-free QW structures.

2.6. Carrier Transport

QW solar cells are p-i-n structures where the QWs are located in the intrinsic (i) layer. Carriers, optically generated in the QWs, are either collected by the built-in field that exists in the QW region or lost due to carrier recombination. There are two QW approaches to collect carriers by drift: (i) use of thin wells, and carriers are transported by electric field via thermionic emission as shown in Figure 2.6(a), and (ii) use of thin barriers and carriers are transported by electric field via tunneling as shown in Figure 2.6(b). Carrier transport, by thermionic emission, requires growing thin wells (~50 Å) with low effective barrier height (~ few kT, where k is Boltzmann's constant and T is temperature). The realization of carrier transport by tunneling requires the use of thin barriers (~20-40 Å) and the reduction of effective barrier heights. The escape lifetime ($\tau_{esc.}$) of a carrier from a QW is determined by the thermionic emission and tunneling lifetimes as follows [64],

$$\frac{1}{\tau_{esc.}} = \frac{1}{\tau_{tun.}} + \frac{1}{\tau_{therm.}}, \quad (2.9)$$

where $\tau_{tun.}$ and $\tau_{therm.}$ are tunneling and thermionic-emission lifetimes, respectively. $\tau_{tun.}$ and $\tau_{therm.}$ can be expressed as [64-66],

$$\frac{1}{\tau_{tun.}} = \frac{n\pi\hbar}{2t_w^2 m_w^*} e^{-\frac{2}{\hbar} \int_0^{t_b} \sqrt{2m_b^*(E_b - E(z))} dz} \quad (2.10)$$

$$\frac{1}{\tau_{therm.}} = \frac{1}{t_w} \sqrt{\frac{kT}{2\pi m_w^*}} e^{-\frac{E_b}{kT}}, \quad (2.11)$$

where m_w^* and m_b^* are the effective masses at the well and the barrier, respectively. E_b is the effective barrier height from the ground state ($n = 1$), and $E(z)$ is the electric field. The escape probability of minority carriers from a single quantum well can be calculated as follows [64],

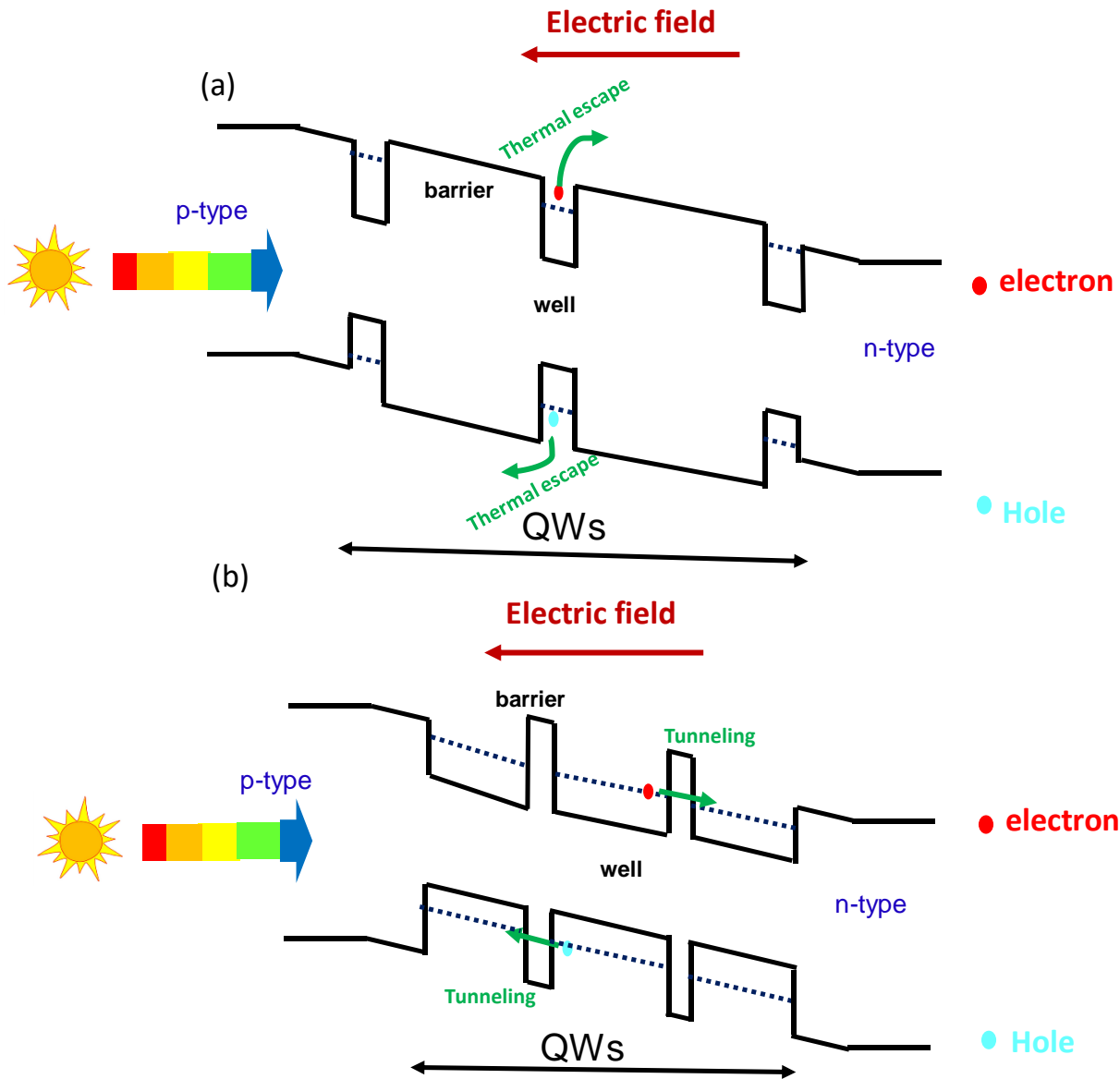


Figure 2.6: Band diagram of quantum well solar cells with two different designs: (a) structure with thin wells and low effective barrier height to promote thermionic emission, and (b) structure with thin barriers to allow carrier tunneling. In both scenarios, the carriers are swept across the depletion region by an electric field.

$$P = \frac{\frac{1}{\tau_{esc.}}}{\frac{1}{\tau_{esc.}} + \frac{1}{\tau_{rec.}}}, \quad (2.12)$$

where $\tau_{rec.}$ is the recombination lifetime. Thus, the probability of carrier collection is high, for QWs with long carrier lifetime and short escape lifetime, i.e. $\tau_{esc.} \ll \tau_{rec.}$. This does impose restrictions on material quality. If we assume that the escape probabilities from all the quantum wells are the same, the total escape probability can be expressed as follows

$$P^{tot.} = P^N, \quad (2.13)$$

where N is the number of quantum wells in the intrinsic region. For example, if the escape probability (P) across a single QW is 0.98, the total escape probability ($P^{tot.}$) across 20 QWs, is $0.98^{20} = 0.67$ which is not high enough to guarantee efficient carrier collection by drift. Hence, the thickness of well and barrier, as well as the effective barrier height should be tuned to maximize the carrier escape probability without sacrificing the material quality. Eqn. (2.13) assumes all carriers generated in the QW and neutral regions will traverse N quantum wells. However, each carrier traverses a different number of wells, depending on the position where the carrier was generated. Thus, Eqn. (2.13) assumes the worst-case scenario for a carrier transport.

For $\text{In}_{0.11}\text{Ga}_{0.89}\text{As}$ (93 Å)/ $\text{GaAs}_{0.93}\text{P}_{0.07}$ (160 Å), the thermionic-emission lifetimes for electrons, calculated using Eqn. (2.11) for the first quantum state is 1.68 psec, which is more than 1000 times shorter than tunneling lifetime (~7 nsec), thus indicating that thermionic emission is the dominant carrier transport. If the QWs are fully strain-balanced with high material quality, the recombination lifetime, $\tau_{rec.}$, will be much longer than $\tau_{therm.}$ and this will lead to a 100% escape probability for the carriers swept by drift as indicated by Eqn. (2.12). If we assume a structure that has a thin barrier thickness such as $\text{In}_{0.18}\text{Ga}_{0.82}\text{As}$ (125 Å)/ $\text{GaAs}_{0.36}\text{P}_{0.64}$ (40 Å), the tunneling and thermionic-emission escape lifetimes, $\tau_{tun.}$ and $\tau_{therm.}$, for electrons are 0.89 nsec and 1.84 μsec, respectively. The shorter tunneling escape time indicates that tunneling is dominating the transport. If a recombination time, $\tau_{rec.}$, of 50 nsec is assumed, the tunneling escape probability across a single QW and 100 QWs will be 0.984 and $0.984^{100} = 0.1686$ as calculated using Eqn. (2.12) and Eqn. (2.13), respectively. The escape probability across the 100 QWs is not sufficiently high for efficient carrier collection. If the $\text{GaAs}_{0.36}\text{P}_{0.64}$ barrier thickness is reduced from 40 Å to 20 Å, $\tau_{tun.}$

will be reduced from 0.89 nsec to 4.1276 psec, thus increasing the escape probability across the 100 QWs from 0.1686 to 0.9918. This indicates that the use of thin-barriers is essential for tunneling to take place efficiently. The same discussion is also valid for the holes. In the next section, different QW material systems are studied and the effects of different QW designs on carrier transport and collection are analyzed.

Chapter 3: Review of Recent Progress in Quantum Well Solar Cells

This chapter presents a literature survey of the recent progress in the field of quantum well solar cells. Two quantum well solar cells that have been widely researched are discussed, strain-balanced InGaAs/GaAsP and strained InGaN/GaN. For each material system, the major advancements in its development and the challenges facing it are discussed. The analysis of carrier transport discussed in Section 2.6 is used to analyze the carrier tunneling and thermionic emission for the structures discussed in this Chapter.

3.1. Strain-balanced InGaAs/GaAsP Quantum Wells (1.1-1.3 eV Subcell)

InGaAs/GaAsP is grown in the unintentionally doped i layer of GaAs n-i-p (or p-i-n) solar cells as shown in Figure 2.1(a). The emitter and base are GaAs doped typically with silicon (or selenium) and zinc (or carbon), respectively. There are several potential applications of this QW structure in multi-junction solar cells. First, InGaAs/GaAsP has been widely used in triple-junction devices (1.8/1.2/0.7 eV) to tune the bandgap of GaAs solar cells to 1.2 eV to increase the short circuit current (J_{sc}) and alleviate the current mismatch between the top and middle cells [37, 39-41, 67]. In addition, InGaAs/GaAsP with a bandgap of 1.1 eV is a potential candidate for the bottom cell material in dual-junction (1.7/1.1 eV) solar cell, with a prospective one-sun AM1.5G efficiency of 36-38% [16]. Recent efforts by NCSU/Spectrolab have shown the successful integration of $\text{In}_{0.49}\text{Ga}_{0.51}\text{P}$ (1.9 eV) top cell with GaAs bottom cell that incorporates InGaAs/GaAsP QWs [67]. Also, InGaAs/GaAsP has been proposed as a 1.15 eV subcell in quad-junction devices with a prospective efficiency of 50% [68].

Researchers have developed InGaAs/GaAsP quantum well solar cells based on the two carrier transport mechanisms discussed in Section 2.6 and Figure 2.6. In order to realize thermionic emission carrier transport in InGaAs/GaAsP, the high-bandgap strain-compensating barrier, GaAsP, must have a composition that yields lattice constant and bandgap close to GaAs substrate such that the effective barrier height for electrons and holes will be sufficiently low to surmount, as shown in band diagram of Figure 2.6 (a). The external quantum efficiency (EQE) of 50-period

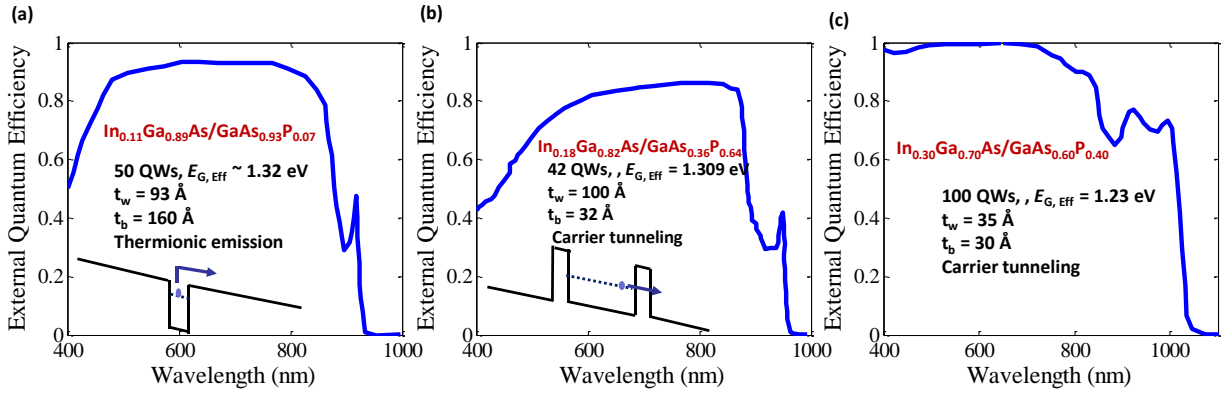


Figure 3.1: External quantum efficiency of multiple InGaAs/GaAsP quantum well solar cells designs: (a) structure with thin wells and low effective barrier height to promote thermionic emission, by Adams et al. [69], (b) structure with thin barriers to allow carrier tunneling, by Bradshaw et al.[41, 70], and (c) high-performance structure with peak excitonic values exceeding 70%, by Fuji et al. [40]. More details about these structures such as the presence of window, back surface field or antireflection coatings are discussed in the references.

$\text{In}_{0.11}\text{Ga}_{0.89}\text{As}$ ($t_w = 93 \text{ \AA}$)/ $\text{GaAs}_{0.93}\text{P}_{0.07}$ ($t_b = 160 \text{ \AA}$), by Adams et al. [69], is shown in Figure 3.1(a). The conduction band diagram for that structure is also shown in the inset of the same figure. It is noted that the phosphorus and indium compositions in the GaAsP barrier and InGaAs layers are only 7% and 11% which will lead to a tensile and compressive strain of -0.25% and 0.8%, respectively. For wavelengths (λ) shorter than the GaAs band-edge (885 nm), absorption occurs in the GaAs:p emitter and GaAs:n base and the high EQE values indicates efficient light absorption and carrier collection. For λ 's longer the GaAs band-edge, absorption occurs in the InGaAs/GaAsP QWs, and the inclusion of QWs in the intrinsic region has extended the absorption threshold to $\sim 932 \text{ nm}$. The high EQE values beyond GaAs-band-edge (hereafter, sub-bandgap EQE) that are exceeding 40% at 920 nm indicates that the electric field sweeps away all the carriers efficiently across the depletion region. The escape probabilities for electrons and holes for this QW structure were calculated using Eqns. (2.9)-(2.13), and the values are summarized in Table 3.1. The effective barrier heights for electrons and holes are 77 meV and 80 meV, respectively which yields to a unity thermionic probability (P_{therm}) across a single QW and across the 50 QWs. The thick GaAs_{0.93}P_{0.07} barrier (160 \AA) leads to zero tunneling probability (P_{tun}) for both electrons and holes, Table 3.1. Even though that research presents efficient light absorption and carrier collection, the percentage of the total absorbing InGaAs well (0.465 μm) represents only 37% of the total period thickness (1.26 μm). This is attributed to the use of the low-phosphorus composition in the GaAsP

Table 3.1: Tunneling (P_{tun}) and thermionic-emission (P_{therm}) escape probabilities for electrons and heavy hole states for different InGaAs/GaAsP QW designs

	$P_{tun.}$		P_{therm}		Carrier transport
	e	hh	e	hh	
In _{0.11} Ga _{0.89} As (93 Å)/ GaAs _{0.93} P _{0.07} (160 Å), 50-period [69]	0	0	0.9983	0.9983	Thermionic emission
In _{0.18} Ga _{0.82} As (100 Å)/ GaAs _{0.36} P _{0.64} (32 Å), 42-period [41, 70]	0.9431	0.94	0.1447	0	Carrier tunneling
In _{0.30} Ga _{0.70} As(35 Å)/ GaAs _{0.60} P _{0.40} (30 Å), 100-period [40]	1	0.9584	0.5672	0	Carrier tunneling

which will limit the increase of the absorbing InGaAs well thickness to maintain the strain-balance condition. If the InGaAs well thickness is further increased, the strain-balance condition will be violated resulting in the presence of defects which will degrade the η . One possible approach to address this issue is to increase the number of QWs to enhance the sub-bandgap EQE. However, increasing the number of QWs is typically accompanied by limitations associated with epitaxial growth challenges such as the strain-balance and CLT issues as discussed in Chapter 2, as well as the difficulty of obtaining a uniform electric field distribution across the QW region as will be discussed later in Chapter 5.

In order to address that limitation, another QW approach was proposed by NCSU that relies on using thicker absorbing wells and thin barriers through the use of high phosphorus in the GaAsP barriers [41, 71, 72]. The high phosphorus composition creates a larger compensating strain, therefore allowing the barriers to be thin enough that carrier tunneling is the dominant transport mechanism [41]. This removes two limitations that exist in the structure shown in Figure 3.1(a) that has low phosphorus GaAsP layers. First, the absorbing InGaAs layers of this approach form the majority of the QW region which can lead to enhancing the sub-bandgap EQE. Second, the indium composition of the InGaAs is not limited by the requirement that effective barrier height should be sufficiently low for the carriers to surmount. For hundred-period In_{0.14}Ga_{0.86}As ($t_w = 115$ Å) and GaAs_{0.24}P_{0.76} ($t_b = 27$ Å) QWs, the thickness of the non-absorbing GaAs_{0.24}P_{0.76} barriers leads to only ~0.27 μm total barrier thickness. Thus, the i -layer will primarily consist of In_{0.14}Ga_{0.86}As optical absorbing films, ~1.1 μm, which is much thicker than the corresponding InGaAs thickness in the structure that relies on thermionic emission transport. This will

correspond to enhancement in the sub-bandgap EQE and will enhance the gain in J_{sc} if compared with that of a GaAs cell that does not include QWs. Figure 3.1(b) shows the EQE of 42-period $\text{In}_{0.18}\text{Ga}_{0.82}\text{As}$ ($t_w = 100 \text{ \AA}$)/ $\text{GaAs}_{0.36}\text{P}_{0.64}$ ($t_b = 32 \text{ \AA}$), by Bradshaw et al. [41, 70]. The EQE values in Figure 3.1(b) indicates efficient light absorption and carrier collection in both the bulk region and the QW region. The values for the probabilities for tunneling and thermionic emission, P_{tun} , and P_{therm} are summarized in Table 3.1. The thin $\text{GaAs}_{0.36}\text{P}_{0.64}$ barriers (30 \AA) allow for the carriers to tunnel efficiently across both single well and the 42-QWs. The P_{therm} across the QWs are less than 15% due to the high effective barrier height (0.413 eV for electrons and 0.2336 eV for holes).

There are several challenges with the growth of the InGaAs/GaAsP QW structure. First, it is challenging in terms of crystal growth to achieve such high phosphorus composition in GaAsP. This is because arsenic incorporates, by order of magnitude, higher than phosphorus when both arsine (AsH_3) and phosphine (PH_3) are present [73, 74]. The success behind growing 70% phosphorus GaAsP was realized by research groups that used tertiarybutylphosphine (TBP) and tertiarybutyl-arsine (TBA), with a $[\text{TBP}]/([\text{TBP}]+[\text{TBA}])$ flow ratio higher than 80% [40, 75].

The second challenge is related to the group V switching at InGaAs/GaAsP interfaces, which results in graded (non-abrupt) interfaces [76]. This leads to the formation of an unintentional quaternary InGaAsP alloy. This difficulty arises due to phosphorus and arsenic atoms intermixing as well as phosphorus carry-over. In order to improve $(\text{In},\text{Ga})\text{As}/\text{Ga}(\text{As},\text{P})$ interface quality, a GaAs interfacial was introduced, by Samberg et al., at both the InGaAs/GaAsP and GaAsP/InGaAs interfaces [76]. The GaAs transition layers have proved to prevent the phosphorus carryover between the barrier and well structures resulting in improvements in the electrical and material characteristics [40, 41, 76, 77].

A 100-period $\text{In}_{0.30}\text{Ga}_{0.70}\text{As}$ (35 \AA)/ $\text{GaAs}(27\text{\AA})/\text{GaAs}_{0.60}\text{P}_{0.40}$ (30 \AA) with an effective bandgap of 1.23 eV has been demonstrated, by Fuji et al. [40], as shown in Figure 3.1(c). The EQE values exceed 80% beyond band-edge of GaAs, thus indicating efficient light absorption and carrier collection, as well as excellent control over growth conditions. The carriers are swept across the depletion and neutral regions through tunneling as indicated by the P_{tun} and P_{therm} values in Table 3.1. The one-sun AM1.5 current density-voltage curve measured for the 100-period device, as well as, a GaAs device that does not include QWs, is shown in Figure 3.2 [40]. A schematic of the two structures is also depicted in the inset of Figure 3.2. The J_{sc} , V_{oc} , FF , and η of the 100-period

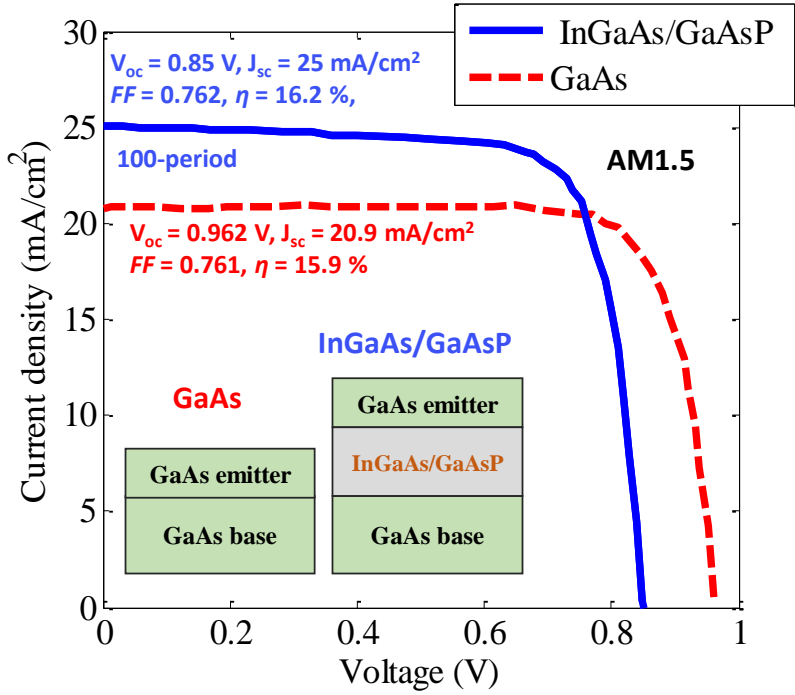


Figure 3.2: AM1.5 current-voltage characteristics of InGaAs/GaAsP QW and GaAs standard solar cells, with the inset showing a schematic of the two structures, by Fuji et al. [40].

$\text{In}_{0.30}\text{Ga}_{0.70}\text{As} / \text{GaAs}_{0.60}\text{P}_{0.40}$ QW device were 25 mA/cm^2 , 0.85 V , 76.2% , and 16.2% , respectively. The corresponding J_{sc} , V_{oc} , FF , and η values of GaAs standard device were 20.9 mA/cm^2 , 0.962 V , 0.761 , and 15.9% , respectively. The reported J_{sc} for the QW device is $\sim 20\%$ higher than the GaAs device [40]. The reason for J_{sc} enhancement is due to the sub-bandgap absorption by the QWs as shown in the EQE of Figure 3.1(c). The V_{oc} of QW device is 115 mV lower than the GaAs device due to extending the bandgap to 1.23 eV . The η of the QW device is higher than the GaAs (w/o QWs) device due to the large J_{sc} boost. Current-voltage characteristics showing J_{sc} and η improvements due to the addition of the QWs were also reported by the NCSU and Imperial College groups [39, 41]. More details about the structures discussed in Figure 3.1 such as the presence of window, back surface field or antireflection coatings are discussed in the references.

The effect of the number of periods on strain-balanced $\text{In}_{0.10}\text{Ga}_{0.90}\text{As}$ ($t_w = 80 \text{ \AA}$)/ $\text{GaAs}_{0.92}\text{P}_{0.08}$ ($t_b = 186 \text{ \AA}$) device performance is depicted in Figure 3.3(a) and Figure 3.3(b), using the tabulated data reported by Bushnell et al. [78]. It is worth pointing out that the carriers in this QW structure will be swept by drift through thermionic emission due to the use of low phosphorus barrier ($\text{GaAs}_{0.92}\text{P}_{0.08}$). There are two competing effects occurring with the increase in the number of QWs.

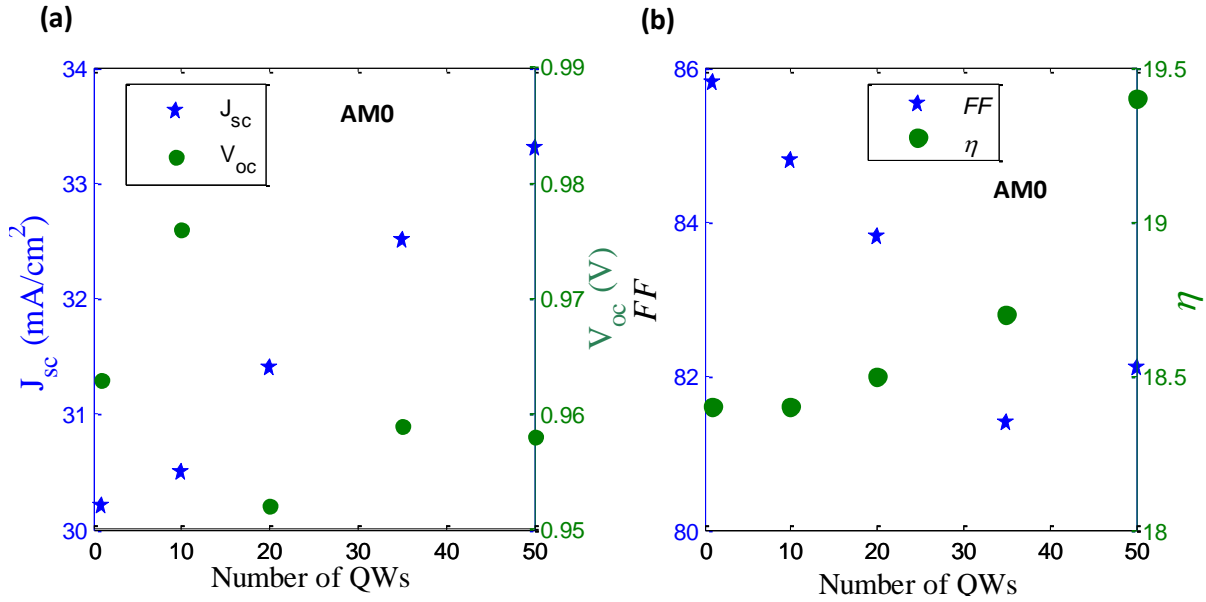


Figure 3.3: The effect of the number of QWs in the intrinsic region on one-sun AM0 current-voltage characteristics: (a) J_{sc} (mA/cm²) and V_{oc} (Volts) and (b) FF and η ; study by Bushnell et al. [78]

First, the increase of the QW number enhances the J_{sc} due to increasing the total thickness of absorbing layers, Figure 3.3(a). Second, a larger number of QWs increases the dark current due to increase in the depletion region thickness and number of interfaces, and thus increases the Shockley Read Hall recombination rate. The increase or decrease of V_{oc} , with the number of QWs, depends on the last two effects, and it typically does not vary significantly with the number of period change, as shown in Figure 3.3(a). Increasing the number of QWs from 1 to 50 has reduced the FF from 85.8 to 82.1%. This can be attributed to an expected increase in the total stress across the QW and improving the FF higher than 85% requires more enhancement of interfaces quality and excellent stress management to reduce the stress across the QW region. High-performance quantum well devices have a boost in J_{sc} that compensate both the V_{oc} and FF deterioration, thus resulting in an increase in efficiency if compared with standard GaAs devices, as shown in Figure 3.2 and Figure 3.3(b).

3.2. Strained InGaN/GaN Quantum Wells (> 2.1 eV subcell)

Strained InGaN/GaN quantum wells are grown in the unintentionally doped i layer of GaN n-i-p solar cells as shown in Figure 2.1(c). The emitter and base are GaN doped typically with magnesium and silicon, respectively. InGaN-based alloys have received tremendous attention for use in photovoltaic devices in the last few years [21, 43-46, 79, 80]. This interest has been driven

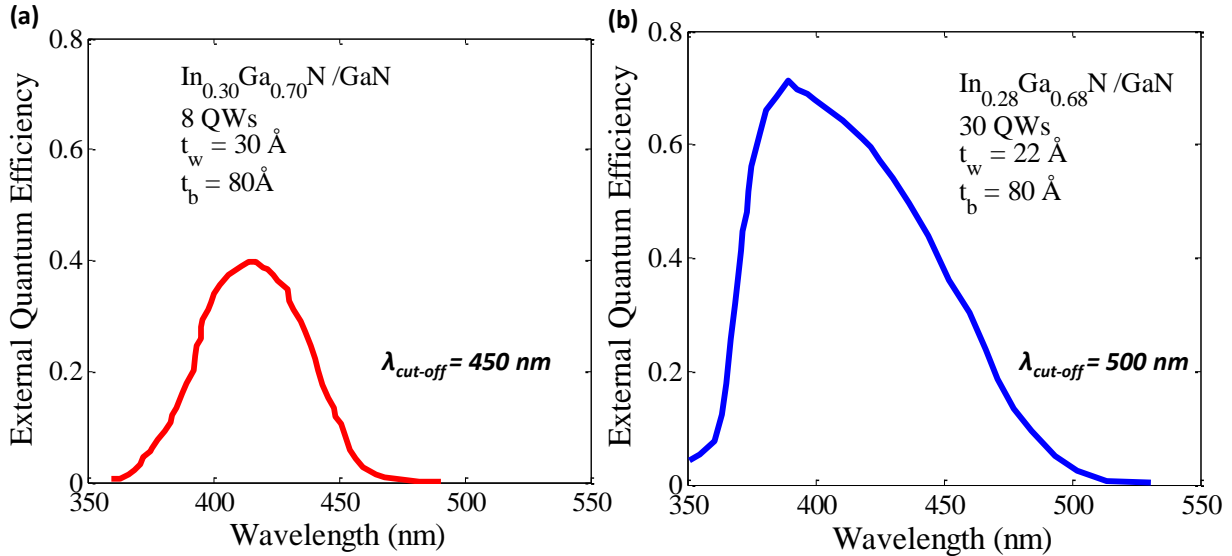


Figure 3.4: External quantum efficiency of InGaN/GaN QW solar cells with high indium percentage ($x > 0.2$): (a) eight periods of $\text{In}_{0.30}\text{Ga}_{0.70}\text{N}$ ($t_w = 30 \text{ \AA}$)/ GaN ($t_b = 80 \text{ \AA}$) that has a cut-off wavelength at $\sim 450 \text{ nm}$, by Dahal et al. [43] and (b) 30-period $\text{In}_{0.28}\text{Ga}_{0.68}\text{N}$ ($t_w = 22 \text{ \AA}$)/ GaN ($t_b = 80 \text{ \AA}$) that has a cut-off wavelength at $\sim 500 \text{ nm}$ by Farrell et al. [46], that includes heavily doped GaN layers to help in screening the polarization-induced in the QW region and rough GaN window to reduce front reflection

by favorable properties of InGaN-based alloys, including a direct band gap ranging from 0.64 eV for InN to 3.4 eV for GaN, high absorption coefficients of 10^5 cm^{-1} near the band edge, as well as high resistance to high energy photon irradiation [79] [81]. $\text{In}_{0.45}\text{Ga}_{0.55}\text{N}$ is also proposed as a potential topcell that can be mechanically stacked with Si in tandem solar cells to achieve η higher than 31% [82]. In addition, developing InGaN with bandgap higher than 2 eV is important for next generation five (or more) junction devices [21, 43-46, 79].

The EQE response of two structures that have indium percentage higher than 20% are reviewed because a bandgap in the 2.0-2.5 eV is required for next generation (five or more) photovoltaic devices. Figure 3.4(a) shows the EQE of eight-period of $\text{In}_{0.30}\text{Ga}_{0.70}\text{N}$ ($t_w = 30 \text{ \AA}$)/ GaN ($t_b = 80 \text{ \AA}$) that has a cut-off wavelength ($\lambda_{\text{cut-off}}$) at about 450 nm, by Dahal et al. [43]. Beyond the band-edge of GaN (365 nm), absorption occurs only in the $\text{In}_{0.30}\text{Ga}_{0.70}\text{N}$ quantum well and the quantum efficiency is limited to less than 10% at 450 nm due to several reasons. First, the total thickness of absorbing $\text{In}_{0.30}\text{Ga}_{0.70}\text{N}$ well is only 24 nm which is very thin to achieve high EQE values. Second, the presence of high lattice-mismatch between GaN and InN of $\sim 11.8\%$ results in highly strained

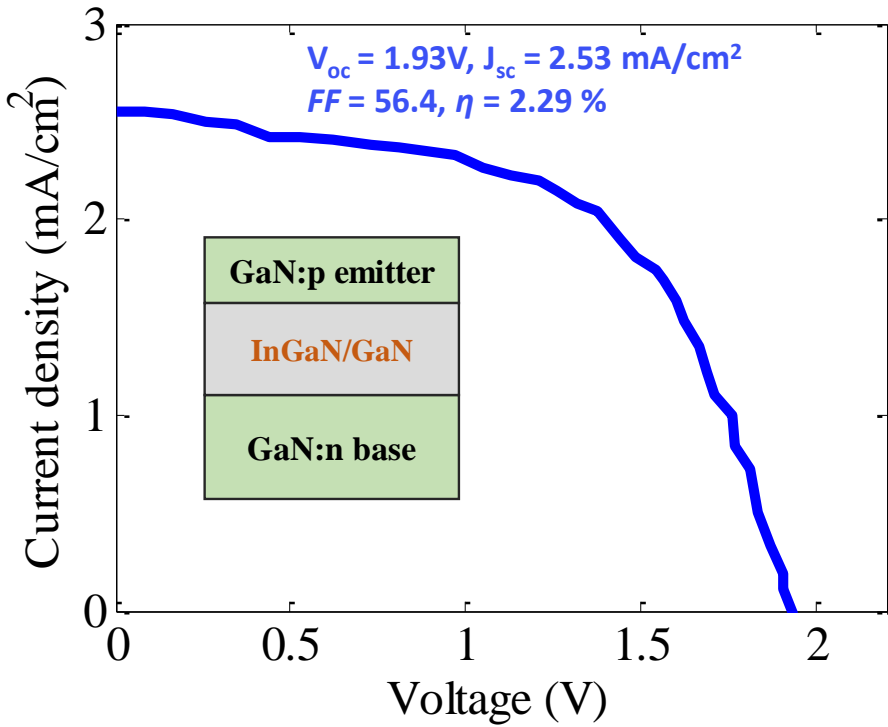


Figure 3.5: 1.2 suns AM1.5 current-voltage characteristics of 30-period $\text{In}_{0.28}\text{Ga}_{0.72}\text{N}$ ($t_w = 22 \text{ \AA}$)/GaN ($t_b = 80 \text{ \AA}$) by Farrell et al. [46], with the inset showing a schematic of this structure.

InGaN films especially for compositions higher than 20%, thus resulting in a highly defective material. This degrades the InGaN film quality and degrades the optical characteristics of the solar cell. Third, the use of high indium percentage results in high polarization field which opposes the carrier collection. To address some of the earlier challenges, Farrell et al. proposed 30-period $\text{In}_{0.28}\text{Ga}_{0.72}\text{N}$ ($t_w = 22 \text{ \AA}$)/GaN ($t_b = 80 \text{ \AA}$) grown in a GaN p-i-n solar cell, Figure 3.4(b) [46]. The growth of 30-periods increases the thickness of absorbing $\text{In}_{0.28}\text{Ga}_{0.72}\text{N}$ well to 66 nm, which is higher than the earlier work by Dahal et al, by a factor of 2.75. The active region, where the QWs are located, is surrounded by highly doped GaN:p and GaN:n layers to assist in screening the polarization-induced field in the QWs which opposes the carrier collection [83, 84].

In addition, to reduce the air/GaN reflection, a roughened GaN:p surface was grown to increase the path length of the light. These enhancements have resulted in EQE values exceeding 60% at 400 nm as shown in Figure 3.4(b) and the absorption threshold was extended to ~ 500 nm. The 1.2 suns AM1.5 current density-voltage curve measured for the 30-period $\text{In}_{0.28}\text{Ga}_{0.72}\text{N}$ /GaN QW device, by Farrell et al. [46], is shown in Figure 3.5. A schematic of the structure is also depicted

in the inset of Figure 3.5. The J_{sc} , V_{oc} , FF , and η of the 30-period $In_{0.28}Ga_{0.72}N / GaN$ QW device, by Farrell et al. [46], were 2.53 mA/cm^2 , 1.93 V , 56.4 , and 2.29% , respectively. Even with the EQE improvement shown in Figure 3.4(b), the reported η is still low because of the low J_{sc} value due to thin absorbing layer (66 nm), and also the QWs are absorbing in a narrow wavelength region in the solar spectrum. The V_{oc} is markedly high, relative to III/V materials, due to the high bandgap of $InGaN/GaN$. The effect of the number of the period on strained $In_{0.28}Ga_{0.72}N / GaN$ QW is depicted in Figure 3.6(a)-(b), using the tabulated data reported by Farrell et al. [46]. The increase of the QW number enhances the J_{sc} due to increasing the total thickness of absorbing layers, Figure 3.5(a). The V_{oc} does not vary significantly with the period change, as shown in Figure 3.6(a). The FF exhibit a slight deterioration due to an increase of number of interfaces, Figure 3.6(b). The overall efficiency of the device increases with the increase of the number of QWs, as shown in Figure 3.6(b).

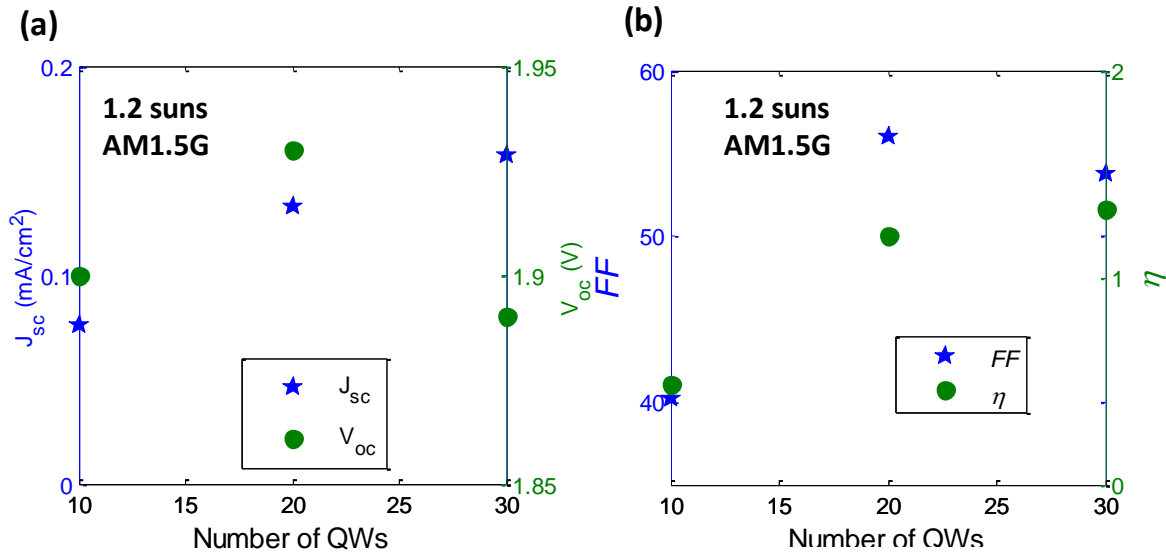


Figure 3.6: The effect of the number of QWs in the intrinsic region on 1.2-suns AM1.5G current-voltage characteristics: (a) J_{sc} (mA/cm^2) and V_{oc} (Volts) and (c) FF and η ; study by Farrell et al. [46].

According to several calculations and experimental investigations for $InGaN/GaN$ structures with different well/barrier thickness and indium compositions, the major carrier escape in this QW structure is tunneling [85-87]. The thermionic emission is less dominant for the $InGaN/GaN$ due to the relatively high effective barrier height for the electrons and holes, especially with high indium percentage. For instance, the τ_{tun} is $\sim 10^{-10} \text{ sec}$ for $In_{0.17}Ga_{0.83}N$ ($t_w = 30 \text{ \AA}$)/ GaN ($t_b = 100$

\AA) which is about 100-times lower than the τ_{therm} . ($\sim 10^{-8}$ sec) [86]. For a fixed well and barrier thickness, increasing the indium percentage in the InGaN will degrade carrier collection for several reasons. First, the use of higher indium percentage will increase the effective barrier height resulting in a reduction in both the tunneling and thermionic escape probabilities, see Eqns. (2.10)-(2.11). For instance, the tunneling and thermionic-emission escape times, τ_{tun} and τ_{therm} , are more than 100-times higher in $\text{In}_{0.25}\text{Ga}_{0.75}\text{N}/\text{GaN}$ than their corresponding values in $\text{In}_{0.17}\text{Ga}_{0.83}\text{N}/\text{GaN}$. Second, an increase in the indium from 17% to 25%, increases the piezoelectric field from 1.74 MV/cm to 2.3 MV/cm, which will result in a more opposition of carrier collection.

There are several challenges that hinder the fabrication of high-quality InGaN-based QW devices. The most challenging issue is the growth of high-quality InGaN with high indium percentage exceeding 20%. InGaN with more than 20% indium, results in a poor solar cell performance due to the formation of high defect density and pits that results in a high non-radiative recombination, increases the dark current, and degrades the V_{oc} and η . The difficulty of InGaN with high indium percentage is attributed to the large difference in the interatomic spacing between GaN and InN thus resulting in a solid-phase miscibility gap [88-90]. Second, there is a lattice-mismatch between GaN and InN on sapphire substrates of -16% and +29%, respectively. Also, the difference in thermal expansion coefficients between epilayer and substrates causes a thermal strain that introduces threading dislocations in the epilayer. To address this issue, a GaN template is typically grown as shown in Figure 2.1(c); however, this will not eliminate the lattice mismatch between InGaN epilayer and GaN template. The latter mismatch will increase with the increase of indium percentage in the well. One possible strategy to address this issue is to grow a relaxed $\text{In}_y\text{Ga}_{1-y}\text{N}$ template on GaN and then grow strain-balanced $\text{In}_x\text{Ga}_{1-x}\text{N}/\text{GaN}$, with $\text{In}_x\text{Ga}_{1-x}\text{N}$ well and GaN grown under compressive stress and tensile stress to the underlying $\text{In}_y\text{Ga}_{1-y}\text{N}$ template, respectively, where $x > y$ [47, 91]. However, only LEDs were fabricated using this approach, and solar cells using the strain-balanced InGaN/GaN approach have not been developed yet [47, 91, 92]. The third challenge is to grow GaN with a hole concentration exceeding $1 \times 10^{18} \text{ cm}^{-3}$ to act as a p-type emitter and ohmic contact with the evaporated metal [93]. Magnesium (Mg) which is an acceptor in GaN has a high activation energy of 0.2 eV that will limit the doping concentration [93, 94]. The activation energy of Mg in GaN decreases with the increase of indium percentage thus allowing high p-type doping than GaN [93, 94]. Finally, most research in InGaN/GaN QW solar cells has focused on developing p on n structures. However, high performance III/V and

silicon subcells have an n on p polarity. The growth of n on p results in built-in and polarization fields in the same direction, which is a problem due to the high sheet resistance of GaN:p and low mobility. Hence, this also represents a challenge that needs to be addressed for developing hybrid tandems that incorporate InGaN-based QWs as a top cell material.

Chapter 4: Growth and Characterization of Strain-Balanced InGaP-based Quantum Wells

Raising the efficiency ceiling of multi-junction solar cells (MJSC) using more optimal bandgap configurations of next-generation MJSC is crucial for concentrator and space systems. Towards this goal, two strain-balanced multiple quantum well (SBMQW) structures to tune the bandgap of InGaP-based solar cells, are reported in this Chapter. These structures are based on $\text{In}_x\text{Ga}_{1-x}\text{As}_{1-z}\text{P}_z/\text{In}_y\text{Ga}_{1-y}\text{P}$ ($x > y$) and $\text{In}_x\text{Ga}_{1-x}\text{P}/\text{In}_y\text{Ga}_{1-y}\text{P}$ ($x > y$) well/barrier combinations, strain-balanced to GaAs in a *p-i-n* solar cell device. The bandgap of $\text{In}_x\text{Ga}_{1-x}\text{As}_{1-z}\text{P}_z/\text{In}_y\text{Ga}_{1-y}\text{P}$ can be tuned from 1.82 to 1.65 eV by adjusting the well composition and thickness, which promotes its use as an efficient subcell for next-generation five and six junction photovoltaic devices. The thicknesses of wells and barriers in both the two strain-balanced QW structure were adjusted using a zero-net stress balance model to prevent the formation of defects. Thin strained layers of InGaAsP wells have been grown thermodynamically stable with compositions within the miscibility gap for the bulk alloy. The growth conditions of the two SBMQWs and the individual layers are reported. The two strain-balanced QW structures are characterized and analyzed by optical microscopy, X-ray diffraction, photoluminescence, current-voltage characteristics, and external quantum efficiency. The proposed SBMQWs allow more flexibility in the design of current multi-junction solar cells and future cells with more than four junctions. InGaAsP/InGaP SBMQWs may also be used in applications other than solar cells, such as light-emitting diodes and lasers, with the advantages of tuning the emission and absorption processes.

This chapter is a paper published in Journal of Applied Physics, 119 (9), 095706, 2016, with some additions and modifications.

4.1. Motivation

III-V compound semiconductors have been used in many optoelectronic devices because the flexibility of their bandgap engineering results in material systems with interesting electrical and optical properties [95]. The ability to tune the bandgap of III-V alloys while maintaining lattice matching to the underlying substrate has promoted their use in solar cells, light-emitting diodes, lasers, photodiodes, optical modulators, etc. The efficient tuning of semiconductors bandgaps has allowed for more flexibility in the design of III-V multijunction solar cells (MJSC)

[30], which are the most efficient photovoltaic system. The maximum efficiency of MJSCs is limited by the number of junctions (subcells) in the structure and the current matching requirement in series connected subcells. The efficiency of MJSC has been improved dramatically in the past few years with four junction cells reaching 46.0% using wafer-bonded structures [6, 11] and 45.7% using inverted metamorphic structures [96]. Even though several record-breaking efficiencies have been realized recently, developing a solar cell with bandgap in the 1.6-1.8 eV is still at the initial phase of development. There are several multi-junction solar cell approaches that will benefit from the realization of high performance subcell with bandgap in 1.6-1.8 eV range:

- 1- The ideal subcell band gaps for five and six junction solar cells are 2.14/**1.67**/1.33/1.01/0.7 eV and 2.24/**1.77**/1.47/1.2/0.96/0.69 eV, respectively using modeled constrained bandgaps under the AM1.5G spectrum [97]. Next-generation five and six junction devices needs a subcell with a bandgap of ~1.7 eV as the second highest energy subcell in these two stacks with a prospective efficiency higher than 50% under high solar concentration[17]. The realization of multi-junction devices with efficiencies higher than 50% is crucial for the cost effectiveness of concentrator and space systems [6].
- 2- Dual-junction device that has a top cell of 1.7 eV bandgap forms the optimal bandgap configuration with a bottom cell of 1.1 eV bandgap, with a prospective one-sun AM1.5G efficiency of 36-38% [16]. Silicon can be used as the 1.1 eV bottom cell and developing a III-V top cell with 1.7 eV is mandatory for stacking it with silicon.
- 3- Triple-junction devices (1.75/1.2/0.7 eV), requires prospective a top cell with bandgap of 1.75 eV to alleviate the current mismatch between top and middle cells.
- 4- Next-generation seven (or more) junction devices, as indicated by modeling [97], need a bandgap of 1.6-1.8 eV with prospective efficiencies higher than 50% [97].

4.2. Potential Solar Cells with Bandgaps in the 1.6-1.8 eV range

There are three potential material systems that can be used to realize a solar cell with a bandgap of 1.6-1.8 eV, as shown in Figure 4.1. The first prospective material is AlGaAs grown lattice matched to GaAs substrates as shown in Figure 4.1(a). The lattice mismatch between GaAs and AlAs is less than 0.12%. Thus, growing AlGaAs with aluminum compositions less than 30%

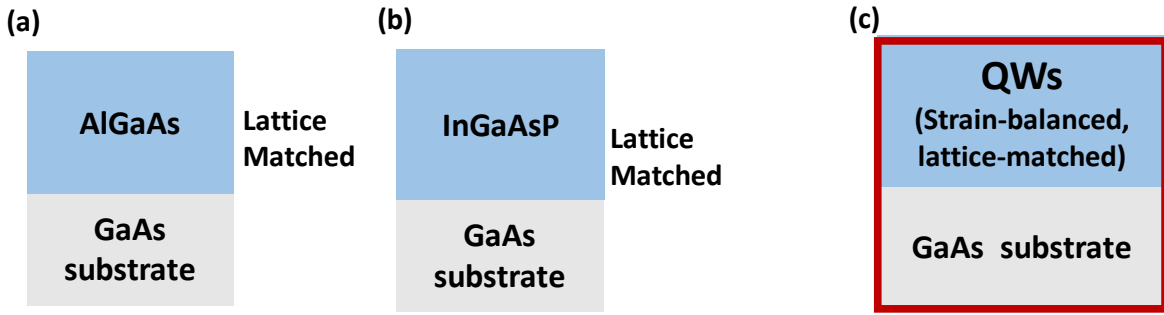


Figure 4.1: Potential solar cells for the 1.6-1.8 eV bandgap range: (a) AlGaAs solar cell lattice matched to GaAs substrate, (b) Bulk InGaAsP solar cell lattice matched to GaAs substrate, and (c) proposed InGaAsP/InGaP quantum wells, strain-balanced or lattice-matched, to GaAs substrates.

to achieve the target bandgap, results in a lattice-mismatch of less than 0.08% which is an advantage from an epitaxial growth perspective. However, the development of Aluminum-based compounds has been historically problematic due to the high reactivity of aluminum with oxygen, thus creating deep level defects which degrade the solar cell performance[24]. Recently, high performance AlGaAs solar cells have been developed [98]. However, growing AlGaAs at temperatures approaching 700 °C is mandatory to minimize the oxygen contamination. Such high temperatures may enhance dopants diffusion in the tunnel junction thus resulting in a degraded tunnel junction performance under thermal load [48-50]. Hence, the growth of AlGaAs solar cell was only successful by very few research groups [17, 98]. In addition, AlGaAs is indirect for aluminum compositions higher than 30%.

The second material system that has a 1.6-1.8 eV bandgap is InGaAsP quaternary lattice-matched to GaAs substrates, as shown in Figure 4.1(b). Quaternary InGaAsP alloys are promising for such applications and have attained many interests recently for the development of optoelectronic devices such as solar cells [99] lasers [100-102], and aluminum-free near-infrared LEDs [103, 104]. However, InGaAsP alloys in the bandgap range (1.4-1.9 eV) suffer from a miscibility gap which prevents growth of high quality bulk material when grown lattice-matched to GaAs [105, 106]. This miscibility gap exists due to the large mismatch in the lattice-constants and electron-negativity of the constituents of InGaAsP. Hence, limited composition range was successfully synthesized [107] and bandgap tunability is limited. Figure 4.2 shows the miscibility gap regions

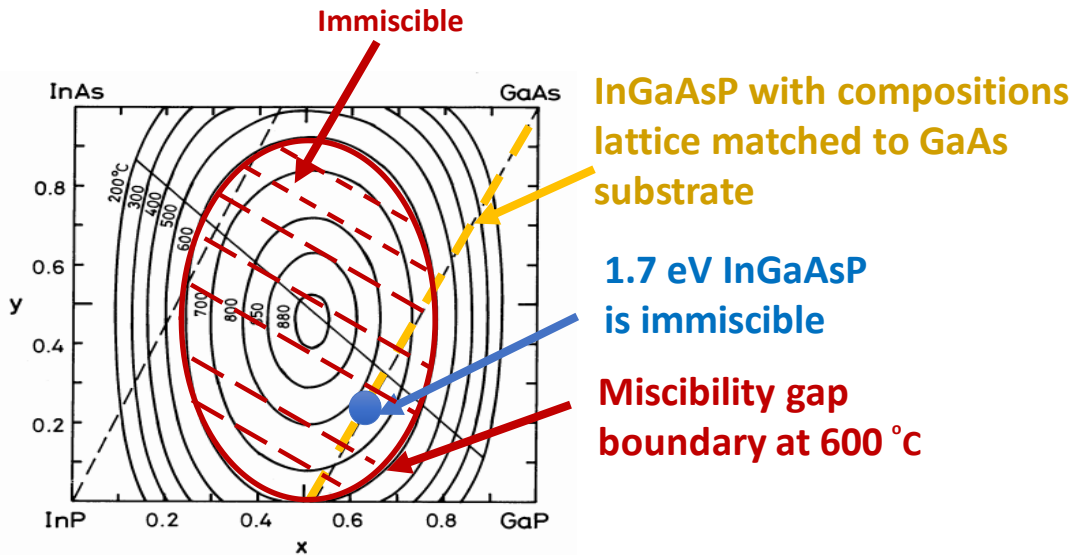


Figure 4.2: Contours for miscibility gap of InGaAsP at different growth temperatures from ref. [105]. The hashed red dotted lines represent the miscibility gap region for the InGaAsP. The orange dotted line represents the compositions of InGaAsP that are lattice-matched to GaAs substrates. InGaAsP with composition that lead to a 1.7 eV is immiscible.

at different growth temperatures as determined by Onabe [105]. A bulk InGaAsP, grown lattice-matched to GaAs substrate at 600 °C, with a bandgap of 1.7 eV is immiscible as shown in Figure 4.2. Therefore, to reach higher efficiencies, it is desirable to obtain an alternate aluminum-free structures which provide an optimal band gap configuration for next-generation MJSC design.

This dissertation reports on novel quantum well structures to tune the bandgap of $\text{In}_{0.49}\text{Ga}_{0.51}\text{P}$ (1.87 eV) solar cells, as shown in Figure 4.1(c). Chapters 4 and 5 reports on novel InGaP-based strain-balanced multiple quantum well (SBMQW) structures. Chapters 6 and 7 reports on a novel InGaP-based lattice-matched quantum well design. The concept of strain-balanced QWs was demonstrated in the eighties by NCSU and was applied to light emitting diodes (LEDs) [36] and solar cells [37, 108]. InGaAs/GaAsP SBMQWs have been widely used to tune the bandgap of GaAs devices to 1.2 eV [39-41]. In this dissertation, the same SBMQW concept was applied to tune the bandgap of InGaP devices to energy values less than 1.85 eV. The InGaP-based quantum well solar cells, demonstrated in this dissertation, can be used for several multi-junction designs as discussed in Section 4.1.

In the QW solar cell device structure, the multiple quantum well (MQW) structures are included in the unintentionally doped intrinsic layer (*i* layer) of InGaP *p-i-n* structures, as shown in Figure 4.3. Two SBMQW structures are fabricated in this work and grown on GaAs substrates. In both structures, the compositions and thicknesses of the layers are chosen such that the compressive stress in the wells is balanced by the tensile stress in the barriers. The active region of the first demonstrated SBMQW device consists of alternating $\text{In}_x\text{Ga}_{1-x}\text{As}_{1-z}\text{P}_z$ wells and $\text{In}_y\text{Ga}_{1-y}\text{P}$ barriers as shown in Figure 4.3(b), where $x > y$. The second SBMQW device's active region consists of alternating $\text{In}_x\text{Ga}_{1-x}\text{P}$ wells and $\text{In}_y\text{Ga}_{1-y}\text{P}$ barriers, where $x > y$, in Figure 4.3(c). In this Chapter, an analysis of both structures material and device characteristics is presented. We show that careful control over the well and barrier compositions and thicknesses is required to efficiently balance the stress in the two layers. The InGaP-based quantum well solar cells extend the absorption edge compared to the standard $\text{In}_{0.49}\text{Ga}_{0.51}\text{P}$ non-MQW cell.

Tuning the bandgap of InGaP solar cells, while maintaining the lattice-matching condition will offer advantages not only in the next-generation photovoltaic devices but also for other optoelectronic applications. For example, InGaAsP/InGaP SBMQWs may also be used in delivering a high output laser with emission in 720-760 nm range, which is required for a variety of applications such as photodynamic therapy [109], pumping of chromium-doped solid state lasers such as Cr:LiSAF [110] and various spectroscopic techniques. It is worth pointing out that the performance of lasers with an active region based on AlGaAs may deteriorate due to the high reactivity of aluminum with oxygen. There is interest in providing Aluminum-free lasers in this wavelength range [100, 101]. In addition to lasers, SBMQWs can be applied to near-infrared (NIR) LEDs and utilized by some telecommunication applications in this wavelength range. NIR LEDs operating in this wavelength range are typically made of double heterojunction AlGaAs, which provides effective confinement and reasonable efficiency, but still suffers quality issues associated with presence of Aluminum in the active region of the device [103, 104].

4.3. Experimental Approaches

In this section, the growth conditions, structural design, and fabrication details of the two-proposed strain-balanced quantum well structures are presented.

4.3.1. Growth details

The samples were grown in a Thomas Swan MOCVD system fitted with a custom reactor, designed and built inhouse [111]. The growth pressure was fixed at 200 Torr and purified N₂/H₂ were used as the carrier gases. The precursors used in this work are tertiarybutylarsine (TBAs), tertiarybutylphosphine (TBP), trimethylindium (TMIn), trimethylgallium (TMGa), dimethylzinc (DMZn) and disilane for arsenic, phosphorus, indium, gallium, zinc, and silicon, respectively. The samples studied were grown on (100) GaAs misoriented by 2° towards <110> direction. Due to the use of organometallic column V sources, we found that several steps are required for the growth of InGaP in our reactor that might not be needed in case of using arsine and phosphine. Each sample employs a standard GaAs buffer layer grown at 640 °C followed by a 50 Å GaAsP interfacial layer with the arsenic ramping down through 3 steps each of 4 seconds, before the In_{0.49}Ga_{0.51}P base growth. This interfacial layer has minimized the arsenic carryover from GaAs to InGaP and prevented the forming of compositional mixing at the GaAs/InGaP interface. The nucleation of the In_{0.49}Ga_{0.51}P base layer starts at 575 °C to avoid three-dimensional nucleation and the temperature is subsequently ramped up in a minute to 650 °C with a growth rate of 5.0 Å/Sec. One minute before the end of the base growth, the temperature is ramped down to 585 °C for the SBMQW growth. Details on the choice of quantum wells growth temperature are mentioned later. Similarly, the temperature is ramped up to 650 C to grow the emitter after growing the SBMQWs. The base and emitter thickness are 1.0 and 0.1 μm with doping concentration of 1×10¹⁷ and 1×10¹⁸ cm⁻³ using silicon and zinc, respectively.

Two SBMQW structures are grown in a *p-i-n* solar cell device as shown in in Figure 4.3.

4.3.1. In_xGa_{1-x}As_{1-z}P_z/ In_yGa_{1-y}P ($x > y$) SBMQWs

The In_xGa_{1-x}As_{1-z}P_z/In_yGa_{1-y}P ($x > y$) SBMQWs is grown in the intrinsic (i) region of In_{0.49}Ga_{0.51}P *p-i-n* solar cell structure. In_xGa_{1-x}As_{1-z}P_z/In_yGa_{1-y}P ($x > y$) SBMQWs consist of alternating In_xGa_{1-x}As_{1-z}P_z wells and In_yGa_{1-y}P barriers that are under compressive and tensile stress, respectively, in Figure 4.3(b). Several fundamental issues related to the growth of InGaAsP quaternary alloy have to be discussed first. These issues make the choice of the quantum wells growth temperature more challenging. Two competing factors affect the choice of the growth temperature: phase separation and three-dimensional nucleation. InGaAsP quaternary alloy has an immiscible region that is more thermodynamically favored at low growth temperature for comparable As and P content, as shown

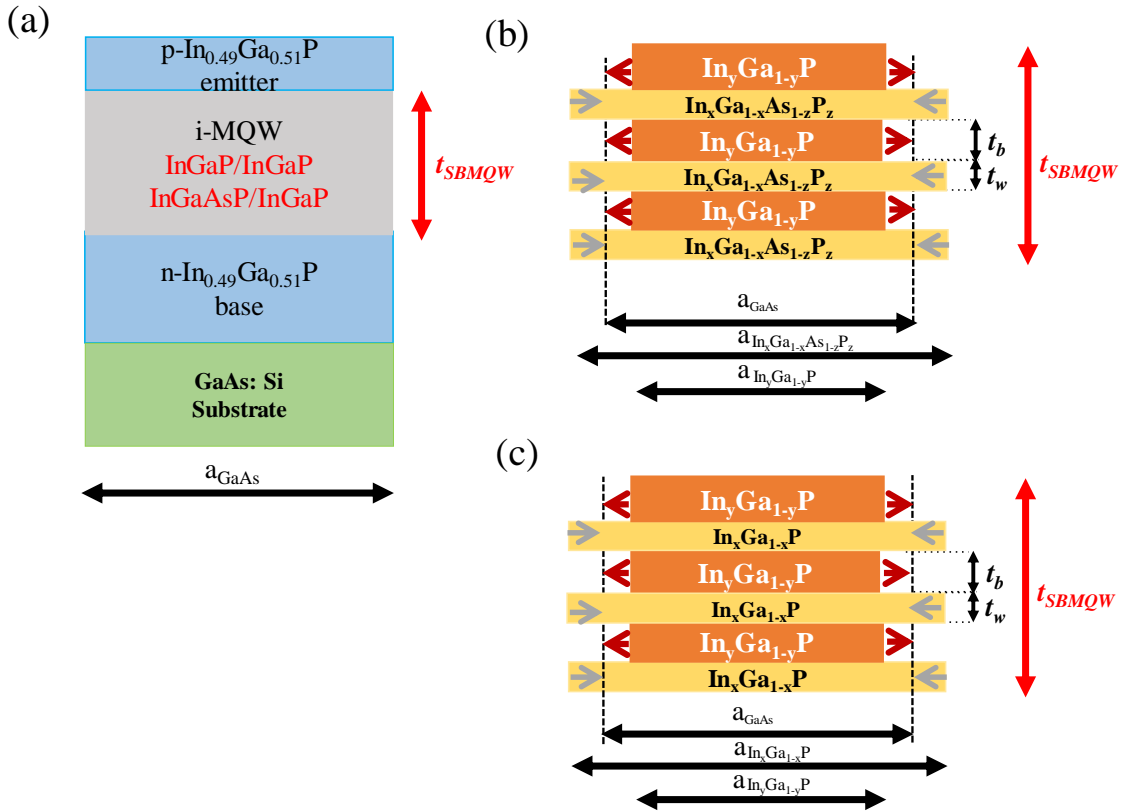


Figure 4.3: Schematics of (a) InGaP *p-i-n* solar cell structure, (b) $\text{In}_x\text{Ga}_{1-x}\text{As}_{1-z}\text{P}_z/\text{In}_y\text{Ga}_{1-y}\text{P}$ ($x > y$) SBMQWs, and (c) $\text{In}_x\text{Ga}_{1-x}\text{P}/\text{In}_y\text{Ga}_{1-y}\text{P}$ ($x > y$) SBMQWs.

in Figure 4.2 [105, 106]. But for sufficiently thin strained InGaAsP films the driving forces for immiscibility is reduced and miscible films can be grown [112]. Spinodal decomposition occurs by migration at the growing surface and the homogenous alloy is stabilized by the strain with respect to the substrate [112]. Thus, there is a limit to the thicknesses of miscible quaternary layers that can be grown, and this limit depends on the composition and the growth temperature. In order to reduce the miscibility gap range, InGaAsP should be grown at high temperatures as shown in Figure 4.2. However it becomes more difficult to grow strained quantum well structures at high temperatures as three dimensional nucleation and surface morphology issues start to appear. In order to grow miscible InGaAsP thin films and maintain a good surface morphology, the quantum wells are grown at a relatively low temperature (585 °C). However this temperature is relatively low to grow miscible InGaAsP film with high arsenic content (> 10%), which is important to achieve the required bandgap. We compensated for that by increasing the indium content in the

wells to achieve the required bandgap. The V/III ratio of bulk $\text{In}_{0.49}\text{Ga}_{0.51}\text{P}$, $\text{In}_y\text{Ga}_{1-y}\text{P}$ barrier, and $\text{In}_x\text{Ga}_{1-x}\text{As}_{1-z}\text{P}_z$ well are 50, 60, and 150, respectively. The relatively high V/III ratio of InGaAsP wells is necessary to obtain arsenic composition of 5%. The $\text{In}_x\text{Ga}_{1-x}\text{As}_{1-z}\text{P}_z/\text{In}_y\text{Ga}_{1-y}\text{P}$ SBMQWs have been grown with compositions of $0.60 < x < 0.75$, $0.35 < y < 0.43$, and $0.9 < z < 0.98$ and periods ranging from 80 Å to 230 Å. In this work, the indium (x) and phosphorus (z) compositions in the $\text{In}_x\text{Ga}_{1-x}\text{As}_{1-z}\text{P}_z$ wells are set at 0.70 and 0.95, respectively. In the barrier, the indium composition (y) is set at 0.40. These conditions realize the requirements of both the strain-balance and the target bandgap range. No antireflection coatings or windows are used in this study.

4.3.2. $\text{In}_x\text{Ga}_{1-x}\text{P}/\text{In}_y\text{Ga}_{1-y}\text{P}$ ($x > y$) SBMQWs

In order to avoid the phase separation issues related to the growth of InGaAsP quaternary alloy we have also investigated the growth of SBMQWs made of two InGaP ternary compounds, with different indium compositions. The $\text{In}_x\text{Ga}_{1-x}\text{P}/\text{In}_y\text{Ga}_{1-y}\text{P}$ ($x > y$) SBMQWs is grown in the intrinsic (i) region of $\text{In}_{0.49}\text{Ga}_{0.51}\text{P}$ p-i-n structure. This structure consist of alternating $\text{In}_x\text{Ga}_{1-x}\text{P}$ wells and $\text{In}_y\text{Ga}_{1-y}\text{P}$ barriers that are under compressive and tensile stress, respectively, Figure 4.3(c). In both the wells and the barriers, the gallium (Ga) and phosphorus (P) flows are kept the same while the indium flow is ramped up and down to grow the $\text{In}_x\text{Ga}_{1-x}\text{P}$ well and $\text{In}_y\text{Ga}_{1-y}\text{P}$ barrier alternatively. InGaP with indium percentage of 49% is lattice matched to GaAs substrates. Thus, the $\text{In}_x\text{Ga}_{1-x}\text{P}$ well is grown under compressive stress with an indium composition higher than 49% and the $\text{In}_y\text{Ga}_{1-y}\text{P}$ barrier is grown under tensile stress with an indium composition lower than 49% to strain-balance the structure. $\text{In}_x\text{Ga}_{1-x}\text{P}/\text{In}_y\text{Ga}_{1-y}\text{P}$ SBMQWs have been successfully grown with compositions of $0.6 < x < 0.75$ and $0.30 < y < 0.45$ with periods ranging from 100 Å to 250 Å. The V/III ratio of $\text{In}_x\text{Ga}_{1-x}\text{P}$ well and $\text{In}_y\text{Ga}_{1-y}\text{P}$ barrier are 30 and 40. For the SMBQW reported here, the indium compositions in the wells (x) and barriers (y) are set to 0.75 and 0.40, respectively. No antireflection coatings or windows are used in this study.

4.3.2. Fabrication Details

Solar cell devices were fabricated as 2.5 mm × 2.5 mm etched mesas using standard photolithographic procedures. Ge/Pd/Ti/Ag/Au n-type and Ti/Pd/Ag/Pd/Au p-type ohmic contacts were deposited via e-beam evaporation. InGaAsP/InGaP and InGaP/InGaP mesa devices are etched using $\text{H}_2\text{O}_2:\text{HBr}:\text{H}_2\text{O}$ (1:10:20) and $\text{HCl}:\text{H}_3\text{PO}_4:\text{H}_2\text{O}_2$ (5:5:1), respectively. More details about the fabrication are discussed in ref. [70].

4.3.3. Characterization Details

X-ray diffraction (XRD) was used to determine the indium and phosphorus compositions of alloy calibration samples. The XRD superlattices satellite peaks of the MQW structures coupled with the growth rate measurements were used to ensure the strain balance condition had been achieved and to find the thicknesses of the individual layers. Optical microscopy was performed using an Olympus BX41 microscope fitted with a Nikon D3000 camera. Optical emission of MQW structures was evaluated by photoluminescence (PL) using a 532 nm frequency doubled Nd:YAG laser. The external quantum efficiencies (EQE) of the solar cell devices were measured using a quartz tungsten halogen lamp with a Newport ¼-m monochromator, a lock-in amplifier and calibrated Si photodiode. The illuminated current density-voltage (*J-V*) characteristics were measured with an Oriel 1-kW solar simulator with an AM1.5G filter and calibrated with an InGaP reference cell with a known AM1.5G J_{SC} .

4.4. Results and Discussion

In this section, the material and device characteristics of $In_xGa_{1-x}As_{1-z}P_z/In_yGa_{1-y}P$ and $In_xGa_{1-x}P/In_yGa_{1-y}P$ SBMQWs are presented and analyzed. First, the calibrations of the wells and barriers are presented. Then the model used to balance the quantum wells coupled with the (004) XRD results of the two structures are discussed. Next, a comparison between the experimental and modeled PL emissions of the two structures is carried out. Then the quantum efficiency of the two quantum wells devices is compared.

4.4.1. Well and Barrier Calibrations

The compositions of bulk InGaP films ($> 0.5\mu m$) grown at $585^{\circ}C$ were determined by XRD. The InGaP calibrations were used to determine the required flow rates to achieve the target compositions in quantum wells, emitter and base. Due to the periodicity of the atomic lattice, strong interference patterns will occur at the angles that realize the Bragg's condition [113],

$$2d_{hkl} \sin(\theta) = n\lambda, \quad (4.1)$$

where θ is Bragg angle, λ is x-ray wavelength, d_{hkl} is the spacing between the crystal planes, and n is integer.

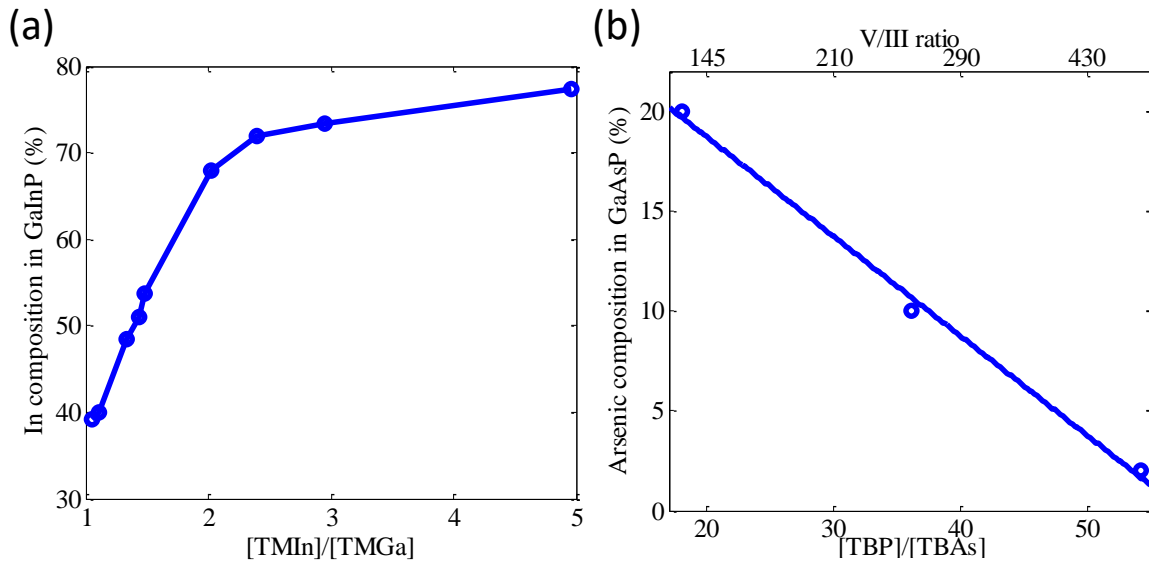


Figure 4.4: (a) Indium compositions of InGaP with $[TMIn]/[TMGa]$. (b) Arsenic compositions of GaAsP with $[TBP]/[TBAs]$. The substrate temperature is 585 °C for the two presented SBMQWs.

The indium composition in InGaP is plotted versus the ratio of the input partial pressure, $[TMIn]/[TMGa]$, as shown in Figure 4.4(a). It is noted that for $[TMIn]/[TMGa]$ ratios less than 2.5, the indium incorporation in InGaP is linear with the input partial pressure ratio. For higher $[TMIn]/[TMGa]$ ratios, the incorporation of indium increases slowly implying that indium evaporation or surface segregation is taking place.

The indium and the arsenic content of the quaternary alloy (InGaAsP) are estimated using XRD of ternary InGaP and GaAsP calibration curves shown in Figure 4.4. In this work, the compositions of InGaAsP was assumed the same as determined from separate XRD of InGaP and GaAsP ternaries. PL was not used here to determine the bandgap of the quaternary alloy by growing bulk epitaxial films for two reasons. First, thick films ($>0.5\ \mu m$) of InGaAsP with compositions similar to those used in the quantum well structure will exceed the critical layer thickness (CLT) and will be highly defective. Second, bulk InGaAsP at grown at 585 °C might be immiscible as mentioned earlier, [105] and the surface morphology for thick bulk InGaAsP, as indicated by optical microscopy, was rough.

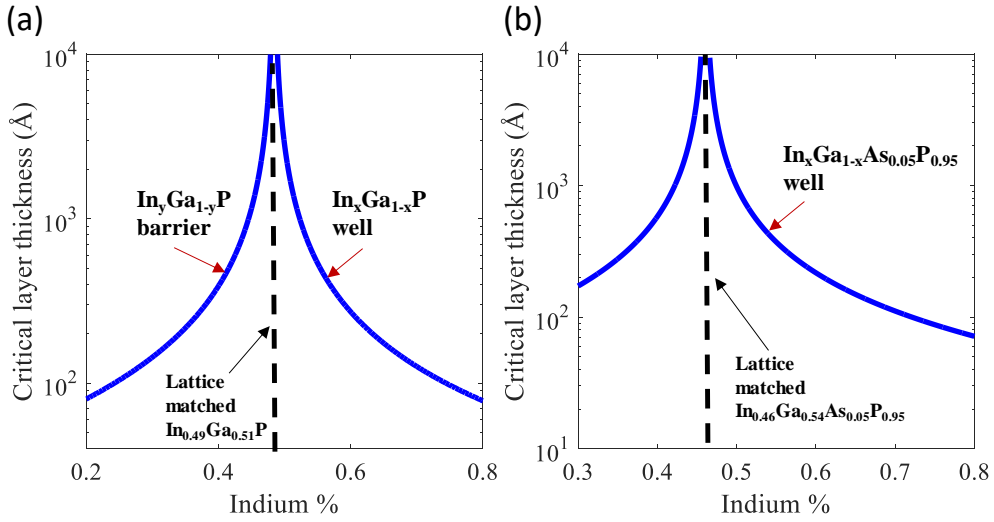


Figure 4.5: Calculated critical layer thickness using Matthews and Blakeslee model of: (a) $\text{In}_x\text{Ga}_{1-x}\text{As}_{1-z}\text{P}_z$ and $\text{In}_x\text{Ga}_{1-x}\text{P}$ wells used in strain-balanced $\text{In}_x\text{Ga}_{1-x}\text{As}_{1-z}\text{P}_z/\text{In}_y\text{Ga}_{1-y}\text{P}$ and $\text{In}_x\text{Ga}_{1-x}\text{P}/\text{In}_y\text{Ga}_{1-y}\text{P}$ quantum wells, respectively, (b) $\text{In}_y\text{Ga}_{1-y}\text{P}$ barrier used in the two strain-balanced QW structures.

Figure 4.4(b) shows the arsenic composition in GaAsP versus the input partial pressure ratio, $[\text{TBP}]/[\text{TBAs}]$ at 585 °C. For convenience, the V/III ratio is shown too on the same plot. The incorporation of arsenic is linear with the change of flow at 585 °C as shown in Figure 4.4(b).

4.4.2. Critical Layer Thickness Constraints

$\text{In}_x\text{Ga}_{1-x}\text{As}_{1-z}\text{P}_z$ and $\text{In}_x\text{Ga}_{1-x}\text{P}$ quantum wells can be grown compressively strained to GaAs substrates provided that their thicknesses remain less than the CLT as discussed in Section 2.4 of Chapter 2. The CLT of $\text{In}_x\text{Ga}_{1-x}\text{As}_{1-z}\text{P}_z$ and $\text{In}_x\text{Ga}_{1-x}\text{P}$ quantum wells are calculated using Matthews and Blakeslee [58]. As shown in Figure 4.5, the calculated CLT depends critically on the value of indium for the two QW structures. The CLT of $\text{In}_x\text{Ga}_{1-x}\text{As}_{0.05}\text{P}_{0.95}$ wells with $x = 55\%$, 65% , and 75% are 369 Å, 146 Å, and 85.1 Å, respectively as shown in Figure 4.5(a). The CLT of $\text{In}_x\text{Ga}_{1-x}\text{P}$ wells is reduced from 530 Å for an indium percentage of 55 to 94.7 Å for an indium percentage of 75. The CLT of InGaP films with indium compositions of less than 49% that will be grown under tensile stress for the barrier in the two QW structures is shown in Figure 4.5(b). The CLT is higher as the indium percentage approach 48% due to approaching the lattice-matching condition to GaAs substrate.

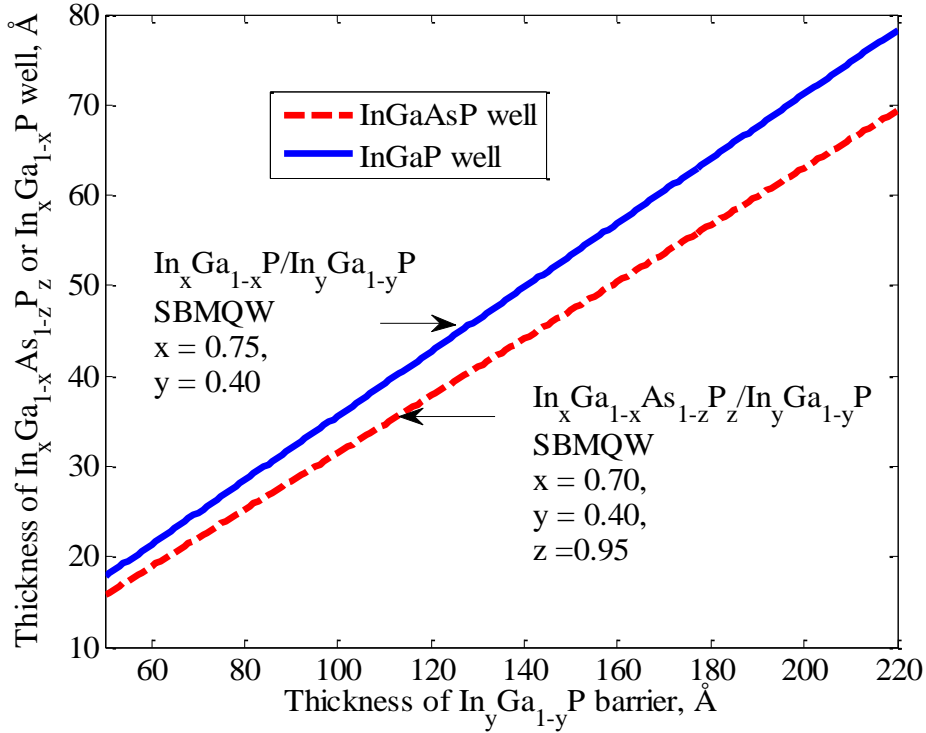


Figure 4.6: Thickness of wells and barriers as estimated by zero-stress balance model to strain-balance both the $\text{In}_{0.70}\text{Ga}_{0.30}\text{As}_{0.05}\text{P}_{0.95}/\text{In}_{0.40}\text{Ga}_{0.60}\text{P}$ and $\text{In}_{0.75}\text{Ga}_{0.25}\text{P}/\text{In}_{0.40}\text{Ga}_{0.60}\text{P}$ structures to the GaAs substrates.

4.4.3. Zero-stress Balance Model and X-ray Diffraction

To balance the SBMQWs, a zero-stress balance model is used where the average in-plane stress due to biaxial strain in the quantum wells/barriers should be zero [63]. Details about this model was discussed in Section 2.5 of Chapter 2. The thicknesses of wells and barriers obtained from the zero-stress model for the two quantum well structures are shown in Figure 4.6. The values obtained from this model serves as a better measure of the balancing of the two structures compared to the thicknesses obtained from the average-lattice method or the thickness-weighted method [63]. XRD was used to ensure the stress balance condition on GaAs substrates was met. The period of the quantum well, D , was calculated by modifying the Bragg's law [113],

$$D = \frac{(n_i - n_j)\lambda}{2(\sin(\theta_i) - \sin(\theta_j))}, \quad (4.2)$$

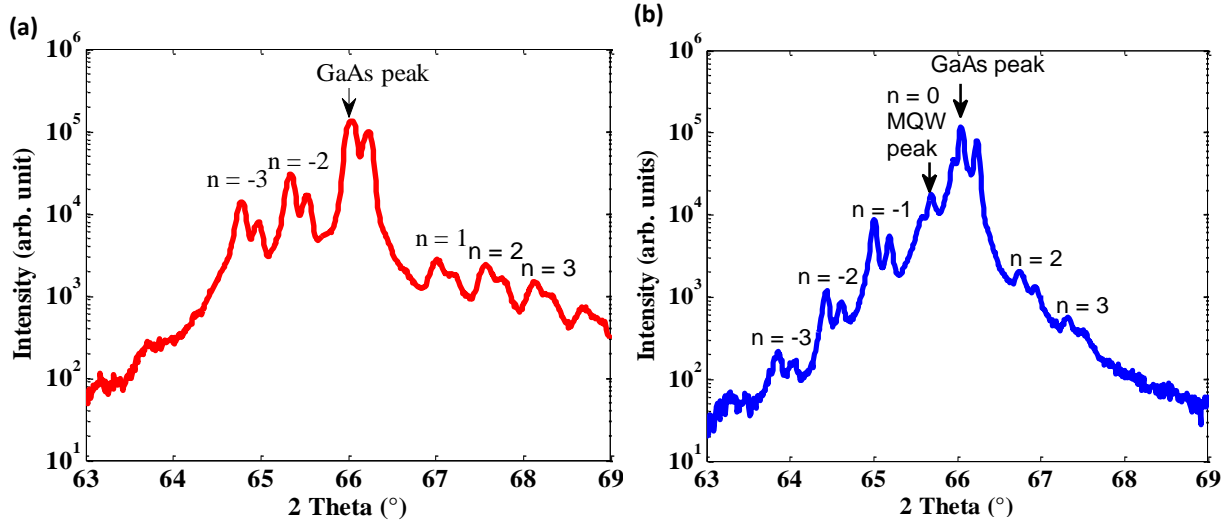


Figure 4.7: Single crystal XRD of (a) $\text{In}_{0.70}\text{Ga}_{0.30}\text{As}_{0.05}\text{P}_{0.95}/\text{In}_{0.40}\text{Ga}_{0.60}\text{P}$ and (b) $\text{In}_{0.75}\text{Ga}_{0.25}\text{P}/\text{In}_{0.40}\text{Ga}_{0.60}\text{P}$ SBMQWs, of 30 periods.

where n_i and n_j are the order of the satellite peaks, θ_i and θ_j are the Bragg's angles.

(004) XRD scans of the two SBMQWs are shown in Figure 4.7. The diffraction pattern consists of the (004) GaAs substrate reflection peak and several weaker satellite peaks due to the periodicity of the QWs. The number shown above each peak is the order of the satellite. The presence of clear peaks indicates that MQW regions of well-defined periodicity were formed and the presence of higher-order satellite peaks indicates abrupt interfaces. The $n = 0$ peak corresponds to the MQW average lattice constant perpendicular to the surface and differs from that of the GaAs substrate due to the difference in the elastic properties of the two alloys [63]. Periodicity calculations based on the satellite peaks and growth rate measurements for the $\text{In}_{0.70}\text{Ga}_{0.30}\text{As}_{0.05}\text{P}_{0.95}/\text{In}_{0.40}\text{Ga}_{0.60}\text{P}$ SBMQWs indicate that the period thickness was 160 Å. Growth rate measurements for the $\text{In}_{0.70}\text{Ga}_{0.30}\text{As}_{0.05}\text{P}_{0.95}/\text{In}_{0.40}\text{Ga}_{0.60}\text{P}$ SBMQWs indicate that the wells are around 40 Å and the barrier around 120 Å. The corresponding well and barrier thicknesses for $\text{In}_{0.75}\text{Ga}_{0.25}\text{P}/\text{In}_{0.40}\text{Ga}_{0.60}\text{P}$ structure are 65 and 170 Å, respectively. These values are close to the initial estimate from the zero-stress balance model and indicate that we have good control over the growth conditions.

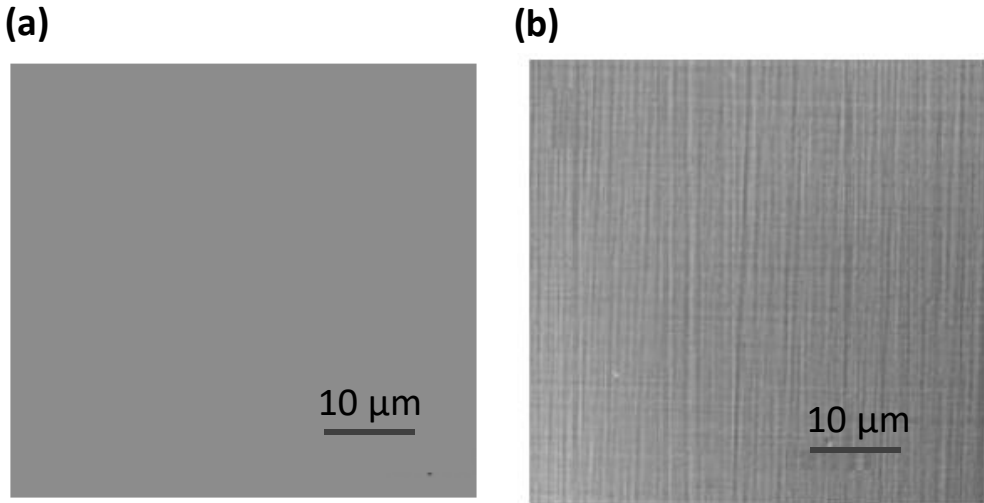


Figure 4.8: Nomarski interference contrast micrographs of the 30 periods InGaAsP/InGaP MQWs. (a) A mirrorlike surface indicates that the MQWs is closely lattice matched to the GaAs substrate. (b) Crosshatching feature indicates misfit dislocations in the MQW structure.

4.4.4. Optical Microscopy

The critical layer thickness (CLT) of the $\text{In}_{0.70}\text{Ga}_{0.30}\text{As}_{0.05}\text{P}_{0.95}$ wells grown at the previously mentioned conditions is 90 Å, by our estimate using Matthews-Blakeslee model [58]. The lattice constant of InGaAsP used in the model is based on the linear interpolation of that of binary compounds. Nomarski differential interference microscopy images of the surfaces of the InGaAsP/InGaP SBMQWs are shown in Figure 4.8. A mirror-like surface for InGaAsP/InGaP SBMQW of well thickness of 45 Å (< CLT) is shown in Figure 4.8(a), indicating that the MQW is closely lattice matched to the GaAs substrate. If the quantum wells are not strain-balanced or if the individual layers thickness are above the CLT, crosshatching will appear as shown in Figure 4.8(b) for a well thickness of 100 Å (> CLT). A similar behavior was observed for InGaP/InGaP structures (not shown).

4.4.5. Photoluminescence Results of InGaAsP/InGaP and InGaP/InGaP SBMQWs (emission and modeling)

The motive of this work is to tune the bandgap of $\text{In}_{0.49}\text{Ga}_{0.51}\text{P}$ (1.87 eV) based structures to lower energy values (1.65-1.8 eV) while maintaining lattice matching conditions to GaAs substrates. As an illustration of the bandgap tunability in these QW structures, the photoluminescence

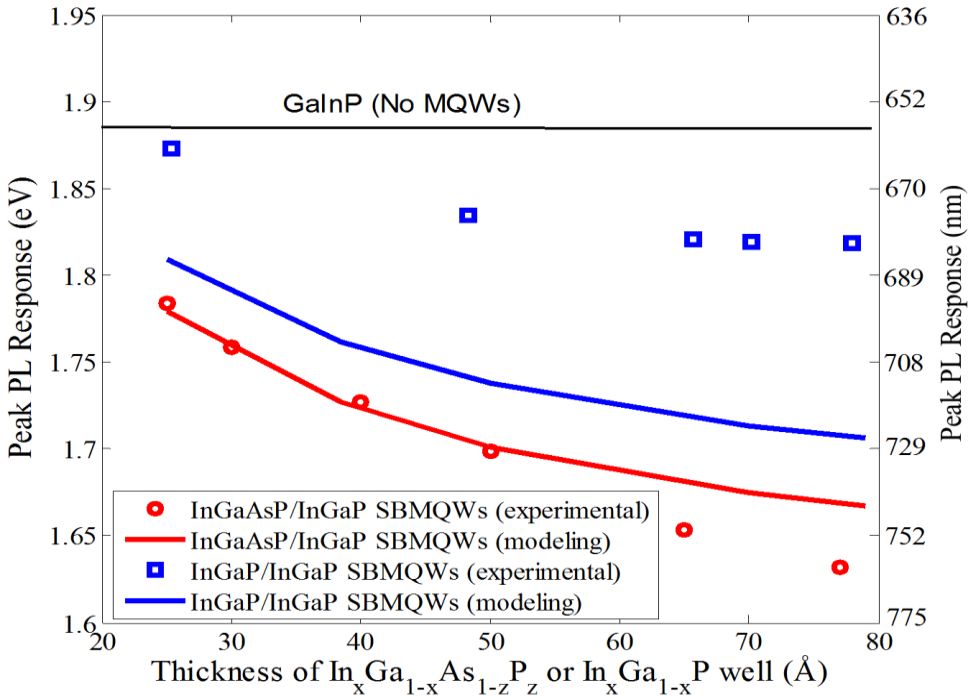


Figure 4.9: Experimental and modeling results of the emission wavelength (energy) versus well thickness for both $\text{In}_{0.70}\text{Ga}_{0.30}\text{As}_{0.05}\text{P}_{0.95}/\text{In}_{0.40}\text{Ga}_{0.60}\text{P}$ and $\text{In}_{0.75}\text{Ga}_{0.25}\text{P}/\text{In}_{0.40}\text{Ga}_{0.60}\text{P}$ SBMQWs.

characteristics of the two QWs are depicted in Figure 4.9. Modeling of the QWs emission is shown in the same figure too. The model is based on estimating the conduction and valence bands offset using the Anderson's rule [114] based on the electron affinities values given for the binary compounds [52] and interpolated linearly to calculate the corresponding values for ternary and quaternary compounds. Strain effects [52] and quantum size effects [115] are included in the model. Kronig-Penney model is used to calculate the first electron and hole states [116]. The details of this model are discussed in Section 2.3 of Chapter 2. The thicknesses of wells and barriers used in the model are inferred by total period thickness measured by XRD and growth rate measurements. As shown in Figure 4.9, the QWs emission are tuned by varying the thickness of the well from ~ 30 Å to 90 Å for the two QW devices. The thicknesses of the barriers in the two structures are adjusted accordingly to balance the structure. The peak PL wavelength emission increases as the thickness of the well increases. This can be attributed to a reduced quantum size effect (QSE) associated with thicker wells, leading to decrease in emission energy since the compositions are fixed in this study. The peak PL emission of $\text{In}_{0.70}\text{Ga}_{0.30}\text{As}_{0.05}\text{P}_{0.95}/\text{In}_{0.40}\text{Ga}_{0.60}\text{P}$

SBMQWs can be tuned from 1.85 to 1.65 eV. The average of the full width half maximum (FWHM) of these structure is \sim 25 meV and increases to \sim 40 meV for the thickest well device which cross the CLT. The wide tunable range of InGaAsP/InGaP promotes their use as efficient aluminum-free subcells for five and six junction's cells. The alternative material system for that wavelength-range is AlGaAs which may suffer from growth and long-term reliability problems related to oxygen contamination.

On the other hand, the peak PL emission shift of $\text{In}_{0.75}\text{Ga}_{0.25}\text{P}/\text{In}_{0.40}\text{Ga}_{0.60}\text{P}$ SBMQW saturates at \sim 1.82 eV for the thickest well devices, as shown in Figure 4.9. It is noteworthy that the modeled values deviate greatly from the experimental values for the InGaP/InGaP MQWs, as shown in Figure 4.9. For example, the relaxed bandgap of $\text{In}_{0.75}\text{Ga}_{0.25}\text{P}$ well is \sim 1.63 eV, while the modeled strained bandgap is around 1.72 eV for a well thickness of 65 Å, which is lower than the achieved experimental value (1.82 eV). The reason for this discrepancy between the theoretical values and the experimental results is not clear. However, a possible issue might be indium segregation (surface accumulation) taking place during the growth of the $\text{In}_{0.75}\text{Ga}_{0.25}\text{P}$ well. Recent work has shown indium segregation initiates at the start of lattice matched $\text{In}_{0.49}\text{Ga}_{0.51}\text{P}$ growth and saturates when the grown layer thickness is \sim 150 Å [117]. We are using well thicknesses of less than 90 Å to maintain efficient carrier transport and to make sure the well thickness is less than the CLT. Accordingly, it is likely that this indium surface accumulation smears out the profile of incorporated indium in the well. Thus the profile is not a rectangular shape, as usually assumed for calculating subband states [118]. Another possible issue is the composition pulling effect taking place at the well growth resulting in effectively reduced indium composition than expected from bulk calibration. It is also possible that graded quantum well interfaces are formed. Carlin et al. have previously shown by modeling that the formation of graded interfaces may lead to thinner wells than expected and increases the bandgap of InGaAs/GaAsP quantum wells [119]. These aforementioned effects will modify the electronic states of the quantum wells and lead to a blue shift in the transition energies compared to the modeled quantum well with abrupt interfaces, as shown in Figure 4.9[120]. It is worth pointing out that the limited minimum achievable effective bandgap for the InGaP/InGaP may limit its use an efficient subcell for next-generation photovoltaic devices.

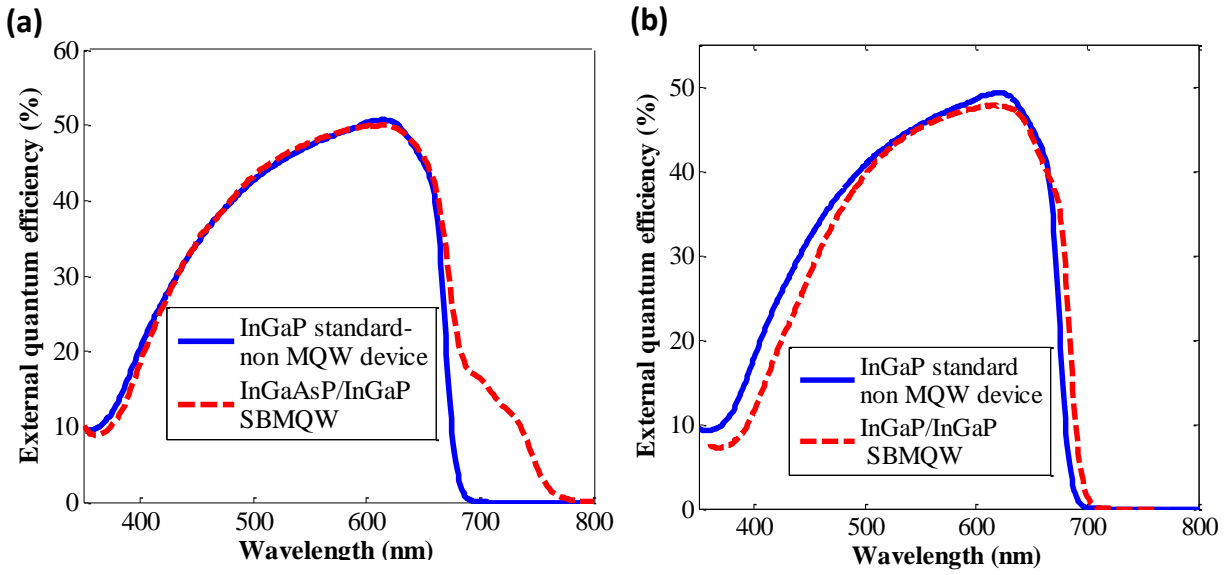


Figure 4.10: External quantum efficiency (EQE) for (a) $\text{In}_{0.70}\text{Ga}_{0.30}\text{As}_{0.05}\text{P}_{0.95}/\text{In}_{0.40}\text{Ga}_{0.60}\text{P}$ SBMQWs and InGaP standard p-i-n device, and (b) $\text{In}_{0.75}\text{Ga}_{0.25}\text{P}/\text{In}_{0.40}\text{Ga}_{0.60}\text{P}$ SBMQWs and InGaP standard p-i-n device. No window or antireflection coatings are used.

4.4.6. Quantum Efficiency and Light Current-voltage Characteristics

The study of minority carrier transport across the MQWs is important for the understanding and optimization of the performance of these devices. The transport properties of QW devices can be dominated by tunneling, for thin barriers, or thermionic emission. Figure 4.6 shows that in order to balance the two QW structures presented here, the average thickness of the barriers is around 2-3 times thicker than that the well. For example, the barrier thicknesses for $\text{In}_{0.70}\text{Ga}_{0.30}\text{As}_{0.05}\text{P}_{0.95}/\text{In}_{0.40}\text{Ga}_{0.60}\text{P}$ and $\text{In}_{0.75}\text{Ga}_{0.25}\text{P}/\text{In}_{0.40}\text{Ga}_{0.60}\text{P}$ are 135 Å and 110 Å, respectively, for a well thickness of 40 Å. This implies that carrier tunneling across barriers cannot take place in this structure even with very thin wells where the QSE effects are dominant. The thermionic emission will thus be the dominant transport mechanism if the carriers at the ground state are able to surmount the effective barrier height and are transported across the depletion region. We estimate the barrier height for electrons and holes at $n = 1$ state to be 0.1672 and 0.2152 eV for $\text{In}_{0.75}\text{Ga}_{0.25}\text{P}/\text{In}_{0.40}\text{Ga}_{0.60}\text{P}$ SBMQW for 65 Å well. The corresponding values for $\text{In}_{0.70}\text{Ga}_{0.30}\text{As}_{0.05}\text{P}_{0.95}/\text{In}_{0.40}\text{Ga}_{0.60}\text{P}$ are 0.1497 eV and 0.2089 for 45 Å well.

Figure 4.10 shows the quantum efficiency of the two SBMQW structures in comparison to standard InGaP p-i-n structures lattice matched to GaAs. The i layer of InGaAsP/InGaP SBMQWs

is made of 30 period quantum wells of 45 Å $\text{In}_{0.70}\text{Ga}_{0.30}\text{As}_{0.05}\text{P}_{0.95}$ wells and 140 Å $\text{In}_{0.40}\text{Ga}_{0.60}\text{P}$ barriers. The i layer of InGaP/InGaP SBMQWs is made of 30 period quantum wells of 65 Å $\text{In}_{0.75}\text{Ga}_{0.25}\text{P}$ wells and 170 Å $\text{In}_{0.40}\text{Ga}_{0.60}\text{P}$ barriers. The i layer of the standard device is made of undoped $\text{In}_{0.49}\text{Ga}_{0.51}\text{P}$ and with a thickness same as that of the QW region in both the two structures. We first note that the EQE of the standard device falls rapidly at around 663 nm (1.87 eV), which is the band-edge of $\text{In}_{0.49}\text{Ga}_{0.51}\text{P}$. In addition, the quantum efficiency for light in the bulk absorption range of both the two QW structures is close to the standard device, this implies that the thermionic carrier transport is efficient. Due to absorption in the i -SBMQW region, the EQE of the QW devices extends beyond the $\text{In}_{0.49}\text{Ga}_{0.51}\text{P}$ band-edge approaching 682 and 750 nm for InGaP/InGaP and InGaAsP/InGaP MQWs, respectively. The absorption edge obtained from the quantum efficiency measurements is consistent with that obtained from the PL emission in Figure 4.6 for both QW structures. It is noteworthy that in InGaP/InGaP the achieved red-shift is low relative to InGaAsP/InGaP, which may limit its use in five and six MJSCs. However, the red-shift achieved using the latter makes this structure a promising candidate for next-generation photovoltaic subcells.

Figure 4.11 shows the illuminated J-V characteristics of the InGaAsP/InGaP SBMQWs in addition to an InGaP standard device. The open circuit voltage and short circuit current density of the InGaAsP/InGaP SBMQW device are 1.11 eV and 8.6 mA/cm², respectively. The corresponding values for the standard device are 1.23 eV and 7.425 mA/cm². The improved short circuit of SBMQW over the standard device is due to an extension in the absorption threshold as indicated by the EQE of Figure 4.10(a). It is worth noting that the InGaAsP/InGaP SBMQW device exhibit a relative efficiency increase of about 4% over the standard device.

Based on the EQE, LIV, and PL results discussed in the last few sections, the potential for using strain-balanced InGaAsP/InGaP quantum wells is higher than strain-balanced InGaP/InGaP quantum well. Hence, Chapter 5 will focus on the effect of well thickness, well number, and barrier heights on the performance of strain-balanced InGaAsP/InGaP.

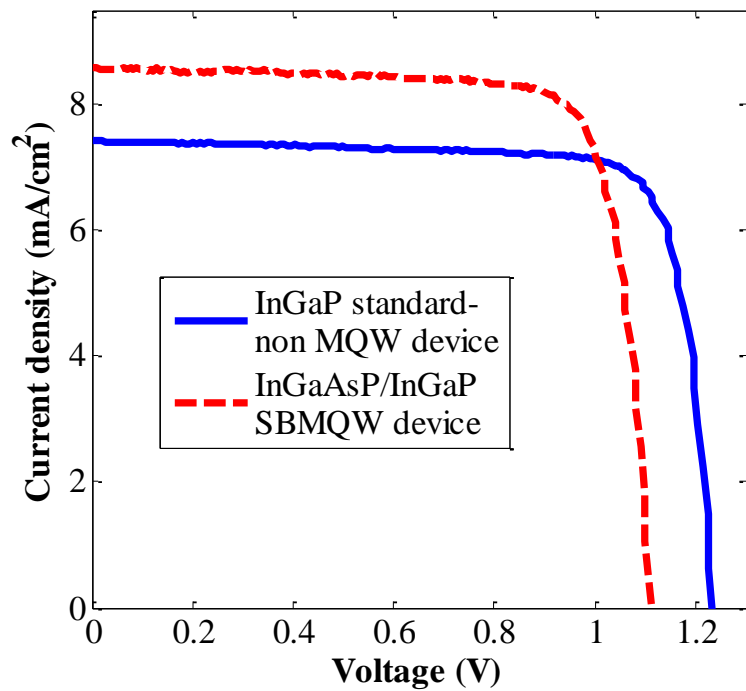


Figure 4.11: Illuminated current voltage characteristics for $\text{In}_{0.70}\text{Ga}_{0.30}\text{As}_{0.05}\text{P}_{0.95}/\text{In}_{0.40}\text{Ga}_{0.60}\text{P}$ SBMQWs and InGaP standard p-i-n device. No window or antireflection coatings are used.

Chapter 5: Strain-balanced InGaAsP/ InGaP Quantum Well Solar Cells

Currently available materials for III-V multijunction solar cells lattice matched to GaAs covering the spectral range from 1.65 eV to 1.82 eV are composed of either immiscible quaternary alloys or contain aluminum. We report the fabrication of a novel aluminum-free $\text{In}_x\text{Ga}_{1-x}\text{As}_{1-z}\text{P}_z/\text{Ga}_{1-y}\text{In}_y\text{P}$ ($x > y$) strain balanced multiple quantum well (SBMQW) *p-i-n* solar cell structure lattice matched to GaAs. SBMQWs consist of alternating layers of $\text{In}_x\text{Ga}_{1-x}\text{As}_{1-z}\text{P}_z$ wells and $\text{In}_y\text{Ga}_{1-y}\text{P}$ barriers ($x > y$) under compressive and tensile strain, respectively. When compared to standard InGaP devices, SBMQW structures exhibit longer photoluminescence wavelength (680-780 nm) emission and enhanced light absorption beyond 1.85 eV with improved short circuit current density. In this Chapter, the SBMQW emission and absorption wavelength is controlled by adjusting the layer thickness of InGaAsP wells while the arsenic and indium compositions are fixed. We show that carriers generated in quantum wells are extracted via thermionic emission. The effect of well thickness and number of period on the performance of this QW device is studied. The proposed SBMQWs allow more flexibility in the design of current multi-junction solar cells and future cells with more than four junctions.

This chapter is a paper published in IEEE Journal of Photovoltaics, 6 (4), 997-1003, 2016, with some additions and modifications.

5.1. Introduction

As discussed in Chapter 4, strain-balanced InGaAsP/InGaP incorporated into the intrinsic region of solar cells have been shown to extend the absorption threshold to 1.6-1.7 eV [121]. The ultimate goal of this research is to include strain-balanced multiple quantum well (SBMQWs) into a multijunction solar cell device. This chapter reports on the electrical characterization of strain-balanced InGaAsP/InGaP quantum well solar cell. The effect of quantum well thickness on causing a red-shift in the absorption threshold of these quantum wells is studied. The effect on the number of periods on enhancing the sub-bandgap external quantum efficiency values is also discussed. The contribution of these quantum wells in the total quantum efficiency response is studied through modeling the drift-diffusion through this solar cell structure.

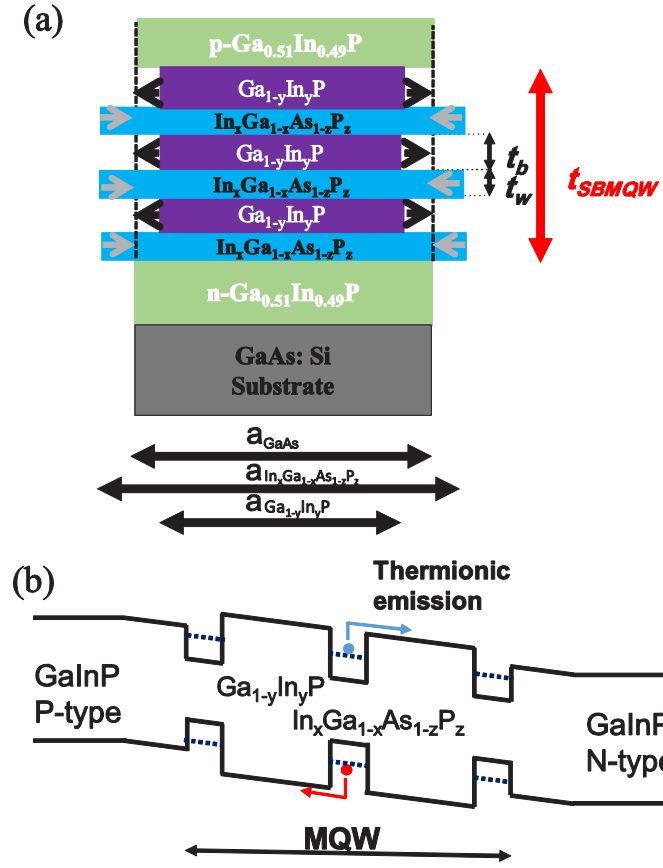


Figure 5.1: Schematics of (a) the InGaAsP/GaInP SBMQW structure grown on a GaAs substrate and (b) the energy band diagram of SBMQW, illustrating thermionic emission dominating the current transport in this structure. The compressive stress in InGaAsP wells is balanced by the tensile stress in GaInP barriers. The MQWs are grown unintentionally doped. The doping level used here for the emitter and base 1×10^{17} and $1 \times 10^{18} \text{ cm}^{-3}$, respectively. The thickness of the well is altered in this study to tune the emission of the wells and understand the carrier transport. The well and barrier thicknesses are adjusted for each structure to achieve the strain-balanced condition.

5.2. Experimental Details

The SBMQWs consist of alternating layers of In_xGa_{1-x}As_{1-z}P_z wells and Ga_{1-y}In_yP (or, In_yGa_{1-y}P) barriers ($x > y$), that are under compressive and tensile strain, respectively, as shown in Figure 5.1(a). Figure 5.1(b) shows the energy band diagram of the structure. The SBMQW active region thicknesses and compositions are chosen such that the compressive stress in the wells is balanced by the tensile stress in the barriers [63]. Details of the growth of this structure and how the miscibility gap problem in the InGaAsP layer have been published elsewhere and discussed in

Chapter 4 [121]. Our earlier attempts to approach the 1.65-1.82 eV bandgap range by growing strain balanced $\text{In}_x\text{Ga}_{1-x}\text{P}/\text{In}_y\text{Ga}_{1-y}\text{P}$ ($x>y$) or $\text{InGaP}/\text{GaAsP}$, were both unsuccessful. The absorption threshold of $\text{In}_x\text{Ga}_{1-x}\text{P}/\text{In}_y\text{Ga}_{1-y}\text{P}$ ($x>y$) SBMQWs was not extended to an effective bandgap of less than 1.82 eV as discussed in Chapter 4 [121]. $\text{InGaP}/\text{GaAsP}$ SBMQWs had several growth problems and we did not detect any photoluminescence (PL) emission, nor achieved a good surface morphology for this structure. One possible source for this can be arsenic carry over from GaAsP to InGaP resulting in the formation of InGaAsP interfacial layer that is not miscible.

All samples studied were grown on (100) GaAs mis-oriented by 2° towards the $<110>$ direction by metal organic chemical vapor deposition (MOCVD) at 200 torr. The precursors used in this work are tertiarybutyl-arsine (TBAs), tertiarybutylphosphine (TBP), trimethylindium (TMIn), and trimethylgallium (TMGa). The bulk GaInP was grown at 650°C and the SBMQW structure at 585°C . The base and emitter thicknesses are 1.0 and 0.1 μm , respectively. The doping of base and emitter are 1×10^{17} and $1 \times 10^{18} \text{ cm}^{-3}$, respectively. The background doping in the MQW region is p-type and was estimated to be around $4 \times 10^{15} \text{ cm}^{-3}$ using Hall measurements, which would correspond to $\sim 0.8 \mu\text{m}$ depleted region. A highly doped GaAs cap layer was applied for ohmic contact. The devices were fabricated as $2.5 \text{ mm} \times 2.5 \text{ mm}$ etched mesas using standard photolithographic procedures. Pd/Ge/Pd/Ti/Ag/Au n-type and Ti/Pd/Ag/Pd/Au p-type ohmic contacts were deposited via e-beam evaporation. All cells were grown without an antireflection coating or a window. The indium and arsenic compositions in the quaternary alloy are estimated using X-ray diffraction (XRD) based on our growth experience with the ternaries GaInP and GaAsP . Optical emission of MQW structures was evaluated by PL using a 532 nm frequency doubled Nd:YAG laser. The external quantum efficiencies (EQE) of the solar cell devices were measured using a quartz tungsten halogen lamp with a Newport $\frac{1}{4}\text{-m}$ monochromator, and calibrated Si photodiode. The illuminated current density-voltage ($J\text{-}V$) characteristics were measured with a 1-kW solar simulator set at one sun AM1.5G intensity and calibrated with a GaInP reference cell with a known AM 1.5G J_{SC} .

5.3. Results and Discussion

In this section, we first present and analyze the results of PL. Then we compare the XRD results of SBMQWs with different well thicknesses. Next, we discuss the current transport in this

SBMQW structure. Finally, we compare the quantum efficiency and current-voltage characteristics of InGaAsP/InGaP SBMQWs and standard InGaP cell.

5.3.1. Photoluminescence and Electroluminescence of SBMQWs: red-shift

The MQW structures were first investigated optically and electrically using PL and electroluminescence (EL) with a range of well thickness from 25 Å to 75 Å, as shown in Figure 5.2. The barrier thickness (t_B) is adjusted for each structure to achieve the strain balanced condition. In this study, the indium compositions in the well (x) and barrier (y) were fixed at about 70% and 40%, respectively, while the phosphorus composition (z) in the InGaAsP is fixed at about 95%. The critical layer thicknesses of InGaAsP wells and InGaP barriers are estimated to be 90 Å and 390 Å, respectively, using Matthews-Blakeslee model [58]. The emission was tuned by altering the thickness of the well to approach the 680-780 nm wavelength range, as shown in Figure 5.2. It is noted that the emission wavelength increases with increasing well thickness consistent with the trend expected for the quantum size effect (QSE). In addition, the peak values for the emission are consistent as shown in the PL spectrum shown in Figure 5.2(a) and the EL spectrum shown in Figure 5.2(b). In addition, it is clear that the PL spectrum of thick well structures are broader and less intense compared to those of thin wells. This behavior can be due to some surface crosshatching we noticed for thicker well samples indicating that the well is approaching or exceeding our estimate for the critical thickness (~90 Å).

In discussing the following SBMQW results, the model used to predict the effective band gap ($E_{G,Eff}$) of the MQW structures is:

$$E_{G,Eff} = E_G^{well,relaxed} + \Delta E_G^{Strain} + \Delta E_G^{QSE}, \quad (5.1)$$

Details about this model was discussed in Section 2.3 of Chapter 2. The relaxed bandgap of $\text{In}_{0.70}\text{Ga}_{0.30}\text{As}_{0.05}\text{P}_{0.95}$ is estimated to be ~ 1.54 eV. The predicted ΔE_G^{Strain} value is ~ 56 meV for various well thicknesses, while ΔE_G^{QSE} varies with the well thickness.

The PL data were then graphed against the inverse of the well thickness squared ($1/t_w^2$), as the energy levels within the well vary proportionally with this parameter, Figure 5.3. For the thinnest wells, the measured peak PL values correspond well to the theoretical values. However, the PL measurements for the thick wells deviated from the expected values. The reason behind this

discrepancy can be explained by the strain relaxation relaxation, partial or complete of the well material as the thickness of the well approaches CLT. Relaxation will reduce or eliminate the strain-related increase of the bandgap of the well material. As shown in Figure 5.2, the presence of secondary longer wavelength peak for the 75 Å well sample indicates partial relaxation.

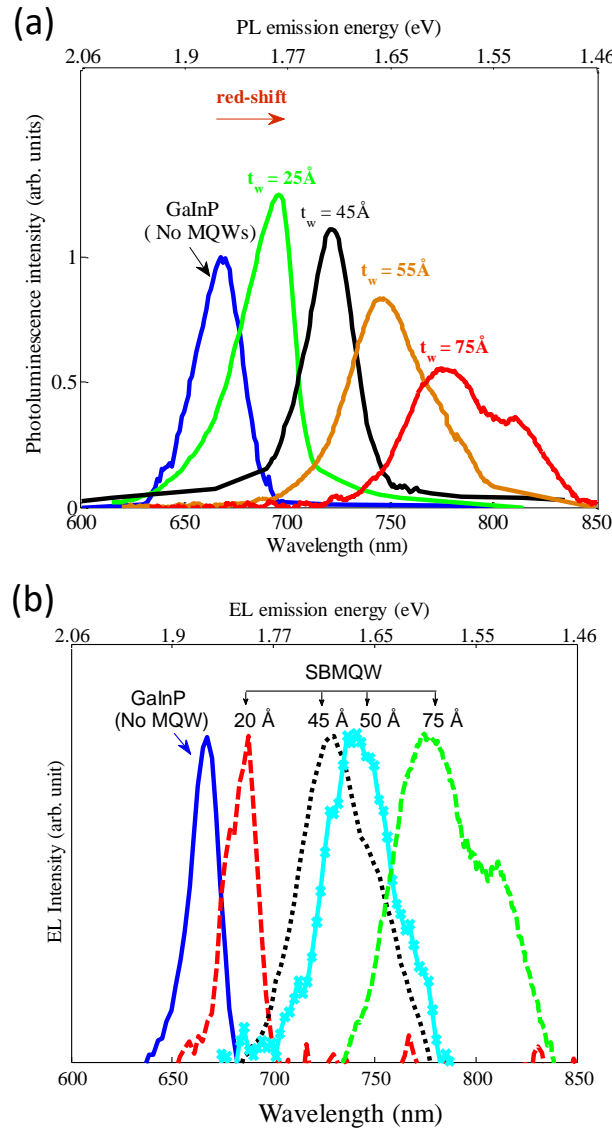


Figure 5.2: The (a) photoluminescence spectra and (b) photoluminescence spectra, for a series of $\text{In}_{0.70}\text{Ga}_{0.30}\text{As}_{0.05}\text{P}_{0.95}$ / $\text{In}_{0.40}\text{Ga}_{0.60}\text{P}$, 30-period MQW with varying well thickness. The MQWs tune the bandgap of GaInP to lower energy values. The emission energy decreases with the increase of the well thickness. Thicker wells exhibit wider full width half maximum and lower intensity.

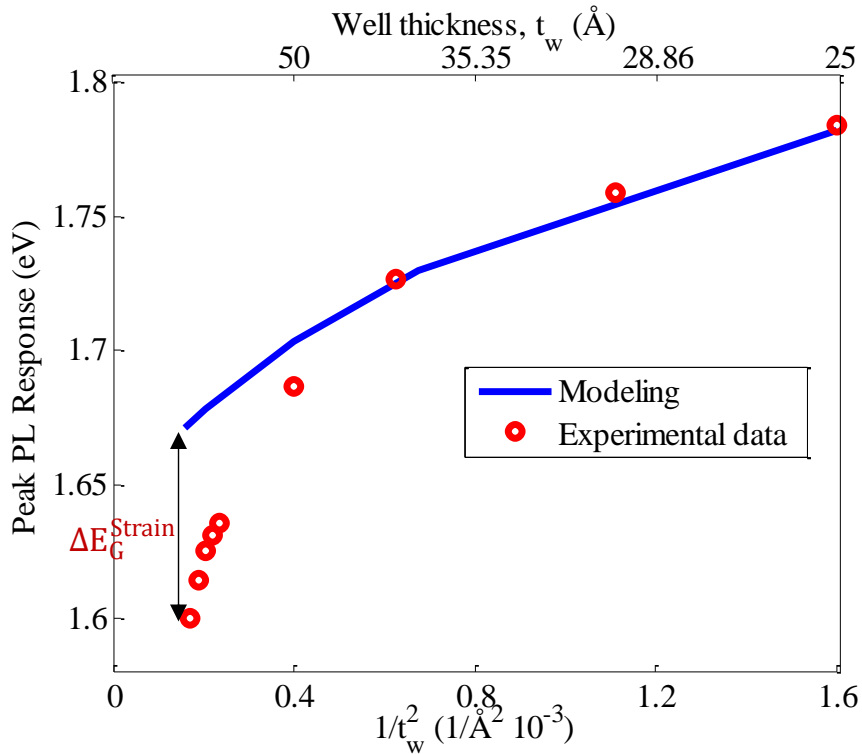


Figure 5.3: The peak PL emission of $\text{In}_{0.70}\text{Ga}_{0.30}\text{As}_{0.05}\text{P}_{0.95}/\text{Ga}_{0.60}\text{In}_{0.40}\text{P}$ SBMQWs versus $1/t_w^2$. $E_{\text{G}}^{\text{InGaAsP,relaxed}} = 1.54 \text{ eV}$, $\Delta E_{\text{G}}^{\text{Strain}} = 56 \text{ meV}$. $\Delta E_{\text{G}}^{\text{QCSE}}$ and $\Delta E_{\text{G}}^{\text{QSE}}$ varies with the well thickness. The measured values for the thick wells do not follow the trend as the thin ones due to relaxation taking place for layers approaching the critical layer thickness.

5.3.2. X-ray Diffraction

The relationship between well thickness and strain relaxation has been investigated using XRD. As shown in Figure 5.4, the presence of strong satellite peaks on the thin well (45 Å) device indicates the presence of sharp interfaces and confirms the strain balanced condition is met. However, the weak satellite peaks with wider full width half maximum for the thick well (75 Å) device indicates the quantum wells have relaxed as indicated earlier by the PL response of the wider well devices in Figure 5.2.

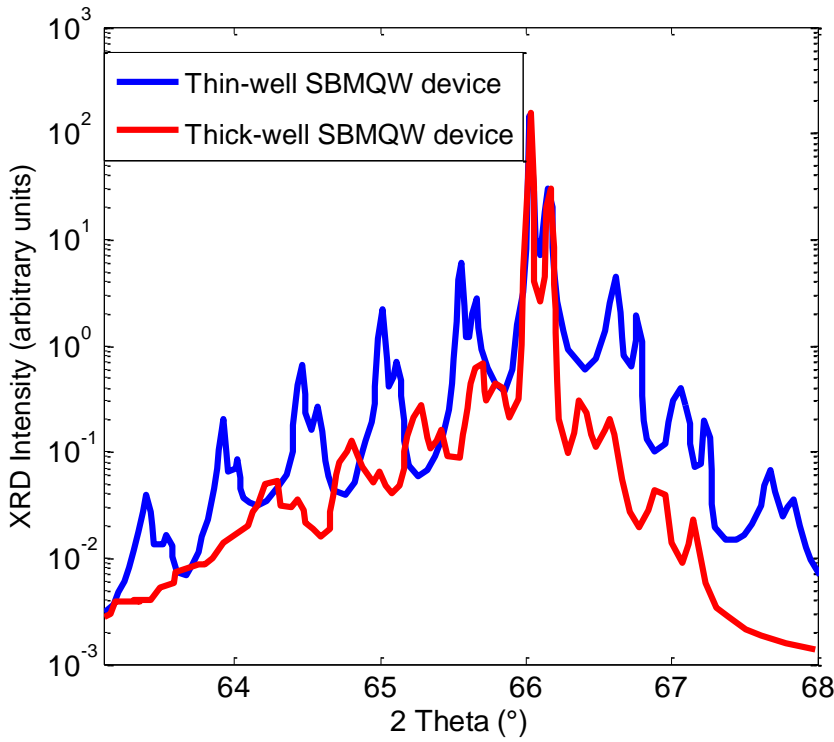


Figure 5.4: Single XRD Diffraction of $\text{In}_{0.70}\text{Ga}_{0.30}\text{As}_{0.05}\text{P}_{0.95}/\text{Ga}_{0.60}\text{In}_{0.40}\text{P}$ SBMQWs of thin-well ($t_w = 45 \text{ \AA}$) device and thick-well device ($t_w = 75 \text{ \AA}$).

5.3.3. Carrier Transport and Well Thickness Effect

Solar cells require minority carriers generated in the neutral and QW absorption regions to be transported across the depletion region which is the MQW in this design. Two main mechanisms can be responsible for carrier transport in these MQW structures as discussed in Section 2.6 of Chapter 2: thermionic emission and carrier tunneling across the barriers [41, 122]. Since the design of the quantum wells and barriers depends upon these mechanisms, it is important to briefly discuss the conditions of each. As shown in Eqn. (2.10), the tunneling lifetime τ_{tun} is strongly dependent on the thickness of the barrier and less dependent on the barrier height. However, the thermal escape life time τ_{therm} is more dependent on the effective barrier height and does not depend on the barrier thickness, see Eqn. (2.11). Based on our growth estimates, carrier tunneling is excluded in this structure due to the relatively thick barriers ($>100 \text{ \AA}$) which are needed to strain-balance the structure. Tunneling is expected to take place for a t_b of less than 35 \AA . The only condition that may lead to achieving tunneling current is through the use of both thin wells and barriers. This, accordingly, will increase the quantum size effects resulting in an effective bandgap close to or

higher than 1.8 eV as shown in the PL spectra of Figure 5.2, while the motivation of this work is to tune the bandgap to 1.65-1.8 eV range. However, energy band theory shows that thermionic emission (field assisted) is more likely the dominant current transport mechanism for thin wells. For example, the bulk bandgap of $\text{In}_{0.70}\text{Ga}_{0.30}\text{As}_{0.05}\text{P}_{0.95}$ wells and $\text{Ga}_{0.60}\text{In}_{0.40}\text{P}$ barriers can result in conduction and valence band offsets of about 0.2062 and 0.2679 eV, respectively. These values may make thermionic emission unlikely. However, for thin wells ($\sim 30\text{-}60 \text{ \AA}$), QSE shifts the energy level of carriers of the $n = 1$ quantum state upwards and thus reduces the effective barrier height for thermionic emission. For example, the barrier heights for electrons and light holes for 40 \AA thick wells are 0.1324 eV and 0.1812, respectively, which increases the thermionic emission probability.

Table 5.1: Thickness of well and barrier, peak PL emission, short circuit current density, open circuit voltage, bandgap-voltage offset (W_{oc}), FF and efficiency (η) for standard cell and SBMQW cells. The devices did not contain antireflection coatings or a window.

	t_w (\AA)	t_B (\AA)	peak PL (nm)	J_{sc} (mA/cm 2)	V_{oc} (V)	W_{oc} (V)	FF (%)	η (%)
InGaP standard	N/A	N/A	670	7.425	1.23	0.62	80	7.3
SBMQW1	45	140	725	8.015	1.18	0.53	79.5	7.5
SBMQW2	55	170	750	8.596	1.11	0.54	79.4	7.6
SBMQW3	75	200	775	1.2	0.84	0.76	N/A	N/A

5.3.4. Quantum Efficiency and Current Voltage Characteristics (well thickness effects)

To experimentally investigate the carrier transport in these QW structures, three SBMQW devices of 30 periods in addition to $\text{In}_{0.49}\text{Ga}_{0.51}\text{P}$ standard device were fabricated. In these structures, the well thickness is altered: 45 \AA (SBMQW1), 55 \AA (SBMQW2), and 75 \AA (SBMQW3). The arsenic and indium compositions are kept the same in the well. The total MQW-region thicknesses of the three devices are less than the thickness of the depletion region such that the

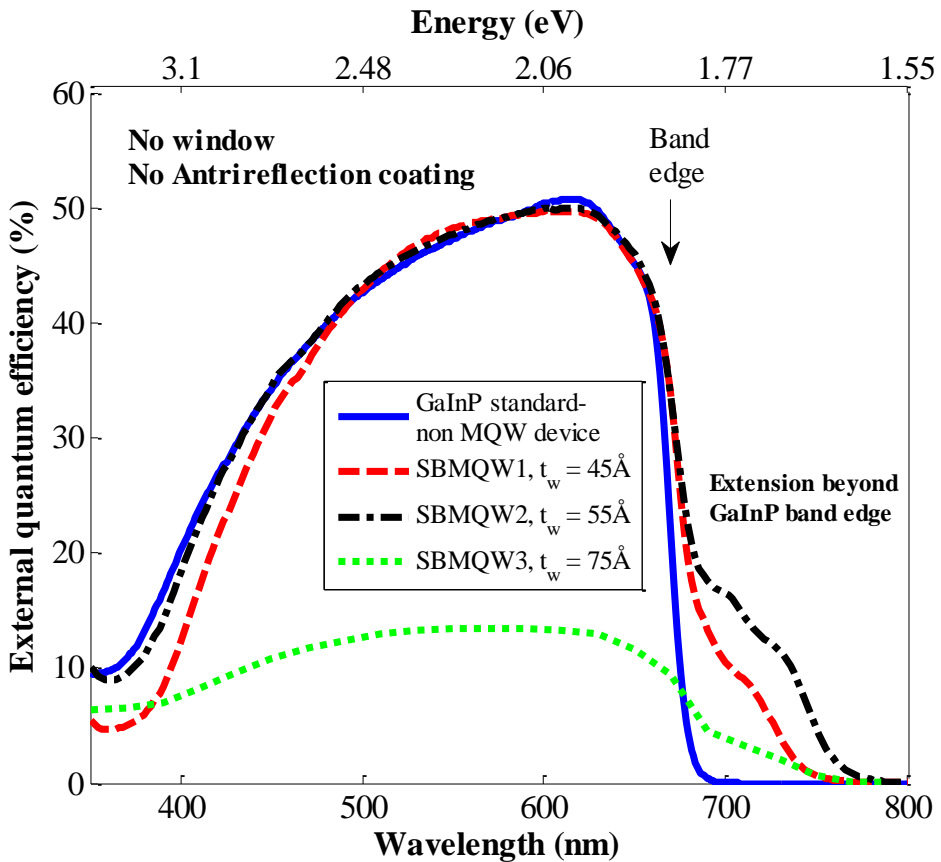


Figure 5.5: External quantum efficiency (EQE) versus wavelength (energy) for series of SBMQWs with different well thickness and GaInP standard device measured at room temperature. SBMQWs exhibit absorption beyond the band-edge of GaInP due to the inclusion of the quantum wells in the intrinsic region of the p-i-n structure. MQW with thick wells exhibits poor quantum efficiency.

transport can be only correlated to the well thickness effect. Information about these samples is shown in Table 5.1. As seen in Figure 5.5, the EQE for a standard InGaP cell will rapidly fall off at the $In_{0.49}Ga_{0.51}P$ band edge near 670 nm corresponding to $E_{G,eff}$ of about 1.85 eV. However, measurements show that the inclusion of SBMQW layers in the depletion region of GaInP device extends the EQE spectrum beyond the InGaP band-edge (670 nm) due to sub-band gap absorption by the QWs. The absorption edges in the red-region are 730 nm, 757 nm, and 780 nm, respectively for the SBMQW1, SBMQW2, and SBMQW3. It is worth pointing out that the SBMQW2 exhibits a higher absorption edge than SBMQW1 due to the thicker well, which implies less QSE and lower effective bandgap, according to Eqn. (5.1) and the PL spectra of Figure 5.2. SBMQW1 and SBMQW2 have almost the same EQE of the standard cell indicating that carrier transport through

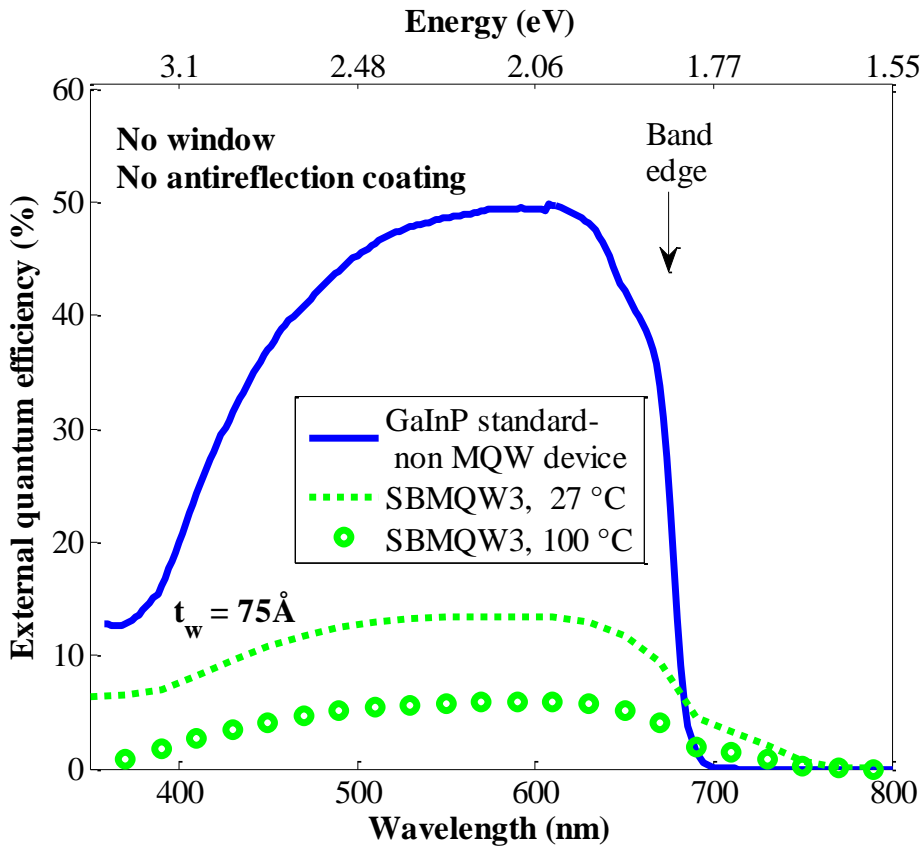


Figure 5.6: External quantum efficiency (EQE) versus wavelength (energy) for SBMQW3 measured at room temperature and 100 °C in addition to the standard device. The well thickness of the SBMQW device is 75 Å. The EQE degrades at high temperature for thick-well devices.

the MQW region is almost perfect. It is noted that the EQE of the thick-well device, SBMQW3, is reduced in comparison to the first two devices. This behavior can be due to two reasons. First, the reduced minority carrier lifetime in the quantum wells as indicated by the drastic reduction in the photoluminescence intensity (Figure 5.2) and the weak satellite XRD peaks for thicker wells approaching the CLT (Figure 5.4). This will result in some carriers recombining before they can traverse the SBMQW region and will reduce both the emitter and base responses as shown in Figure 5.5. Second, thicker wells will lead to less severe QSE (effectively a deeper level) which implies that the electrons and holes will have a lower thermionic emission rate due to the increased conduction and valence band barriers, resulting in less efficient carrier transport.

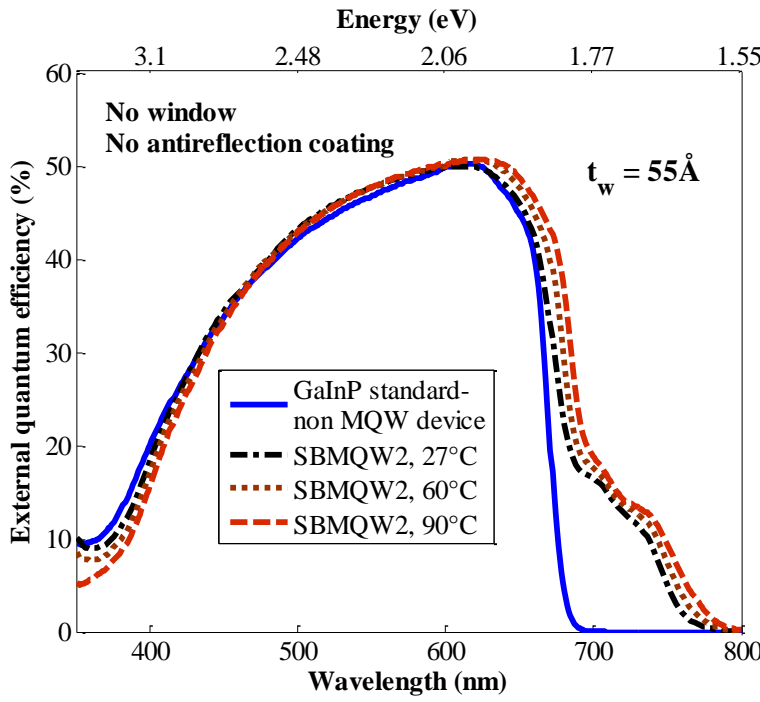


Figure 5.7: External quantum efficiency (EQE) versus wavelength (energy) for SBMQW2 measured at different temperatures in addition to the standard device. The well thickness of the SBMQW device is 55 Å.

In order to investigate whether the well relaxation or the thermionic probability degradation is the reason for the poor SBMQW3 efficiency, EQE is measured at elevated temperatures as shown in Figure 5.6. The predominance of the well relaxation effect for thick-well devices is supported by the second spectral response curve for SBMQW3 which was measured at 100 °C, as shown in Figure 5.6. The response is further reduced under elevated temperatures measurements, which is opposite to what would be expected if the thermionic emission probability was the limiting regime. The EQE spectrum of the thin-well device, SBMQW2, at elevated temperatures is shown in Figure 5.7. The EQE is relatively unaffected by the increase in temperature. This indicates the thermionic emission probability is already effective at room temperature. The red shift in the absorption edge with the temperature increase is due to expected decrease in the bandgap with temperature.

The *J-V* curves of the SBMQWs are shown in Figure 5.8. The open-circuit voltage (V_{oc}), short-circuit current density (J_{sc}), bandgap-voltage offset (W_{oc}), fill factor (FF) and efficiency (η) are

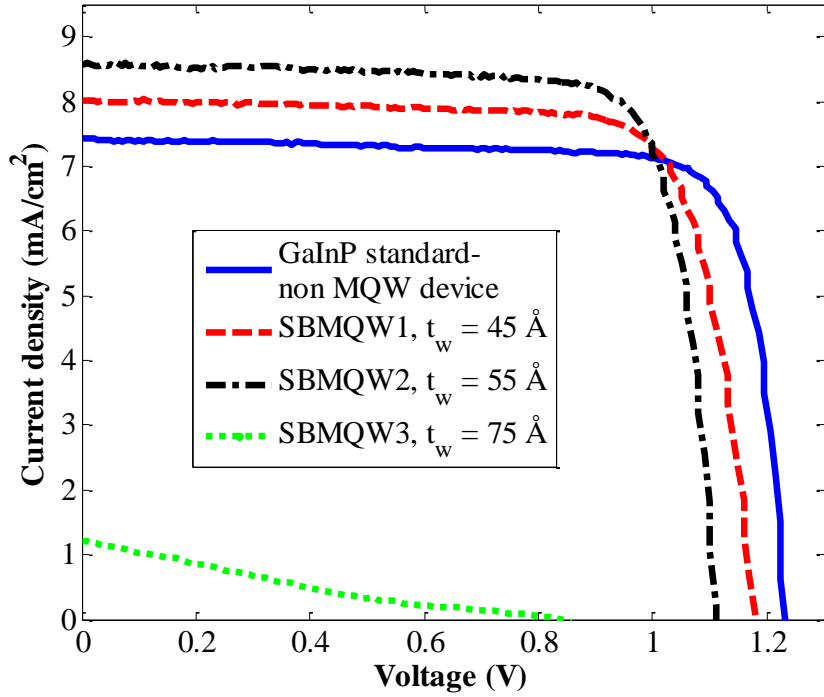


Figure 5.8: 1 sun current density vs voltage curves for the standard GaInP cell and SBMQW devices. Thin-well SBMQWs have higher J_{sc} in comparison to the standard device. Thick-well SBMQW device has degraded current.

listed in Table 5.1. Compared to the standard cell, all of the SBMQWs have a lower V_{oc} which is due to the lower effective bandgap associated with these structures. For example, the V_{oc} of SBMQW1 is 0.07 eV higher than that of SBMQW2 due to more severe quantum size effects in its thinner well. However, the two thinner well samples (SBMQW1 and SBMQW2) have lower W_{oc} than the bulk sample, possibly due to better photon-recycling of the below-bandgap quantum well radiation. The J_{sc} of SBMQW1 and SBMQW2 are markedly improved by 8% and 16% respectively compared to those of the standard cell. The increased J_{sc} is ascribed to the sub-bandgap photo absorption by the QWs in conjunction with the EQE improvement in the wavelength region below the GaInP band-edge. It is worth noting that the two thinner well devices exhibit efficiency slightly higher than standard GaInP cell, as shown in Table 5.1. Among the SBMQWs, the SBMQW3 has the lowest J_{sc} and V_{oc} and the highest W_{oc} due to low minority carrier lifetime in the MQW region in addition to the loss of thermally generated minority carriers due to the relatively thicker well. Therefore, optimizing the current structure to achieve the desired red-shift

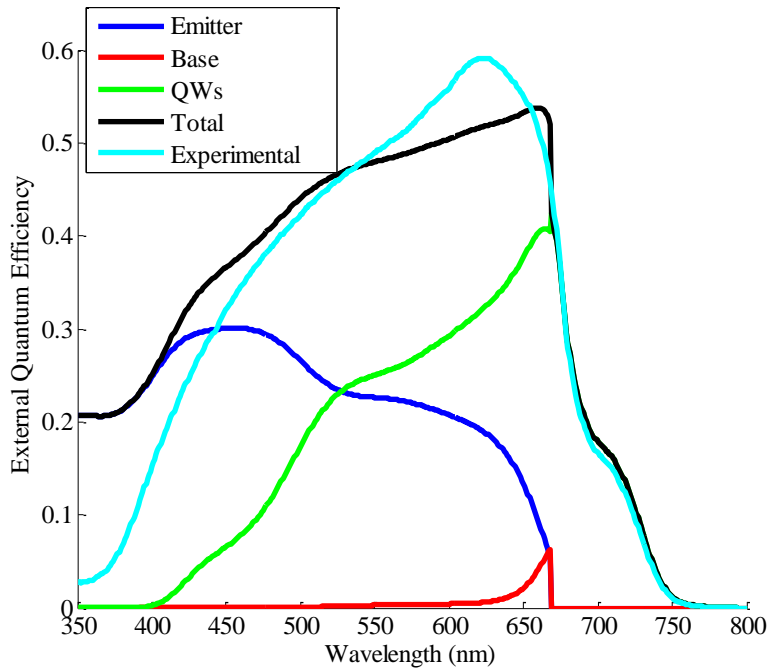


Figure 5.9: Modeling of external quantum efficiency of strain-balanced InGaAsP/InGaP quantum well solar cells showing the contributions of the emitter, base, and quantum wells into the total response.

without sacrificing the carrier transport is a challenging issue. Further optimization of the structure will lead to extending the absorption of the quantum wells to longer wavelengths and improving the quantum efficiency of the device.

5.3.5. Quantum Efficiency: Measurements and Modeling

The external quantum efficiency of the InGaAsP/InGaP quantum wells was modeled to explore the contributions of each of the emitter, base, and the QWs, as shown in Figure 5.9. The analysis in Nelson's book is followed to solve the drift-diffusion and continuity equations [7]. The contribution of each region is considered independently considering the wavelength absorption dependence of the preceding layers. The absorption coefficient of the MQWs (α_{MQW}) is extracted from the measured spectral response assuming fully depleted region, where

$$\alpha_{MQW}(\lambda) = -\frac{1}{t_{QW}} \ln(1 - EQE(\lambda)), \quad (5.2)$$

where t_{QW} is the total thickness of the QW region. The extracted absorption coefficient of the InGaAsP/InGaP QWs is $\sim 2 \times 10^4 \text{ cm}^{-1}$. Tabulated values for the mobilities (μ) and lifetimes (τ) are used in the model: $\mu_p = 60 \text{ cm}^2/\text{Vs}$, $\mu_n = 300 \text{ cm}^2/\text{Vs}$, $\tau_p = 1 \text{ ns}$, and $\tau_n = 50 \text{ ns}$ [123]. The front and back surface recombination velocity are parameterized to $9 \times 10^5 \text{ cm/sec}$ and $1 \times 10^4 \text{ cm/sec}$, respectively, to give the best fit to the measured results. Tabulated data for the absorption coefficient of InGaP emitter and base are used. The modeling results indicate that both the emitter and the depletion region (including the SBMQWs) contribute significantly to the total response with relatively minor contribution from the base. Beyond the $\text{In}_{0.49}\text{Ga}_{0.51}\text{P}$ cut-off, the modeling results matches with the measured response. The preliminary experimental and modeling results presented here indicate that improving the efficiency of the SBMQW device requires improving the blue and red response through both optimization of the AlInP window growth conditions and extending the absorption threshold to longer wavelengths or increasing the number of wells to improve the excitonic absorption.

5.3.6. Effect of Number of Period on InGaAsP/InGaP SBMQWs

We experimentally investigate the effect of increasing the number of quantum wells on the performance of $\text{In}_{0.70}\text{Ga}_{0.30}\text{As}_{0.05}\text{P}_{0.95}/\text{In}_{0.40}\text{Ga}_{0.60}\text{P}$ SBMQWs. In this study, only the number of periods is altered: 10 (SBMQW10), 20 (SBMQW20), 30 (SBMQW30), and 45 (SBMQW45). The well and barrier thickness are kept at 45 Å and 140 Å, respectively, across all these devices. These four SBMQW samples have the same PL emission, 750 nm (1.65eV). Data about these samples is summarized in Table 5.2. Figure 5.10 shows the XRD scans taken across (004) reflection for samples SBMQW10, SBMQW20, SBMQW30, and SBMQW45. The vertical dotted lines on the superlattices peaks indicate that the period thickness and compositions of the layers in the InGaAsP/InGaP SBMQW active regions were identical for all four samples. The full width half maximum of the satellite peaks is almost identical which signify that no relaxation has been observed with increasing the number of QWs.

Table 5.2: Number of periods, grown MQW layer thickness, short circuit current density, open circuit voltage, and fill factor for series of InGaAsP/InGaP SBMQW cells. The devices did not contain antireflection coatings or windows.

	Number of periods	<i>i</i> layer thickness (μm)	J_{sc} (mA/cm ²)	V_{oc} (V)	FF (%)
InGaP standard	N/A	N/A	7.425	1.23	80
SBMQW10	10	0.185	7.8	1.1	80
SBMQW20	20	0.37	8.183	1.08	77.5
SBMQW30	30	0.55	8.6	1.11	79.4
SBMQW45	45	0.83	5.22	1.12	76

The EQE of the four samples is depicted in Figure 5.11. As the number of periods increases from 10 to 30 the excitonic quantum efficiency of the structure is improved. This can be attributed to higher light absorption taking place due to inclusion of more wells in the intrinsic layer of the device. The enhanced EQE at wavelengths below the bulk InGaP band edge is due to drift assisted carrier collection. As the number of periods increases further (30 to 45), the EQE is reduced. This is accompanied by degradation in the quantum efficiency of the device across the bulk part of the spectrum, especially the blue region. This can be attributed to the thickness of the grown MQW region (0.83 μm) is approaching or exceeding the depletion region of the device. The background doping in the MQW region is 4×10^{15} cm⁻³ as measured using Hall measurements, which corresponds to about 0.8 μm depleted region. This will result in the formation of an undepleted region with a few QWs which will inhibit the transport of minority carriers through this region due to the absence of a significant electric field. The current-voltage is measured under one sun illumination. The short circuit current density (J_{sc}), open circuit voltage (V_{oc}) and fill factor (FF) are summarized in Table 5.2. The effect of number of period on J_{sc} is shown in Figure 5.12. It is noted that the J_{sc} increases with the increase of period number for period range of 10 to 30, correlating with the EQE shown in Figure 5.10. For higher number of periods, the J_{sc} degrades as might be expected if the current from the emitter and base is inhibited.

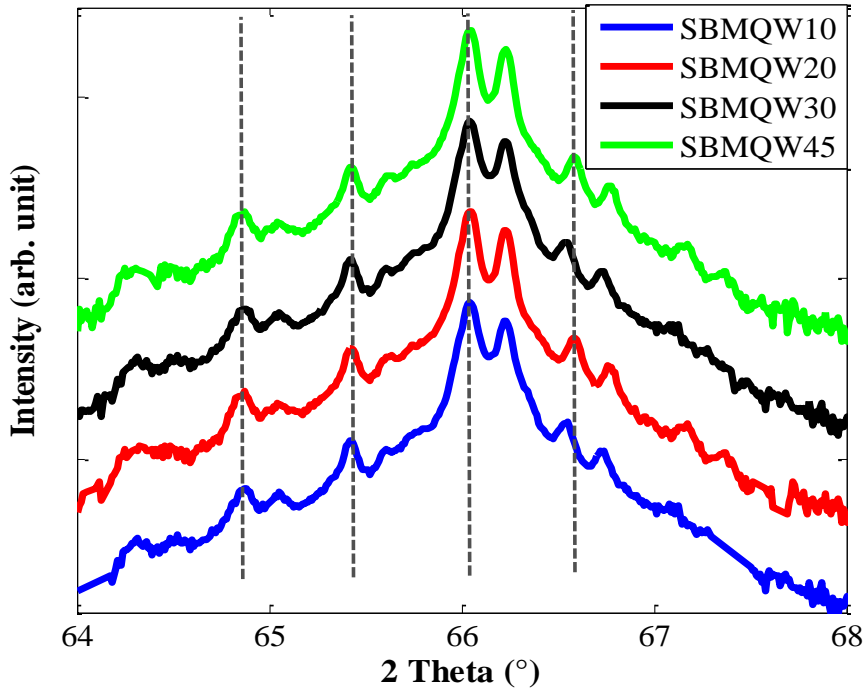


Figure 5.10: XRD scans for samples SBMQW10, SMQW20, SBMQW30 and SBMQW45.

The impact of the background doping concentrations on the maximum depletion widths is shown in Figure 5.14. A background doping of $4 \times 10^{15} \text{ cm}^{-3}$ would correspond to $\sim 0.82 \mu\text{m}$ depletion region, which is less the thickness of the 45 QWs device. This results in the formation of few undepleted QWs and the presence of a low electric field region where recombination may take place. This will limit the carrier collection as implied by the degradation of the quantum efficiency response of the 45 periods device shown in Figure 5.11. The Poisson equation was solved using the PC1D [8] to simulate the electric field across the QW region. The effective medium dielectric function of the QW region is calculated using Aspnes formula [124, 125]. The impact of the number of quantum wells on the electric field across the QW region for a *p*-type background concentration equals to $4 \times 10^{15} \text{ cm}^{-3}$ is shown in Figure 5.14. The electric field across the 10, 20, and 30 QWs devices is strong enough to sweep the carriers across the QW region. However, for the 45 QW device, a region of approximately zero field exists where carriers will recombine. This implies that the quantum efficiency across these devices will be limited by the maximum undepleted thickness that can be grown. This suggests that the optimum well number for this MQW structure and growth conditions is about 30 for the unintentional background doping present in the intrinsic region.

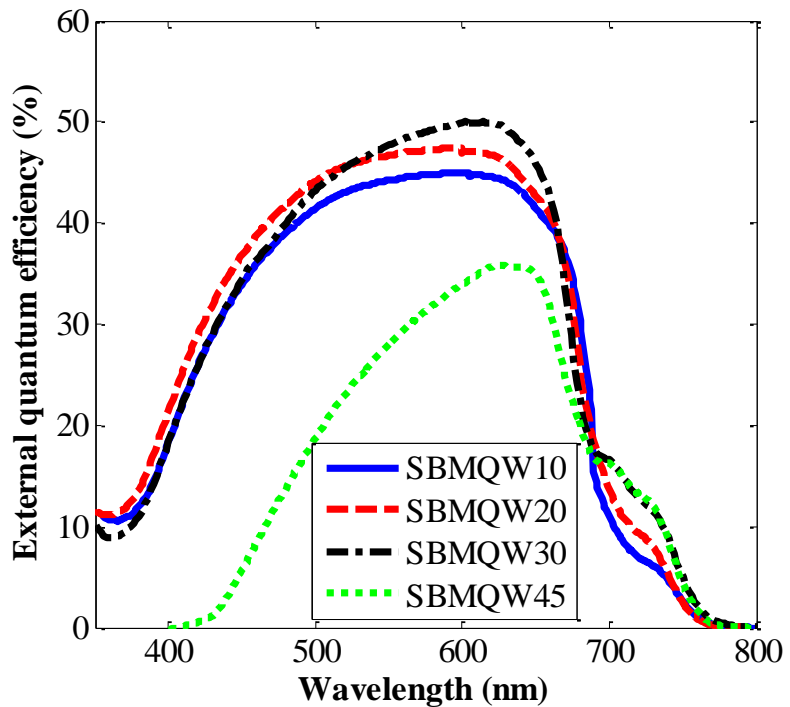


Figure 5.11: External quantum efficiency for $\text{In}_{0.70}\text{Ga}_{0.30}\text{As}_{0.05}\text{P}_{0.95}/\text{In}_{0.40}\text{Ga}_{0.60}\text{P}$ with varying number of periods.

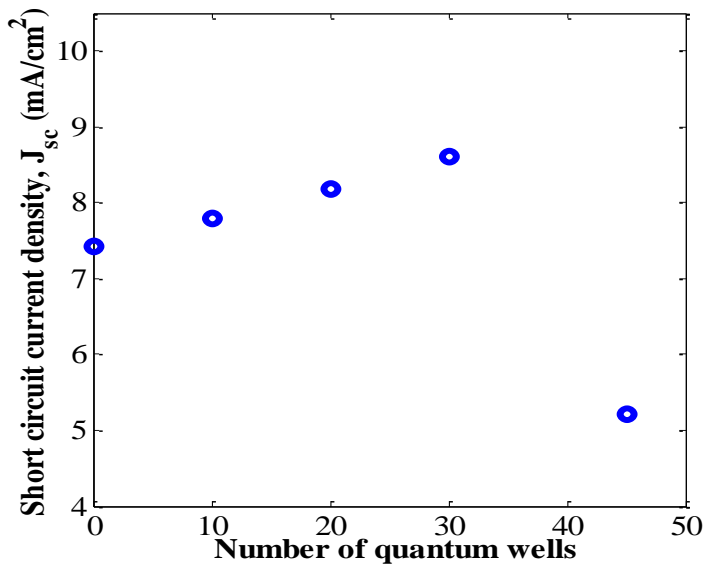


Figure 5.12: Effect of number of quantum wells on J_{sc} .

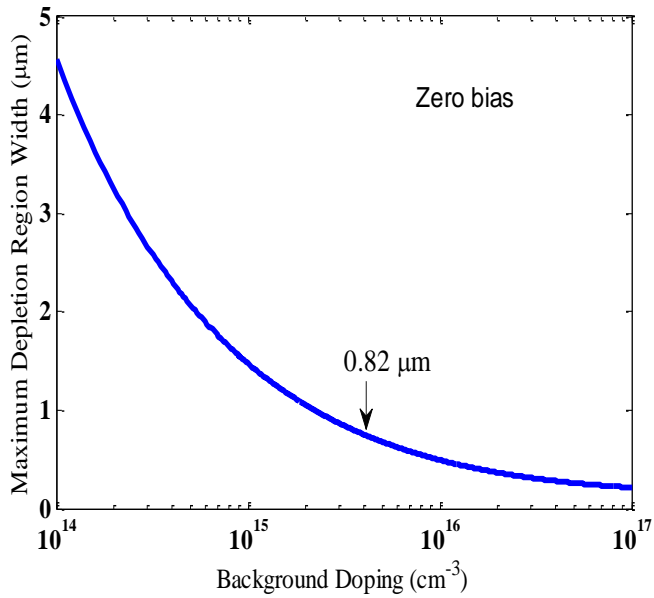


Figure 5.13: Simulation of the maximum depletion width as a function of p-type background doping at zero bias. The intrinsic carrier concentration (n_i) used was 100 cm^{-3}

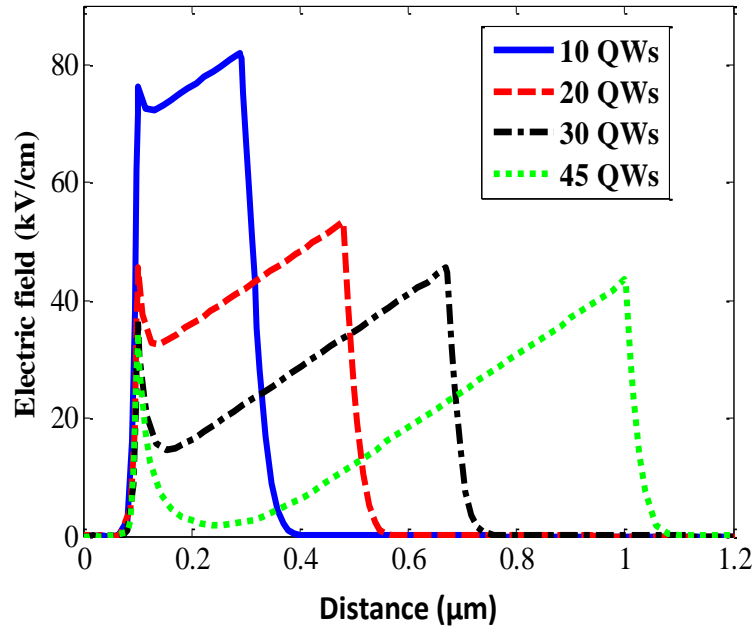


Figure 5.14: Simulation of the impact of the number of quantum wells on the electric field across the MQW region at zero bias for a constant background p-type background doping equals to $4 \times 10^{15} \text{ cm}^{-3}$

5.4. Advantages and Limitations of Strain-balanced InGaAsP/InGaP Quantum Well Solar Cells

In this Section, the advantages and limitations of strain-balanced InGaAsP/InGaP are discussed. The advantages of this QW structure can be summarized as follows:

- Bandgap tunability. This QW structure has a wide and tunable bandgap from 1.6 to 1.8 eV. Once the strain-balance condition is fully realized, scaling the period thickness can tune the quantum size effects and cause a red/blue shift in the response. This can be achieved by scaling the well thickness. Thus, the absorption threshold of solar cells that incorporate the strain-balanced InGaAsP/InGaP QW structure into it can be extended to longer wavelengths.
- Aluminum-free. AlGaAs, which is other potential structure that operate in the same bandgap range is more challenging to grow. This is because the presence of aluminum creates deep levels centers which increases the dark current due to non-radiative recombination and degrades overall cell efficiency.
- Low growth temperature. This QW structure can be grown at low temperature (550-600 °C). The low growth temperature results in less thermal degradation effects on the tunnel junctions. On other hand, high performance AlGaAs solar cells were grown at temperatures approaching 700 °C, which may degrade the tunnel junction performance.

However, there are several challenges with the growth of this QW solar cell that needs to be addressed, as summarized in Figure 5.15. The first challenge is the related to thermionic emission and critical layer thickness constraints as shown in Figure 5.15(a). For the strain-balanced InGaAsP/InGaP QW structures presented in Chapter 4 and this Chapter, the thickness of the absorbing InGaAsP well is about 25% of the total QW region thickness. This indicates that if the total thickness of the QW i-region is 1 μm, only 250 nm will be absorbing the light. One strategy to address this issue is to increase the thickness of the absorbing InGaAsP well. But this InGaAsP thickness increase is limited by the critical layer thickness constraints as discussed in Section 4.4.2 and Section 2.4. Increasing the well thickness beyond the CLT has degraded the overall EQE response as shown in Figure 5.15(a) as discussed in Section 5.3.4 of this Chapter.

The second challenge that needs to be addressed is the background doping in the QW region which limits the increase of the number of QWs as shown in Figure 5.15(b). The limited number of

quantum wells hinders further increase in the EQE beyond the band-edge of $\text{In}_{0.49}\text{Ga}_{0.51}\text{P}$. If the QWs are grown in the undepleted region, a weak electric field will exist which will limit the carrier collection. This will result in a poor EQE response as shown in Figure 5.15(b).

Some of these challenges will be addressed in Chapters 6 and 7 by using lattice-matched InGaAsP/InGaP quantum well structures.

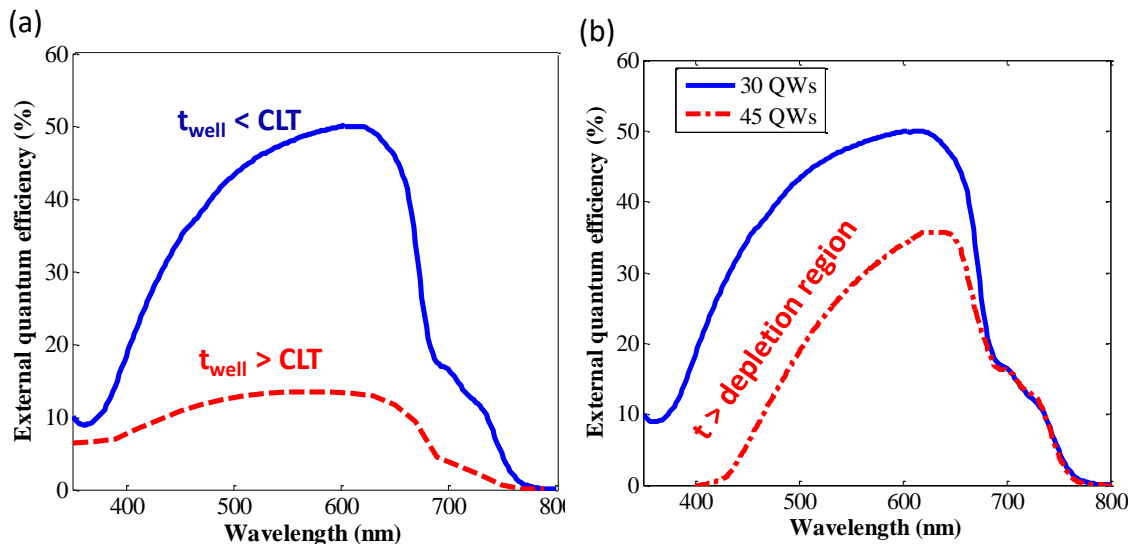


Figure 5.15: External quantum efficiency of strain-balanced InGaAsP/InGaP showing two challenges that are hindering further development: (a) critical layer thickness limitation, (b) background doping constraints and its impact on the depletion region width.

Chapter 6: Growth and Characterization of Lattice-matched InGaAsP/InGaP Quantum Wells

The use of InGaAsP/InGaP quantum well structures is a promising approach for subcells in next generation multi-junction devices due to their tunable bandgap (1.50-1.80 eV) and for being aluminum-free. Despite these potentials, the accumulation of stress during the growth of these structures and the high background doping in the quantum well region as discussed in Chapters 4-5 have limited the maximum number of quantum wells and barriers that can be included in the intrinsic region and the sub-bandgap external quantum efficiency to less than 30.0%. Some of these issues will be addressed in this chapter in order to increase the number of quantum wells that can be included and thus improve the sub-bandgap external quantum efficiency. In this chapter, we report on the use of *in-situ* curvature monitoring by multi-beam optical stress (MOS) sensor measurements during the growth of this quantum well structure to monitor the stress evolution in these thin films. A series of $\text{In}_{0.32}\text{Ga}_{0.68}\text{AsP}/\text{In}_{0.49}\text{Ga}_{0.51}\text{P}$ quantum wells with various arsine to phosphine ratios have been analyzed by *in-situ* curvature monitoring and X-ray diffraction (XRD) to obtain nearly strain-free lattice matched structures. Sharp interfaces, as indicated by the XRD fringes, have been achieved by using triethyl-gallium and trimethyl-gallium as gallium precursors in InGaAsP and InGaP, respectively, with constant flows of trimethyl-indium and phosphine through the entire quantum well structure. The effect of the substrate miscut on quantum well growth was compared and analyzed using XRD, photoluminescence and time resolved photoluminescence, highlighting nearly equivalent or similar performance on both miscuts. A 100-period quantum well device was successfully grown with minimal stress and approximately flat *in-situ* curvature.

This chapter is a paper published in Journal of Crystal Growth, 465, 171-177, 2017, with some modifications and additions. This research was performed by Islam Sayed at the National Renewable Energy Laboratory.

6.1. Introduction

In this chapter, we report on the growth of nominally lattice-matched InGaAsP/InGaP quantum wells by metal organic vapor phase epitaxy (MOVPE). This structure could potentially be used in any of the different multijunction solar cell approaches such as monolithic lattice-

matched, inverted-metamorphic, or wafer-bonded structures. The objective of creating this structure is to maximize the number of QWs that can be included in the depletion region for improved solar cell absorption beyond that of other strain-balanced structures that we presented in Chapters 4-5[126, 127]. In this work, both the barrier and well are nearly lattice matched to the substrate, providing great latitude in adjusting the thicknesses of each layer, because the strain-balanced condition is automatically achieved, and the restriction due to critical layer thickness is not of concern. This structure differs from previously reported strain-balanced or nearly lattice-matched InGaAsP/InGaP approaches where the barrier material occupies up to 75% of the *i*-layer thickness [42, 126, 128, 129][130]. The large relative thickness of the barriers compared with that of the wells in [8, 9], was required to satisfy the strain-balance condition. In addition, the use of tertiarybutyl-arsine (TBA) and tertiarybutyl-phosphine (TBP) as arsenic and phosphorus precursors in those experiments [126, 127] resulted in high carbon incorporation during the decomposition process which limits the depletion region thickness and accordingly the number of quantum wells that can be included. The latter two factors limit the sub-bandgap external quantum efficiency peak values to less than 25.0% [126, 127]. However, growing the QWs close to the lattice matching condition offers more design flexibility in choosing the wells and barriers thicknesses and accordingly the carrier transport mechanism. In addition, the use of arsine (AsH_3) and phosphine (PH_3) in this work rather than TBA and TBP results in lower carbon incorporation, which increases the number of quantum wells that can be included in the intrinsic region. These major enhancements hold the potential of achieving peak external quantum efficiency values of more than 50.0% beyond $\text{In}_{0.49}\text{Ga}_{0.51}\text{P}$ band-edge (680 nm).

Increasing the absorption beyond the band-edge of $\text{In}_{0.49}\text{Ga}_{0.51}\text{P}$ requires maximizing the number of quantum wells in the depletion region. However, the inclusion of a large number of quantum wells can result in high stress leading to partial or relaxation which will create non-radiative recombination centers. We report on the use of *in-situ curvature* monitoring by multi-beam optical stress (MOS) sensor to analyze the stress during the growth of these new QWs. X-ray diffraction (XRD) is also used to assess the interfaces quality and is correlated with the MOS results. A series of quantum wells with various arsine to phosphine ratios in InGaAsP were grown on lattice matched $\text{In}_{0.49}\text{Ga}_{0.51}\text{P}$ barriers to analyze the stress evolution in this structure. Sharp interfaces have been achieved by using triethyl-gallium (TEGa) and trimethyl-gallium (TMGa) as gallium precursors in the growth of InGaAsP and InGaP, respectively, while using fixed trimethylindium

(TMIn) and phosphine flows. The use of two gallium sources has the advantage of achieving sharp interfaces since there is no need to ramp up or down any of the group III flows to achieve the required different compositions. In previous experiments [126, 127], the indium flow was cycled up and down to grow the InGaAsP and InGaP layers, which may reduce the interface sharpness because of the relatively slow response of flow changes through the solid-source TMIn. In addition, TEGa pyrolysis occurs through β -hydride elimination which leaves hydrogen rather than carbon attached to the gallium atom [131, 132]. This reduces carbon incorporation, increasing the depletion layer thickness and allowing more QWs to be grown in the high electric field region [131-133]. The growth of quantum wells on substrates with 2° 111B and 6° 111A offcuts have been analyzed using XRD, time resolved photoluminescence (TRPL) and photoluminescence (PL). The effect of growth pauses on QWs is studied where a growth interruption of 3 seconds was found to improve the interface quality relative to a no-growth pause structure. The effect of strain accumulation during the growth of multiple QWs with thin- and thick- periods is studied using *in-situ* curvature monitoring.

6.2. Experimental Details

The InGaAsP/InGaP QWs were grown by MOVPE reactor operating at 620 torr at the National Renewable Energy Laboratory, in Golden, Colorado. The precursors used in this work are: TMGa, TEGa, TMIn, AsH₃, PH₃, diethylzinc, and hydrogen selenide (H₂Se/H₂). The quantum wells were grown at 600 °C on GaAs substrates mis-oriented by either 6° toward <111>A (6° A) direction or 2° toward $(\bar{1}11)$ B (2° B) direction. The V/III ratio and nominal growth rate of the In_{0.49}Ga_{0.51}P barrier are 885 and 1.66 μ m/hr, respectively. The ratio of indium to group III flows of InGaAsP is fixed at 0.6 and the nominal growth rate is about 2.6 μ m/hr. The arsine to phosphine ratio is varied in order to reduce the stress in these structures, as will be discussed in section 6.3.1.

The stress evolution during the growth of the quantum wells is monitored using MOS based on the curvature measurements [134-136]. Figure 6.1 shows the working principle of the MOS. The biaxial stress induced in the film will result in biaxial stress on the substrate and bending moment on the substrate [137]. If the film has a lattice constant less than the underlying substrate, the substrate will bend resulting in the convex shape of Figure 6.1(a). The spacing between the beams becomes smaller as shown in the Figure 6.1(a). If the film has a lattice constant larger than the underlying substrate, the substrate will bend resulting in the concave shape of Figure 6.1(b) and

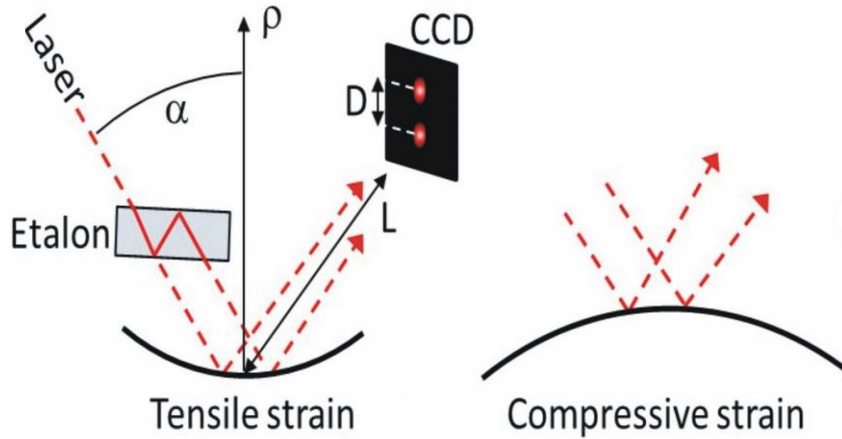


Figure 6.1: Illustration of the working principle of MOSS. A courtesy of Dieter Stender and Aline Fluri.

the spacing between the beams becomes larger as shown in the Figure 6.1(b). The reflected beams from the substrate surface were imaged by a charge-coupled device (CCD) camera and analyzed to determine the curvature change [136]. The relative position between the reflected beams are recorded, and the movement of the laser spots were measured during growth. The curvature is monitored above the MOVPE reactor during the growth using a k-space Associates MOS apparatus. A 622 nm laser beam split into an array of nine parallel beams is reflected from the sample through a quartz window. Two orthogonal directions, k_x and k_y , are measured due to the presence of two-dimensional array of beams. The curvature change during growth is related to the stress that develops from lattice mismatch through Stoney's formula for a thin film of thickness (h_f) and stress (s_f) grown on a substrate of thickness (h_s) and biaxial modulus (Y_s) of substrate as follows [134] [138]

$$k = -\frac{6h_f s_f}{h_s^2 Y_s} \quad (6.1)$$

In addition to *in-situ* MOS analysis, the (004) XRD scans of the QW structures were measured *ex-situ* on a Bede D1 diffractometer. The superlattices' satellite peaks of the MQW structures were analyzed to infer the total period thickness [139] and to compare the sharpness of the intensity of higher order satellite satellite peaks for QWs grown with various arsine to phosphine ratios. XRD

was also used to analyze the effects of QWs growth on different substrate miscuts and growth interruptions to establish the conditions producing sharp interfaces.

The optical emission of QW structures was measured by room temperature PL using a HeCd probe laser at 442 nm wavelength. The emitted light is directed into a Newport MS260i spectrometer with a 300/500 grating. A 495 nm long pass filter was used to filter out the laser line. The carrier lifetime was measured using two-photon excitation time resolved photoluminescence (2PE-TRPL) [140]. The excitation was at 1030 nm (Yb:KGW laser system), 0.2 ps pulse length, 1.1 MHz laser repetition rate, average excitation power 0.5 mW. PL was measured with Si avalanche photo diode (APD), 820 nm bandpass (10nm) filter, and time correlated single photon counting.

6.3. Results and Discussion

In this section, we present and analyze the MOS curvature and stress, PL and XRD results of $\text{In}_{0.32}\text{Ga}_{0.68}\text{AsP}/\text{In}_{0.49}\text{Ga}_{0.51}\text{P}$ QWs with various arsine to phosphine ratio and fixed group-III flows. We compare and discuss the effects of the quantum wells growth on 6°A and 2°B miscuts using XRD, TRPL and PL. The effects of growth interruptions between well/barrier and barrier/well interfaces on the sharpness of peaks for quantum wells is studied. Finally, the effects of strain accumulation during the growth of QWs with large number of periods is studied for structures with varying period thicknesses.

6.3.1. Effect of Arsenic to Phosphorus Ratio in InGaAsP on Stress and XRD Peaks Sharpness

The distribution coefficient of group V is temperature dependent and is not close to unity [24]. In other words, the compositions in the solid phase of arsenic and phosphorus do not change linearly with the partial pressure of these two compounds. This leads to difficulties in achieving the required compositions for the quaternary to obtain strain-free layers. The growth approach we followed to obtain nearly strain-free structures is to fix the ratio of trimethyl-indium flow to total group III flows in InGaAsP at 0.6 which approximately fixes the solid compositions of indium and gallium to about 32% and 68%, respectively. Then a series of $\text{In}_{0.32}\text{Ga}_{0.68}\text{As}_x\text{P}_{1-y}/\text{In}_{0.49}\text{Ga}_{0.51}\text{P}$ QWs with various arsine ($[\text{AsH}_3]$) to phosphine ($[\text{PH}_3]$) flow ratios are grown and analyzed as shown in Figures 6.2-6.5. In this study, only the As flow to group V ratio is altered: $x = 0.15$ (MP096), $x = 0.19$ (MP091), $x = 0.22$ (MP092), $x = 0.27$ (MP101), and $x = 0.35$ (MP108), where $x = [\text{AsH}_3]/([\text{AsH}_3]+[\text{PH}_3])$. The change in the ratio of indium to gallium incorporated in the solid was assumed

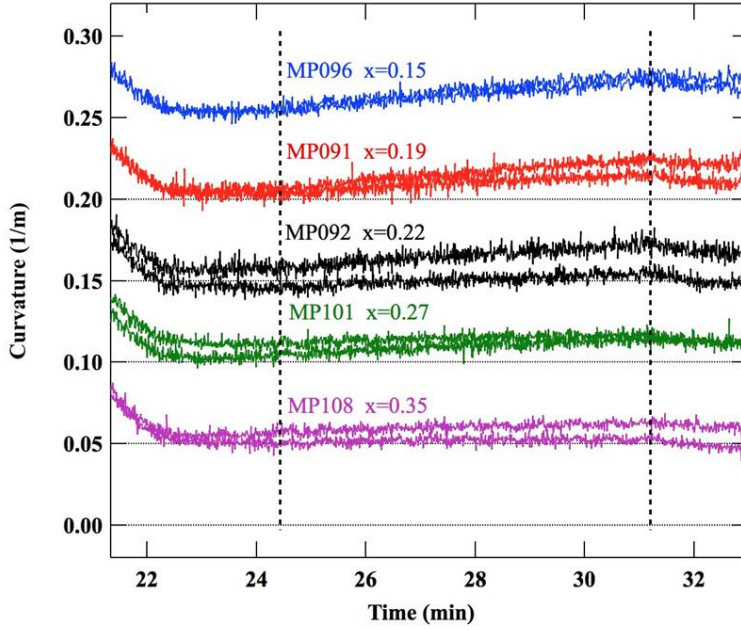


Figure 6.2: *in-situ* curvature monitoring of a series of $\text{In}_{0.32}\text{Ga}_{0.68}\text{AsP}/\text{In}_{0.49}\text{Ga}_{0.51}\text{P}$ quantum wells with fixed group III flows and various arsenic to phosphorus ratio, $x = [\text{AsH}_3]/([\text{AsH}_3] + [\text{PH}_3])$. The data of each sample is shifted by 0.5 m^{-1} along the vertical axis for visual clarity. The vertical dotted lines indicate the start and the end of QWs growth. The QWs in this study were grown on 6°A substrates.

to be negligible with the change in the $[\text{AsH}_3]/[\text{PH}_3]$ flows. In this study, the QWs are grown on 6°A miscut with a 3 second growth pause between well/barrier and barrier/well interfaces. The number of the period was fixed at 10, and the thickness of $\text{In}_{0.32}\text{Ga}_{0.68}\text{AsP}$ wells and $\text{In}_{0.49}\text{Ga}_{0.51}\text{P}$ barriers are 90\AA and 85\AA , respectively.

Figure 6.2 depicts the *in-situ* MOS curvature measurements during the growth of these quantum wells, as measured using the procedure of Section 6.2. The vertical dotted lines indicate the start and the end of QWs growth and the curvature measurements in Figure 6.2 are shifted by 0.5 m^{-1} along the vertical axis for visual clarity. It is worth pointing out that a positive (negative) slope of the curvature signal arises from the tensile (compressive) stress in these QWs, indicating growth of layers of effective lattice constants smaller (larger) than the GaAs substrate [134]. The curvature, k , of MP096 ($x = 0.15$) is rising up with an average slope, $\frac{dk}{dt}$, equal to $+4.4 \times 10^{-5} \text{ m}^{-1}\text{s}^{-1}$

¹, indicating that the quantum wells are grown mismatched with effective lattice constant less than the GaAs substrate. By increasing the arsenic to phosphorus ratio, the curvature slope is reduced to be 3.46×10^{-5} , 2.5×10^{-5} , 1.44×10^{-5} , and $0.8 \times 10^{-5} \text{ m}^{-1}\text{s}^{-1}$, for MP091, MP092, MP101, and MP108, respectively. MP108 exhibits a nearly flat curvature indicating that the quantum wells are grown with effective lattice constant close to the underlying layers. The total stress (s_t) was then calculated across the QW region, as the slope of the stress-thickness versus thickness data (Figure 6.3) assuming known growth rates and elastic properties of each layer [134]:

$$s_t = \frac{d(s_f h_f)}{dh_f} \quad (6.2)$$

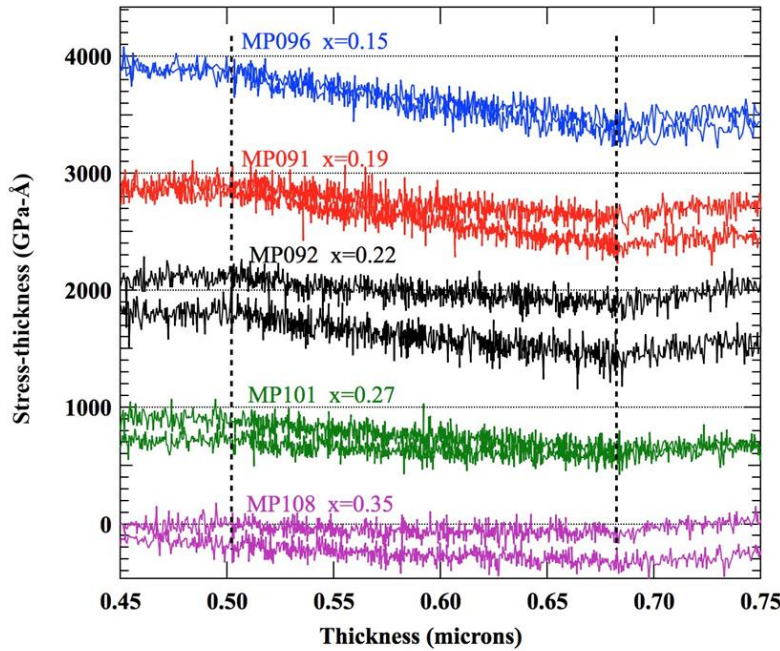


Figure 6.3: Stress-times-thickness of a series of $\text{In}_{0.32}\text{Ga}_{0.68}\text{As}_y\text{P}_{1-y}/\text{In}_{0.49}\text{Ga}_{0.51}\text{P}$ quantum wells as a function of thickness. The vertical dotted lines indicate the start and the end of QWs growth and the data of each sample is shifted by 1000 GPa*Å along the vertical axis for visual clarity. The QWs in this study were grown on 6°Å substrates.

The stress across the QW region of MP096A, MP091A, MP092A, MP101A, and MP108A are 0.25, 0.21, 0.15, 0.08, and 0.04 GPa, respectively. The stress was reduced from 0.25 GPa for sample MP096 to 0.04 GPa for sample MP108 by increasing the arsenic to group V ratio from 0.15 to 0.35. Based on previous experiences in growing compositionally graded buffers [35, 134], a stress in the range of -0.1 to 0.1 GPa should be reasonably good indicator of avoiding nucleation

of dislocations in relatively thick layers, and the stress of samples MP108 and MP101 lies within the acceptable margin.

The diffraction pattern of the grown QWs consists of the (004) GaAs peak and several other satellite peaks due to the periodicity of the quantum wells, as shown in Figure 6.4. The satellite peaks are shifted towards the compressive side of the GaAs substrate peak by increasing the arsenic to phosphorus ratio due to reduction in the tensile stress, consistent with the MOS stress results. In addition, the intensity and full width half maximum (FWHM) of satellite peaks are improved by reducing the stress in these quantum wells, consistent with the trend of the MOS analysis observed in Figure 6.2 and Figure 6.3. Specifically, the XRD of MP096 shows only peaks on the tensile side of the GaAs substrate due to the severe tensile stress in this structure as indicated by the MOS results of Figure 6.2 and Figure 6.3. The intensity and FWHM of satellite peaks of MP108 is higher and narrower than MP096, respectively, indicating sharper interfaces and minimal stress relaxation. It should be mentioned that the $n = 0$ superlattice peak differs from the GaAs peak. The *in-situ* curvature monitoring indicates that MP108 is under slight tensile stress (+0.04 GPa). The fact that the $n = 0$ peak appears instead on the compressive side of the (004) scan, suggests that the structure could be internally strain balanced rather than lattice matched. This would be due to possible differences in the elastic properties of the two alloys[63]. This study thus highlights the complication of interpreting the XRD results for strain-balancing and the superiority of *in-situ* curvature analysis in realizing a nearly strain-free structure.

The QWs are also investigated optically using PL as shown in Figure 6.5. As expected, the effective bandgap reduces from 1.68 eV to 1.51 eV by increasing the arsenic to group V ratio. The PL FWHM is \sim 50 meV for most of the samples in this study. The QWs grown on 2°B substrates exhibit a similar behavior to that on 6°A as will be shown in the next subsection.

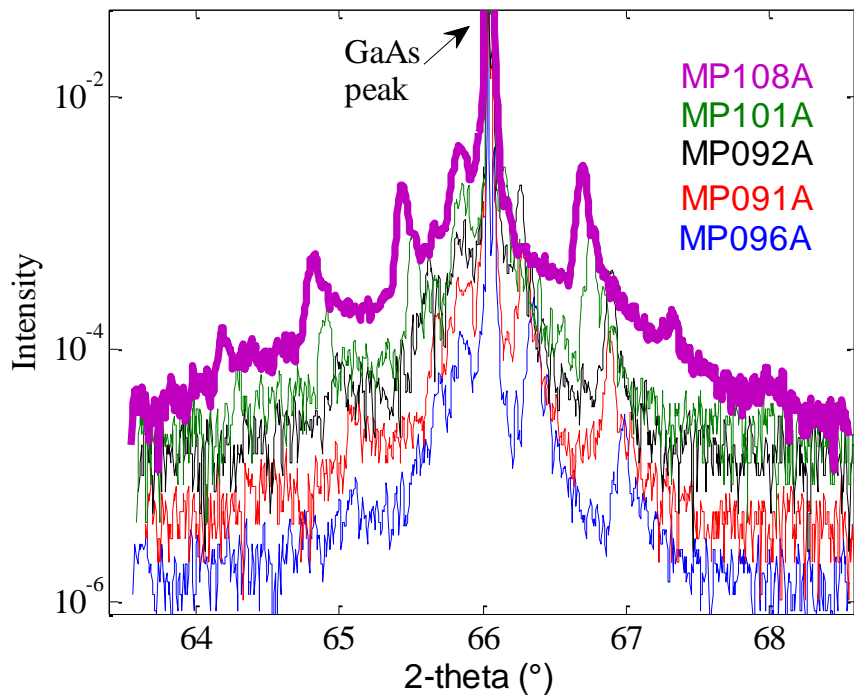


Figure 6.4: (004) XRD scans of a series of $\text{In}_{0.32}\text{Ga}_{0.68}\text{As}_y\text{P}_{1-y}/\text{In}_{0.49}\text{Ga}_{0.51}\text{P}$ quantum wells with fixed group III flows and various arsenic to phosphorus ratio. The QWs in this study were grown on 6°A substrates.

6.3.2. Effect of Substrate Miscut

Future photovoltaic devices with a prospective efficiency of higher than 50.0% will have five or more junctions [141][142]. The highest energy subcell in these devices will be AlInGaP with bandgap of 2.0-2.10 eV [141, 143, 144]. High performance AlInGaP solar cells have been reported recently on GaAs substrates that were miscut by 6° towards $<111>$ A direction [143]. The growth on 6°A miscuts substrate results in less oxygen incorporation [145] and more disordered AlInGaP than on 6°B and 2°B substrates, thus achieving the desired 2.0-2.10 eV bandgap with a lower aluminum composition [143]. Therefore, the growth conditions of the QWs were optimized for growth on 6°A substrates. However, several authors have reported that substrates with high misorientation result in step bunching and thickness modulation for GaAs-based quantum wells [146, 147]. Specifically, Sodabanlu et al. have reported on severe degradation in the carrier lifetime and

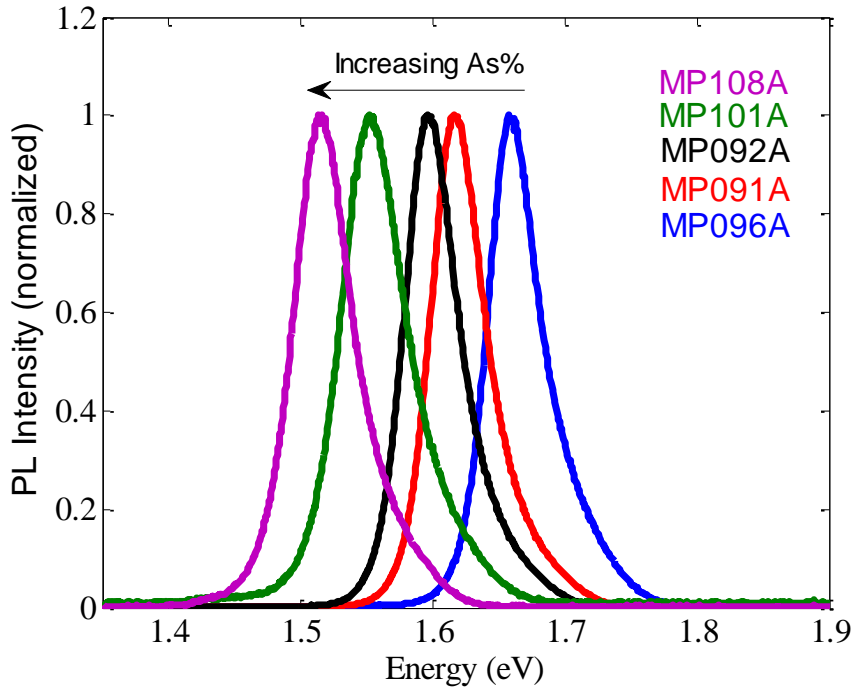


Figure 6.5: Photoluminescence spectra of a series of $\text{In}_{0.32}\text{Ga}_{0.68}\text{As}_y\text{P}_{1-y}/\text{In}_{0.49}\text{Ga}_{0.51}\text{P}$ quantum wells with fixed group III flows and various arsenic to phosphorus ratio. The QWs in this study were grown on 6°A substrates.

XRD superlattice peaks intensity of InGaAs/GaAsP QWs when grown at temperatures close to 600°C on 6°B miscuts [147]. That degradation has been attributed to fast surface migration across the step edges leading to step bunching [147]. Even though InGaAsP/InGaP QWs is a different material system, it is important to compare and analyze the effect of substrate miscut on the growth of these new quantum wells, since it is not well studied. The QWs are grown on 6°A and 2°B substrates placed side by side inside the growth chamber to avoid run-to-run variation. A comparison between the XRD, PL emission and TRPL for different miscuts is shown in Figure 6.6.

From Figure 6.6(a), the intensity and FWHM of the QWs XRD satellite peaks on both the 6°A and 2°B are comparable, which indicates sharp interfaces for the QWs growth on the two different miscuts. In this study, the nominal period thickness was 175 \AA , and the analysis of the superlattices' satellite peaks indicates that the period thickness of the QWs on the 6°A substrate and 2°B substrate are 168 \AA and 164 \AA , respectively. The well and barrier thickness were inferred from the total period thickness and growth times. The 6°A QW structure has a well and barrier

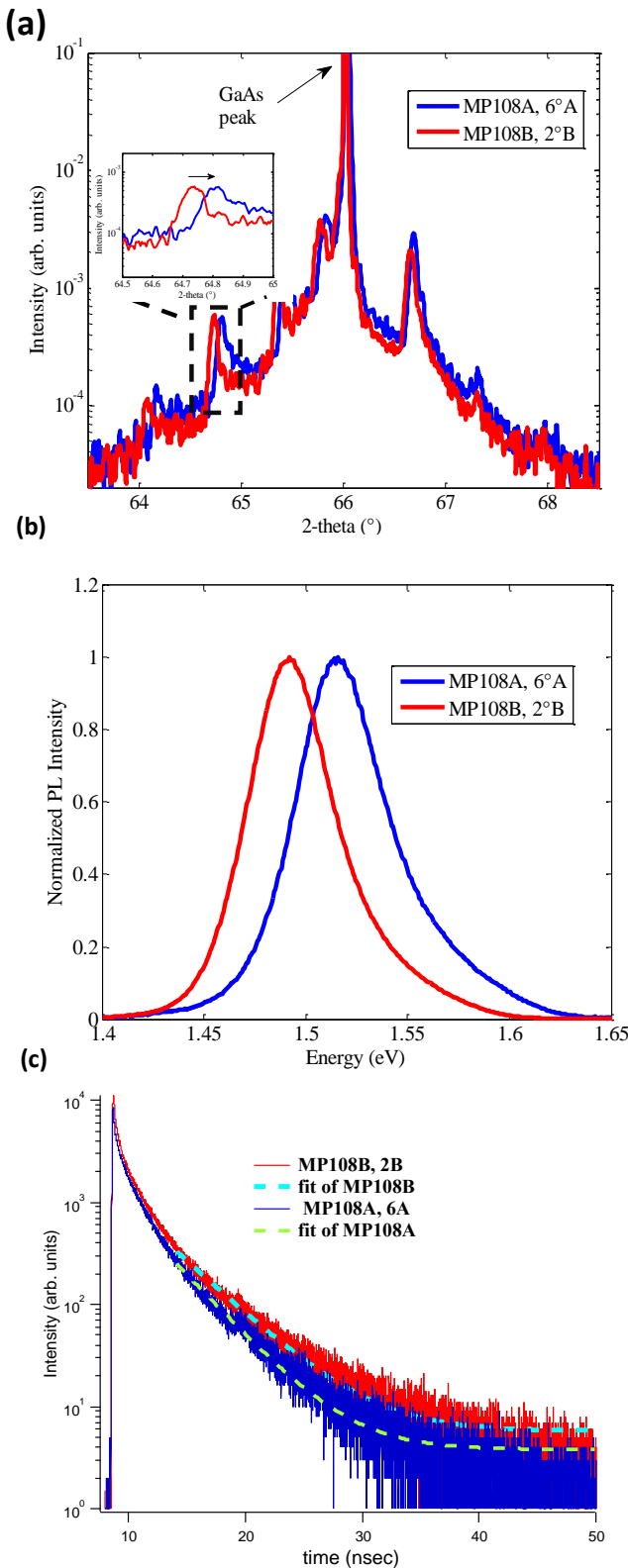


Figure 6.6: Effects of quantum wells growth on 6 $^{\circ}$ A and 2 $^{\circ}$ B substrates: (a) (004) XRD scans, (b) PL emission, and (c) 2PE- TRPL decays.

thickness of 78 and 90 Å, respectively. The 2°B structure has a well and barrier thickness of 74 and 90 Å, respectively. XRD shift of 540 arcsec toward the compressive side of GaAs substrate for QWs grown on 2°B relative to 6°A has been observed for all the superlattice peaks as shown in the inset of Figure 6.6 (a). The 2°B behavior is attributed to an expected change in the arsenic/phosphorus ratio for growth on different miscuts [148]. A slight increase in the indium to gallium ratio is also possible for the growth on low-mis cut substrates.

The 6°A substrate yields a higher peak emission bandgap of about 20 meV higher than the 2°B substrates as shown in Figure 6.6(b). This can be attributed to two reasons. First, the change in alloy composition in the InGaAsP and InGaP as noticed by the XRD shift of 6°A sample shown in Figure 6.6(a) should lead to higher effective bandgap relative to the 2°B one. Second, the use of 6°A substrates reduces the CuPt ordering on the group-III sublattice of InGaP and should slightly increase the bandgap [24, 149]. Since both the wells and barriers are based on InGaP, it is possible that the peaks shifts observed in Figure 6.6(b), are *partially* associated with the disordering effects. It should be mentioned that the measured energy shift is not associated with differences in quantum confinements because the QW structure grown on 6°A has a slightly thicker well, and a reduction in the PL energy would have been expected if quantum size effects were dominating the emission.

The carrier lifetimes in these two samples were measured using 2PE-TRPL as shown in Figure 6.6(c). The quantum wells are grown in double heterostructures with 0.1 μm In_{0.49}Ga_{0.51}P cladding layers in order to reduce the surface recombination effects. The excitation TRPL decay in Figure 6.6(c) can be fit with carrier lifetimes of 3.6 ns and 4.0 ns for the 6°A and 2°B sample, respectively. If compared to lifetimes reported in the literature for InGaAs/GaAsP QWs [150, 151], the measured carrier lifetimes for both the 6°A and 2°B samples are reasonably good indicator of radiative recombination dominance in these structures. It should be mentioned that the carrier lifetimes of the QWs grown on higher miscuts at 600 °C were comparable and no degradation has been observed as shown by other researchers in the GaAs-based QWs [146, 147].

6.3.3. Effect of Growth Interruptions

We have studied the effect of using a growth pause on the quantum wells, as shown in Figure 6.7. The growth pause is conducted by flowing 99 sccm of PH₃ between InGaAsP/InGaP and InGaP/InGaAsP interfaces. In this study, only the growth pause time is varied: zero seconds

(MP146), 3 seconds (MP108), and 5 seconds (MP147). By including an intentional growth pause of 3 seconds for MP108, improvements in the XRD satellite peaks intensity and full width half maximum have been observed compared to continuously grown QWs (MP146), as shown in Figure 6.7. A growth pause typically results in surface stabilization and smoothening of growth surface due to rearrangement of terrace geometries [74]. We think that the improvements in the interface abruptness are due to suppressing indium surface segregation and/or arsenic carryover from InGaAsP to InGaP. This study suggests the importance of a growth pause for these structures and highlights the importance of interface management to improve the growth quality of quantum well structures. It is noted that increasing the growth pause to 5 seconds in sample MP147 has not shown any noticed improvements in the interfaces relative to MP108.

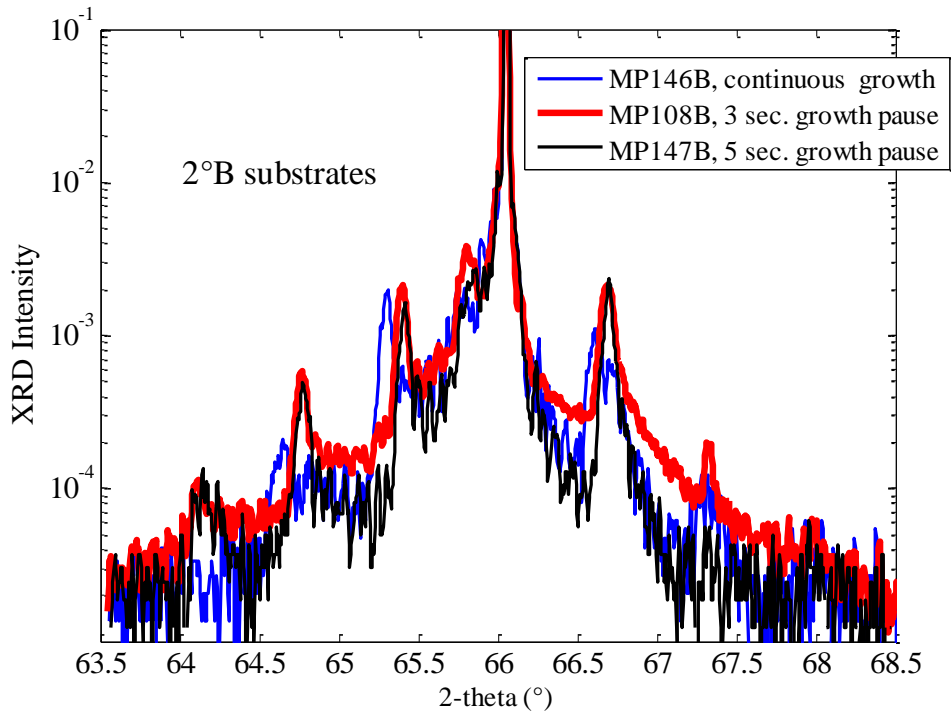


Figure 6.7: Effect of growth interruptions on quantum wells

6.3.4. Growth of 100-period QW with minimal stress relaxation

Designing high efficiency QW devices requires increasing the number of periods in the depletion region in order to improve the solar cell absorption beyond the band-edge of $\text{In}_{0.49}\text{Ga}_{0.51}\text{P}$ (~ 1.85 eV). However, increasing the number of interfaces may degrade the crystal quality due to expected accumulated stress during the growth of these structures. We studied the effect of increasing the number of periods on the accumulation of stress in four cells with two different period thicknesses. The thick-period devices, MP159 (20 QWs) and MP161 (40 QWs), have nominal well thickness (t_w) of 70 Å and a barrier thickness (t_b) of 32 Å. The thin-period devices, MP189 (40 QWs) and MP197 (100 QWs), have a t_w of 55 Å and a t_b of 25 Å. The *in-situ* curvature monitoring is measured during the growth of these QWs, and the stress-times-thickness versus the QW thickness is depicted in Figure 6.8. The stress across the QW region, calculated from the fit slope using Eqn. (6.2), of MP159, MP161, MP189, and MP197 are 0.084, 0.11, 0.047, and 0.087 GPa respectively.

We first note that the thick-period devices (MP159 and MP161) exhibit a stress higher than the thin-period devices (MP189 and MP197). Specifically, the two 40 period QW devices (MP161 and MP189) differ in the accumulated stress even though the two structures have been grown with the same solid compositions in wells and barriers. The stress of MP161 is outside the acceptable margin and may result in generation of detrimental dislocations. On the contrary, growing the quantum wells with thinner periods as shown for samples MP189 and MP197 have resulted in less stress and flat curvature than MP159 and MP161. Since the quantum wells are grown nearly lattice matched, the only layer that may result in building strain during the growth of these films is the InGaAsP. Growing thinner layers of InGaAsP followed by lattice matched $\text{In}_{0.49}\text{Ga}_{0.51}\text{P}$ reduces the accumulating stress. The calculated average stress from the *in-situ* curvature of the 100-period thin-device (MP197) shown in Figure 6.8, is 0.087 GPa, resulting in minimal strain relaxation.

There are a few implications that using thinner structures may have on the performance of solar cell devices. The reduction in the stress should result in a lower non-radiative recombination rate, which accordingly affect the solar cell efficiency. In addition, the effective bandgap on the thinner-wells device will be a few milli-volts higher than that with thicker-wells due to quantum size effects. Thus, tuning the effective bandgap of the QWs to the desired bandgap involves adjusting the indium to gallium and arsenic to phosphorous ratios in addition to the well thickness. Changing the various layer thicknesses may affect the carrier collection in the QW region because this

directly dictates whether carrier tunneling across the barriers, thermally-assisted tunneling, or thermionic emission dominate the minority carrier transport mechanism in the QW region. Future work will focus on growth and fabrication of InGaAsP/InGaP QW solar cells devices and optimization of growth conditions to use this cell in next generation PV devices.

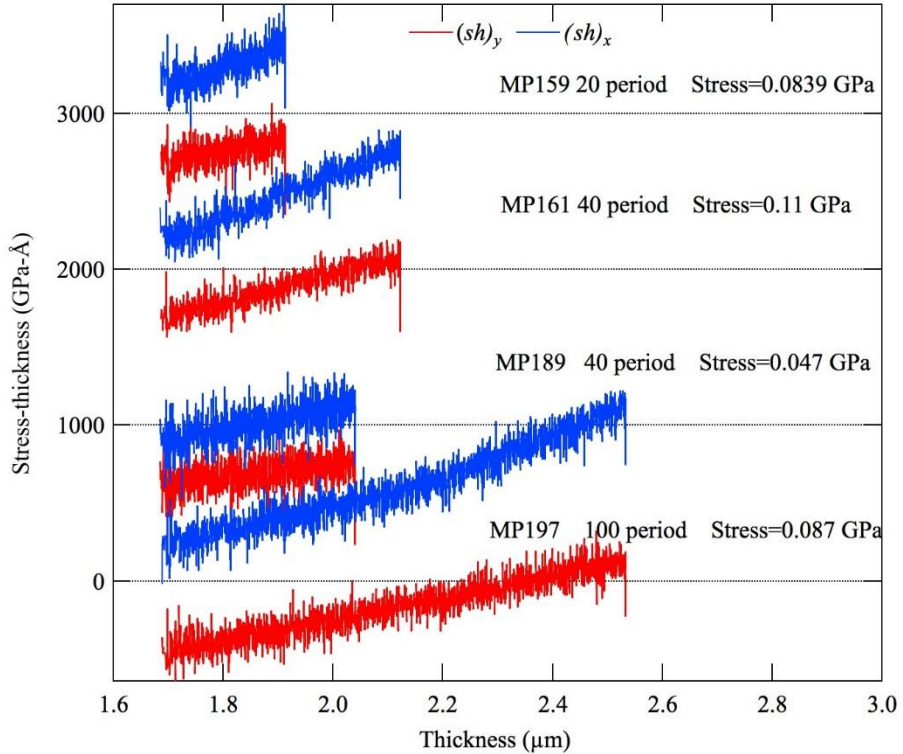


Figure 6.8: Stress-thickness versus thickness as a function of thickness, of a series of InGaAsP/InGaP QWs with 20 periods (MP159), 40 periods (MP161 and MP189), and 100 periods (MP197). The stress is calculated using Eqn. (6.2) for each structure from the fit slope. The curvature of each sample is shifted along the vertical axis for visual clarity and the vertical dotted lines indicate the start and the end of the growth of these QWs. The QWs in this study were grown on 2°B substrates

Chapter 7: Lattice-matched InGaAsP/ InGaP Quantum Well Solar Cells

InGaAsP/InGaP quantum well (QW) structures are promising materials for next generation photovoltaic devices because of their tunable bandgap (1.50-1.80 eV) and being aluminum-free. However, the strain-balance limitations have previously limited light absorption in the QW region and constrained the external quantum efficiency (EQE) values beyond the $\text{In}_{0.49}\text{Ga}_{0.51}\text{P}$ band-edge to less than 25% as discussed in Chapters 4-5. In this chapter, we show that implementing a hundred-period lattice matched InGaAsP/InGaP superlattice solar cell with more than 65% absorbing InGaAsP well, resulted in more than 2x improvement in EQE values than the previously reported strain balanced approaches in Chapter 5. In addition, processing the devices with a rear optical reflector resulted in strong Fabry-Perot resonance oscillations and the EQE values were highly improved in the vicinity of these peaks, resulting in short circuit current improvement of 10% relative to devices with rear optical filter. These enhancements have resulted in an InGaAsP/InGaP superlattice solar cell with improved peak sub-bandgap EQE values exceeding 75% at 700 nm, improvement in the short circuit current of 26% relative to standard InGaP devices, and enhanced bandgap-voltage offset (W_{oc}) of 0.4 V.

This chapter is a paper published in Applied Physics Letters, 111 (8), 082107, 2017, Editors' Pick [152]. This research was performed by Islam Sayed at the National Renewable Energy Laboratory.

7.1. Introduction

The inclusion of strain-balanced InGaAsP/InGaP quantum well (QW) in the intrinsic (i) region of InGaP n-i-p structures, can tune the effective bandgap (E_g) of $\text{In}_{0.49}\text{Ga}_{0.51}\text{P}$ -based cells into a wide range (1.5-1.8 eV), while maintaining the lattice-matched condition to GaAs substrates [126, 127]. However, strain-balanced InGaAsP/InGaP QW solar cell suffer from inefficient light absorption, resulting in external quantum efficiency (EQE) values beyond the band-edge of $\text{In}_{0.49}\text{Ga}_{0.51}\text{P}$ (hereafter, sub-bandgap EQE) less than 25% and bandgap-voltage offset ($W_{oc} = V_{oc} - E_g$) values higher than 520 mV[126, 127], where V_{oc} is the open circuit voltage. The reported insufficient light absorption in these initial devices is attributed to a few reasons. First, strain-balance limitations have limited the total thickness of the absorbing InGaAsP wells to about 18-

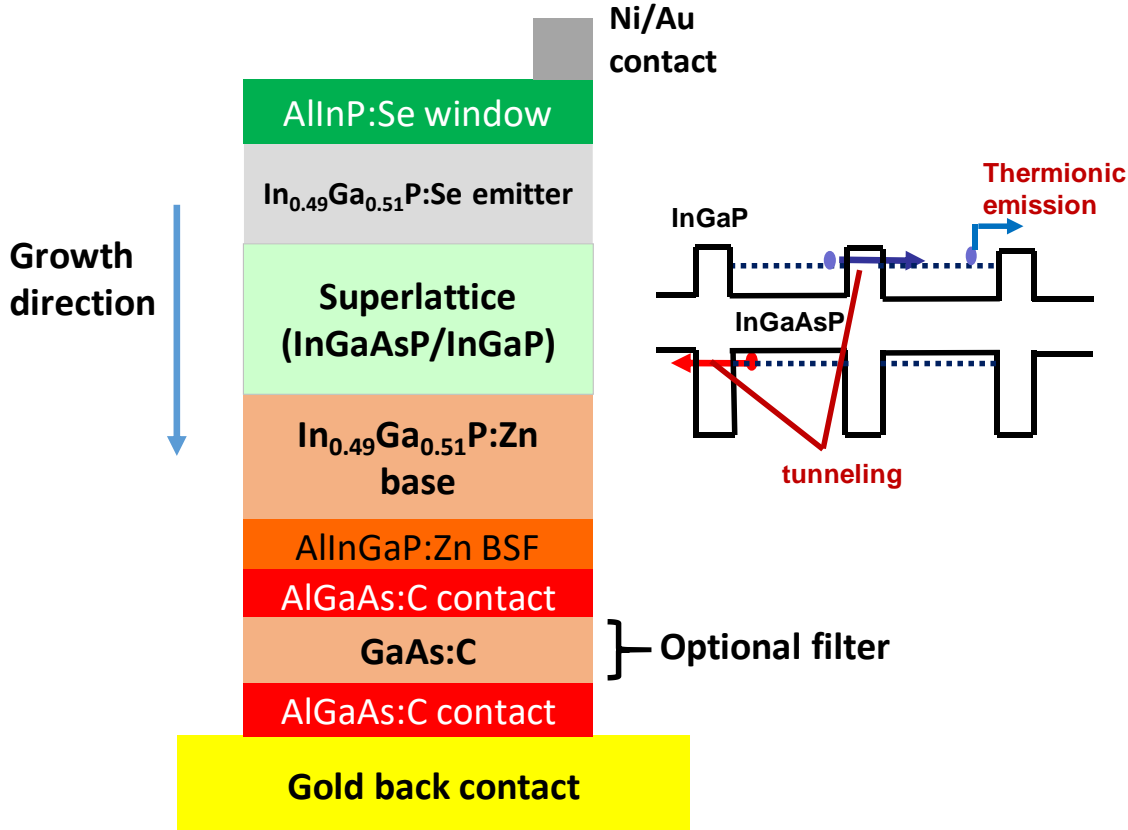


Figure 7.1: (left) Schematic of lattice matched InGaAsP/InGaP superlattice structure, grown in the unintentionally doped *i* layer in In_{0.49}Ga_{0.51}P n-i-p solar cell structure. Samples were grown with an optional 1.2 μm GaAs filter, and two samples of each device structure were processed separately, with and without etching the GaAs filter. (right) schematic of the energy band diagram, illustrating tunneling and thermionic-emission carrier transports in this structure.

25% of the total period thickness [126, 127, 153]. Second, any increase in the well thickness to enhance light absorption will also increase the barrier heights for electrons and holes, and will result in a poor carrier transport [129]. Finally, the number of QWs is limited to 30 periods due to high carbon background doping of $4 \times 10^{15} \text{ cm}^{-3}$ which corresponds to $\sim 0.7 \mu\text{m}$ depletion region thickness [126-128].

In this work, light absorption in InGaAsP/InGaP QWs is improved through several strategies. First, the QWs were grown lattice-matched rather than strain-balanced to increase the thickness of the absorbing InGaAsP well relative to that of the barrier. Improvements in both light absorption and carrier collection were achieved by growing a larger percentage of the depletion region occupied by the InGaAsP wells and allowing carrier tunneling through InGaP barriers. Second, the growth of lattice-matched QWs results in less accumulated stress if compared with the strain-balanced

structures and has allowed the growth of 100-period QW device with minimal stress relaxation. Third, light absorption in InGaAsP/InGaP QWs was further improved by etching off the GaAs substrate during processing and depositing a planar back surface reflector (BSR) to double the optical path length [154]. Finally, the use of arsine, phosphine, and triethylgallium precursors resulted in carbon background doping of $\sim 2 \times 10^{15} \text{ cm}^{-3}$ [155], which is about half the corresponding value in the initial devices [126] that used tertiarybutyl-arsine, tertiarybutylphosphine, and trimethylgallium. Reducing the background doping, increased the depletion region to $\sim 1 \mu\text{m}$, and allowed the inclusion of 100 depleted QWs ($\sim 0.8 \mu\text{m}$). These changes led to greatly enhanced sub-bandgap peak EQE values above 75% at 700 nm, reduction in the W_{oc} to $\sim 0.4 \text{ V}$ and a boost in the short circuit current (J_{sc}) to 20.5 mA/cm^2 which is about 4 mA/cm^2 higher than a standard InGaP device without the QWs.

7.2. Experimental Details

Samples were grown on (100) GaAs substrates mis-oriented by 2° towards B direction, by metal organic vapor phase epitaxy. A schematic of the InGaAsP/InGaP QWs grown in the *i* layer of $\text{In}_{0.49}\text{Ga}_{0.51}\text{P}$ n-i-p solar cell structure and band-diagram, is shown in Figure 7.1. The devices were grown with 20 nm $\text{Al}_{0.52}\text{In}_{0.48}\text{P:Se}$ window, 90 nm $\text{In}_{0.49}\text{Ga}_{0.51}\text{P:Se}$ emitter, 500 nm $\text{In}_{0.49}\text{Ga}_{0.51}\text{P:Zn}$ base, and AlInGaP:Zn back surface field. The QWs were grown lattice-matched at 600°C , and consisted of alternating layers of $\text{In}_{0.32}\text{Ga}_{0.68}\text{As}_{60}\text{P}_{40}$ well ($E_g = 1.5 \text{ eV}$) and $\text{In}_{0.49}\text{Ga}_{0.51}\text{P}$ barrier ($E_g = 1.85 \text{ eV}$) of thicknesses, $t_w = 55\text{-}70\text{\AA}$ and $t_b = 25\text{-}32\text{\AA}$, respectively. The devices were grown inverted to allow etching of the GaAs substrate and deposition of a planar gold BSR. Samples were grown with an optional $1.2 \mu\text{m}$ GaAs filter [Figure 7.1] between the GaAs absorber and BSR (hereafter, back-filter). Two samples of each device structure were processed separately, with and without etching away the back filter. The back filter absorbs photons in the $1.4\text{-}1.85 \text{ eV}$ energy range that were not absorbed in the QWs in their first pass, thus simulating the optical environment of the QW cell in a multi-junction. A ZnS (45 nm)/ MgF_2 (96 nm) antireflection coating (ARC) was deposited on the AlInP window after processing.

7.3. Results and Discussion

Figure 7.2 shows the EQE of a lattice-matched InGaAsP/InGaP superlattice with different number of periods, at wavelengths beyond the band-edge of $\text{In}_{0.49}\text{Ga}_{0.51}\text{P}$. Three samples were

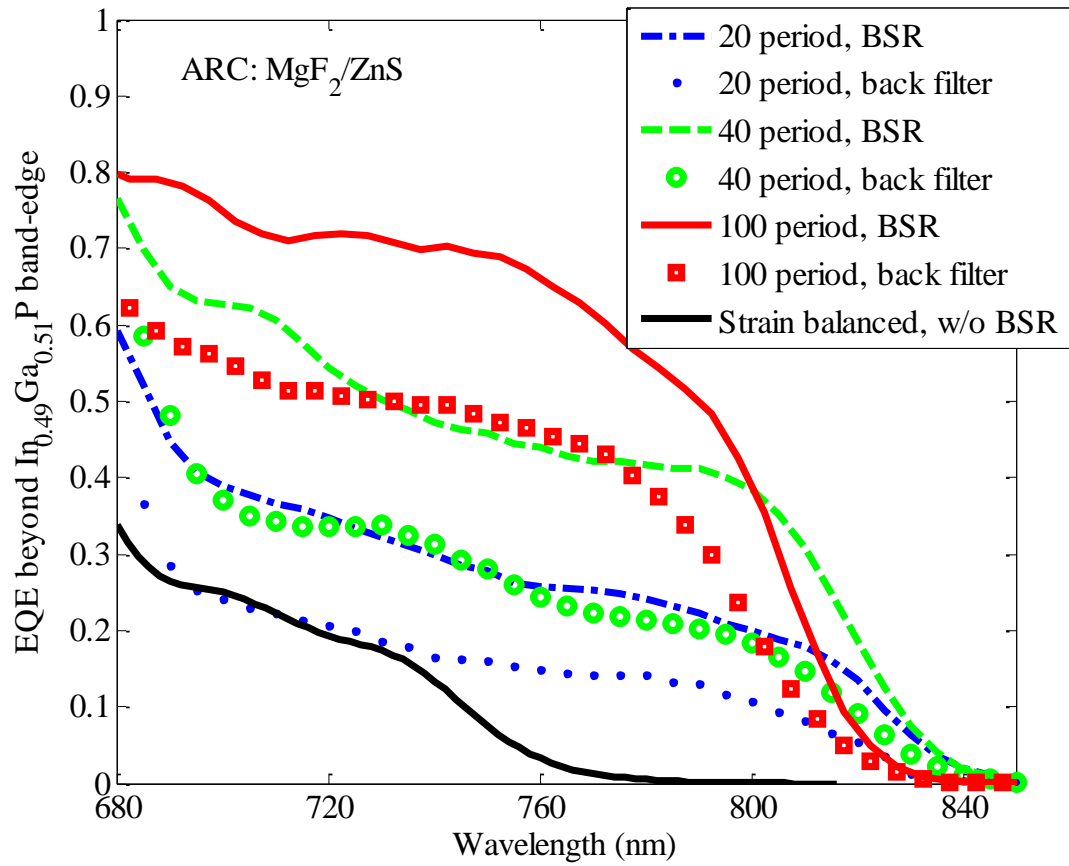


Figure 7.2: External quantum efficiency (EQE) beyond the band-edge of $\text{In}_{0.49}\text{Ga}_{0.51}\text{P}$ (680 nm) versus wavelength, of InGaAsP/InGaP superlattice solar cell with different number of period. All samples are coated with ZnS/MgF_2 . EQE showing improvements over strain balanced InGaAsP/InGaP QW approach.

studied: MP159 ($t_w = 70 \text{ \AA}$, $t_b = 32 \text{ \AA}$, 20-period), MP161 ($t_w = 70 \text{ \AA}$, $t_b = 32 \text{ \AA}$, 40-period), and MP197 ($t_w = 55 \text{ \AA}$, $t_b = 25 \text{ \AA}$, 100-period). The slight difference in the period thickness of MP197 was because we found a reduction in the accumulated stress when thinner periods were grown [155]. The total thickness of InGaAsP wells of MP159, MP161, MP197 are 140, 280, 550 nm, respectively, which are about 70% of the total QW region thickness. As shown in Figure 7.2, the growth of lattice-matched InGaAsP/InGaP with a larger percentage of the depletion region occupied by InGaAsP, greatly improved the EQE across all wavelengths beyond 680 nm. From the EQE measurements, the one-sun AM1.5 short circuit current contribution of the QWs, ΔJ_{sc} , is shown in Table 7.1. The ΔJ_{sc} was improved by increasing the number of periods. The 100-period device, with back-filter, exhibits a significantly high absorption in the QW region as shown in

Figure 7.2, resulting in a ΔJ_{sc} value of 4.37 mA/cm^2 , which contributes to about 23% to the total J_{sc} of the device (18.54 mA/cm^2).

Processing of devices with BSR has improved ΔJ_{sc} as shown in Figure 7.2 and Table 7.1. A perfect planar BSR results in an optical path length that is double the physical thickness of the QWs. From Table 7.1, ΔJ_{sc} of the 20-period/BSR sample is 2.82 mA/cm^2 , which is close to that of the 40-period/back-filter sample (3.08 mA/cm^2). The BSR results in 1.65x, 1.5x, and 1.3x increases in the ΔJ_{sc} values of MP159, MP161, and MP197, respectively. The BSR effect is more significant on MP159 because it is optically-thin (200 nm) and is weakly absorbing the long wavelength photons. The EQE values of the 100-period device (MP197), with BSR, are higher than 70% in the 680-720 nm wavelength range, resulting in a ΔJ_{sc} value of 5.38 mA/cm^2 , which contributes to about 26% to the total J_{sc} of the device (20.54 mA/cm^2). The EQE can be further enhanced by increasing the percentage of absorbing InGaAsP well from 70% to 80-85%, increasing the number of QWs in the depletion region through reducing the carbon background doping to $\sim 10^{14} \text{ cm}^{-3}$ [132, 156], and optimizing the carrier transport.

Table 7.1: One-sun AM1.5 short circuit current contribution of the QWs (ΔJ_{sc}), effective junction bandgap (E_g), open circuit voltage (V_{oc}), and bandgap-voltage offset (W_{oc}) for the studied samples.

Sample #	Description	ΔJ_{sc} (mA/cm^2) with ARC	E_g (eV)	V_{oc} (V)	W_{oc} (V)
MP159 20-period	Back filter	1.70	1.568	1.176	0.392
	BSR	2.82	1.548	1.173	0.375
MP161 40-period	Back filter	3.08	1.536	1.139	0.397
	BSR	4.67	1.526	1.151	0.375
MP197 100-period	Back filter	4.37	1.543	1.126	0.417
	BSR	5.83	1.528	1.136	0.392

Figure 7.2 shows also a comparison between this QW design and previously reported strain-balanced approaches ($\text{In}_{0.70}\text{Ga}_{0.30}\text{As}_{0.10}\text{P}_{0.90}/\text{In}_{0.40}\text{Ga}_{0.60}\text{P}$, $t_w = 55 \text{ \AA}$, $t_b = 150 \text{ \AA}$, 30-period) [127].

The EQE values of lattice-matched 20-period device (MP159), with back filter, are close to those of the strain-balanced structure because the total thickness of the absorbing InGaAsP wells in the two structures is close (\sim 140 nm). However, the total thickness of the QW region in MP159 is 200 nm, which is less than one-third the thickness of the strain-balanced structure (615 nm). Therefore, this indicates that growing the QWs lattice-matched with thicker wells, has allowed thinner structures to achieve the same EQE values as that of the strain-balanced design.

Figure 7.3 depicts the EQE of MP159 and MP197 processed with BSR and back filter, with and without ARC, across the entire wavelengths. The photoluminescence (PL) spectra of these QW structures is also shown in Figure 7.3. The inclusion of BSR slightly improves the EQE at wavelengths around 630-680 nm due to enhancing absorption in the $In_{0.49}Ga_{0.51}P$ base because it was grown optically thin (0.5 μm) and is weakly absorbing close to the band-edge. At wavelengths longer than $In_{0.49}Ga_{0.51}P$ band-edge (680 nm), light absorption occurs only in the InGaAsP well. Peaks in the EQE spectra for the QW devices with BSR and without ARC are observed and are associated with Fabry-Perot resonances. The Fabry-Perot cavity exists due to interference from back and front reflection of photons at the AlGaAs/Au and AlInP/air interfaces with optical reflectance of about \sim 90% and \sim 26%, respectively. If the cavity length is integer-multiples of half-wavelengths, photons that were not absorbed in the QWs in their second pass, will interfere constructively with the incident light at resonance wavelengths, λ_{res} . At normal incidence, these λ_{res} , can be estimated as follows

$$\lambda_{res} = \frac{2nt}{m + 1/2} \quad (7.1)$$

where n is the refractive index, m is the resonance mode order, and t is the thickness of the cavity. Using Eqn. (7.1) and assuming $n = 3.5$, the resonance modes of the 20-period device ($t = 1.064 \mu m$) are estimated to be at: 648 nm at $m = 11$, 709 nm at $m = 10$, and 784 nm at $m = 9$. These calculated values are close to the measured values: 655, 705, 765 nm. The EQE, without ARC, of the 20-period device at the Fabry-Perot resonances, 705 nm and 765 nm, peaks at 63% and 51%, respectively, which are at least 3-times higher than the corresponding values without BSR, as shown in Figure 7.3(a). Increasing the number of QWs, increases the cavity length and enhance the EQE values at the resonance peaks, as shown in Figure 7.3(b). The deposition of MgF₂/ZnS ARC on the samples, with BSR, smears out all these resonance peaks, as shown in the EQE of

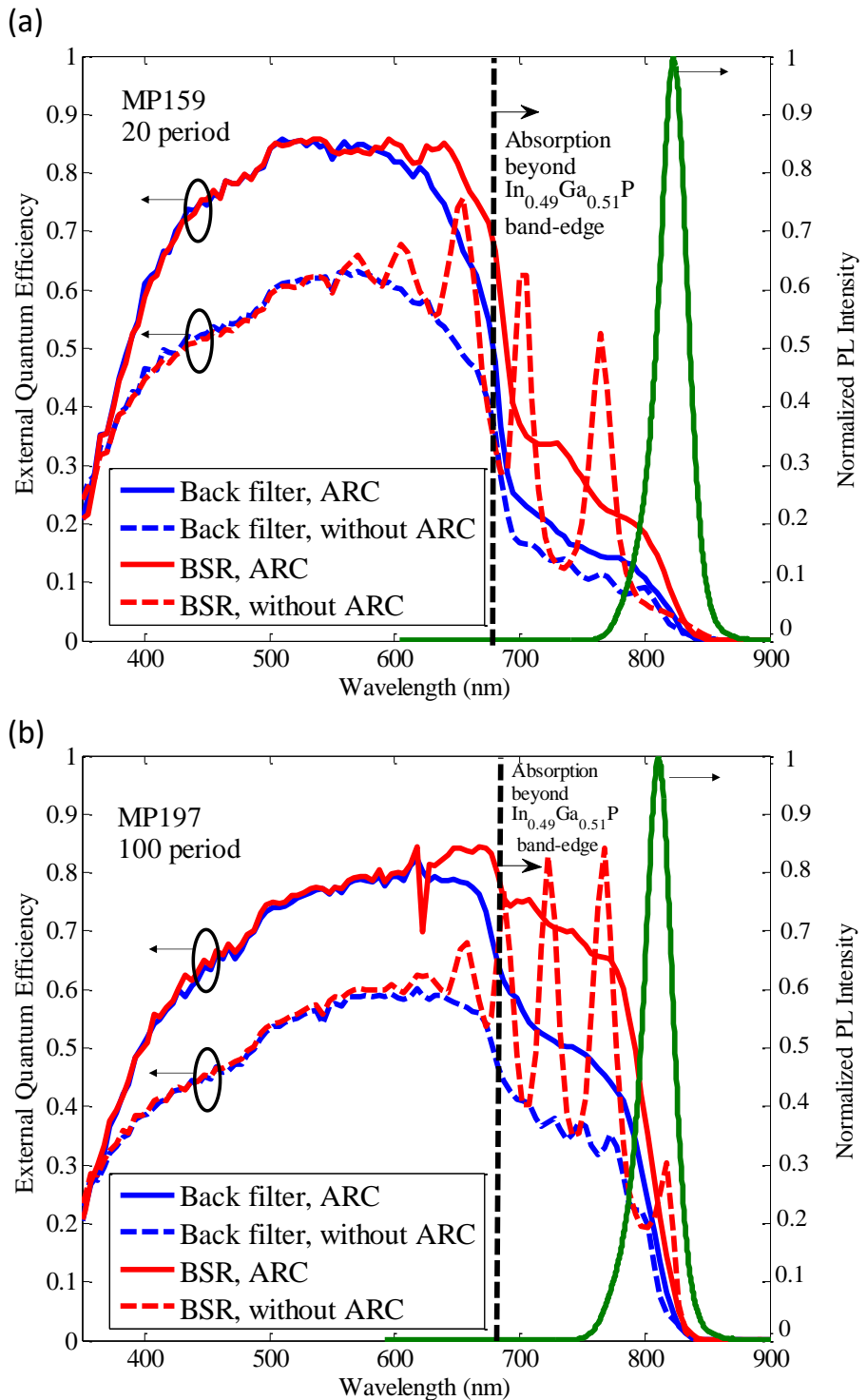


Figure 7.3: External quantum efficiency (EQE) and photoluminescence (PL) spectra of (a) 20-period device (MP159) and (b) 100-period device (MP197), with and without ARC, processed with a gold BSR and with back-filter.

devices in Figure 7.3. The ARC reduces the interference between the incident light and the fraction of reflected photons that were not absorbed in the QWs after their second pass. This is because the front reflectance at the AlInP/ZnS interface is ~3% which is much less than the corresponding value (26%) of the no-ARC case.

The one-sun AM1.5 current density-voltage curve measured for the 100-period device is shown in Figure 7.4. The J_{sc} , V_{oc} , fill factor (FF), and η of the back-filter/ARC device were 18.5 mA/cm², 1.126 V, 72.3%, and 14.7%, respectively. The corresponding J_{sc} , V_{oc} , FF , and η of the BSR/ARC device were 20.5 mA/cm², 1.136 V, 75.3%, and 17.6%, respectively. Standard InGaP cell (~1.81 eV) with BSR/ARC has a J_{sc} of 16 mA/cm² and the reported J_{sc} value here is markedly 26% higher than that [10]. The reason of the J_{sc} enhancement is the sub-bandgap absorption by the QWs as shown in Figure 7.3(b). Processing the QWs with BSR improved the J_{sc} by 10.0% relative to the back-filter case. The FF is not high and improving it to 80-85% requires more enhancement of QW interfaces quality and precise stress management to reduce the stress across the QW region [155].

We use the bandgap-voltage offset ($W_{oc} = V_{oc} - E_g$) as a figure of merit to evaluate the performance of these QW devices because it evaluates how close the V_{oc} to the fundamental limit set by radiative recombination [51]. The appropriate bandgap to use for QW solar cells can be an ambiguous quantity to determine. We used an effective junction bandgap from a detail-balanced viewpoint based on the EQE as described in [157, 158]. The measured V_{oc} , and calculated bandgaps and W_{oc} at one-sun are given in Table 7.1. A W_{oc} , approaching or less than 0.4 V, indicates a high solar cell voltage, and the values reported in Table I indicate excellent voltages and high internal and external radiative efficiencies. The W_{oc} slightly increases (V_{oc} slightly decreases) with the increase of well number for a few reasons. First, an increase in the QW region thickness, increases the SRH recombination and increases the dark currents [70]. Second, the unintentional carbon background doping (2×10^{15} cm⁻³) in the QW region affects the electric field distribution and forms a junction between emitter (n-doped) and QW region (unintentionally p-doped). Increasing the depletion region thickness may lead to the presence of a weak electric field region close to base where carriers are more susceptible to recombination effects and will increase dark current and may reduce W_{oc} . Third, the possible presence of defects or non-abrupt interfaces at well/barrier and/or barrier/well interface due to arsenic on/off switching may lead to an increase

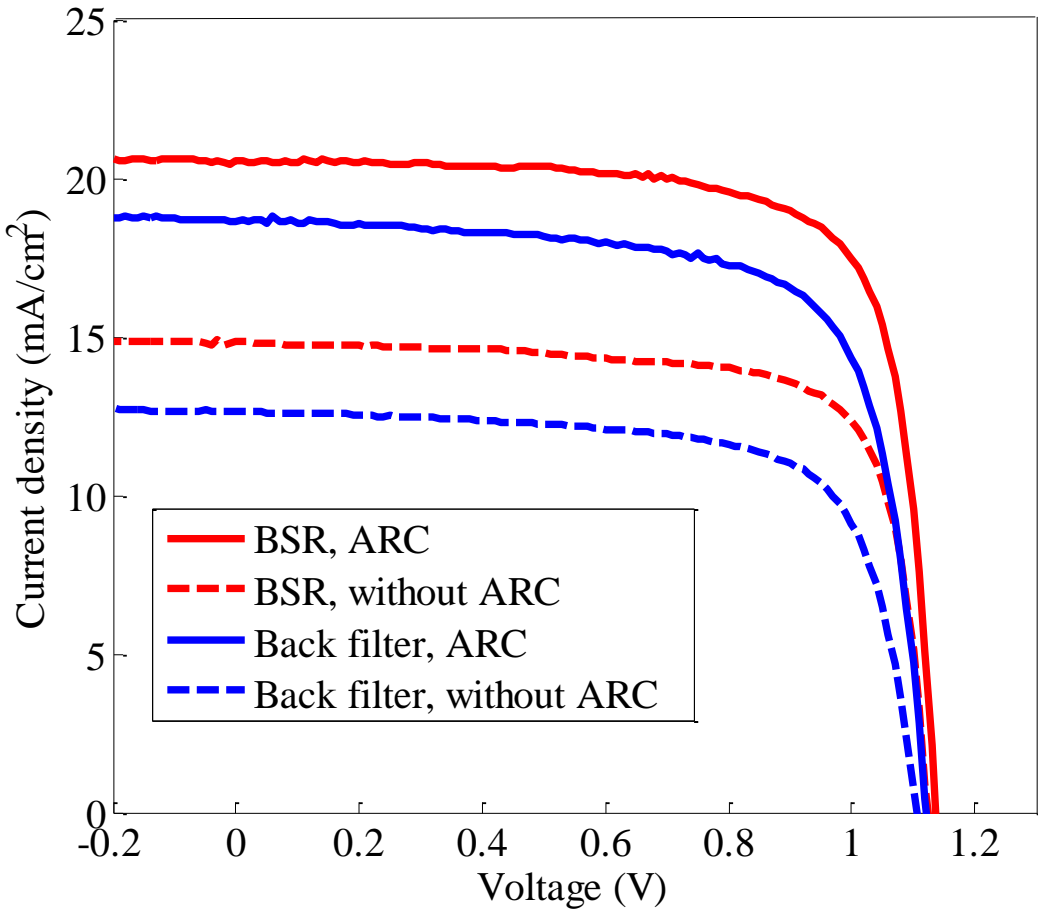


Figure 7.4: Light IV characteristics of 100-period device (MP197), with and without ARC, with a gold BSR and with back-filter.

in dark current with the increase of number of interfaces. The dark I-V (DIV) characteristics of the 20-period and 100-period devices, are shown in Figure 7.5. The DIV were analyzed using a two-diode model as discussed in Chapter 1, where the first term with ideality factor $n = 1$ represents recombination in the quasi-neutral regions, and the second term with ideality factor $n = m$ (1.5 or 2) represents the SRH recombination in the depletion region. The dotted lines in the DIV of Figure 7.5, represent the slope of diodes with ideality factors, $n = 1$, $n = 1.5$, and $n = 2$. Analysis of DIV measurements indicates that the performances of 100-period and 20-period devices are dominated by recombination in the depletion region, with $n = 2$ and $n = 1.5$, across the entire I-V sweep, with dark current densities, $J_{0,2} = 4 \times 10^{-9} \text{ mA/cm}^2$ and $J_{0,1.5} = 3 \times 10^{-13} \text{ mA/cm}^2$, respectively.

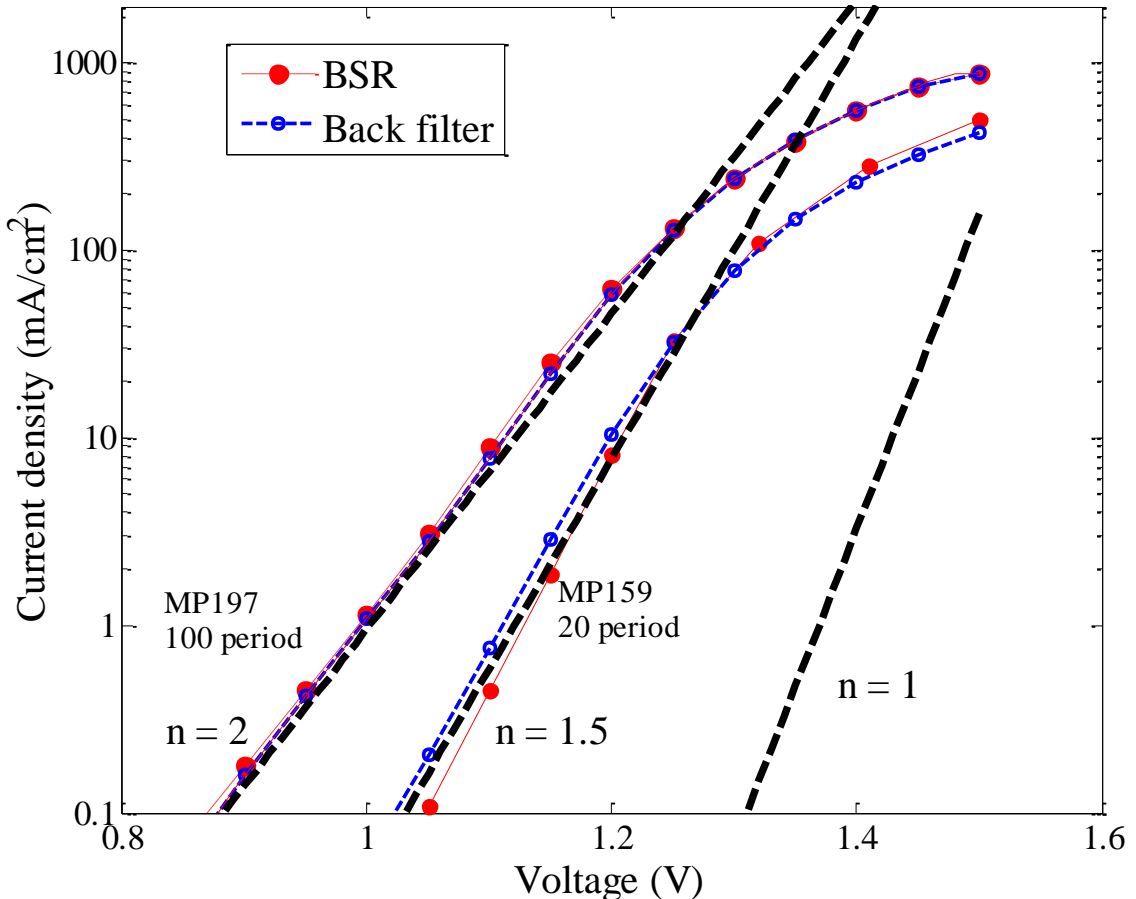


Figure 7.5: Dark current voltage characteristics of 20-period QW device (MP159) and 100-period QW device (MP197), with a BSR and with a back-filter. The dotted lines represent diodes with ideality factors $n = 1$, $n = 1.5$, and $n = 2$.

We studied the carrier escape mechanisms in this QW design to provide more insights into the EQE improvements shown in Figure 7.2 and Figure 7.3. Two mechanisms can allow a carrier to escape from QWs and contribute to photocurrent: carrier tunneling and thermionic emission. The competition between carrier escape lifetime ($\tau_{esc.}$) and non-radiative recombination lifetime (τ_r) determines whether the photo-generated carriers are lost or contribute to photocurrent. The probability of carrier escape from a single QW, can be evaluated as follows [64],

$$P = \frac{\frac{1}{\tau_{esc.}}}{\frac{1}{\tau_{esc.}} + \frac{1}{\tau_{rec.}}}, \quad (7.2)$$

The total probability of carriers escape through the entire QW structure is P^N , for N quantum wells [41]. The escape lifetime for tunneling and thermionic emission were evaluated as described in [66] [65]. We used the Anderson's rule to estimate the conduction and valence band and the quantum confined eigenstates were modeled using Kronig-Penney model. Table 7.2 summarizes the escape probability for tunneling ($P_{tun.}$) and thermionic emission ($P_{therm.}$) for $n = 1$ electron and heavy-hole states. From Table 7.2, we can conclude that both carrier transport mechanisms exist in the lattice matched structure, with tunneling being more predominant. The tunneling probability for electrons and holes is ~ 1 due to the thin barriers (25-32 Å) for carriers to tunnel. The P_{therm} for electrons is ~ 1 due to the fact that only 13% of the total band-offset occur in the conduction band, thus resulting in low barrier height for electrons (0.0684V). The P_{therm} for holes is 0 due to the high effective barrier heights (~ 0.32 V). For the strain-balanced structure [127], the P_{therm} of n=1 electron and heavy hole states are 99% and 58%, respectively and $P_{tun.}$ are zero because of the relatively thick barrier (~ 150 Å) for carriers to tunnel.

Table 7.2: Tunneling escape and thermionic emission escape probabilities for electrons and heavy hole states

	$P_{tun.}$		P_{therm}	
	e	hh	e	hh
MP159, 20-period	0.9999	0.9839	0.9999	0.0217
MP161, 40-period	0.9998	0.9629	0.9996	2.8×10^{-6}
MP197, 100-period	0.9998	0.9846	0.9991	8.62×10^{-14}
Strain-balanced structure, Chapter 5 [127]	0.0	0.0	0.99999	0.5824

We compared the performance of InGaAsP/InGaP superlattice solar cell to bulk InGaAsP and AlGaAs solar cells. At this initial phase of development, the FF and long wavelength EQE of these QW solar cell structures are lower than bulk InGaAsP and AlGaAs as mentioned earlier. The EQE of QW solar cells (no-BSR) needs to be further improved for future use in multijunction solar cells as previously discussed. The W_{oc} at one-sun of QW solar cells is ~ 0.08 V better than that of bulk InGaAsP cells [99, 159] and is similar to AlGaAs cells [98]. The QW structures were grown at

temperatures (550-600 °C) less than that of high performance AlGaAs (640 °C) [98] and bulk InGaAsP cells (600-650 °C) [99, 159]. The low-temperature growth may result in less thermal degradation effects on the connecting tunnel junction grown underneath the subcell [48-50]. This work presents an alternative pathway to achieve a 1.5-1.8 eV subcell which is important for several multijunction solar cell approaches.

Chapter 8: Photon recycling in multi-junction solar cells using the Inter-Metallic Bonding Approach: Concept

In this chapter, a new approach for enabling photon recycling in multi-junction solar cells, in a two-terminal device configuration, is presented. This approach is based on recent research efforts in Bedair's lab that focus on developing two-terminal tandem solar cells of two dissimilar material systems using the Inter-Metallic Bonding (IMB) approach [28]. The IMB approach allows combining two cells that differ in their crystalline, electrical, thermal and optical characteristics and the use of off the shelf cells to be integrated into to a multi-junction structure, in two-terminal device configurations [28]. As a proof of concept, a tandem solar cell of GaAs/Si was fabricated using the IMB approach. This chapter does not address the development of this concept but rather focus on photon recycling, which is a feature that the IMB approach can enable. In this chapter, a review of the current status of photon recycling in *single-junction* and *multi-junction* solar cells is presented. Then the possibility of enabling photon recycling in multi-junction solar cells using the IMB approach is discussed. The modeling of open circuit voltages and reflectance in multiple structures are also discussed.

8.1. Motivation

Shockley and Queisser (SQ) proposed the detailed balance limit for the efficiency of a single junction solar cell [14]. Their prediction initiated activities to improve the efficiency of p-n junction solar cell to approach the practical limit [160, 161]. Solar cells with higher efficiencies have been reported in multi-junctions (MJ) structures [30]. Record efficiencies of 35% and 45.7% were reported in the four-junction structure at one sun and 234 suns, respectively [162]. Higher efficiency that can be close to 50% at high solar concentration can be realized by growing five and six junction devices. However, this approach is accompanied by material and interconnect complications, which may make the trend of increasing efficiencies by assembling more junctions suffer from diminishing returns. It is worth pointing out that the current record performances of the MJ structures fall short of the predicted efficiencies based on the detailed balance limit. Several researchers have extended the Shockley and Queisser analysis to obtain the limiting efficiencies for tandem cells based on optimum bandgaps configurations, and have reported at least 15.0%

higher than the current state of the art solar cells [163-166]. Recently, Yablonovitch et al. reported the theoretical efficiency limits for optimum bandgap combinations and selective reflectors at each cell to be 45.7%, 51.5%, and 55.3 % for two-junction (2J), three-junction (3J) and four-junction (4J) structures, respectively [167]. These efficiency limits are based on the SQ model under the optimal conditions. These efficiency gaps were successfully addressed in *single-junction* GaAs and InGaP devices and record-efficiencies approaching the SQ limit have been realized [10, 161], however, this gap still exists for the MJ structures [167]. This chapter will address the photon-recycling in multi-junction devices using the intermetallic bonding approach.

The detailed balance model efficiency for single or MJ structures assumes the presence of a maximum degree of ***photon recycling (PR)***, where photons from radiative recombination of an electron-hole pair, that is not emitted from the front surface, will be reabsorbed and generate new electron-hole pairs, as shown in Figure 8.1(b). The absorption of the radiated photons increases the minority carrier concentration, carrier lifetimes, and boost the external luminescence efficiency and the open circuit voltage. This will provide multiple opportunities for photon recycled luminescence to escape out of the front surface of the cell for optically thin films.

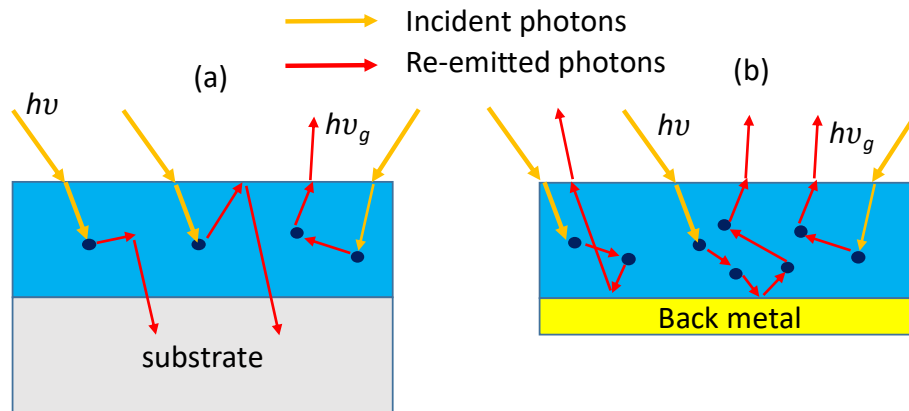


Figure 8.1: Photon dynamic of solar cells at open circuit voltages: (a) cell grown on substrate, (b) cell grown with epitaxial lift-off approach where photon recycling is taking place.

In a MJ structure, photon recycling requires the insertion of a selective photon reflector at the back surface of each junction as shown in Figure 8.2. This is very challenging due to lack of accessibility of the rear surface of all junction except the bottom cell as will be discussed later in details in this Chapter.

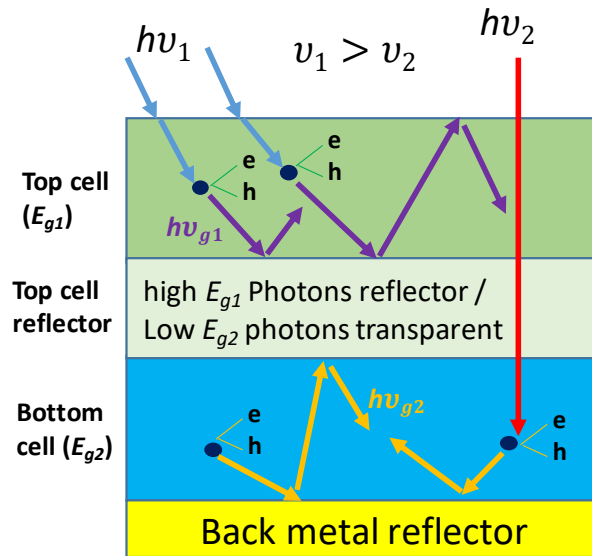


Figure 8.2: Schematic of photon dynamic in multi-junction cells with an ideal reflector placed at the back of top cell. Antireflection coatings (ARCs) are not shown for simplicity.

8.2. Current status of photon recycling and light trapping in “single-junction” cells

Using the photon recycling concept, several record-breaking solar cell efficiencies have been achieved for *single-junction* devices in the past five years. For example, Alta Devices has realized a 29.1% thin-film GaAs device with open circuit voltages (V_{oc}) of 1.122 eV on a flexible substrate using the epitaxial lift-off process compared to a ~1.0 eV with the substrate-on case[168]. Also NREL has fabricated a 1.81 eV InGaP cell with a 20.8% efficiency at one-sun and open circuit voltages of ~1.45 V with increase of about 50 mV relative to the conventional upright structures, along with a boost in the short circuit current (J_{sc}) from 14.8 mA/cm² to 15-16 mA/cm² [10]. These reported efficiencies for single junction cells GaAs and InGaP are about 2.5% higher than the corresponding cells that do not employ photon recycling, at one sun. The reason behind these high efficiencies single-junction cells has been attributed with the careful management of optical emission and arises from the concept that “**A Good Solar Cell Absorber is a Good Light Emitting Diode**” [160]. The optical management is realized using a metal back reflector of gold and growing the junction at the rear end of the device with a high bandgap back surface field, thus improving the light extraction and boosting the open circuit voltages. This concept has also been applied recently to non-III/V solar cells. For example, recent modeling results for perovskite solar

cells have shown the applicability of boosting the V_{oc} by ~ 100 meV using the PR approach [169, 170]. Figure 8.1 shows the photon dynamics at open circuit for the case with the on-substrate and substrate lifted-off. At V_{oc} , the generated electron-hole pairs due to incident light absorption are either emitted from front/back or recombine non-radiative. Comparing Figure 8.1(a) and Figure 8.1(b) under the assumption of perfect internal radiative efficiency (neglected Shockley-Read-Hall recombination), the generated electron-hole pair in Figure 8.1(a) recombine to emit photons with energy equal to bandgap energy that can be directly absorbed in the substrate. However, in the lift-off substrate case, shown in Figure 8.1(b), photons are being recycled and this will result in all photons emitted from the front surface, thus resulting in high external luminescence efficiency which is the reason for the large boost in the V_{oc} that resulted in the recent single-junction records.

Another approach for enhancing solar cells performance through optical management is light trapping which has been applied in the last twenty years to improve the short circuit current through enhancing the optical path length [154, 171]. This approach is effective if the materials have low absorption coefficient such as Si or the diffusion length is small such as amorphous silicon. Using this approach, thin-film low-cost Silicon solar cells with 25.6% efficiency has been achieved by Panasonic using a heterojunction design of amorphous silicon, thus reducing recombination and increasing the probability of photons absorption through effective manipulation of light propagation [168]. Figure 8.3(a) shows solar cells with no surface texturing or back metal; light escapes out the rear if not absorbed. When a back-metal reflector is added, the optical path length is double the physical device length. Surface texturing increases the path length but light escapes after two passes. Front or rear surface texturing can trap light for multiple passes due to total internal reflection, Figure 8.3(b).

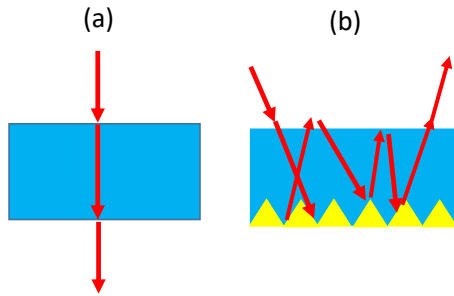


Figure 8.3: (a) solar cell with no surface texturing or back reflector, (b) solar cells with rear surface texturing.

8.3. Current status and approaches of photon recycling in “MJ solar cells” and limitations (Review)

Applying the photon recycling concept in MJ solar cells is still in the infant phase due to the difficulty in accessing the rear side of the top cell tandem efficiently. There are several strategies to apply the photon recycling in MJ solar cells, these efforts are highlighted, and their current limitations are briefly explained.

8.3.1. Use of Distributed Bragg Reflectors (DBRs)

Use of Distributed Bragg Reflectors (DBRs) of a multilayered stack of high and low- index films, all one quarter-wavelength thick [172], Figure 8.4(a).The DBRs should be designed to have a maximum reflectivity at energies higher than E_{g1} . As the refractive index contrast of the materials used in DBRs increase, the percentage of reflected photons of energy $< E_{g1}$ will increase and the bandwidth of maximum reflectivity will increase. However, for applying this concept in multi-junction solar cells, the DBRs should be also transparent to photons of energies less than E_{g1} and greater than E_{g2} . In addition, the reflectivity heavily depends on the incident angle and DBRs will be practically designed at the optimum point at a single incident angle. This makes the design of DBRs too complicated and limited success has been shown using this approach. In addition, the growth adds extra growth time and cost. Moreover, this approach is not universal and cannot be applied in case of using two dissimilar materials in a tandem cell such as perovskite and silicon.

8.3.2. Use of buried Al₂O₃ through lateral oxidation of AlAs [173]

This process was developed to enhance photon recycling in single-junction devices through oxidizing AlAs in a tube furnace to create an Al₂O₃ layer of a 1.75 refractive index, thus creating a large index-mismatch between the absorber ($n \sim 3.5$) and the Al₂O₃, which increases the

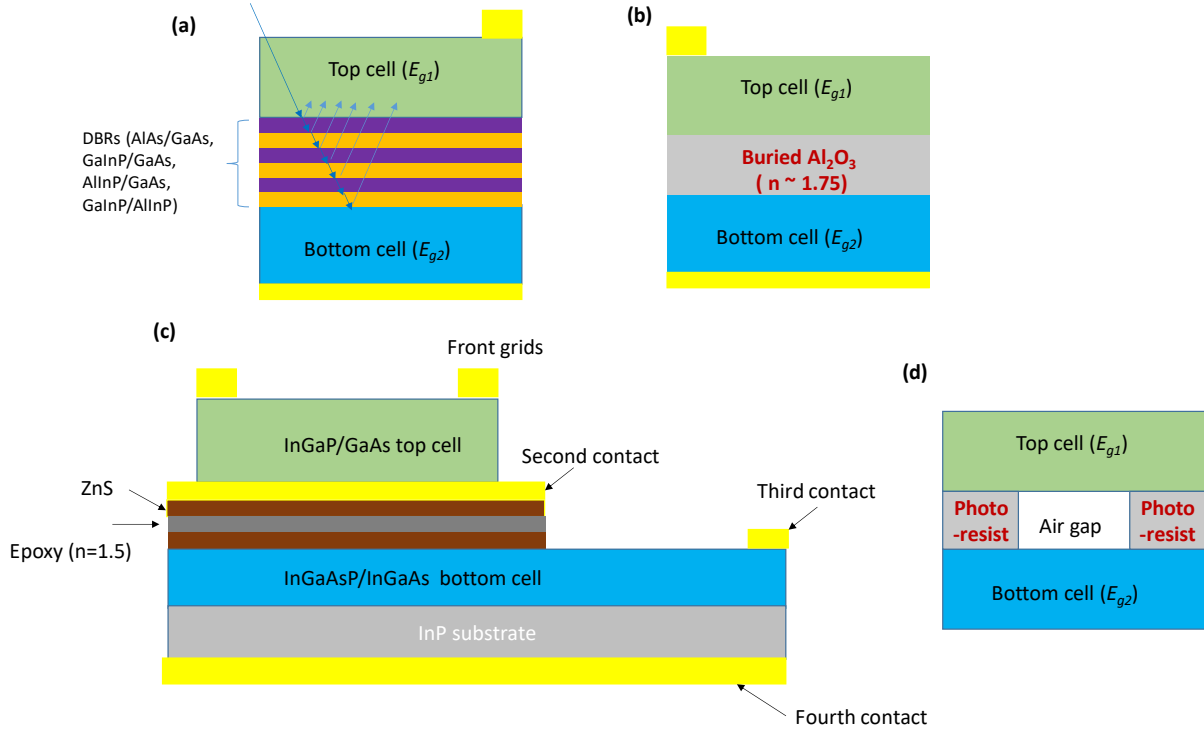


Figure 8.4: Previous activities for applying photon recycling in MJ solar cells. (a) DBRs used in the connection between upper and lower tandem [172], (b) oxidized AlAs layer [173], (c) low index epoxy with ARC on either side of the epoxy [174], and (d) top cell printed on a bottom cell using a photoresist [175].

reflectivity of remitted photons back to the absorbing layers. This approach in tandem cells could be impractical due to the difficulty in tuning the Al_2O_3 to transmit all the sub-bandgap light of energy $< E_{g1}$. In addition, this approach can only be applied to III-V compounds and will result in a four-terminal structure.

8.3.3. Use of $n = 1.5$ epoxy as a reflector and ZnS as an antireflection coating [174]

NREL/Spectrolab fabricated a 4 junction device made of two tandems grown on GaAs and InP substrates with a 38.8% one-sun efficiency. The two tandems are connected together using a transparent epoxy of refractive index, n , equals to 1.5. The strong index contrast between the epoxy and the absorbing layers in the upper tandem resulted in a back reflectance in the top cells of about 83%. To transmit the sub-bandgap photons to the bottom tandem, an ARC of ZnS was deposited on either side of the epoxy as shown in Figure 8.4(c). Even though encouraging results have been shown using this approach, possible limitations that may hinder the scalability of this device must be taken in to account. First, these results were achieved in a four-terminal configuration with the

two tandems biased at their maximum operating points, which adds more complexity due to the additional processing steps, making it not appealing at a module/system level. Second, the efficiency of the four-junction device drops from 38.8% to ~33.9% in case of shortening the second and third contacts for use in a two-terminal configuration because of expected transparency losses in addition to current mismatch.

8.3.4. Use of photoresist to print one cell on another

Use of photoresist to print one cell on another to form an air gap as shown by Rogers group [175] as shown in Figure 8.4(d). This work showed interesting initial results for a selective photon reflector between two junctions due to index contrast between air and the top cell. However, two major drawbacks may hinder the use of this approach in MJ solar cells; first, the use of SU8 photoresist to print the two junctions does not form a good interconnect in tandem cells due to the high electrical resistivity of the photoresist. Second, this design is a 4-terminal configuration which is a drawback.

8.4. Photon recycling in 2J tandem cells by an Intermetallic Bonding (IMB) approach

In order to effectively apply the photon recycling approach in MJ solar cells, a photon reflector should exist at the rear of the top cell (or cells). The photon reflector should satisfy the following two requirements, as shown in Figure 8.2, for top and bottom cells of bandgaps E_{g1} and E_{g2} , respectively: (i) The selective reflector should *ideally* reflect all incident photons with energies greater than or equal to E_{g1} , thus trapping the light for more than a single-pass due to internal reflection, leading to improvements in the open circuit voltages of top cell, (ii) and should *ideally* be transparent to incident photons of energies less than E_{g1} , thus not depriving the bottom cell (or cells) from the sub-bandgap photons. It is worth pointing out that these two requirements could be hard to achieve and makes the design of this reflector a challenging issue, and the cell acquiring full benefit from the presence of the back metal is the lowest bandgap subcell in the bottom stack. The IMB approach introduces an air gap between the top and bottom cells that will act as photon reflector due to the difference in the index of refraction between air and semiconductors, thus realizing the first requirement of an ideal selective reflector as mentioned earlier. This will be based on the Inter-Metallic Bonding (IMB) approach *between any two cells, in a two-terminal device configuration* as shown in Figure 8.5. In order to satisfy the second requirement and

transmit the photons of energies less than E_{g1} to the bottom cell (or cells), ARCs are deposited on the back of the top cell and top of bottom cells, Figure 8.6. The development of IMB approach will be the research project of another student in Bedair's laboratory. This section will be to estimate the gain in V_{oc} of both cells due to photon recycling. Also, the impacts of ARC on the reflectivity at the top and bottom surface of the high bandgap cells will also be addressed. The following results can serve as a guideline for enhancing the efficiency by applying the photon recycling concept using the IMB approach.

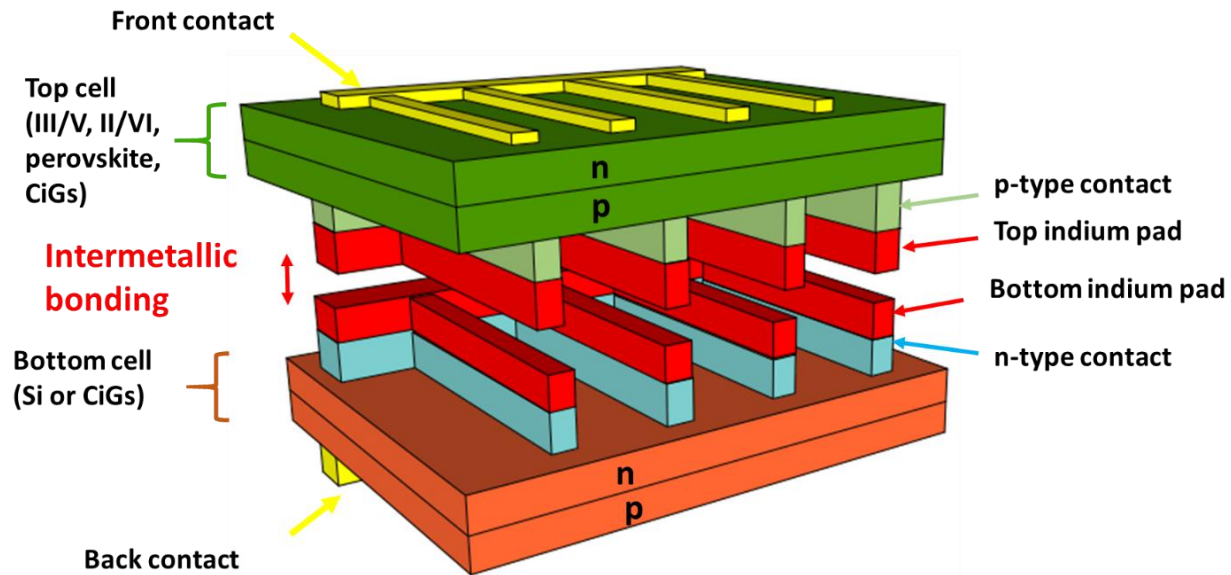


Figure 8.5: Schematic of the proposed IMB approach between two dissimilar cells in a two-terminal structure for enhancing photon recycling in MJ solar cells [28].

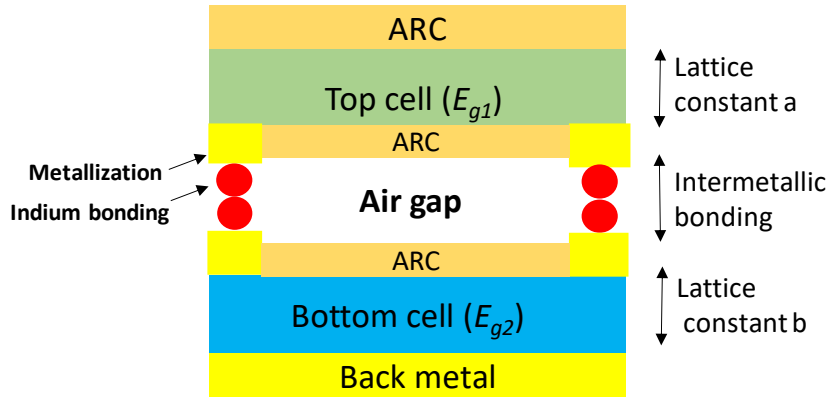


Figure 8.6: Photon dynamic of solar cells at open circuit voltages. (a) cell is grown on the substrate, (b) cell grown with epitaxial lift-off approach

8.5. Analysis of photon recycling in dual-junction solar cell structures: Open circuit voltage and external Luminescence efficiency

In this section, initial modeling and analysis results that demonstrate the concept of photon recycling with an air gap made possible by the IMB approach, is presented. The impact of photon recycling on improving the V_{oc} and thus the efficiency is discussed.

The dependence of open circuit voltage (V_{oc}) on the external luminescence efficiency (η_{ext}) can be expressed as [160],

$$V_{oc} = V_{db} + \frac{kT}{q} \ln(\eta_{ext}) = V_{db} + \frac{kT}{q} \ln\left(\frac{\eta_{int} P_{esc}}{1 - \eta_{int} P_{abs}}\right) \quad (8.1)$$

where V_{db} is the ideal open circuit voltage obtained from the detailed balance model, η_{ext} is equal to unity at the detailed balance limit, η_{int} is the internal radiative efficiency. P_{esc} and P_{abs} are the averaged probabilities of photon escape and reabsorption, respectively. P_{esc} and P_{abs} will both depend on the optical properties of the absorber in addition to *the index contrast between the absorber and the underlying photon reflector/Substrate*.

The internal luminescent efficiency, η_{int} , is given by [176]

$$\eta_{int} = \frac{U_{rad}}{U_{rad} + U_{nr}} \quad (8.2)$$

where U_{rad} and U_{nr} are the radiative and non-radiative recombination rates, respectively. To increase η_{int} , U_{rad} should be increased and U_{nr} should be decreased.

In order to analyze the presented approach, we consider the case of a tandem cell of InGaP (1.85 eV) top cell and GaAs (1.42 eV) bottom cell connected in three different ways:

- (a) grown lattice matched on GaAs substrate, with an ARC on the top cell, as shown in Figure 8.7(a). Solar cells are connected by tunnel junctions, and photon recycling is not feasible in this approach for both cells.
- (b) with a back metal reflector at the rear of the bottom cell and no intermediate mirror reflector between the two cells as shown in Figure 8.7(b). Photon recycling is feasible for the bottom cell only.
- (c) with a back metal reflector at the rear of the bottom cell and the two subcells connected using the proposed IMB approach with ARC on the front and back of the top cell and on the front of the bottom cell as shown in Figure 8.7(c). Photon recycling is feasible for both cells.

In all these cases, all cells are assumed optically thin and non-radiative recombination is neglected ($\eta_{int} = 1$). Table 8.1 shows the ideal open circuit voltage in the top and bottom cell in each of the three presented cases, calculated using Eqn. (8.1). In this part, the same analysis of ref. [167] is followed to calculate the η_{ext} and V_{oc} in each case. The η_{ext} of both top and bottom cell for the structure shown in Figure 8.7(a), is $\frac{1}{4n^2}$, where n is the refractive index ($n \sim 3.5$ for InGaP and GaAs) [167]. This value for η_{ext} is based on that the probability of front surface escape, relative to substrate absorption, is the fraction of solid angle that is subtended by the escape cone. The escape cone, in this case is given as, $\sin^{-1}(1/3.5) = 17^\circ$. The V_{oc} of InGaP and GaAs will then be 1.49 and 1.06, respectively. For the back-metal reflector case of Figure 8.7(b), η_{ext} and V_{oc} of bottom cell are 1 and 1.17 eV, respectively. This value of η_{ext} for the bottom cell is based on the presence of a perfect back reflector, since all photons must eventually escape out from the front of the MJ structure. The corresponding values of η_{ext} and V_{oc} for the top cell are $\frac{1}{4n^2}$ and ~ 1.49 eV, respectively, as shown in Table 8.1. It should be mentioned that the rear metal reflector boosts the voltage of the bottom cell; however the top cell does not get the same voltage boost.

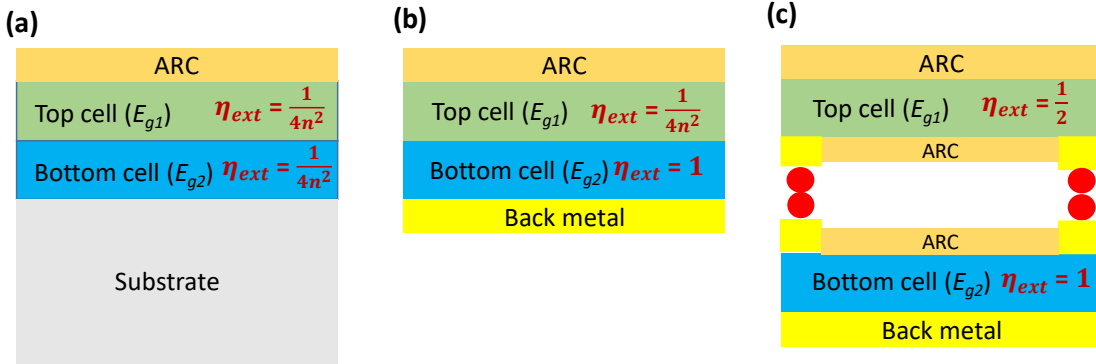


Figure 8.7: Comparison between tandem cells grown using three different approaches:
 (a) lattice matched to the index-matched substrate, (b) on a perfect metal reflector, (c) the proposed IMB approach. The expressions for the η_{ext} in the figures are from ref. [167]

Table 8.1: Comparison between the ideal V_{oc} of the tandem cell connected using the three approaches of Figure 8.7, as calculated by Eqn. (8.1). The expressions for the η_{ext} in the figures are from ref. [167]

	Structure a	Structure b	Structure c
V_{oc} (top cell) Ex: InGaP	1.4897 V	1.4897 V	1.5725 V
V_{oc} (Bottom cell) Ex: GaAs	1.06 V	$V_{db} = 1.172$ V	$V_{db} = 1.172$ V
Total V_{oc}	2.55 V	2.6617 V	2.7445 V

For the structure shown in Figure 8.7(c), the proposed IMB approach develops an intermediate mirror reflector between the two connecting cells, which will reflect the internally emitted photons of the top cell due to the index contrast between top cell and air. It should be also mentioned that the airgap created by the IMB approach will transmit the sub-bandgap photons to the bottom cell due to the presence of an ARC between the bottom cells. In this case, η_{ext} of bottom cell will still be 1 and that of the top cell will be equal to $\frac{1}{2}$ [167] since the front and back interfaces of the top cell are identical. Thus the voltage of the top cell in the structure of Figure 8.7(c) will be boosted by $\frac{kT}{q} \ln(2n^2)$ relative to that of Figure 8.7(b). We assume that short circuit current and the fill factor in the three structures are 14.8 mA/cm^2 and 85%, respectively. The AM1.5G efficiency of structures A, B, C can then be estimated as 32.07%, 33.4%, and 34.5%, respectively. This analysis

thus indicate that the efficiency of multi-junction solar cells can be improved by a one-percent point by applying the photon recycling concept in multi-junction devices. It is worth pointing out the same analysis and conclusions exist for non-III/V based solar cells materials with different values of n . It should be mentioned that there will be a slight decrease in J_{sc} of the bottom cell due to the loss of the radiative emission out of the rear of the top cell, that is then absorbed by the bottom cell.

8.6. Analysis of photon recycling in dual-junction solar cell structures: Air gap effects

The analysis in Section 8.5 assumed that all photons with energies less than the bandgap of the top cell will be transmitted to the bottom cell. These sub-bandgap photons can be transmitted to the bottom cell if ARC is deposited on the front surface of the bottom cell and the front of the top cell. In this section, the dependences of the back reflectance at the top cell/airgap interface on the air gap thicknesses in case of having rear ARCs or not, are discussed. The effect of front and back ARC and air-gap thickness on the front and back reflectance will be also analyzed to maximize the back reflectance at top cell/air-gap interface and maximize the transmittance of sub-bandgap photons to the lower cell. The propagation of electromagnetic waves through the multiple interface layers was modeled using the transfer matrix method [177, 178].

8.6.1. Modeling the front and back reflectance across multiple layers

To understand the reflection/transmission issue, a simulation to model the reflection/transmission in multi-layer structures, similar to that shown in Figure 8.8, is developed [177]. The model takes into account the following input parameters: (i) polarization type (transverse electric, transverse magnetic), (ii) angle of incidence, and (iii) frequency dependent refractive indices. The following assumption are made: (i) coherence propagation of electromagnetic waves and (ii) the photons originate in a non-absorbing medium. The light passing through this structure can be described with the scattering-matrix formalism as follows [177],

$$\begin{bmatrix} E_{inc}^+ \\ E_{inc}^- \end{bmatrix} = S \begin{bmatrix} E_{trans}^+ \\ E_{trans}^- \end{bmatrix} \quad (8.3)$$

where E_{inc} and E_{trans} are the electric field components before the first interface and after the last interface, respectively. E_{inc}^+ is the incident electric field before the first interface, E_{inc}^- is the sum of the reflected electric field components before the first interface, E_{trans}^+ is the transmitted electric field component after the last interface, and S is 2x2 scattering matrix which is defined as follows [177]

$$S = I_{o1} L_1 I_{12} L_1 \dots L_m I_{m+1} \quad (8.4)$$

where $I_{J(J+1)}$ is wave propagation matrix at the interface between the film J and $J+1$, and L_J is the wave propagation matrix through the film J . The two matrices I and L are defined as follows [177],

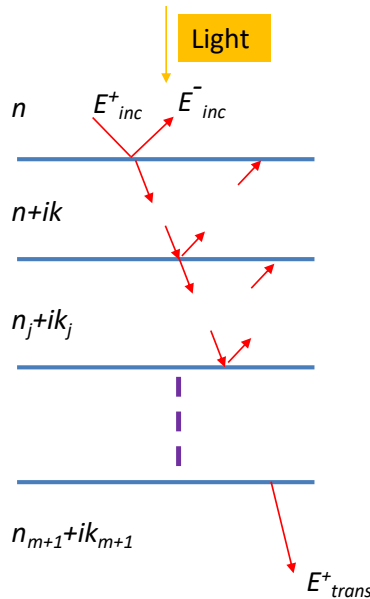


Figure 8.8: Schematic representation of a multilayer with forward and backward-propagating electric field components shown.

$$I_{i,j} = \frac{1}{t_{i,j}} \begin{pmatrix} 1 & r_{ij} \\ r_{ij} & 1 \end{pmatrix} \quad (8.5a)$$

$$L_j = \begin{pmatrix} e^{-\beta_j} & 0 \\ 0 & e^{+\beta_j} \end{pmatrix} \quad (8.5b)$$

where r_{ij} and $t_{i,j}$ are the Fresnel coefficients at the interface i, j for transverse electric and transverse magnetic waves; β is the phase shift that is due to the wave passing through the film j . From the scattering matrix, it is possible to calculate the front-reflectance coefficient, r , as follows [177],

$$r = \frac{E_{inc}^-}{E_{inc}^+} = \frac{S_{21}}{S_{11}} \quad (8.6)$$

The reflectance at a given angle, θ , can then be calculated for both the transverse electric and magnetic waves as follows [177],

$$R(\theta) = |r|^2 \quad (8.7)$$

The angle average reflectance by integrating $R(\theta)$ over all the possible incidence angle as follows [177],

$$R = \int_0^{\pi/2} R(\theta) \sin(\theta) d\theta \quad (8.8)$$

Using the propagation matrices I and L , the reflectance and transmittance at any interface can be calculated.

8.6.2. Front and back reflectance results

Figure 8.9 shows three tandem cells bonded using the IMB (Figure 8.5) for three different cases: (a) no front or rear ARCs deposited on the two cells, (b) only front ARC (MgF_2/ZnS) deposited on top of upper cell, and (c) front ARC (MgF_2/ZnS) deposited on top of two cells and back ARC deposited on back of top cell.

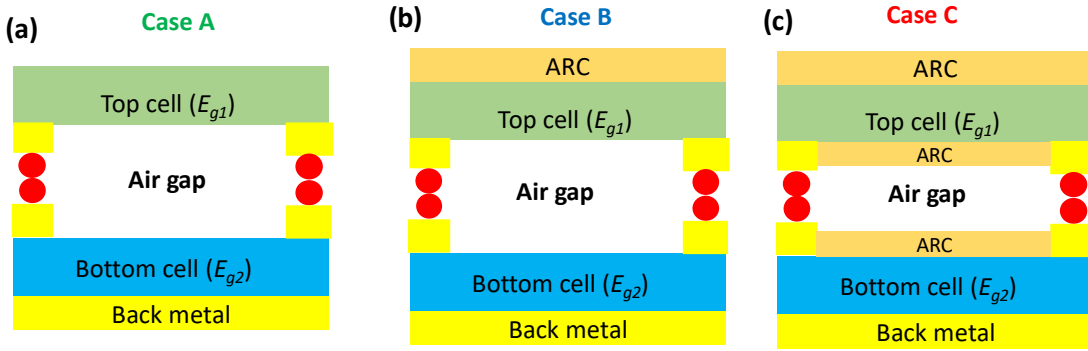


Figure 8.9: Two cells bonded together using the proposed IMB approach with air gap provided between them: (a) no front or rear ARCs on the two cells, (b) only front ARC on top of upper cell, and (c) front ARC on top of two cells and back ARC on back of top cell.

Figure 8.10 shows the front reflectance at the front interface for an InGaP/Air/GaAs solar cell for these three cases. It is noted that the addition of MgF_2/ZnS ARC suppresses the reflectance to less than 5% at energy values above the top cell bandgap, as expected. Additionally, the insertion of ARCs at the rear of the top cell and top of bottom cell greatly suppresses the front reflectance at the absorption window $E_{g1} > E > E_{g2}$. This is critical since it is important to make sure that the sub-bandgap photons ($E < E_{g1}$) are fully transmitted to lower tandem cell, as shown in Figure 8.2.

The reflectance at the back of InGaP/Air interface is modeled taking into account different light polarizations and propagation angles, Figure 8.11. The inset of Figure 8.11 shows where the back reflectance is calculated for the two cases under study. The back reflectance of the top cell increases with the increase of the air gap thickness and saturates at about 98% for the cases with and without rear ARCs. Interestingly, the insertion of rear ARCs suppresses the evanescent coupling at low air-gap thicknesses and higher optical reflectance at the back of the upper subcell can be realized with thinner airgap in case of having ARCs at the rear of the top cell.

Based on the analysis presented in Figure 8.10 and Figure 8.11, we can conclude that both front and rear ARCs are mandatory to apply photon recycling in multi-junction using the IMB approach. The thickness of the airgap should be larger than 1 μm .

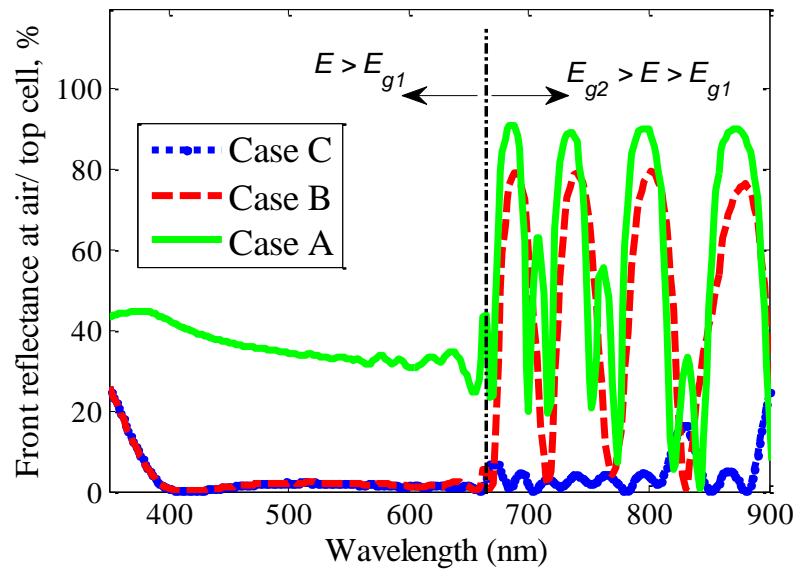


Figure 8.10: Front reflectance at air/ front of top cell interface for the structures showed in Figure 8.9, for the InGaP/Air/GaAs case.

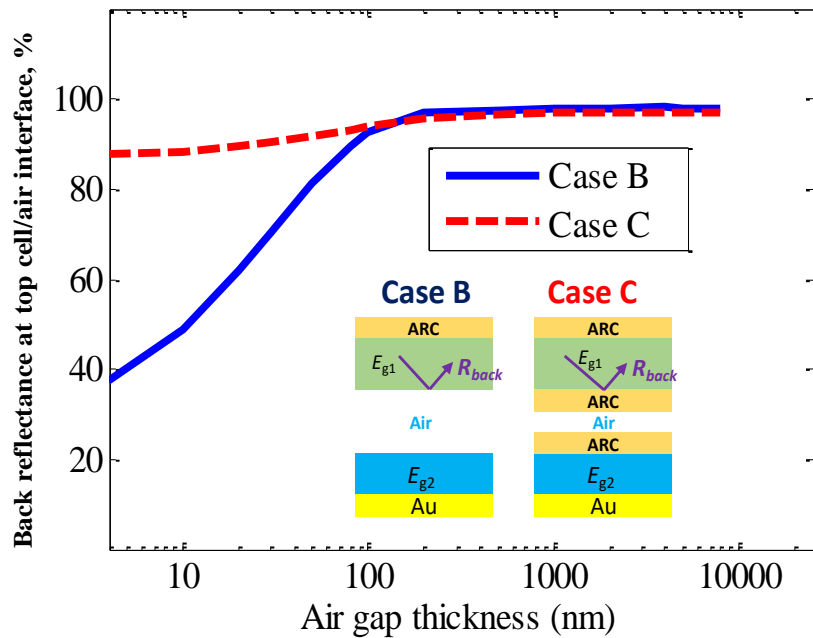


Figure 8.11: Back reflectance at top subcell/air interface. The inset shows where the back reflectance was calculated.

Chapter 9: Summary and Future Outlook

In this chapter, a summary of the research demonstrated in this dissertation is presented. The main challenges that need to be addressed for further improvements are discussed with a future guideline.

9.1. Summary of Research

In this dissertation, three InGaP-based quantum well solar cells were demonstrated. The three quantum wells (QWs) are grown in the unintentionally doped region of $\text{In}_{0.49}\text{Ga}_{0.51}\text{P}$ p-i-n solar cells that are lattice-matched to GaAs substrates.

The aim of developing these quantum well structures is to demonstrate a solar cell with a bandgap in the 1.6-1.8 eV range. There are several multi-junction solar cell designs that will benefit from this work as was discussed in Section 4.2 of Chapter 4. For example, next-generation five and six junction devices need a subcell with a bandgap of ~1.7 eV as the second highest energy subcell in these two stacks with a prospective efficiency higher than 50% under high solar concentration. In addition, a dual-junction device that has a top cell of 1.7 eV and a bottom cell of 1.1 eV forms the optimal bandgap configuration, with a prospective one-sun AM1.5G efficiency of 36-38%. Also, triple-junction devices (1.75/1.2/0.7 eV), requires prospective top cell with a bandgap of 1.75 eV to alleviate the current mismatch between top and middle cells. Finally, next-generation seven (or more) junction devices, as indicated by modeling, need a bandgap of 1.6-1.8 eV with prospective efficiencies higher than 50%.

In Chapters 4-7, these quantum well solar cells were presented, with the advantages and challenges of each structure are being discussed.

The first quantum well solar cell presented in this dissertation is strain-balanced $\text{In}_x\text{Ga}_{1-x}\text{P}/\text{In}_y\text{Ga}_{1-y}\text{P}$, where the $\text{In}_x\text{Ga}_{1-x}\text{P}$ well and the $\text{In}_y\text{Ga}_{1-y}\text{P}$ barrier is grown under compressive stress and tensile stress, respectively, where $x > 0.49$ and $y < 0.49$. The strain-balanced $\text{In}_x\text{Ga}_{1-x}\text{P}/\text{In}_y\text{Ga}_{1-y}\text{P}$ quantum wells are grown in the unintentionally doped i layer of $\text{In}_{0.49}\text{Ga}_{0.51}\text{P}$ p-i-n solar cells that are lattice-matched to GaAs substrates. X-ray diffraction (XRD) results confirm that multiple quantum well regions of well-defined periodicity were formed, and the presence of higher-order satellite peaks indicates the formation of defined interfaces between well/barrier and barrier/well. The mirror-like surface as indicated by optical microscopy confirms that strain-balance condition

was met. Both the XRD and optical microscopy results confirm success in growing these quantum wells from an epitaxial growth perspective. However, the external quantum efficiency shows very limited extension for the absorption threshold beyond the band-edge of $\text{In}_{0.49}\text{Ga}_{0.51}\text{P}$ (680 nm). More details are discussed in Chapter 4.

The second quantum well solar cell structure presented in this dissertation is strain-balanced $\text{In}_x\text{Ga}_{1-x}\text{As}_{1-z}\text{P}_z/\text{In}_y\text{Ga}_{1-y}\text{P}$, where the $\text{In}_x\text{Ga}_{1-x}\text{As}_{1-z}\text{P}_z$ well and the $\text{In}_y\text{Ga}_{1-y}\text{P}$ barrier is grown under compressive stress and tensile stress, respectively. The $\text{In}_x\text{Ga}_{1-x}\text{As}_{1-z}\text{P}_z/\text{In}_y\text{Ga}_{1-y}\text{P}$ SBMQWs have been grown with compositions of $0.60 < x < 0.75$, $0.35 < y < 0.43$, and $0.9 < z < 0.98$ and periods of total thickness ranging from 80 Å to 230 Å. The diffraction pattern consists of the (004) GaAs substrate reflection peak and several satellite peaks due to the periodicity of the QWs. Nomarski differential interference microscopy images of the surfaces show a mirror-like surface for InGaAsP/InGaP SBMQW of well thickness of 45 Å. Quantum well solar cells with thicker wells have a more surface cross-hatched surface indicating the presence of dislocation. This is attributed to approaching or exceeding the critical layer thickness constraints. The peak photoluminescence (PL) emission of $\text{In}_{0.70}\text{Ga}_{0.30}\text{As}_{0.05}\text{P}_{0.95}/\text{In}_{0.40}\text{Ga}_{0.60}\text{P}$ SBMQWs can be tuned from 1.85 to 1.65 eV. The peak PL wavelength emission increases as the thickness of the well increases. This behavior can be attributed to a reduced quantum size effect (QSE) associated with thicker wells, leading to a red-shift in emission energy since the compositions are fixed in this study. The PL spectrum of thick well structures is broader and less intense compared to those of thin wells. This behavior is because samples with thicker-wells are approaching or exceeding our estimate for the critical thickness (~90 Å). External quantum efficiency measurements show that the inclusion of strain-balanced layers in the depletion region of InGaP device extends the EQE spectrum beyond the InGaP band-edge due to sub-bandgap absorption by the quantum wells. The absorption edge was extended into the red-region to 730 nm, 757 nm, and 780 nm, respectively using well thickness of 45 Å, 55 Å, and 75 Å, respectively. The thin-well quantum well solar cells have almost the same quantum efficiency of the standard cell indicating that carrier transport through the quantum well region is almost perfect. The quantum efficiency of the thick-well device is reduced. This behavior can be due to two reasons. First, the reduced minority carrier lifetime in the quantum wells as indicated by the drastic reduction in the photoluminescence intensity and the weak satellite XRD peaks for thicker wells approaching the CLT. The effect of the quantum well number of the sub-bandgap EQE values was also studied. The external quantum efficiency results indicate that

increasing the number of quantum wells increase the sub-bandgap EQE values up to a certain limit. Further increase in the number of quantum wells does not enhance the EQE more due to the presence of a weak electric field region. More details are discussed in Chapter 4 and Chapter 5.

The third quantum well solar cell structure presented in this dissertation is the lattice-matched InGaAsP/InGaP grown in the unintentionally doped region of InGaP p-i-n solar cells. We have grown nominally lattice matched InGaAsP/InGaP quantum wells to tune the bandgap of InGaP-based solar cells. By analyzing the *in-situ* curvature monitoring and X-ray diffraction results, the quantum wells have been grown with minimal stress and sharp interfaces. The quantum wells have been grown with fixed indium and phosphorous precursor flows and two different gallium precursors to obtain sharp interfaces. The effect of growing the quantum wells on 6°A and 2°B miscuts have been analyzed and compared, highlighting nearly equivalent or similar performance on both miscuts. We studied the effect of growth pauses on different substrate miscuts where a 3-second growth pause with phosphine improves the interfaces, as indicated by the XRD results. Thick-period devices suffer more from accumulating strain than the thin-well devices. A nearly-strain-free, thin-period QW device has been successfully grown with 100 periods. More details are presented in Chapter 6. The sub-bandgap EQE of lattice-matched InGaAsP/InGaP QW solar cell from 25% to higher than 75% at 700 nm. The improvements were realized by modifying the QW design to grow the InGaAsP wells and InGaP barriers lattice-matched with more than 65% absorbing wells; growing a 100-period QW with minimal stress and removing the substrate during processing and depositing BSR. Strong Fabry-Perot resonance peaks were measured in devices with a BSR but no front antireflective-coating and the EQE values were highly improved in the proximity of these peaks. The bandgap-voltage offset of these QW devices indicates excellent voltages while maintaining efficient carrier transport for both electrons and holes. The short circuit current density is 26% higher than that of a standard InGaP cell. More details are presented in Chapter 7.

9.2. Challenges and Future Outlook

In this section, the challenges with developing higher-efficiency quantum well solar cells and the potential for incorporating quantum wells in next-generation multi-junction devices are discussed. There are two main issues that need to be addressed to realize high-efficiency solar cells that incorporate QWs, as shown in Figure 9.1: (1) enhancing the sub-bandgap EQE to higher

values, and (2) extending the absorption threshold to longer wavelengths (lower energies) to optimize the bandgap. The discussion in this section is not limited to the strain-balanced or lattice-matched InGaAsP/InGaP quantum well solar cells demonstrated in this dissertation. The discussion is further extended to include other QWs such as the strain-balanced InGaAs/GaAsP and strained InGaN/GaN quantum well solar cells that were reviewed in Chapter 3.

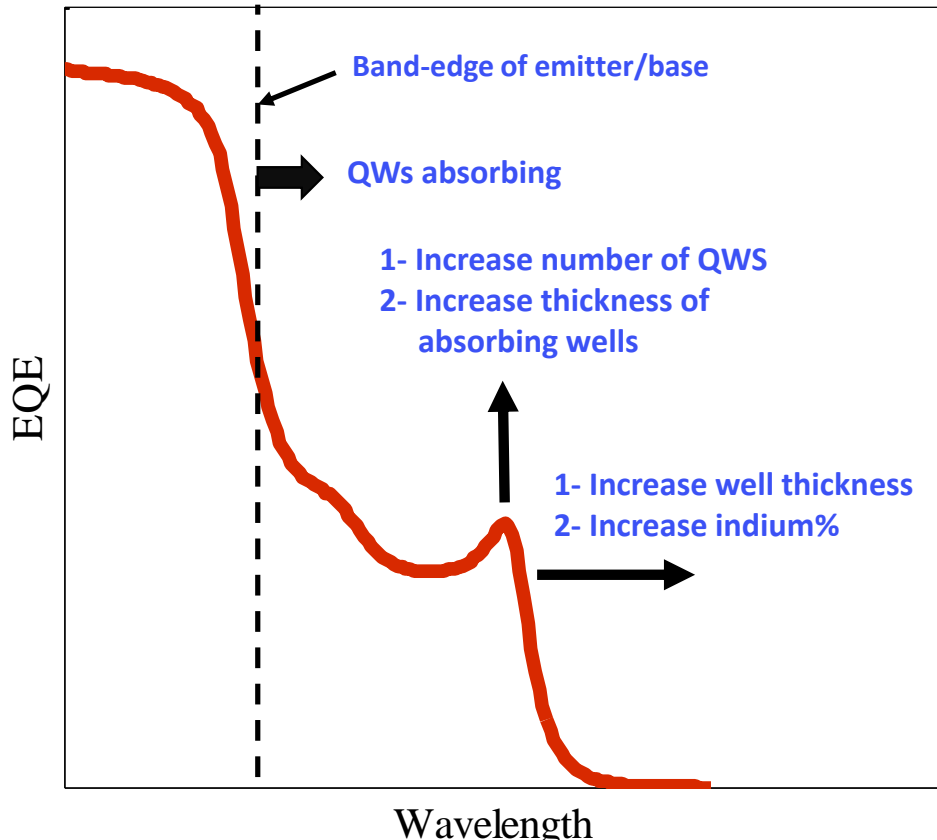


Figure 9.1: External quantum efficiency versus wavelength, showing the potential strategies for enhancing the sub-bandgap quantum efficiency of QW solar cell devices. The vertical dotted line is the band-edge of emitter/base. The region beyond the band-edge is where the QWs are absorbing.

There are two main strategies to enhance the sub-bandgap EQE: (i) increasing the number of QWs, and (ii) increasing the thickness of the absorbing quantum well relative to the barrier, Figure 9.1. First, an increase in the number of QWs improves the short-circuit current and efficiency as discussed in Chapter 5 for the InGaAsP/InGaP QW structure and as previously discussed in Chapter 3 in the review of InGaN/GaN and InGaAs/GaAsP. There are three main issues that challenge the high number of QWs growth and few potential strategies to address these challenges:

9.2.1 Stress management issue

Increasing the number of QWs requires proper management of stress buildup during growth. This is because increasing the number of interfaces might induce defects/dislocations which degrade the efficiency if the strain-balance condition was not fully realized. This requires adjusting the thicknesses of wells/barriers as well as the compositions to realize the strain-balance condition as discussed in Chapters 2 and 4. In order to address the stress management issue, researchers have used approaches like in-situ curvature discussed in Chapter 5 of this dissertation and reflection measurements to estimate the stress build-up during growth using Stoney's formula [137, 155, 179, 180]. These techniques can offer the flexibility of adjusting the growth conditions in the middle of the experiment to manage the stress. For example, if the net stress during the growth of the first few QWs in InGaAsP/InGaP is tensile, the thickness of InGaAsP should be increased or the InGaP should be decreased, in order to balance the tensile stress by a compressive stress.

9.2.2 Carrier transport issue

The second issue that needs to be addressed with increasing the number of QWs, is to guarantee efficient carrier collection across the QW region. For instance, the tunneling probability ($P_{tun.}$) for heavy holes of a single $\text{In}_{0.32}\text{Ga}_{0.68}\text{As}_{0.55}\text{P}_{0.45}/\text{In}_{0.49}\text{Ga}_{0.51}\text{P}$ (40 Å) QW is 99.2%. Increasing the number of QWs to 20 and 100 will lead to a tunneling escape probability of 85.1% and 44.67%, respectively. Hence this indicates the QW design is not fully optimized to guarantee carrier collection by drift for the heavy holes in the 100-period QW device. To address this issue, the layers' thicknesses should be optimized to increase the probabilities for tunneling and thermionic-emission. For example, reducing the $\text{In}_{0.49}\text{Ga}_{0.51}\text{P}$ barrier thickness from 40 Å to 25 Å will enhance the probability of tunneling from 44.67% to 98.48% across the 100 QWs, thus indicating the heavy holes can be efficiently collected.

9.2.3 Electric field and background doping issue

Increasing the number of QWs might result in including few QWs in a region where the electric field is very low or the SRH recombination rate is very high. It is thus crucial to guarantee a uniform electric field distribution across the QW region. Hence, strategies such as reducing the background doping through compensation doping or use of precursors that result in less p-type contamination might be essential to guarantee both efficient light absorption and carrier collection.

The second strategy that leads to enhancing the sub-bandgap EQE is to increase the percentage of absorbing well thickness relative to the barrier thickness and using thin barriers to enable carrier tunneling, as discussed in Chapter 7 for InGaAsP/InGaP and in the review of the recent progress of InGaAs/GaAsP presented in Chapter 3. For instance, the use of 100-period $\text{In}_{0.11}\text{Ga}_{0.89}\text{As}$ (93 Å)/ $\text{GaAs}_{0.93}\text{P}_{0.07}$ (160 Å) results in a total absorbing $\text{In}_{0.11}\text{Ga}_{0.89}\text{As}$ thickness of 0.93 μm and total QW region thickness of ~2.5 μm. However, the use of a structure which relies on high-phosphorous in the barrier such as $\text{In}_{0.14}\text{Ga}_{0.86}\text{As}$ (115 Å)/ $\text{GaAs}_{0.24}\text{P}_{0.76}$ (27 Å) and growing an 80-period device will result in the same total absorbing InGaAs thickness (~0.93 um) with much thinner QW region (~1.13 μm). Thus, this will allow a further increase in the number of QWs to enhance the sub-bandgap EQE. It is also worth pointing out that the well thickness should be kept less than the critical layer thickness as discussed in Chapter 2.

If the two previously mentioned strategies are combined, increasing both the number of QWs and the thickness of absorbing wells, this should correspond to a major enhancement in the sub-bandgap EQE.

To extend the absorption threshold to longer wavelengths, two main strategies can be followed: (i) increasing the quantum well thickness to reduce quantum size effects, and (ii) increasing the indium percentage in the quantum well. The well-thickness/indium-content increase might have negative effects on the performance of the QW solar cell, if not addressed properly. The first effect is an increase in the compressive stress which might result in a violation of strain-balance condition if tensile stress was not increased to strain-balance the QW structure. This can be addressed in any strain-balanced QW structure such as InGaAsP/InGaP demonstrated in this dissertation and in other QWs such InGaAs/GaAsP by adjusting the compositions and the thicknesses of GaAsP and InGaP barriers to meet the strain-balance condition. However, increasing the thickness or indium percentage in strained InGaN/GaN might degrade the InGaN film quality especially for indium compositions higher than 20%. The second effect, due to well-thickness/indium-content increase, is the increase in the effective barrier height for both the electrons and heavy holes to maintain the strain-balance condition. This will reduce the tunneling and thermionic-emission probabilities, as implied by Eqns. (2.10) and (2.11) and will affect the carrier collection (by drift).

To address the increase in the barrier height issue, a barrier of composition that is closer to the lattice constant of GaAs substrate can be used. This is more effective in a QW structure that relies

on thermionic emission carrier transport. For example, strain-balanced $\text{In}_{0.73}\text{Ga}_{0.27}\text{As}_{0.05}\text{P}_{0.95}$ (45 Å)/ $\text{In}_{0.32}\text{Ga}_{0.68}\text{P}$ (150 Å) structure has a barrier height for electrons of 0.188 eV and thermionic-emission probability for electrons across 50 QWs is 92.75%. If the well thickness was increased from 45 Å to 80 Å to enhance the sub-bandgap EQE, the barrier height will also be increased from 0.188 to 0.2247 V and the thermionic emission probability will be reduced from 92.75% to 57.6%, which will degrade the device performance. If an $\text{In}_{0.45}\text{Ga}_{0.55}\text{P}$ barrier (80 Å) was used, instead of $\text{In}_{0.32}\text{Ga}_{0.68}\text{P}$ (80 Å), the barrier height for n=1 electrons will be reduced from 0.2247 to 0.15 V and this will enhance the thermionic emission probability to 96%. The thickness of the barrier should be adjusted in all structures to maintain the strain-balanced condition.

In addition to enhancing the sub-bandgap EQE values and extending the absorption threshold, one has to deal with the challenges associated with each material system such as the phase separation issue in InGaAsP and InGaN, the group V switching issue in InGaAs/GaAsP system, and the difficulty of high quality InGaN with with 20% or higher indium as discussed in Chapters 3 and 6.

There are several potential applications for QWs in next-generation solar cell devices. These applications are driven by favorable properties of QWs such as bandgap tunability, the growth of structures that are lattice matched to substrates, the low-temperature of growth of the QWs which prevents any thermal degradation of the tunnel junction, and the complexity of achieving high-efficiency bulk absorbers of similar bandgaps to QWs. The optimum bandgaps needed for subcells in 2-8 junction devices, under constrained AM1.5G, are shown in Figure 9.2 [97]. The horizontal dotted lines in Figure 9.2, represent the bandgap range that can be realized using the InGaAs/GaAsP, InGaAsP/InGaP, and InGaN/GaN. As shown in Figure 9.2, there is a potential for using QWs in several multijunction devices. For example, strain-balanced or lattice-matched InGaAsP/InGaP can be used as a 1.6-1.8 eV subcell in five (or more) multi-junction cells. Also, if a 1.1 eV InGaAs/GaAsP structure is used as a bottom cell and a 1.7 eV InGaAsP/InGaP QW is grown on top of it, the two QWs will be grown strain-balanced to GaAs substrates and there will not be a need for a compositionally graded buffer as in the inverted metamorphic approach. It should be also mentioned that the use of AlInGaP might be inefficient for the subcells with bandgaps higher than 2.2 eV shown in Figure 9.2, due to the unavailability of higher bandgap windows that are lattice-matched to GaAs substrates. On the other hand, using the nitride-based

InGaN/GaN QW system, these bandgaps can be accessible as shown in Figure 9.2. Hence, the growth of high quality of InGaN films with indium percentage that is higher than 20% is mandatory for next-generation six (or more) junctions. It should be mentioned that the values for the optimum bandgaps might change under high solar concentrations and this might open up new avenues for the use of different QW structures or designs [97].

By increasing the number of junctions in the multi-junction stack, there will be less current generated from each subcell. Comparing multi-junction solar cell devices based on four junction and seven junctions, the seven-junction device will exhibit a lower-current and a higher voltage than the four-junction device. Thus, it is important to guarantee that each subcell in next-generation five (or more) junction devices, generates voltage close to the fundamental limit. To assess how close the solar cells to the fundamental limit set by Shockley-Quassier, the bandgap-voltage offset, $W_{oc} = E_g - V_{oc}$, is typically used as a figure of merit [51]. A W_{oc} close to 0.4 V indicates high internal radiative efficiency. Quantum well solar cells, typically attain W_{oc} values close to 0.4 V. The W_{oc} of the InGaAsP/InGaP, demonstrated in Chapter 7, is 0.41V Similarly, The InGaAs/GaAsP, reviewed in Chapter 3, has a W_{oc} value of 0.38 V. Thus, quantum well solar cells offers this advantage and can potentially be incorporated in multi-junction solar cells to enhance the cell efficiency. Beyond the use of QWs in solar cells, various QW structures and designs have also shown significant promise in other optoelectronic devices such as light emitting diodes, modulators, photodiodes, and lasers.

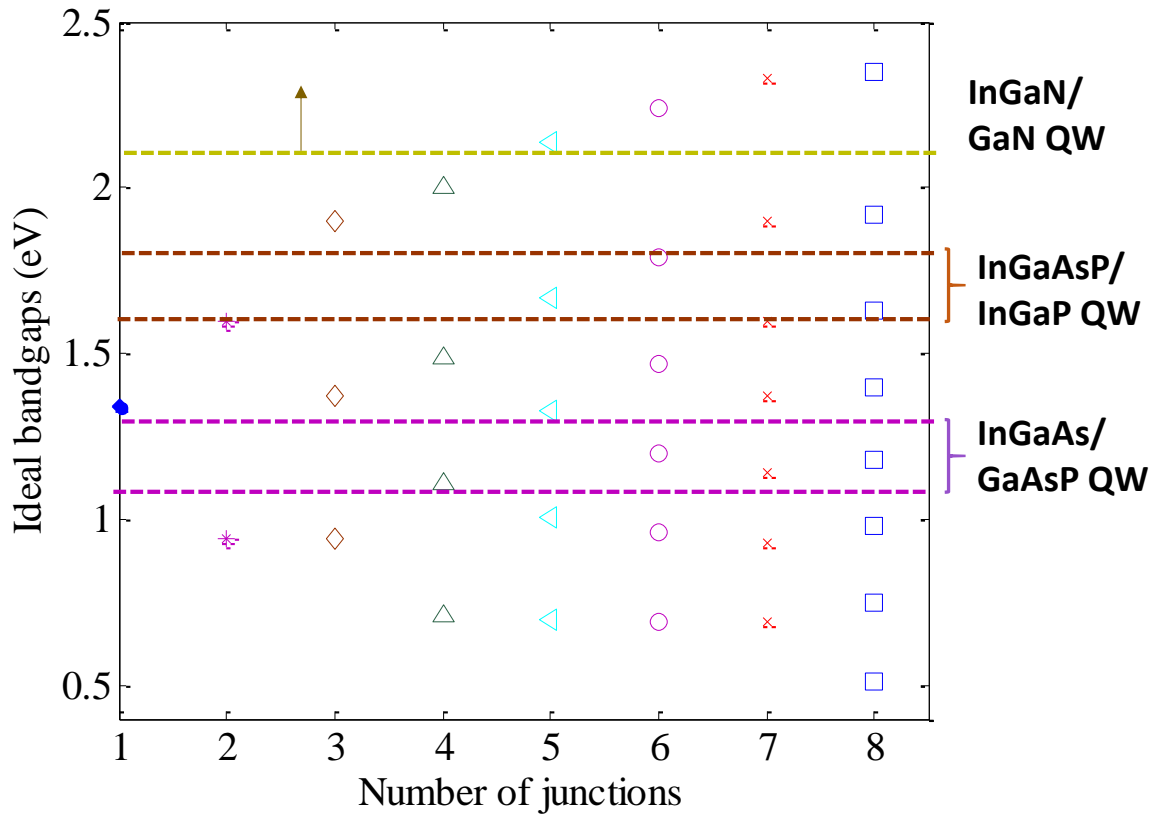


Figure 9.2: Ideal bandgap energy for each junction in a multi-junction solar cell as the number of junctions is increased from one to eight. InGaAs/GaAsP, InGaAsP/InGaP, and InGaN/GaN quantum well solar cell structures can be used to realize the bandgap range identified by the horizontal dotted lines. The data for ideal bandgaps are plotted from ref. [97].

Bibliography

- [1] *Key World Energy Statistics, International Energy Agency, 2017.* Available: <https://www.iea.org/publications/freepublications/publication/KeyWorld2017.pdf>
- [2] S. Shafiee and E. Topal, "When will fossil fuel reserves be diminished?," *Energy policy*, vol. 37, no. 1, pp. 181-189, 2009.
- [3] U. G. C. R. Program, *Global climate change impacts in the United States*. Cambridge University Press, 2009.
- [4] S. J. Smith, J. v. Aardenne, Z. Klimont, R. J. Andres, A. Volke, and S. Delgado Arias, "Anthropogenic sulfur dioxide emissions: 1850–2005," *Atmospheric Chemistry and Physics*, vol. 11, no. 3, pp. 1101-1116, 2011.
- [5] M. A. Green *et al.*, "Solar cell efficiency tables (version 50)," *Progress in Photovoltaics*, vol. 25, no. 7, 2017.
- [6] S. Philipps, A. Bett, K. Horowitz, and S. Kurtz, "Current Status of Concentrator Photovoltaic (CPV) Technology," National Renewable Energy Laboratory (NREL), Golden, CO.2015.
- [7] J. Nelson, *The physics of solar cells*. World Scientific Publishing Company, 2003.
- [8] D. A. Clugston and P. A. Basore, "PC1D version 5: 32-bit solar cell modeling on personal computers," in *Photovoltaic Specialists Conference, 1997., Conference Record of the Twenty-Sixth IEEE*, 1997, pp. 207-210: IEEE.
- [9] R. M. France *et al.*, "Quadruple-junction inverted metamorphic concentrator devices," *IEEE Journal of Photovoltaics*, vol. 5, no. 1, pp. 432-437, 2014.
- [10] J. F. Geisz, M. A. Steiner, I. Garcia, S. R. Kurtz, and D. J. Friedman, "Enhanced external radiative efficiency for 20.8% efficient single-junction GaInP solar cells," *Applied Physics Letters*, vol. 103, no. 4, p. 041118, 2013.
- [11] F. Dimroth *et al.*, "Wafer bonded four-junction GaInP/GaAs//GaInAsP/GaInAs concentrator solar cells with 44.7% efficiency," *Progress in Photovoltaics: Research and Applications*, vol. 22, no. 3, pp. 277-282, 2014.
- [12] B. G. Streetman and S. K. Banerjee, *Solid State Electronic Devices: Global Edition*. Pearson education, 2016.
- [13] Solar spectrum irradiance, AM0, AM1.5G, and AM1.5D. Link: <http://rredc.nrel.gov/solar/spectra/>
- [14] W. Shockley and H. J. Queisser, "Detailed balance limit of efficiency of p-n junction solar cells," *Journal of applied physics*, vol. 32, no. 3, pp. 510-519, 1961.
- [15] S. Bedair, M. Lamorte, and J. R. Hauser, "A two-junction cascade solar-cell structure," *Applied Physics Letters*, vol. 34, no. 1, pp. 38-39, 1979.
- [16] S. Essig *et al.*, "Progress towards a 30% efficient GaInP/Si tandem solar cell," *Energy Procedia*, vol. 77, pp. 464-469, 2015.
- [17] J. F. Geisz *et al.*, "Building a Six-Junction Inverted Metamorphic Concentrator Solar Cell," *IEEE Journal of Photovoltaics*, 2017.
- [18] R. M. France *et al.*, "Design Flexibility of Ultrahigh Efficiency Four-Junction Inverted Metamorphic Solar Cells," *IEEE Journal of Photovoltaics*, vol. 6, no. 2, pp. 578-583, 2016.
- [19] A. Luque, "Will we exceed 50% efficiency in photovoltaics?," *Journal of Applied Physics*, vol. 110, no. 3, p. 031301, 2011.

- [20] C. H. Henry, "Limiting efficiencies of ideal single and multiple energy gap terrestrial solar cells," *Journal of applied physics*, vol. 51, no. 8, pp. 4494-4500, 1980.
- [21] N. G. Toledo and U. K. Mishra, "InGaN solar cell requirements for high-efficiency integrated III-nitride/non-III-nitride tandem photovoltaic devices," *Journal of Applied Physics*, vol. 111, no. 11, p. 114505, 2012.
- [22] N. G. Toledo *et al.*, "Design of integrated III-nitride/non-III-nitride tandem photovoltaic devices," *Journal of Applied Physics*, vol. 111, no. 5, p. 054503, 2012.
- [23] G. Letay, C. Baur, and A. Bett, "Theoretical investigations of III-V multi-junction concentrator cells under realistic spectral conditions," in *Presented at the 19th European Photovoltaic Solar Energy Conference*, 2004, vol. 7, p. 11.
- [24] G. B. Stringfellow, *Organometallic vapor-phase epitaxy: theory and practice*. Academic Press, 1999.
- [25] R. King *et al.*, "Next-generation, high-efficiency III-V multijunction solar cells," in *Photovoltaic Specialists Conference, 2000. Conference Record of the Twenty-Eighth IEEE*, 2000, pp. 998-1001: IEEE.
- [26] W. Guter *et al.*, "Current-matched triple-junction solar cell reaching 41.1% conversion efficiency under concentrated sunlight," *Applied Physics Letters*, vol. 94, no. 22, p. 223504, 2009.
- [27] T. Katsuyama, S. Bedair, N. Giles, R. Burns, and J. Schetzina, "Growth and characterization of InGaAs/GaAsP strained layer superlattices," *Journal of applied physics*, vol. 62, no. 2, pp. 498-502, 1987.
- [28] S. Bedair, "Intermetallic bonded multi-junction structures," US Patent, application number: 15593414, 2017.
- [29] D. M. Chapin, C. Fuller, and G. Pearson, "A new silicon p-n junction photocell for converting solar radiation into electrical power," *Journal of Applied Physics*, vol. 25, no. 5, pp. 676-677, 1954.
- [30] S. Bedair, M. Lamorte, and J. Hauser, "A two-junction cascade solar-cell structure," *Applied Physics Letters*, vol. 34, no. 1, pp. 38-39, 1979.
- [31] N. Jain *et al.*, "High-efficiency inverted metamorphic 1.7/1.1 eV GaInAsP/GaInAs dual-junction solar cells," *Applied Physics Letters*, vol. 112, no. 5, p. 053905, 2018.
- [32] M. A. Green, K. Emery, Y. Hishikawa, W. Warta, and E. D. Dunlop, "Solar cell efficiency tables (version 47)," *Progress in Photovoltaics: Research and Applications*, vol. 24, no. 1, pp. 3-11, 2016.
- [33] T. Takamoto, H. Washio, and H. Juso, "Application of InGaP/GaAs/InGaAs triple junction solar cells to space use and concentrator photovoltaic," in *Photovoltaic Specialist Conference (PVSC), 2014 IEEE 40th*, 2014, pp. 0001-0005: IEEE.
- [34] J. Geisz *et al.*, "Pathway to 50% Efficient Inverted Metamorphic Concentrator Solar Cells," The 13th International Conference on Concentrator Photovoltaics (CPV-13), Ottawa, Canada, 2017
- [35] I. Garcia *et al.*, "Metamorphic III–V Solar Cells: Recent Progress and Potential," *IEEE Journal of Photovoltaics*, vol. 6, no. 1, pp. 366-373, 2016.
- [36] S. Bedair, T. Katsuyama, M. Timmons, and M. Tischler, "A new GaAsP—InGaAs strained-layer super-lattice light-emitting diode," *Electron Device Letters, IEEE*, vol. 5, no. 2, pp. 45-47, 1984.

- [37] T. Katsuyama, M. Tischler, D. Moore, N. Hamaguchi, N. Elmasry, and S. Bedair, "New approaches for high efficiency cascade solar cells," *Solar cells*, vol. 21, no. 1, pp. 413-418, 1987.
- [38] X. Li, V. D. Dasika, P.-C. Li, L. Ji, S. R. Bank, and E. T. Yu, "Minimized open-circuit voltage reduction in GaAs/InGaAs quantum well solar cells with bandgap-engineered graded quantum well depths," *Applied Physics Letters*, vol. 105, no. 12, p. 123906, 2014.
- [39] N. Ekins-Daukes *et al.*, "Strain-balanced GaAsP/InGaAs quantum well solar cells," *Applied Physics Letters*, vol. 75, no. 26, pp. 4195-4197, 1999.
- [40] H. Fujii, K. Toprasertpong, Y. Wang, K. Watanabe, M. Sugiyama, and Y. Nakano, "100-period, 1.23-eV bandgap InGaAs/GaAsP quantum wells for high-efficiency GaAs solar cells: toward current-matched Ge-based tandem cells," *Progress in Photovoltaics: Research and Applications*, 2013.
- [41] G. K. Bradshaw, C. Z. Carlin, J. P. Samberg, N. A. El-Masry, P. C. Colter, and S. M. Bedair, "Carrier transport and improved collection in thin-barrier InGaAs/GaAsP strained quantum well solar cells," *Photovoltaics, IEEE Journal of*, vol. 3, no. 1, pp. 278-283, 2013.
- [42] K.-H. Lee *et al.*, "Demonstration of photon coupling in dual multiple-quantum-well solar cells," *Photovoltaics, IEEE Journal of*, vol. 2, no. 1, pp. 68-74, 2012.
- [43] R. Dahal, B. Pantha, J. Li, J. Lin, and H. Jiang, "InGaN/GaN multiple quantum well solar cells with long operating wavelengths," *Applied Physics Letters*, vol. 94, no. 6, p. 063505, 2009.
- [44] R. Dahal, J. Li, K. Aryal, J. Lin, and H. Jiang, "InGaN/GaN multiple quantum well concentrator solar cells," *Applied Physics Letters*, vol. 97, no. 7, p. 073115, 2010.
- [45] K. Lai, G. Lin, Y.-L. Lai, Y. Chen, and J. He, "Effect of indium fluctuation on the photovoltaic characteristics of InGaN/GaN multiple quantum well solar cells," *Applied Physics Letters*, vol. 96, no. 8, p. 081103, 2010.
- [46] R. M. Farrell *et al.*, "High quantum efficiency InGaN/GaN multiple quantum well solar cells with spectral response extending out to 520 nm," *Applied Physics Letters*, vol. 98, no. 20, p. 201107, 2011.
- [47] D. Van Den Broeck, D. Bharrat, A. Hosalli, N. El-Masry, and S. Bedair, "Strain-balanced InGaN/GaN multiple quantum wells," *Applied Physics Letters*, vol. 105, no. 3, p. 031107, 2014.
- [48] S. Bedair, J. L. Harmon, C. Z. Carlin, I. E. H. Sayed, and P. Colter, "High performance as-grown and annealed high band gap tunnel junctions: Te behavior at the interface," *Applied Physics Letters*, vol. 108, no. 20, p. 203903, 2016.
- [49] S. M. Bedair, J. L. Harmon, C. Z. Carlin, I. E. H. Sayed, and P. Colter, "Annealed high band gap tunnel junctions with peak current densities above 800 A/cm²," in *Photovoltaic Specialists Conference (PVSC), 2016 IEEE 43rd*, 2016, pp. 2320-2322: IEEE.
- [50] S. Bedair, C. Z. Carlin, J. L. Harmon, I. E. H. Sayed, and P. Colter, "High performance tunnel junction with resistance to thermal annealing," in *AIP Conference Proceedings*, 2016, vol. 1766, no. 1, p. 020003: AIP Publishing.
- [51] R. King *et al.*, "Band gap-voltage offset and energy production in next-generation multijunction solar cells," *Progress in Photovoltaics: Research and Applications*, vol. 19, no. 7, pp. 797-812, 2011.
- [52] S. Adachi, "Material parameters of In_{1-x}Ga_xAs_yP_{1-y} and related binaries," *Journal of Applied Physics*, vol. 53, no. 12, pp. 8775-8792, 1982.

- [53] P. Harrison and Q. Wells, "Wires and Dots: Theoretical and Computational Physics," ed: Wiley, New York, 2000.
- [54] H. Asai and K. Oe, "Energy band-gap shift with elastic strain in Ga_xIn_{1-x}P epitaxial layers on (001) GaAs substrates," *Journal of Applied Physics*, vol. 54, no. 4, pp. 2052-2056, 1983.
- [55] G. Bastard, E. Mendez, L. Chang, and L. Esaki, "Variational calculations on a quantum well in an electric field," *Physical Review B*, vol. 28, no. 6, p. 3241, 1983.
- [56] M. Buongiorno Nardelli, K. Rapcewicz, and J. Bernholc, "Polarization field effects on the electron-hole recombination dynamics in In_{0.2}Ga_{0.8}N/In_{1-x}Ga_xN multiple quantum wells," *Applied physics letters*, vol. 71, no. 21, pp. 3135-3137, 1997.
- [57] B. A. Foreman, "Analytic model for the valence-band structure of a strained quantum well," *Physical Review B*, vol. 49, no. 3, p. 1757, 1994.
- [58] J. Matthews and A. Blakeslee, "Defects in epitaxial multilayers: I. Misfit dislocations," *Journal of Crystal Growth*, vol. 27, pp. 118-125, 1974.
- [59] J. Matthews and A. Blakeslee, "Defects in epitaxial multilayers: III. Preparation of almost perfect multilayers," *Journal of Crystal Growth*, vol. 32, no. 2, pp. 265-273, 1976.
- [60] D. Holec, Y. Zhang, D. S. Rao, M. J. Kappers, C. McAleese, and C. J. Humphreys, "Equilibrium critical thickness for misfit dislocations in III-nitrides," *Journal of Applied Physics*, vol. 104, no. 12, p. 123514, 2008.
- [61] C. Parker, J. Roberts, S. Bedair, M. Reed, S. Liu, and N. El-Masry, "Determination of the critical layer thickness in the InGaN/GaN heterostructures," *Applied Physics Letters*, vol. 75, no. 18, pp. 2776-2778, 1999.
- [62] M. Reed, N. El-Masry, C. Parker, J. Roberts, and S. Bedair, "Critical layer thickness determination of GaN/InGaN/GaN double heterostructures," *Applied Physics Letters*, vol. 77, no. 25, pp. 4121-4123, 2000.
- [63] N. Ekins-Daukes, K. Kawaguchi, and J. Zhang, "Strain-balanced criteria for multiple quantum well structures and its signature in X-ray rocking curves," *Crystal Growth & Design*, vol. 2, no. 4, pp. 287-292, 2002.
- [64] J. Nelson, M. Paxman, K. Barnham, J. Roberts, and C. Button, "Steady-state carrier escape from single quantum wells," *Quantum Electronics, IEEE Journal of*, vol. 29, no. 6, pp. 1460-1468, 1993.
- [65] H. Schneider and K. v. Klitzing, "Thermionic emission and Gaussian transport of holes in a GaAs/Al_xGa_{1-x}As multiple-quantum-well structure," *Physical Review B*, vol. 38, no. 9, p. 6160, 1988.
- [66] D. A. Miller, G. Livescu, J. Cunningham, and W. Y. Jan, "Quantum well carrier sweep out: relation to electroabsorption and exciton saturation," *Quantum Electronics, IEEE Journal of*, vol. 27, no. 10, pp. 2281-2295, 1991.
- [67] G. K. Bradshaw *et al.*, "GaInP/GaAs Tandem Solar Cells With InGaAs/GaAsP Multiple Quantum Wells," *IEEE Journal of Photovoltaics*, vol. 4, no. 2, pp. 614-619, 2014.
- [68] K. Toprasertpong *et al.*, "Absorption threshold extended to 1.15 eV using InGaAs/GaAsP quantum wells for over-50%-efficient lattice-matched quad-junction solar cells," *Progress in Photovoltaics: research and applications*, vol. 24, no. 4, pp. 533-542, 2016.
- [69] J. Adams *et al.*, "Recent results for single-junction and tandem quantum well solar cells," *Progress in Photovoltaics: research and applications*, vol. 19, no. 7, pp. 865-877, 2011.
- [70] G. K. Bradshaw, "Characterization and Analysis of Multi-Quantum Well Solar Cells," *Ph.D. Dissertation*. North Carolina State University, 2014.

- [71] B. F. Moody, "Strained layer superlattice solar cells, Ph.D. Dissertation," 2007.
- [72] G. K. Bradshaw, C. Z. Carlin, P. C. Colter, J. L. Harmon, J. P. Samberg, and S. M. Bedair, "Effects of barrier width on spectral response of strained layer superlattices for high efficiency solar cells," *MRS Online Proceedings Library Archive*, vol. 1211, 2009.
- [73] B. Miller, E. Schubert, U. Koren, A. Ourmazd, A. Dayem, and R. Capik, "High quality narrow GaInAs/InP quantum wells grown by atmospheric organometallic vapor phase epitaxy," *Applied physics letters*, vol. 49, no. 20, pp. 1384-1386, 1986.
- [74] T. Wang, E. Reihlen, H. Jen, and G. Stringfellow, "Systematic studies on the effect of growth interruptions for GaInAs/InP quantum wells grown by atmospheric pressure organometallic vapor-phase epitaxy," *Journal of applied physics*, vol. 66, no. 11, pp. 5376-5383, 1989.
- [75] J. Samberg, C. Carlin, G. Bradshaw, P. Colter, and S. Bedair, "Growth and Characterization of $In_xGa_{1-x}As/GaAs_{1-y}Py$ Strained-Layer Superlattices with High Values of y ($\sim 80\%$)," *Journal of Electronic Materials*, vol. 42, no. 5, pp. 912-917, 2013.
- [76] J. P. Samberg *et al.*, "Interface properties of Ga (As, P)/(In, Ga) As strained multiple quantum well structures," *Applied Physics Letters*, vol. 103, no. 7, p. 071605, 2013.
- [77] Y. Wen, Y. Wang, and Y. Nakano, "Suppressed indium diffusion and enhanced absorption in InGaAs/GaAsP stepped quantum well solar cell," *Applied Physics Letters*, vol. 100, no. 5, p. 053902, 2012.
- [78] D. Bushnell *et al.*, "Effect of well number on the performance of quantum-well solar cells," *Journal of applied physics*, vol. 97, no. 12, p. 124908, 2005.
- [79] A. G. Bhuiyan, K. Sugita, A. Hashimoto, and A. Yamamoto, "InGaN solar cells: present state of the art and important challenges," *IEEE Journal of photovoltaics*, vol. 2, no. 3, pp. 276-293, 2012.
- [80] E. Berkman, N. El-Masry, A. Emara, and S. Bedair, "Nearly lattice-matched n, i, and p layers for InGaN p-i-n photodiodes in the 365–500 nm spectral range," *Applied Physics Letters*, vol. 92, no. 10, p. 101118, 2008.
- [81] J. Wu *et al.*, "Superior radiation resistance of In $1-x$ Ga x N alloys: full-solar-spectrum photovoltaic material system," *Journal of Applied Physics*, vol. 94, no. 10, pp. 6477-6482, 2003.
- [82] L. Hsu and W. Walukiewicz, "Modeling of InGaN/Si tandem solar cells," *Journal of Applied Physics*, vol. 104, no. 2, p. 024507, 2008.
- [83] C. J. Neufeld *et al.*, "Effect of doping and polarization on carrier collection in InGaN quantum well solar cells," *Applied Physics Letters*, vol. 98, no. 24, p. 243507, 2011.
- [84] J. Wierer Jr, A. Fischer, and D. Koleske, "The impact of piezoelectric polarization and nonradiative recombination on the performance of (0001) face GaN/InGaN photovoltaic devices," *Applied physics letters*, vol. 96, no. 5, p. 051107, 2010.
- [85] J. Wierer Jr, D. Koleske, and S. R. Lee, "Influence of barrier thickness on the performance of InGaN/GaN multiple quantum well solar cells," *Applied Physics Letters*, vol. 100, no. 11, p. 111119, 2012.
- [86] J. Lang, N. Young, R. M. Farrell, Y.-R. Wu, and J. Speck, "Carrier escape mechanism dependence on barrier thickness and temperature in InGaN quantum well solar cells," *Applied Physics Letters*, vol. 101, no. 18, p. 181105, 2012.
- [87] S.-B. Choi *et al.*, "Effect of indium composition on carrier escape in InGaN/GaN multiple quantum well solar cells," *Applied Physics Letters*, vol. 103, no. 3, p. 033901, 2013.
- [88] S. J. Pearton, *GaN and related materials II*. CRC Press, 2000.

- [89] I. h. Ho and G. Stringfellow, "Solid phase immiscibility in GaInN," *Applied Physics Letters*, vol. 69, no. 18, pp. 2701-2703, 1996.
- [90] M. Behbehani, E. Piner, S. Liu, N. El-Masry, and S. Bedair, "Phase separation and ordering coexisting in In_x Ga 1–x N grown by metal organic chemical vapor deposition," *Applied physics letters*, vol. 75, no. 15, pp. 2202-2204, 1999.
- [91] D. Van Den Broeck, D. Bharrat, Z. Liu, N. El-Masry, and S. Bedair, "Growth and Characterization of High-Quality, Relaxed In_yGa_{1-y}N Templates for Optoelectronic Applications," *Journal of Electronic Materials*, vol. 44, no. 11, pp. 4161-4166, 2015.
- [92] D. M. Van Den Broeck, "Engineering Strain for Improved III-Nitride Optoelectronic Device Performance," *North Carolina State University*, Ph.D. Dissertation 2016.
- [93] S. Yamasaki *et al.*, "p-type conduction in Mg-doped Ga_{0.91}In_{0.09}N grown by metalorganic vapor-phase epitaxy," *Applied physics letters*, vol. 66, no. 9, pp. 1112-1113, 1995.
- [94] K. Kumakura, T. Makimoto, and N. Kobayashi, "Activation energy and electrical activity of Mg in Mg-doped In_xGa_{1-x}N (x< 0.2)," *Japanese Journal of Applied Physics*, vol. 39, no. 4B, p. L337, 2000.
- [95] F. Capasso, "Band-gap engineering: From physics and materials to new semiconductor devices," *Science*, vol. 235, no. 4785, pp. 172-176, 1987.
- [96] France, Ryan M., John F. Geisz, Myles A. Steiner, Daniel J. Friedman, J. Scott Ward, Jerry M. Olson, Waldo Olavarria, Ryan M. France, John F. Geisz, Ivan Garcia, Myles A. Steiner, William E. McMahon, Daniel J. Friedman, Tom E. Moriarty, Carl Osterwald, J. Scott Ward, Anna Duda, Michelle Young, Waldo Olavarria. "Design Flexibility of Ultra-High Efficiency 4-Junction Inverted Metamorphic Solar Cells." presented in Photovoltaic Specialists Conference (PVSC), 2015 IEEE 42nd
- [97] S. Bremner, M. Levy, and C. B. Honsberg, "Analysis of tandem solar cell efficiencies under AM1.5G spectrum using a rapid flux calculation method," *Progress in photovoltaics: Research and Applications*, vol. 16, no. 3, pp. 225-233, 2008.
- [98] S. Heckelmann, D. Lackner, C. Karcher, F. Dimroth, and A. W. Bett, "Investigations on AlGaAs Solar Cells Grown by MOVPE," *IEEE Journal of Photovoltaics*, vol. 5, no. 1, pp. 446-453, 2015.
- [99] N. Jain, J. F. Geisz, R. M. France, A. G. Norman, and M. A. Steiner, "Enhanced Current Collection in 1.7 eV GaInAsP Solar Cells Grown on GaAs by Metalorganic Vapor Phase Epitaxy," *IEEE Journal of Photovoltaics*, vol. 7, no. 3, pp. 927 - 933, 2017.
- [100] G. Erbert *et al.*, "High-power tensile-strained GaAsP-AlGaAs quantum-well lasers emitting between 715 and 790 nm," *Selected Topics in Quantum Electronics, IEEE Journal of*, vol. 5, no. 3, pp. 780-784, 1999.
- [101] A. Al-Muhanna, J. Wade, L. Mawst, and R. Fu, "730-nm-emitting Al-free active-region diode lasers with compressively strained InGaAsP quantum wells," *Applied physics letters*, vol. 72, no. 6, p. 641, 1998.
- [102] D. Z. Garbuзов *et al.*, "High-power 0.8. mu. m InGaAsP-GaAs SCH SQW lasers," *IEEE Journal of Quantum Electronics (Institute of Electrical and Electronics Engineers);(United States)*, vol. 27, no. 6, 1991.
- [103] F. Yam and Z. Hassan, "Innovative advances in LED technology," *Microelectronics Journal*, vol. 36, no. 2, pp. 129-137, 2005.
- [104] F. M. Steranka, "AlGaAs red light-emitting diodes," *Semiconductors and Semimetals*, vol. 48, pp. 65-96, 1997.

- [105] K. Onabe, "Calculation of miscibility gap in quaternary InGaPAs with strictly regular solution approximation," *Japanese Journal of Applied Physics*, vol. 21, no. 5R, p. 797, 1982.
- [106] G. Stringfellow, "Immiscibility and spinodal decomposition in III/V alloys," *Journal of Crystal Growth*, vol. 65, no. 1, pp. 454-462, 1983.
- [107] Y. Konaka, K.-i. Ono, Y. Terai, and Y. Fujiwara, "Coexistence properties of phase separation and CuPt-ordering in InGaAsP grown on GaAs substrates by organometallic vapor phase epitaxy," *Journal of Crystal Growth*, vol. 312, no. 14, pp. 2056-2059, 2010.
- [108] M. Tischler, T. Katsuyama, N. El-Masry, and S. Bedair, "Defect reduction in GaAs epitaxial layers using a GaAsP-InGaAs strained-layer superlattice," *Applied Physics Letters*, vol. 46, no. 3, pp. 294-296, 1985.
- [109] M. Alexiades-Armenakas, "Laser-mediated photodynamic therapy," *Clinics in Dermatology*, vol. 24, no. 1, pp. 16-25, 1// 2006.
- [110] J.-M. Hopkins, G. J. Valentine, B. Agate, A. J. Kemp, U. Keller, and W. Sibbett, "Highly compact and efficient femtosecond Cr: LiSAF lasers," *Quantum Electronics, IEEE Journal of*, vol. 38, no. 4, pp. 360-368, 2002.
- [111] Moody, Baxter F. "Strained Layer Superlattice Solar Cells," PhD Thesis, North Carolina State University. (2007)
- [112] T. Kato, T. Matsumoto, T. Kobatake, and T. Ishida, "Strain-Energy-Stabilized Growth of InGaAsP Layers on GaAs (111) A Substrates in Immiscible Region," *Japanese journal of applied physics*, vol. 26, no. 7A, p. L1161, 1987.
- [113] G. Bauer and W. Richter, *Optical characterization of epitaxial semiconductor layers*. Springer Science & Business Media, 2012.
- [114] B. L. Sharma and R. K. Purohit, *Semiconductor heterojunctions*. Elsevier, 2013.
- [115] D. Miller *et al.*, "Band-edge electroabsorption in quantum well structures: the quantum-confined Stark effect," *Physical Review Letters*, vol. 53, no. 22, p. 2173, 1984.
- [116] H.-S. Cho and P. R. Prucnal, "New formalism of the Kronig-Penney model with application to superlattices," *Physical Review B*, vol. 36, no. 6, p. 3237, 1987.
- [117] O. Ichikawa *et al.*, "Characterization of Indium Segregation in Metalorganic Vapor Phase Epitaxy-Grown InGaP by Schottky Barrier Height Measurement," *Japanese Journal of Applied Physics*, vol. 50, no. 1R, p. 011201, 2011.
- [118] G. G. de la Cruz, "The influence of surface segregation on the optical properties of quantum wells," *Journal of applied physics*, vol. 96, no. 7, pp. 3752-3755, 2004.
- [119] C. Zachary Carlin, "MOCVD growth and modeling of quantum-well solar cells and tunnel junctions," PhD Thesis (2015).
- [120] J. R. Jensen, J. M. Hvam, and W. Langbein, "Optical properties of InAlGaAs quantum wells: Influence of segregation and band bowing," *Journal of applied physics*, vol. 86, no. 5, pp. 2584-2589, 1999.
- [121] I. E. Hashem, C. Z. Carlin, B. G. Hagar, P. C. Colter, and S. Bedair, "InGaP-based quantum well solar cells: Growth, structural design, and photovoltaic properties," *Journal of Applied Physics*, vol. 119, no. 9, p. 095706, 2016.
- [122] C. Z. Carlin, G. K. Bradshaw, J. P. Samberg, P. C. Colter, and S. M. Bedair, "Minority Carrier Transport and Their Lifetime in InGaAs/GaAsP Multiple Quantum Well Structures," *Electron Devices, IEEE Transactions on*, vol. 60, no. 8, pp. 2532-2536, 2013.

- [123] A. W. Haas, J. R. Wilcox, J. L. Gray, and R. J. Schwartz, "Design of a GaInP/GaAs tandem solar cell for maximum daily, monthly, and yearly energy output," *Journal of Photonics for Energy*, vol. 1, no. 1, pp. 018001-018001-23, 2011.
- [124] D. E. Aspnes, "Optical properties of thin films," *Thin solid films*, vol. 89, no. 3, pp. 249-262, 1982.
- [125] R. Hoheisel *et al.*, "Quantum-well solar cells for space: The impact of carrier removal on end-of-life device performance," *Photovoltaics, IEEE Journal of*, vol. 4, no. 1, pp. 253-259, 2014.
- [126] I. E. Hashem, C. Zachary Carlin, B. G. Hagar, P. C. Colter, and S. M. Bedair, "InGaP-based quantum well solar cells: Growth, structural design, and photovoltaic properties," *Journal of Applied Physics*, vol. 119, no. 9, p. 095706, 2016.
- [127] I. E. H. Sayed, C. Z. Carlin, B. G. Hagar, P. C. Colter, and S. Bedair, "Strain-Balanced InGaAsP/GaInP Multiple Quantum Well Solar Cells With a Tunable Bandgap (1.65–1.82 eV)," *IEEE Journal of Photovoltaics*, vol. 6, no. 4, pp. 997-1003, 2016.
- [128] I. E. H. Sayed, B. G. Hagar, C. Z. Carlin, P. C. Colter, and S. Bedair, "InGaP-based quantum well solar cells," in *Photovoltaic Specialists Conference (PVSC), 2016 IEEE 43rd*, 2016, pp. 0147-0150: IEEE.
- [129] I. E. H. Sayed, B. G. Hagar, C. Z. Carlin, P. C. Colter, and S. M. Bedair, "Extending the absorption threshold of InGaP solar cells to 1.60 eV using quantum wells: Experimental and modeling results," in *Photovoltaic Specialists Conference (PVSC), 2016 IEEE 43rd*, 2016, pp. 2366-2370: IEEE.
- [130] J. Roberts, "A quantum well photovoltaic cell," U.K. Patent GB2463905A, 2010
- [131] N. Kobayashi and T. Makimoto, "Reduced carbon contamination in OMVPE grown GaAs and AlGaAs," *Japanese journal of applied physics*, vol. 24, no. 10A, p. L824, 1985.
- [132] H. Fujii, K. Toprasertpong, H. Sodabanlu, K. Watanabe, M. Sugiyama, and Y. Nakano, "InGaAs/GaAsP superlattice solar cells with reduced carbon impurity grown by low-temperature metal-organic vapor phase epitaxy using triethylgallium," *Journal of Applied Physics*, vol. 116, no. 20, p. 203101, 2014.
- [133] T. Kuech and R. Potemski, "Reduction of background doping in metalorganic vapor phase epitaxy of GaAs using triethylgallium at low reactor pressures," *Applied physics letters*, vol. 47, no. 8, pp. 821-823, 1985.
- [134] J. Geisz, A. Levander, A. Norman, K. Jones, and M. Romero, "In situ stress measurement for MOVPE growth of high efficiency lattice-mismatched solar cells," *Journal of Crystal Growth*, vol. 310, no. 7, pp. 2339-2344, 2008.
- [135] S. Ma, H. Sodabanlu, K. Watanabe, M. Sugiyama, and Y. Nakano, "Strain-compensation measurement and simulation of InGaAs/GaAsP multiple quantum wells by metal organic vapor phase epitaxy using wafer-curvature," *Journal of Applied Physics*, vol. 110, no. 11, p. 113501, 2011.
- [136] C. Lynch, R. Beresford, and E. Chason, "Real-time stress evolution during growth of In_xAl_{1-x}As/GaAs metamorphic buffer layers," *Journal of Vacuum Science & Technology B*, vol. 22, no. 3, pp. 1539-1543, 2004.
- [137] J. A. Floro and E. Chason, "Curvature based techniques for realtime stress measurements during thin film growth," *In-Situ Characterization of Thin Film Growth Processes*, p. 191, 2001.

- [138] G. G. Stoney, "The tension of metallic films deposited by electrolysis," *Proceedings of the Royal Society of London. Series A, Containing Papers of a Mathematical and Physical Character*, vol. 82, no. 553, pp. 172-175, 1909.
- [139] B. L. Jiang, F. Shimura, G. Rozgonyi, N. Hamaguchi, and S. Bedair, "Single-crystal x-ray diffraction study of the InGaAs-GaAsP/GaAs superlattice system," *Applied physics letters*, vol. 52, no. 15, pp. 1258-1260, 1988.
- [140] D. Kuciauskas *et al.*, "Minority carrier lifetime analysis in the bulk of thin-film absorbers using subbandgap (two-photon) excitation," *IEEE Journal of Photovoltaics*, vol. 3, no. 4, pp. 1319-1324, 2013.
- [141] K. L. Schulte, R. M. France, and J. F. Geisz, "Highly Transparent Compositinally Graded Buffers for New Metamorphic Multijunction Solar Cell Designs," *IEEE Journal of Photovoltaics*, vol. 7, no. 1, pp. 347-353, 2017.
- [142] J. Geisz *et al.*, "Pathway to 50% Efficient Inverted Metamorphic Concentrator Solar Cells," The 13th International Conference on Concentrator Photovoltaics (CPV-13), Ottawa, Canada, 2017
- [143] E. E. Perl *et al.*, "Development of high-bandgap AlGaInP solar cells grown by organometallic vapor-phase epitaxy," *IEEE Journal of Photovoltaics*, vol. 6, no. 3, pp. 770-776, 2016.
- [144] E. E. Perl *et al.*, "Development of a 2.0 eV AlGaInP solar cell grown by OMVPE," in *Photovoltaic Specialist Conference (PVSC), 2015 IEEE 42nd*, 2015, pp. 1-6: IEEE.
- [145] M. Kondo, C. Anayama, N. Okada, H. Sekiguchi, K. Domen, and T. Tanahashi, "Crystallographic orientation dependence of impurity incorporation into III-V compound semiconductors grown by metalorganic vapor phase epitaxy," *Journal of applied physics*, vol. 76, no. 2, pp. 914-927, 1994.
- [146] D. Alonso-Álvarez *et al.*, "InGaAs/GaAsP strain balanced multi-quantum wires grown on misoriented GaAs substrates for high efficiency solar cells," *Applied Physics Letters*, vol. 105, no. 8, p. 083124, 2014.
- [147] H. Sodabanlu, Y. Wang, K. Watanabe, M. Sugiyama, and Y. Nakano, "Growth of InGaAs/GaAsP multiple quantum well solar cells on mis-orientated GaAs substrates," *Journal of Applied Physics*, vol. 115, no. 23, p. 233104, 2014.
- [148] King, Richard R., et al. "Multijunction photovoltaic cell grown on high-miscut-angle substrate." U.S. Patent No. 7,812,249. 12 Oct. 2010.
- [149] L. Su, I. Ho, and G. Stringfellow, "Effects of substrate misorientation and growth rate on ordering in GaInP," *Journal of applied physics*, vol. 75, no. 10, pp. 5135-5141, 1994.
- [150] C. Z. Carlin, G. K. Bradshaw, J. P. Samberg, P. C. Colter, and S. M. Bedair, "Minority carrier transport and their lifetime in InGaAs/GaAsP multiple quantum well structures," *IEEE Transactions on Electron Devices*, vol. 60, no. 8, pp. 2532-2536, 2013.
- [151] K. Toprasertpong, H. Fujii, Y. Wang, K. Watanabe, M. Sugiyama, and Y. Nakano, "Carrier escape time and temperature-dependent carrier collection efficiency of tunneling-enhanced multiple quantum well solar cells," *IEEE Journal of Photovoltaics*, vol. 4, no. 2, pp. 607-613, 2014.
- [152] I. E. Sayed, N. Jain, M. A. Steiner, J. F. Geisz, and S. Bedair, "100-period InGaAsP/InGaP superlattice solar cell with sub-bandgap quantum efficiency approaching 80%," *Applied Physics Letters*, vol. 111, no. 8, p. 082107, 2017.

- [153] I. E. H. Sayed, C. Z. Carlin, B. Hagar, P. C. Colter, and S. M. Bedair, "Tunable GaInP solar cell lattice matched to GaAs," in *Photovoltaic Specialist Conference (PVSC), 2015 IEEE 42nd*, 2015, pp. 1-4: IEEE.
- [154] E. Yablonovitch and G. D. Cody, "Intensity enhancement in textured optical sheets for solar cells," *IEEE Transactions on Electron Devices*, vol. 29, no. 2, pp. 300-305, 1982.
- [155] I. E. Sayed *et al.*, "In-situ curvature monitoring and X-ray diffraction study of InGaAsP/InGaP quantum wells," *Journal of Crystal Growth*, vol. 475, 2017.
- [156] H. Fujii, Y. Wang, K. Watanabe, M. Sugiyama, and Y. Nakano, "Compensation doping in InGaAs/GaAsP multiple quantum well solar cells for efficient carrier transport and improved cell performance," *Journal of Applied Physics*, vol. 114, no. 10, p. 103101, 2013.
- [157] M. Steiner *et al.*, "Apparent bandgap shift in the internal quantum efficiency for solar cells with back reflectors," *Journal of Applied Physics*, vol. 121, no. 16, p. 164501, 2017.
- [158] J. F. Geisz *et al.*, "Generalized optoelectronic model of series-connected multijunction solar cells," *IEEE Journal of Photovoltaics*, vol. 5, no. 6, pp. 1827-1839, 2015.
- [159] N. Jain *et al.*, "Development of lattice-matched 1.7 eV GalnAsP solar cells grown on GaAs by MOVPE," in *Photovoltaic Specialists Conference (PVSC), 2016 IEEE 43rd*, 2016, pp. 0046-0051: IEEE.
- [160] O. D. Miller, E. Yablonovitch, and S. R. Kurtz, "Strong internal and external luminescence as solar cells approach the Shockley–Queisser limit," *IEEE Journal of Photovoltaics*, vol. 2, no. 3, pp. 303-311, 2012.
- [161] B. M. Kayes *et al.*, "27.6% conversion efficiency, a new record for single-junction solar cells under 1 sun illumination," in *Photovoltaic Specialists Conference (PVSC), 2011 37th IEEE*, 2011, pp. 000004-000008: IEEE.
- [162] R. M. France *et al.*, "Design flexibility of ultra-high efficiency 4-junction inverted metamorphic solar cells," in *Photovoltaic Specialist Conference (PVSC), 2015 IEEE 42nd*, 2015, pp. 1-3: IEEE.
- [163] A. De Vos, "Detailed balance limit of the efficiency of tandem solar cells," *Journal of Physics D: Applied Physics*, vol. 13, no. 5, p. 839, 1980.
- [164] I. Tobias and A. Luque, "Ideal efficiency of monolithic, series-connected multijunction solar cells," *Progress in Photovoltaics: Research and Applications*, vol. 10, no. 5, pp. 323-329, 2002.
- [165] A. Marti and G. L. Araújo, "Limiting efficiencies for photovoltaic energy conversion in multigap systems," *Solar Energy Materials and Solar Cells*, vol. 43, no. 2, pp. 203-222, 1996.
- [166] J. Parrott, "The limiting efficiency of an edge-illuminated multigap solar cell," *Journal of Physics D: Applied Physics*, vol. 12, no. 3, p. 441, 1979.
- [167] V. Ganapati, C.-S. Ho, and E. Yablonovitch, "Air gaps as intermediate selective reflectors to reach theoretical efficiency limits of multibandgap solar cells," *IEEE Journal of Photovoltaics*, vol. 5, no. 1, pp. 410-417, 2015.
- [168] M. A. Green, K. Emery, Y. Hishikawa, W. Warta, and E. D. Dunlop, "Solar cell efficiency tables (version 47)," *Progress in Photovoltaics: Research and Applications*, vol. 24, no. NREL/JA-5J00-65643, 2016.
- [169] L. M. Pazos-Outón *et al.*, "Photon recycling in lead iodide perovskite solar cells," *Science*, vol. 351, no. 6280, pp. 1430-1433, 2016.

- [170] T. Kirchartz, F. Staub, and U. Rau, "Impact of Photon-Recycling on the Open-Circuit Voltage of Metal Halide Perovskite Solar Cells," *ACS Energy Letters*, 2016.
- [171] V. E. Ferry *et al.*, "Light trapping in ultrathin plasmonic solar cells," *Optics express*, vol. 18, no. 102, pp. A237-A245, 2010.
- [172] I. García, J. Geisz, M. Steiner, J. Olson, D. Friedman, and S. Kurtz, "Design of semiconductor-based back reflectors for high V_{oc} monolithic multijunction solar cells," in *Photovoltaic Specialists Conference (PVSC), 2012 38th IEEE*, 2012, pp. 002042-002047: IEEE.
- [173] I. García, C. Kearns-McCoy, J. Ward, M. Steiner, J. Geisz, and S. Kurtz, "Back reflectors based on buried Al₂O₃ for enhancement of photon recycling in monolithic, on-substrate III-V solar cells," *Applied Physics Letters*, vol. 105, no. 13, p. 133507, 2014.
- [174] M. A. Steiner *et al.*, "Optically enhanced photon recycling in mechanically stacked multijunction solar cells," *IEEE Journal of Photovoltaics*, vol. 6, no. 1, pp. 358-365, 2016.
- [175] X. Sheng *et al.*, "Device Architectures for Enhanced Photon Recycling in Thin-Film Multijunction Solar Cells," *Advanced Energy Materials*, vol. 5, no. 1, 2015.
- [176] M. Steiner, J. Geisz, I. Garcia, D. Friedman, A. Duda, and S. Kurtz, "Optical enhancement of the open-circuit voltage in high quality GaAs solar cells," *Journal of Applied Physics*, vol. 113, no. 12, p. 123109, 2013.
- [177] E. Centurioni, "Generalized matrix method for calculation of internal light energy flux in mixed coherent and incoherent multilayers," *Applied Optics*, vol. 44, no. 35, pp. 7532-7539, 2005.
- [178] C. C. Katsidis and D. I. Siapkas, "General transfer-matrix method for optical multilayer systems with coherent, partially coherent, and incoherent interference," *Applied optics*, vol. 41, no. 19, pp. 3978-3987, 2002.
- [179] Y. Wang, R. Onitsuka, M. Deura, W. Yu, M. Sugiyama, and Y. Nakano, "In situ reflectance monitoring for the MOVPE of strain-balanced InGaAs/GaAsP quantum-wells," *Journal of Crystal Growth*, vol. 312, no. 8, pp. 1364-1369, 2010.
- [180] Y. P. Wang, S. J. Ma, K. Watanabe, M. Sugiyama, and Y. Nakano, "Management of highly-strained heterointerface in InGaAs/GaAsP strain-balanced superlattice for photovoltaic application," *Journal of Crystal Growth*, vol. 352, no. 1, pp. 194-198, 2012.